



TECHNISCHE
UNIVERSITÄT
WIEN
Vienna University of Technology

INSTITUT FÜR
MECHANIK UND
MECHATRONIK
Mechanics & Mechatronics



Die approbierte Originalversion dieser Diplom-/
Masterarbeit ist in der Hauptbibliothek der Tech-
nischen Universität Wien aufgestellt und zugänglich.

<http://www.ub.tuwien.ac.at>



The approved original version of this diploma or
master thesis is available at the main library of the
Vienna University of Technology.

<http://www.ub.tuwien.ac.at/eng>

Diplomarbeit

Comparison of optimal and robust MIMO control concepts for active vibration damping of a flexible beam laboratory setup

ausgeführt zum Zwecke der Erlangung des akademischen Grades eines Diplom-Ingenieurs
unter der Leitung von

Ao.Univ.Prof. Dipl.-Ing. Dr.techn. Martin Kozek
Univ.Ass. Dipl.-Ing. Dr.techn. Alexander Schirrer
Institut für Mechanik und Mechatronik
E325/A5

eingereicht an der Technischen Universität Wien

Fakultät für Maschinenwesen und Betriebswissenschaften

von

Christian Dullinger
Matr.Nr.: 0426533
Bahnhofsiedlung 20/23
4840 Vöcklabruck

Wien, am 25. Juli 2013

Christian Dullinger

Eidesstattliche Erklärung

Ich erkläre eidesstattlich, dass ich die Arbeit selbständig angefertigt, keine anderen als die angegebenen Hilfsmittel benutzt und alle aus ungedruckten Quellen, gedruckter Literatur oder aus dem Internet im Wortlaut oder im wesentlichen Inhalt übernommenen Formulierungen und Konzepte gemäß den Richtlinien wissenschaftlicher Arbeiten zitiert, durch Fußnoten gekennzeichnet bzw. mit genauer Quellenangabe kenntlich gemacht habe.

Wien, am 25. Juli 2013

Christian Dullinger

Acknowledgements

First of all I would like to thank Prof. Martin Kozek, who gave me the opportunity to write this thesis at the Vienna University of Technology, Institute of Mechanics and Mechatronics, Workgroup of Control and Process Automation. I am thankful for his support and professional advice.

Furthermore I want to thank Prof. Horst Ecker and Prof. Franz Rammerstorfer for fruitful discussions and their feedback concerning my thesis. I am especially thankful to my advisor Dr. Alexander Schirrer for all of his support, helpfulness and his personal commitment. Through a lot of motivating discussions and inspiration he motivated me to work in the exciting field of robust control.

Above all I am very grateful for the support of my parents, Brigitta and Erhard, as well as of my sisters Silvia; in many different ways during my study as well as all through my whole life.

Christian Dullinger

Kurzfassung

In dieser Arbeit werden optimale und robuste Regelkonzepte zur aktiven Dämpfung der Biegeschwingungen eines beidseitig gelenkig gelagerten, dünnen Aluminiumbalkens mit rechteckigem Querschnitt entworfen, getestet und verglichen. Zu diesem Zweck wird ein „multi-input multi-output“ (MIMO) Regelsystem mit vier in Längsrichtung wirkenden kollokierten Piezo-Patch-Aktoren und Sensoren verwendet, welche eine Schubkraft einbringen bzw. die Randfaserdehnung messen. Ein elektrodynamischer Rüttler wird zur Einbringung einer Störkraft in Schwingungsrichtung verwendet. Nichtlineare Effekte, insbesondere die Hysterese der Piezo-Patch-Aktoren und Sensoren werden nicht näher berücksichtigt bzw. modelliert, was für diesen speziellen Aufbau gerechtfertigt ist.

Da der biegeeweiche Balken bereits bei niedrigen Frequenzen gering gedämpfte Schwingungsmoden aufweist, kann er als eine typische Komponente einer Leichtbaukonstruktion angesehen werden, bei denen aktive Regelkonzepte eine zunehmend wichtige Rolle spielen.

Der Schwerpunkt dieser Arbeit ist es, die Eignung modellbasierter Regler-Entwurfsmethoden (im Speziellen: LQG Regelung, mixed-sensitivity \mathcal{H}_∞ Regelung, \mathcal{H}_∞ loop-shaping Regelung und D(G)K synthetisierte Regelung) in Hinblick auf die erzielbare Verbesserung bei der Störgrößenunterdrückung am experimentellen Regelprüfstand zu untersuchen.

Die Modelle zur Reglerauslegung werden hierzu auf zwei grundlegend verschiedene Arten erhalten.

Das erste Modell wird durch ein messdatenbasiertes Verfahren namens Systemidentifikation erstellt, bei dem gemessene Eingangs- und dazugehörige Ausgangsdaten von Algorithmen verwendet werden um mathematische (black-box) Modelle von dynamischen Systemen, unter Verwendung von statistischen Methoden, zu generieren. Speziell wird hierzu der Unterraum-Algorithmus `n4sid` der MATLAB® System Identification Toolbox™ verwendet, um stabile, lineare MIMO Zustandsraummodelle im diskreten Zeitbereich zu identifizieren.

Der zweite Ansatz besteht darin, ein (zeitkontinuierliches) Modell über die Methode der Finiten Elemente (FEM) zu erhalten. „Hermite’sche Balkenelemente“ (d.h. Euler-Bernoulli-Balken mit Hermite’schen Ansatzfunktionen) werden verwendet, um den Biegebalken zu diskretisieren. Die Aktoren werden mittels Moment-Eingängen modelliert. Kollokation von Sensoren und Aktoren führt zu einer von der Nullmatrix verschiedenen Durchgangsmatrix. Es wird gezeigt, dass der Einfluss eines montierten Rüttlers durch eine Rückkopplungsschleife modelliert werden kann, welche von einem Beschleunigungs- und Verschiebungs-Ausgang und einem Kraft-Eingang Gebrauch macht. Eine detaillierte Validierung der erhaltenen Finite-Elemente (FE) Modelle (in Bezug auf ihre statische Lösung, Eigenfrequenzen und Eigenvektoren) wird durchgeführt. Darüber hinaus zeigt der Vergleich der beiden Modelle eine überraschend gute Übereinstimmung.

Basierend auf beiden Auslegungsmodellen werden umfangreiche Regler-Auslegungsstudien durchgeführt und im Experiment validiert. Es stellt sich heraus, dass mit dem identifizierten Modell als Auslegungsmodell für die genannten Reglerentwurfverfahren ausgezeichnete Ergebnisse erzielt werden können. Darüber hinaus ist auch das auf analytischem Wege erhaltene FE Modell zu einem gewissen Grad zur Reglerauslegung geeignet, was zu Beginn dieser Arbeit fraglich war. Um jedoch zufriedenstellende Ergebnisse bei der Dämpfung der Schwingungsmoden erzielen zu können, muss, wenn das FE Modell als Reglerentwurfmodell verwendet wird, ein erhöhter Aufwand bei der Modellierung von Unsicherheiten in Kauf genommen werden.

Abstract

In this work optimal and robust control design methods are utilized for active damping of bending vibrations of a simply supported thin structural aluminium beam with rectangular cross-section. For this purpose a multi-input multi-output (MIMO) control system setup is used, comprising four collocated piezo patch actuators and sensors acting in longitudinal direction. They introduce a shear force respectively measure the outer fiber strain. An electrodynamic shaker is used to introduce a disturbance force in the direction of oscillation. Nonlinear effects, especially the hysteresis of the piezo patch actuators and sensors are disregarded which is justified for this particular setup.

Because the flexible beam has low-damped oscillatory modes already at low frequencies, it can be considered a typical component of a lightweight construction where active control concepts play an increasingly important role.

The focus of this work is to study the suitability of model-based feedback control design methods (specifically: LQG control, mixed-sensitivity \mathcal{H}_∞ control, \mathcal{H}_∞ loop-shaping control and D(G)K-synthesized control) for improving disturbance rejection of the experimental control system setup.

The design plants are obtained in two fundamentally different ways.

In the first modeling onset a measurement data-driven system identification is utilized, where measured input and associated output data are utilized by algorithms to build mathematical (black-box) models of dynamical systems applying statistical methods. In particular, the subspace algorithm `n4sid` of the MATLAB[®] System Identification Toolbox[™] is used to identify a stable, linear time-invariant (LTI), MIMO state-space model in discrete-time.

The second approach is to obtain a (continuous-time) model via the finite element method (FEM). “Hermitian beam elements” (i.e. Euler-Bernoulli beams with Hermitian shape functions) are utilized to discretize the bending beam. The actuators are modelled by moment inputs. Collocation of sensors and actuators leads to a non-zero feed-through matrix. It is shown that the influence of a mounted shaker can be modelled by a feedback loop utilizing acceleration and displacement outputs and a force input. Detailed validation of the obtained finite element (FE) model (in terms of its static solution, eigenfrequencies, and eigenvectors) is carried out. Furthermore, the comparison of both models reveals a surprisingly good match.

Extensive controller design studies are carried out based on both models and validated on the experiment. It turns out that the identified model as design plant for the mentioned design methods, excellent results can be achieved. Moreover, also the in an analytical manner obtained FE model is suitable for controller design to some extent, which at the beginning of this work was in question. However, in order to attain satisfying improvements in structural mode damping utilizing the FE model as design plant, increased effort in uncertainty modeling is required.

Contents

1	Introduction	1
1.1	Overview and Motivation (for Active Damping of Flexible Structures)	1
1.2	Goal of this Thesis	1
1.3	Structure of this Work	2
1.4	State of the Art	3
2	Experimental Setup	4
2.1	Mechanical Components	5
2.2	Software, Measuring Equipment and Signal Flow	6
3	Partial Differential Equation of Motion for Flexural Beam Vibrations	10
4	Identified Plant Model(s)	15
4.1	Identification Procedure	15
4.2	Extracting the Modes of Interest	17
4.3	Model of the Beam without Shaker	17
4.4	Model of the Beam with Mounted Shaker	20
5	Finite Element Model	25
5.1	Hermitian Beam Element	26
5.1.1	Shape functions φ_i and element displacement field $w(\xi)$	27
5.1.2	Element local stiffness matrix $\mathbf{k}^{(e)}$	28
5.1.3	Element global stiffness matrix $\mathbf{K}^{(e)}$	28
5.1.4	Global stiffness matrix \mathbf{K}	28
5.1.5	Consistent mass matrix for an element in local coordinates $\mathbf{m}^{(e)}$. . .	30
5.1.6	Consistent mass matrix for an element in global coordinates $\mathbf{M}^{(e)}$. .	30
5.1.7	Global consistent mass matrix \mathbf{M}	30
5.1.8	Damping matrix \mathbf{D}	31
5.1.9	Input matrix \mathbf{B} and consistent node loads	32
5.1.10	Output matrices for displacement (\mathbf{C}_q) and velocity (\mathbf{C}_v)	35
5.1.11	Implementation of boundary conditions	36
5.2	Second-Order Structural Model	37
5.2.1	Nodal model in nodal coordinates	37
5.2.2	Modal model in modal coordinates	37
5.2.3	Frequency response matrix of a structure (in modal coordinates) and its distinct modes	39
5.3	State-Space Structural Model	40
5.3.1	Nodal model in nodal coordinates	40

5.3.2	Modal model in modal coordinates	40
5.3.2.1	First model	41
5.3.2.2	Second model	41
5.3.2.3	Third model	41
5.3.3	Modal form (Modal model with block-diagonal state matrix \mathbf{A}_{mb}) . .	41
5.3.3.1	Modal form 1	42
5.3.3.2	Modal form 2	42
5.3.3.3	Modal form 3	42
5.3.4	Introducing a non-zero state-space feed-through matrix \mathbf{D}	43
5.4	Acceleration Output at the Shaker Position \ddot{w}_s	44
5.4.1	Second-order nodal acceleration output matrix \mathbf{C}_a	44
5.4.2	Second-order modal acceleration output matrix \mathbf{C}_{ma}	45
5.4.3	Provisional modal acceleration output matrix $\hat{\mathbf{C}}_{ma}$	45
5.4.4	Provisional modal acceleration output matrix $\hat{\mathbf{C}}_{mba}$ (corresponding to the block-diagonal state matrix \mathbf{A}_{mb})	46
5.4.5	State-space modal acceleration output matrix \mathbf{C}_{mba} and feed-through matrix \mathbf{D}_{mba} (corresponding to the block-diagonal state matrix \mathbf{A}_{mb})	46
5.5	Validation of the FE Model of the Pure Beam	47
5.5.1	Natural frequencies (analytical and FE solution)	47
5.5.2	Eigenmodes of the (pure) beam	48
5.5.3	Statical solution of the FE model (pure beam)	50
5.5.3.1	Additional output matrix for displacement, slope, and curvature (\mathbf{C}_{mbBIG})	50
5.5.3.2	Statical deformation by a single force	50
5.5.3.3	Statical deformation by two opposite single moments	52
5.5.3.4	Convergence study of the statical FE solution	54
5.5.4	Statical solution for the outer fiber strain	56
5.6	Beam with Mounted Shaker	57
5.7	Validation of the FE Model of the Beam with Mounted Shaker	59
5.7.1	Statical deformation by a single force	59
5.7.2	Statical deformation by two opposite single moments	61
5.7.3	Eigenmodes	63
5.8	Modeling a Piezo Patch Actuator as a Static Gain and Regarding its Amplifiers	65
5.9	Shaker Gain $K_{F_{ad}}$	67
5.10	Discussion of unmodelled effects/behaviour	67
6	Preparing and Comparing the Derived Models	68
6.1	Physical Calibration of the Piezo Patch Sensors	68
6.2	Input/Output Scaling	69
6.3	Final Models	70
6.4	Comparing the Identified and FE Models for the Beam without Shaker	72
6.5	Comparing the Identified and FE Models for the Beam with Mounted Shaker	73
7	Modally Weighted LQG Design	79
7.1	The LQG Problem	79
7.2	The LQR Problem	80
7.3	Kalman Filter	80
7.4	Modal Weighting Matrix \mathbf{Q}_m	82

8	Optimal & Robust \mathcal{H}_∞ Control Design Methods	83
8.1	General Control Problem Formulation for \mathcal{H}_∞ Optimization	83
8.2	Prerequisites for Standard \mathcal{H}_∞ Design	84
8.3	\mathcal{H}_∞ (Sub-)Optimal Control	85
8.4	Frequency-Dependent Weighting Functions for \mathcal{H}_∞ Control Design	86
8.5	Mixed-Sensitivity \mathcal{H}_∞ Optimal Control	88
8.6	Fundamentals of Robust Control	90
8.6.1	Control objectives in robust control	91
8.6.2	Uncertainty modeling	91
8.6.2.1	Parametric (real) uncertainty	91
8.6.2.2	Dynamic (frequency-dependent) uncertainty (complex uncertainties)	94
8.6.3	General control configuration with uncertainty (The P-K-Δ -structure)	96
8.6.4	The N-Δ -structure (for robust performance analysis)	98
8.6.5	The uncertain closed-loop transfer function matrix F	99
8.6.6	Definitions for the control objectives in robust control with respect to the \mathcal{H}_∞ norm	99
8.6.7	The M-Δ -structure for robust stability analysis	100
8.6.8	The structured singular value μ	102
8.6.9	Control objectives in robust control with respect to μ	103
8.6.10	Block diagram proof of the robust performance (RP) definition with respect to μ	104
8.6.11	Worst-case gain and skewed- μ value	106
8.6.12	DK-iteration	107
8.7	DK-synthesized μ -“optimal” Controller Design	109
8.8	\mathcal{H}_∞ Loop-Shaping Design Considering Coprime Factor Uncertainty	112
8.8.1	Applying the ideas of classical loop shaping to multivariable systems	112
8.8.2	Robust stabilization with respect to coprime factor uncertainty	114
8.8.3	Regarding performance requirements in the design	115
8.8.4	Deriving a reasonable weight (compensator) $W_1(s)$ for shaping the open-loop plant	116
9	Simulation and Validation of Control Performance	119
9.1	Disturbance Signal(s) and Identification of Spectral “Experimental Validation Models”	119
9.2	Controller Designs Based on the Identified (ID) Model	121
9.2.1	Mixed-sensitivity \mathcal{H}_∞ control	121
9.2.2	Modally weighted LQG design	130
9.2.3	\mathcal{H}_∞ loop-shaping design for coprime factor uncertainty	134
9.2.4	DK synthesized μ -“optimal” controller	139
9.2.5	Summing-up experiences and experimental results for the control designs based on the identified model	147
9.2.5.1	Mixed-sensitivity \mathcal{H}_∞ design	147
9.2.5.2	Modally weighted LQG design	147
9.2.5.3	\mathcal{H}_∞ loop-shaping design with coprime factor uncertainty	148
9.2.5.4	DK synthesized μ -“optimal” controller	148
9.3	Controller designs based on the FE model	148
9.3.1	Mixed-sensitivity \mathcal{H}_∞ control	149

9.3.2	Modally weighted LQG design	151
9.3.3	\mathcal{H}_∞ loop-shaping design for coprime factor uncertainty	154
9.3.4	DK synthesized μ -“optimal” controller	158
9.3.5	DGK synthesized μ -“optimal” controller (considering parametric uncertainty in ω_i)	162
9.3.6	Summing-up experiences and experimental results for the control designs based on the analytical model (FE model)	171
9.3.6.1	Mixed-sensitivity \mathcal{H}_∞ design	171
9.3.6.2	Modally weighted LQG design	171
9.3.6.3	\mathcal{H}_∞ loop-shaping design with coprime factor uncertainty	172
9.3.6.4	DK synthesized μ -“optimal” controller	172
9.3.6.5	DGK synthesized μ -“optimal” controller	172
10	Conclusions	174
10.1	Identified Plant Model	174
10.2	Controller Designs Based on the Identified Model	174
10.3	Analytical Model (FE Model)	175
10.4	Controller Designs Based on the Analytical Model (FE Model)	175
10.5	Tabular Overview of the Investigated Controller Design Methods	175
A	Selected Fundamentals	177
A.1	Transfer Functions for MIMO Systems	177
A.2	A Plant in State-Space and Transfer Function Representation	179
A.2.1	State-space representation	179
A.2.2	Transfer function representation	180
A.3	Proper Systems	181
A.4	Singular Value Decomposition (SVD)	182
A.5	Pseudo-Inverse (Generalized Inverse)	183
A.6	Norms	184
A.6.1	Vector- and matrix norms	184
A.6.2	Signal norms	186
A.6.3	System norms	187
A.6.3.1	\mathcal{H}_∞ system norm	187
	Bibliography	194

Acronyms

ADC analog digital converter

CARE controller algebraic Riccati equation

DAC digital analog converter

DOF degrees of freedom

FARE filter algebraic Riccati equation

FE finite element

FEM finite element method

LFT linear fractional transformation

LHP left half plane

LQG Linear Quadratic Gaussian

LQR Linear Quadratic Regulator

LTi linear time-invariant

MFC macro fiber composites

MIMO multi-input multi-output

NP Nominal Performance

NS Nominal Stability, Internal Stability

ODEs ordinary differential equations

RHP right half plane

RP Robust Performance

RS Robust Stability

RTI Real-Time Interface

SISO single-input single-output

SSV structured singular value

SVD Singular Value Decomposition

Chapter 1

Introduction

1.1 Overview and Motivation (for Active Damping of Flexible Structures)

In lightweight design, the consistent use of lightweight materials and lightweight structures for the purpose of weight reduction and energy saving is encouraged. Optimizing a construction for low weight generally leads to structures with decreased overall stiffness and lower natural frequencies of structure vibrations. Because of low damping, occurring vibrations can show large amplitudes, which can pose a danger to structural stability or in the low frequency range complicate other functions (e.g. passenger ride comfort in vehicles, autopilot in an airplane, etc.).

For these reasons, so called “smart structures” are used more frequently. By utilizing integrated actuators and sensors (often applied in a collocated manner) and the use of a controller, the dynamic properties of the structure can be improved. Due to their low weight, small dimensions, simple embeddability, efficiency, longevity, etc. piezo patch elements are well suited as actuators and sensors for structural control applications, where novel so-called macro fiber composites (MFC) exhibit almost hysteresis-free, linear behaviour.

The flexible beam investigated in this work has low-damped oscillatory modes already at low frequencies, and thus can be considered as a typical component of such lightweight construction.

1.2 Goal of this Thesis

The aim of this work is to study the suitability of state-of-the-art model-based feedback control design methods (specifically: Linear Quadratic Gaussian (LQG) control, mixed-sensitivity \mathcal{H}_∞ control, \mathcal{H}_∞ loop-shaping control and D(G)K synthesized control) for improving disturbance rejection of the experimental control system setup of the flexible beam depicted in Figure 2.1.

Furthermore it is investigated, if, for the case at hand, an analytical model obtained by a simple one-dimensional finite-element model can be used as design plant for the considered control design methods and succeed in the actual experimental setup.

1.3 Structure of this Work

In Chapter 2, the experimental setup is presented (mechanical components, physical dimensions, measurement equipment, software tools, etc.). Individual components are discussed in more detail. Furthermore, a system border of the experimental plant “beam” is defined.

In Chapter 3, the partial differential equation of motion for flexural vibrations of beams is presented and utilizing a separation approach its continuous analytical solution (for free vibration) is outlined.

In Chapter 4, the chosen identification procedure is described and the obtained models of the beam with and without mounted shaker are presented.

In Chapter 5, it is shown how to derive a structural analytical model using the finite element method (FEM). First the “Hermitian beam element” (i.e. an Euler-Bernoulli beam with Hermitian shape functions) is presented and its shape functions are obtained. Then it is demonstrated, both in theory and by means of examples, how to obtain the required mass, damping, stiffness, and input matrices for the nodal equations of motion, as well as the displacement output and the velocity output matrices for the nodal output equations. Subsequently the obtained nodal model is transformed to modal coordinates. Furthermore, appropriate state-space representations for structural models are considered. The (linear) modeling of the actuators is described in detail and it is shown how an acceleration output can be formulated. Then the FE model of the pure beam is validated by investigating its eigenfrequencies and eigenvectors for different clamping conditions. The static solution for different clamping and load conditions is validated and a convergence study is performed. Following this, it is shown that the influence of a mounted shaker can be modelled by feedback loops utilizing acceleration and displacement outputs and a force input. Again, this is followed by a validation in terms of eigenvectors and static solutions of different clamping conditions. Finally, unmodelled effects are discussed and further recommendations for improvements are given.

In Chapter 6, missing gains are derived and an appropriate scaling of the obtained models is performed. All final models are named and listed (Section 6.3). Finally, the identified and analytical models of the beam with and without mounted shaker are compared in the frequency domain.

In Chapter 7, the fundamentals of the LQG-control problem are provided. Furthermore, the benefits of choosing a modal state weighting matrix are shown.

In Chapter 8, fundamentals of state-of-the-art optimal and robust control design methods are given. First the general control problem formulation for \mathcal{H}_∞ optimization and its central preconditions are outlined. Then the standard solution for the \mathcal{H}_∞ (sub-)optimal controller design problem is presented. Following this, considerations on the choice of frequency-dependent weighting functions for \mathcal{H}_∞ optimization are discussed. Next, the mixed-sensitivity \mathcal{H}_∞ optimal control problem for disturbance rejection is presented.

Then, after a short introduction, a detailed consideration of the concept of robust control is presented. For the case at hand appropriate concepts of uncertainty modelling are discussed in detail. The general control configuration with uncertainty is presented, and a powerful tool called “structured singular value” SSV (μ) is introduced and some fundamental definitions in robust control with respect to μ are given. Furthermore, a heuristic approach to synthesize a μ -“optimal” controller, called DK-iteration (algorithm) is explained. Subsequently, the investigated control design problem for DK iteration is presented.

Last but not least the fundamentals of the \mathcal{H}_∞ loop-shaping design procedure are given. It is shown how the ideas of classical loop shaping can be applied to multivariable systems, and

the two-stage design process (shaping of open-loop singular values, robustly stabilizing the shaped plant with respect to the general class of coprime factor uncertainty) is explained. Finally, an idea is presented how to choose reasonable weights for shaping the open-loop plant.

In Chapter 9, on basis of both models (identified/FE model of the beam with mounted shaker) extensive controller design studies (of all previously presented control design methods) are carried out and validated in the experiment. The individual subsections end with a summary of the experiences and experimental results (Section 9.2.5 respectively Section 9.3.6).

In Chapter 10, conclusions are made and a tabular overview (Table 10.1 on page 176) of the achieved improvements and suitability (in the author's opinion) of the investigated controller design methods for structural mode damping is given.

Finally, additional supplementary material is included in Appendix A.

1.4 State of the Art

Fundamentals about system identification can be found in the textbooks of Isermann [1, 2] (also available in English). An insight into the finite element method (FEM) for linear problems are given in the textbooks of Rammerstorfer [3] and Merkel [4]. In [4] the focus lies mainly on one-dimensional finite elements. The textbook of Gawronski [5] presents and integrates the methods of structural dynamics, identification, and control into a common framework. A well-known reference textbook treating robust and optimal control topics has been written by Skogestad and Postlethwaite [6]. Chapter 7 and 8 are basically an extract of [6] and the PhD thesis of Schirrer [7].

Chapter 2

Experimental Setup

Pictures of the actual experimental set-up are shown in Figure 2.1. Figure 2.3 on page 7 shows a schematic illustration of the experimental set-up. The main mechanical dimensions of the beam are found in Table 2.1 and the components of the control system setup are described in Table 2.2.

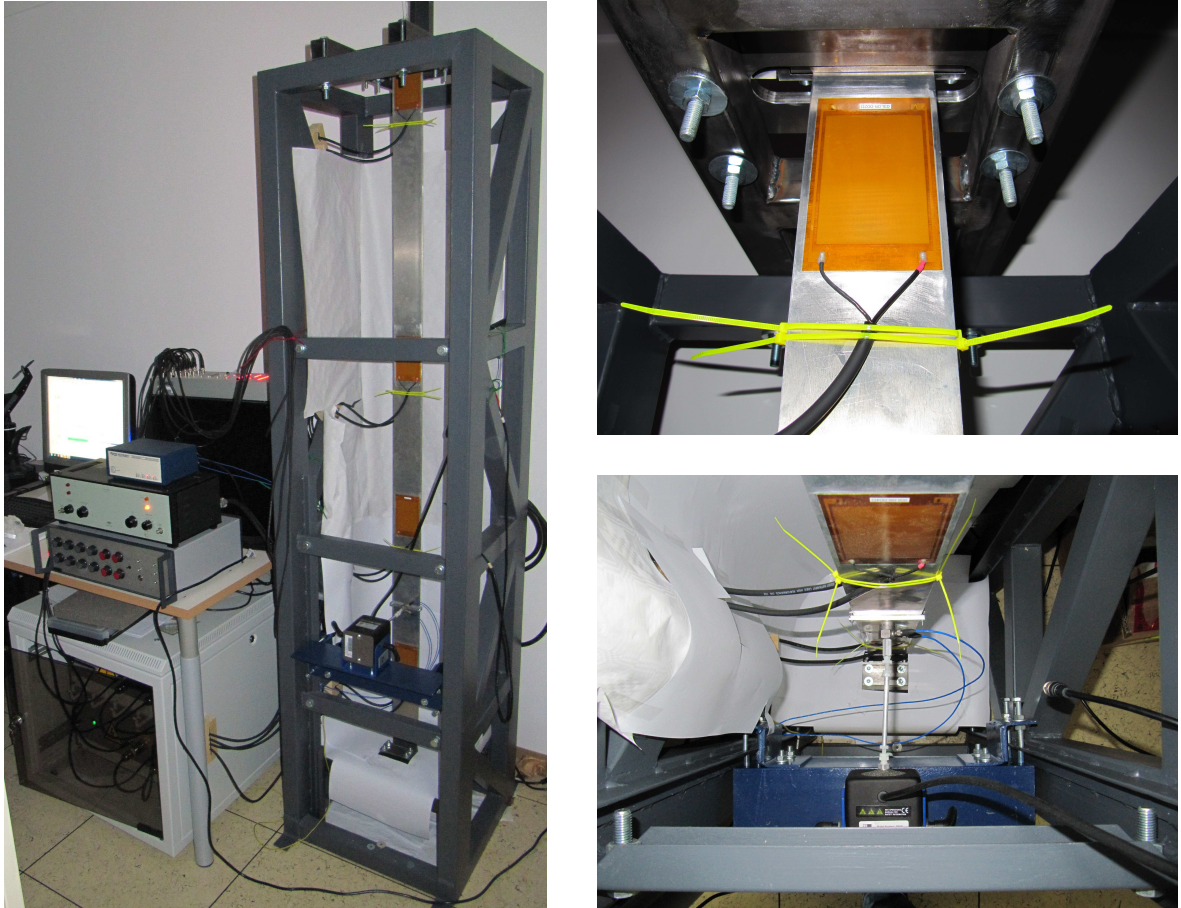


Figure 2.1: Experimental set-up

2.1 Mechanical Components

The test object in this thesis is a hinged-hinged vertically mounted structural bending beam shown schematically in Figure 2.3. The beam is about 2 m long, 75 mm wide and 3 mm thick. It is made of AlMg3. On each side of the beam, four macro fiber composites (MFC) piezo patches are glued to the beam. The piezo patches at the front are used as actuators and the piezo patches at the back are used as sensors. The piezo patch actuators and piezo patch sensors are positioned opposite each other. In this manner applied actuators and sensors are considered collocated. In this thesis the piezo patch actuators and sensors are consecutively numbered top-down.

The actuators utilize the so called “d33” effect, which by applying a positive voltage signal, forces them to elongate. The elongation and, consequently, the force introduced into the elastic structure, do not only depend on the applied electrical potential, but also on the stiffness of the structural component. Assuming linearity, the actuator characteristic curve and a sketch clarifying this fact are shown in Figure 2.2. The corresponding equations are (2.1) to (2.3).

$$\varepsilon = \frac{S}{l_A} \quad (2.1)$$

$$\varepsilon_0 = \frac{S_0}{l_A} \quad (2.2)$$

$$F = F_B \cdot \left(1 - \frac{\varepsilon}{\varepsilon_0}\right) \cdot \frac{U}{U_{\max}} \quad (2.3)$$

- l_A : - active length of a piezo patch actuator
- S_0 : - free displacement
- ε_0 : - free strain
- F_B : - blocking force

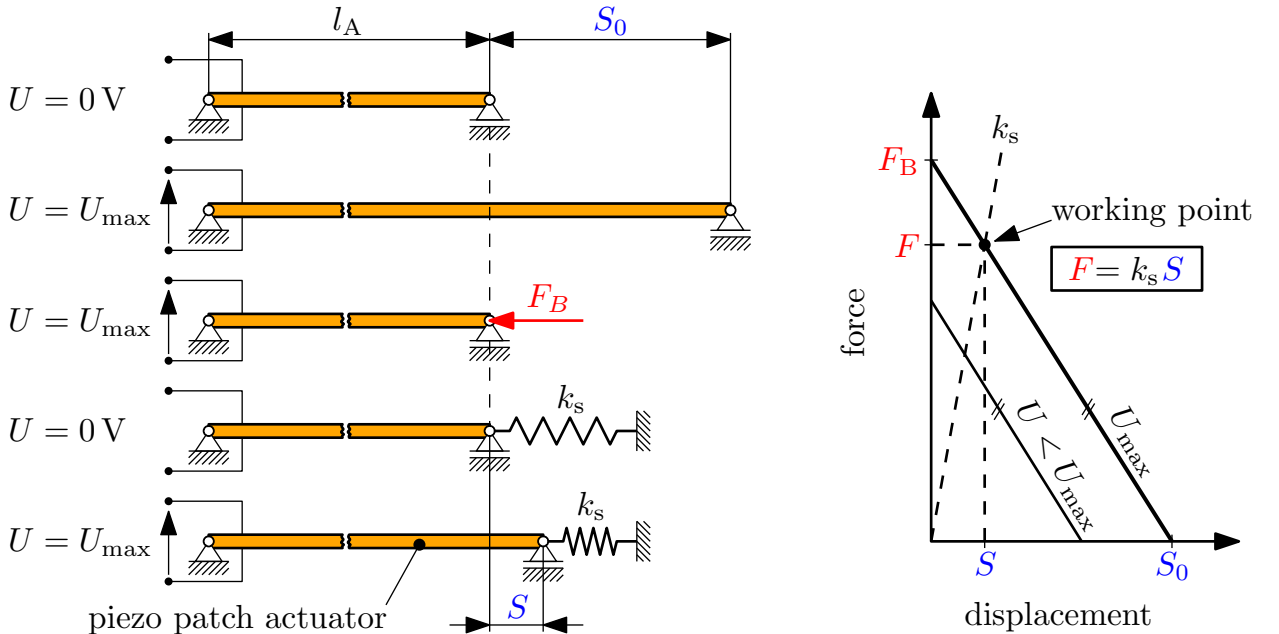


Figure 2.2: Characteristic curve of a piezo patch actuator (assuming **linearity**)
(adopted from [8])

By elongating a piezo patch sensor (“d31” effect), a strain proportional (linearity assumed) electrical charge is generated, resulting in an electric potential difference. It should be pointed out again that the actuators and sensors exhibit hysteresis behavior, which will not be regarded in this work. This is justified because the utilized MFCs show only weak nonlinearities.

An electrodynamic shaker is used to introduce a disturbance force. The point of attachment between beam and shaker can be shifted along the beam, but for all investigations was fixed at a certain value. Design and manufacturing of this shaker coupling was part of this work and is now briefly described.

The beam is pinched via screws between two small aluminium (mounting) prisms ($84\text{ mm} \times 10\text{ mm} \times 5\text{ mm}$) (see Figure 2.3). The acceleration and force sensor is screwed to the prism at the front of the beam. A nylon stinger connects the sensor with the shaker. The former is screwed to a massive, vibration insensible platform whose principal part is an L-120 profile steel. This platform can be shifted vertically along two rails welded at the framework surrounding the beam. Screws can fix the platform at any position on the rails.

2.2 Software, Measuring Equipment and Signal Flow

In MATLAB® Simulink® a subsystem was created, in which the inputs and outputs of the dSPACE 1104 ACE platform are linked with analog digital converter (ADC) and digital analog converter (DAC) blocks from the Real-Time Interface (RTI) Simulink® library. This subsystem, called “MIMO beam”¹ (see Figure 2.4) was used in two superior Simulink® interfaces - one for the identification task and another one for the controller validation(s) in the hardware experiment(s), which both use the fixed-step solver ode3 (Bogacki-Shampine).

Each of the two superior Simulink® interfaces was compiled, creating an “.sdf” file, which was linked to a new project in ControlDesk®. Subsequently, those variables defined by the blocks in the Simulink® models appeared in ControlDesk® and could be linked via drag & drop to buttons, graphs, and displays in a user-defined layout. The final project was uploaded to the dSPACE platform where it was executed in real time. The virtual instrument panel (“layout”) enabled supervision and manipulation of the running program. Selected measurement signals² were streamed continuously to a hard disk for subsequent analysis.

The outputs of the dSPACE 1104 ACE platform are amplified by a power amplifier and a high voltage amplifier to actuate the shaker and the four piezo patch actuators, respectively (see, Figure 2.3) The piezo patch sensors transmit their measurement signal directly back to the dSPACE 1104 ACE platform, while for the acceleration and force sensor at the shaker position the signals are first fed to a signal conditioning box.

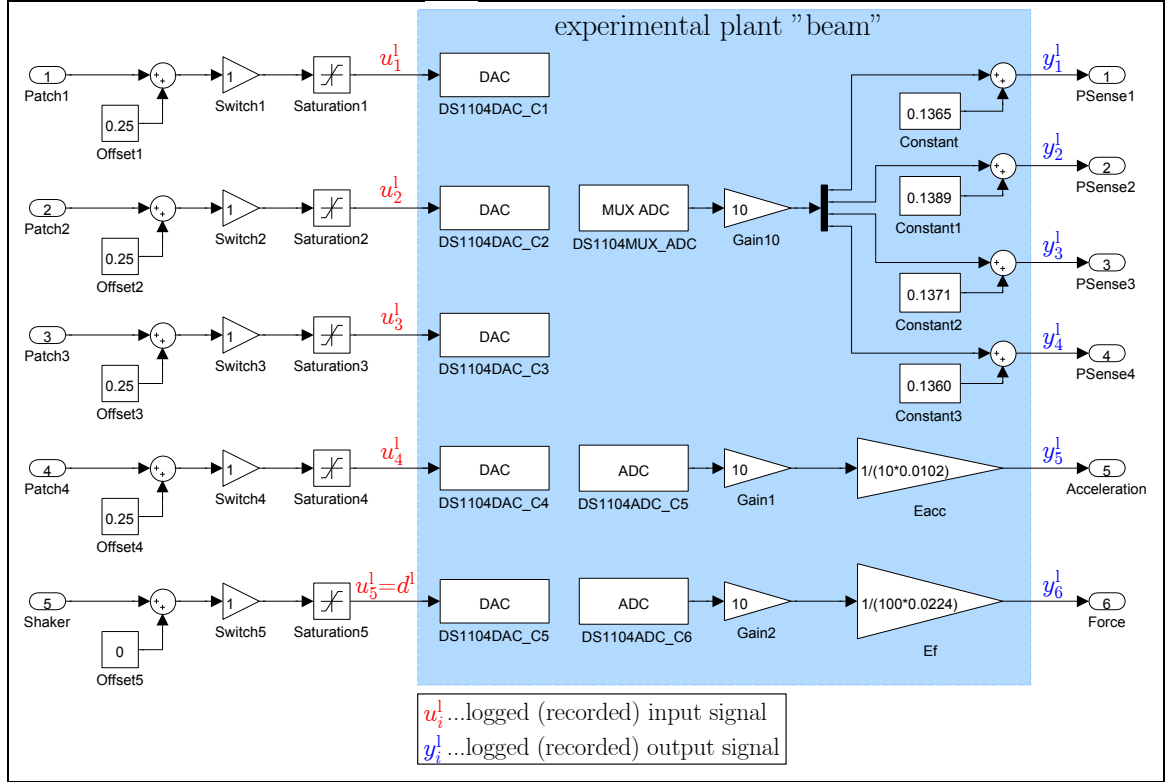
¹The subsystem “MIMO beam” also handles signal offsets, protects against out of range signals via saturation blocks and converts the dSPACE signals for acceleration and force to their mechanical signals.

²The output signals of the saturation blocks 1 to 5 (see Figure 2.4) were taken as inputs (logged excitation signals u_j^l for $j = 1, \dots, 5$) and the inputs to the output ports of the subsystem “MIMO beam” were taken as outputs (logged measurement signals y_i^l for $i = 1, \dots, 6$). The letter “l” stands for logged. By this means a system boundary was drawn around the experimental plant “beam”.

In Table 2.2 a listing of the described components of the control system setup is given.

component	description
electrodynamic shaker	THE MODAL SHOP; Model 2007E <i>stroke length (max):</i> ± 12.7 mm pk <i>acceleration (max):</i> 2.4 m/s^2 pk <i>acceleration (max driven):</i> 265 m/s^2 pk <i>force rating:</i> 31 N sine peak
shaker amplifier (power amplifier)	Brüel & Kjaer; Power Amplifier Type 2712 <i>apparent power:</i> 180 VA
shaker signal conditioner	PCB PIEZOTRONICS; Model 482C15 4-channel, ICP system
acceleration and force sensor	PCB PIEZOTRONICS; impedance head 288D01 <i>sensitivity force ($\pm 10\%$):</i> 22.4 mV/N <i>sensitivity acceleration ($\pm 10\%$):</i> 10.2 mV/m/s^2 <i>measurement range force:</i> ± 222.4 N pk <i>measurement range acceleration:</i> $\pm 490.5 \text{ m/s}^2$ pk
piezo patch actuators	SMART MATERIAL; MFC-M-8557-P1 (d33 effect actuators) <i>blocking force (F_B):</i> 923 N <i>free strain (ε_0):</i> 1800 ppm <i>active length:</i> 85 mm <i>voltage operation range:</i> $-500 \text{ V}/+1500 \text{ V}$
piezo actuator amplifier (high voltage amplifier)	<i>input voltage range:</i> $[-2.5 \text{ V}, +7.5 \text{ V}]$ (custom-built) <i>output voltage range:</i> $0 \text{ V} + 200 \text{ V/V} \times \text{input voltage}$ <i>idle voltage slew rate:</i> $50 \text{ V}/\mu\text{s}$
piezo patch sensors	SMART MATERIAL; MFC-M-2814-P2 (d31 effect sensors) <i>blocking force (F_B):</i> -85 N <i>free strain (ε_0):</i> -700 ppm <i>voltage operation range:</i> $-60 \text{ V}/+360 \text{ V}$
real-time development system	dSPACE; Advanced Control Education Kit 1104 - DS1104 PPC - CLP1104 Connector/LED Panel

Table 2.2: Components of the control system setup



A DAC block converts its input signal range of ± 1 to an analog output voltage of ± 10 V. Each ADC block captures a ± 10 V analog voltage signal and converts it to a Simulink[®] output signal (range of ± 1 V).
 Saturation blocks 1 to 4: $[-0.25, +0.75]$
 Saturation block 5: $[-0.5, +0.5]$

Figure 2.4: Simulink[®] subsystem: "MIMO beam"

Chapter 3

Partial Differential Equation of Motion for Flexural Beam Vibrations

In Figure 3.1 an infinitesimally small beam element of length dx is depicted. The external force per unit length (or line load) $q(x, t)$ acts transversely on the entire beam element.

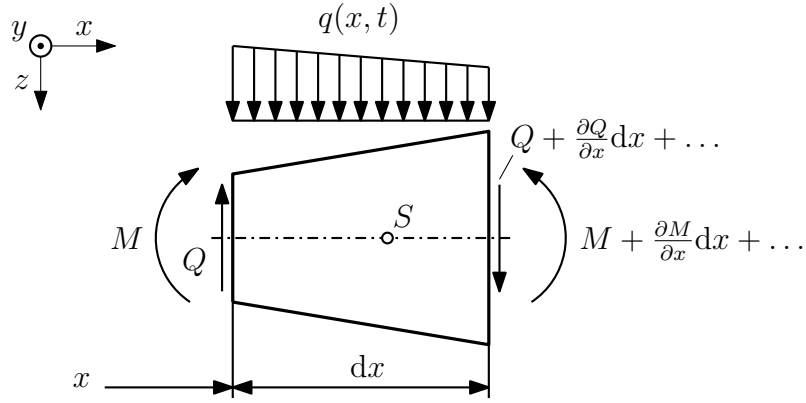


Figure 3.1: Infinitesimally small beam element (adopted from [9])

The equation of motion (centre-of-mass theorem) in the transverse direction (z -direction) for the infinitesimally small beam element is:

$$-Q + q(x, t)dx + Q + \frac{\partial Q}{\partial x}dx + \dots = \rho A dx \frac{\partial^2 w}{\partial t^2} \quad (3.1)$$

Dividing (3.1) by dx and taking the limit as dx tends to zero ($dx \rightarrow 0$) yields:

$$\frac{\partial Q}{\partial x} = \rho A \frac{\partial^2 w}{\partial t^2} - q(x, t) \quad (3.2)$$

The moment of momentum about the y -axis through the center of gravity S is:

$$-M - Qdx + M + \frac{\partial M}{\partial x}dx + \dots = \frac{\partial D_y}{\partial t} \quad (3.3)$$

For the infinitesimally small beam element the angular momentum component D_y is given by:

$$D_y = I_y \omega_y = \rho J_y dx \cdot \omega_y + \dots \quad (3.4)$$

where the angular velocity ω_y is given by

$$\omega_y = -\frac{\partial^2 w}{\partial x \partial t} \quad (3.5)$$

Inserting (3.4) into (3.3), dividing (3.3) by dx and taking the limit as dx tends to zero ($dx \rightarrow 0$) yields:

$$\frac{\partial M}{\partial x} = Q - \rho J_y \frac{\partial^3 w}{\partial x \partial t^2} \quad (3.6)$$

The second term on the right hand side of (3.6) is the rotational inertia of the infinitesimally small beam element, which is usually small and thus is neglected in the following, yielding:

$$\frac{\partial M}{\partial x} = Q \quad (3.7)$$

In elementary beam theory (Bernoulli hypothesis, linear-elastic material) it is assumed that the bending moment and the curvature of the beam axis are linearly linked via the flexural rigidity: [10]

$$M(x) = -E J_y(x) \frac{\partial^2 w}{\partial x^2} \quad (3.8)$$

Partially differentiating (3.8) twice with respect to x and using (3.7) yields:

$$\frac{\partial Q}{\partial x} = -\frac{\partial^2}{\partial x^2} \left(E J_y(x) \frac{\partial^2 w}{\partial x^2} \right) \quad (3.9)$$

Equating equations (3.2) and (3.9) yields the partial differential equation of motion for flexural vibrations

$$\frac{\partial^2}{\partial x^2} \left(E J_y \frac{\partial^2 w}{\partial x^2} \right) = q(x, t) - \rho A \frac{\partial^2 w}{\partial t^2} \quad (3.10)$$

where both $E J_y$ and ρA may vary arbitrarily with x . For a uniform beam, (3.10) simplifies to

$$E J_y \frac{\partial^4 w}{\partial x^4} = q(x, t) - \rho A \frac{\partial^2 w}{\partial t^2} \quad (3.11)$$

and furthermore for the free vibration case, i.e. $q(x, t) = 0$, the equation of motion becomes

$$E J_y \frac{\partial^4 w}{\partial x^4} = -\rho A \frac{\partial^2 w}{\partial t^2} \quad (3.12)$$

The equation of motion (3.12) can be solved by using a separation approach:

$$w(x, t) = \phi(x) \cdot T(t) \quad (3.13)$$

Inserting (3.13) into (3.12) and rearranging (separation of variables) leads to

$$\frac{\ddot{T}(t)}{T(t)} = -\frac{E J_y}{\underbrace{\rho A}_{c^2}} \frac{\phi^{\text{IV}}(x)}{\phi(x)} = -\omega^2 \quad (3.14)$$

The first term is only a function of t , while the second term is only a function of x . Therefore, both terms can only be equal for all x and t , if they are equal to a constant $-\omega^2$. [9] Thus, (3.14) can be rearranged as two ordinary differential equations, (3.15) and (3.19).

$$\phi^{\text{IV}}(x) - \lambda^4 \phi(x) = 0 \quad (3.15)$$

where

$$\lambda^4 = \frac{\omega^2}{c^2} = \frac{\rho A}{E J_y} \omega^2 \quad (3.16)$$

The general solution of (3.15) is a mode shape and given by

$$\phi(x) = A \sin \lambda x + B \cos \lambda x + C \sinh \lambda x + D \cosh \lambda x, \quad (3.17)$$

where the constants A , B , C and D are to be determined so that the kinematic and dynamic boundary conditions are always satisfied. The infinite number of natural frequencies ω_i (for $i = 1, \dots, \infty$) of the beam are obtained from (3.16) as:

$$\omega_i = \lambda_i^2 c = \lambda_i^2 \sqrt{\frac{E J_y}{\rho A}} \quad (3.18)$$

Equation (3.19) is the differential equation of an undamped decoupled system.

$$\ddot{T}_i(t) + \omega_i^2 T_i(t) = 0 \quad i = 1, \dots, \infty \quad (3.19)$$

The general solution of (3.19) is given by

$$T_i(t) = R_i \cos \omega_i t + S_i \sin \omega_i t, \quad (3.20)$$

where the constants R_i and S_i (for $i = 1, \dots, \infty$) must be determined under consideration of the initial conditions ($w(x, 0)$ and $\frac{\partial w}{\partial t}(x, 0)$).

Finally, the overall solution of (3.12) is given by:

$$w(x, t) = \sum_{i=1}^{\infty} T_i(t) \phi_i(x) \quad (3.21)$$

Example 3.1: Eigenfunctions $\phi_i(x)$ of free bending vibrations of a beam simply supported at both ends

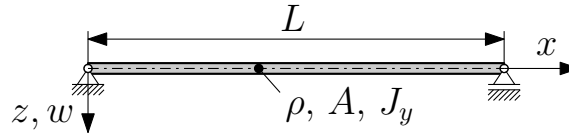


Figure 3.2: Beam simply supported at both ends

For a beam of length L simply supported at both ends (Figure 3.2) the kinematic and dynamic boundary conditions are given by (3.22) respectively (3.23):

$$\begin{aligned} w(0, t) = 0 & \rightarrow \phi(0) = 0 \\ w(L, t) = 0 & \rightarrow \phi(L) = 0 \end{aligned} \quad (3.22)$$

$$\begin{aligned} M(0, t) = 0 & \xrightarrow{(3.8)} w''(0, t) = 0 \rightarrow \phi''(0) = 0 \\ M(L, t) = 0 & \xrightarrow{(3.8)} w''(L, t) = 0 \rightarrow \phi''(L) = 0 \end{aligned} \quad (3.23)$$

By utilizing the boundary conditions (3.22)-(3.23) and the general solution approach (3.17) a homogeneous linear system of equations for the computation of A , B , C and D follows to:

$$\begin{aligned}
\phi(0) &= B + D &= 0 \\
\phi(L) &= A \sin \lambda L + B \cos \lambda L + C \sinh \lambda L + D \cosh \lambda L &= 0 \\
\phi''(0) &= \lambda^2 (-B + D) &= 0 \\
\phi''(L) &= \lambda^2 (-A \sin \lambda L - B \cos \lambda L + C \sinh \lambda L + D \cosh \lambda L) &= 0
\end{aligned} \tag{3.24}$$

From the first and third equation in (3.24) immediately follows:

$$B = D = 0 \tag{3.25}$$

and further

$$\begin{aligned}
A \sin \lambda L + C \sinh \lambda L &= 0 \\
-A \sin \lambda L + C \sinh \lambda L &= 0
\end{aligned} \tag{3.26}$$

For a nontrivial solution of (3.26) the determinant of the coefficient matrix must vanish, i.e.:

$$2 \sin \lambda L \sinh \lambda L = 0 \tag{3.27}$$

Equation (3.27) is called frequency equation. Since $\sinh \lambda L$ vanishes only for $\lambda L = 0$ and $L \neq 0$ ($L \neq 0 \Rightarrow \lambda = 0 \xrightarrow{(3.16)} \omega = 0 \xrightarrow{(3.20)} T(t) = \text{const.}$, i.e. idle state), the solutions of the frequency equation with $\lambda L \neq 0$ are described by

$$\sin \lambda L = 0 \tag{3.28}$$

and thus the eigenvalues λ_i (for $i = 1, \dots, \infty$) are obtained by

$$\lambda_i = \frac{i\pi}{L} \tag{3.29}$$

From (3.18) the corresponding natural frequencies ω_i follow to

$$\omega_i = \lambda_i^2 c = \left(\frac{i\pi}{L} \right)^2 \sqrt{\frac{E J_y}{\rho A}} \tag{3.30}$$

Inserting the eigenvalues λ_i ($\lambda L \neq 0$) in (3.26) yields $C = 0$.

Consequently, the eigenfunctions or eigenmodes $\phi_i(x)$ with corresponding natural frequencies ω_i (for $i = 1, \dots, \infty$) are described by:

$$\phi_i(x) = A_i \sin \frac{i\pi x}{L} \text{ for } i = 1, 2, \dots \tag{3.31}$$

The value of the constant A_i remains undetermined. For convenience, $A_i = 1$ is chosen here.

A possible solution for a frequency ω_i is given by

$$w_i(x, t) = \sin \frac{i\pi x}{L} (R_i \cos \omega_i t + S_i \sin \omega_i t) \tag{3.32}$$

where A_i is included in the constants R_i and S_i . The overall vibration of the beam is a superposition of all modes i , i.e.

$$w(x, t) = \sum_{i=1}^{\infty} \sin \frac{i\pi x}{L} (R_i \cos \omega_i t + S_i \sin \omega_i t),$$

where the infinite number of constants R_i and S_i (for $i = 1, \dots, \infty$) have to be determined so that the initial conditions ($w(x, 0)$ and $\frac{\partial w}{\partial t}(x, 0)$) are satisfied. Further information on this determination of the constants is found in [11].

In Table 3.1 the frequency equations and their roots are given for important boundary conditions. For values $i \geq 4$ an asymptotic formula can be used to compute $\lambda_i L$. [9]

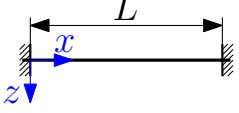
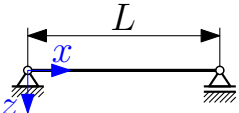
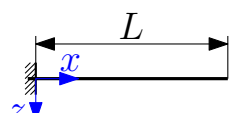
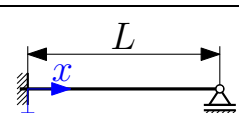
boundary conditions	frequency equation	i	$\lambda_i L$
fixed-fixed 	$1 - \cos \lambda_i L \cosh \lambda_i L = 0$	1	4.730
		2	7.853
		3	10.996
		i	$(2i + 1)\frac{\pi}{2}$
hinged-hinged 	$\sin \lambda_i L = 0$	1	π
		2	2π
		3	3π
		i	$i\pi$
fixed-free 	$1 + \cos \lambda_i L \cosh \lambda_i L = 0$	1	1.875
		2	4.694
		3	7.855
		i	$(2i - 1)\frac{\pi}{2}$
fixed-hinged 	$\tan \lambda_i L = \tanh \lambda_i L$	1	3.927
		2	7.069
		3	10.210
		i	$(4i + 1)\frac{\pi}{4}$

Table 3.1: Frequency equations and their roots for important boundary conditions. The natural frequencies can be computed by $\omega_i = \lambda_i^2 \sqrt{\frac{EJ_y}{\rho A}}$. (adopted from [9])

Chapter 4

Identified Plant Model(s)

The test bed described in Chapter 2 (see Figure 2.3) has five inputs (four piezo patch actuator signals and a shaker signal) and six outputs (four piezo patch sensors, an acceleration sensor and a force sensor).

Because significant interaction between each input and each output is expected, a single-input single-output (SISO)-based identification procedure is not suitable for this configuration. A subsequent merging of SISO transfer functions would be possible in theory, but because the eigenfrequencies obtained from different SISO models would not exactly match, a mode matching process would be needed. SISO model merging faces several problems (mode consistency, recovering coupling terms) and still would lead to a suboptimal MIMO representation. [12] As a consequence, a MIMO identification procedure has to be used for the problem at hand to include the physical couplings between inputs and outputs directly.

4.1 Identification Procedure

To concentrate the excitation on the modes below 50 Hz and to avoid ringing in the frequency domain, discrete white noise signals (i.e. Gaussian random amplitudes at the chosen sampling frequency of $5 \cdot 10^3$ Hz) with a variance of 0.64 for the piezo actuators and a variance of 0.4 for the shaker are fed to five first-order low pass filters in series all with a cutoff frequency of 100 Hz. The outputs of the filters are fed to the Simulink[®] subsystem “MIMO beam”, described in Section 2.2.

Data sets of about $2.2 \cdot 10^7$ samples have been recorded using a sampling time $T_s = 2 \cdot 10^{-4}$ s. The reason why a high sampling rate was used, although the task was to identify the low-frequency characteristic of the beam only, is briefly discussed in the following.

The piezo patch actuators are very fast (very large mechanical bandwidth of several kHz) and follow a new input signal immediately (sharp edge). When an input signal, such as a ramp signal (see Figure 4.1) is sampled with a low sampling rate, the stroke on the system due to a high step size between consecutive input signal values is intense, leading to a strong excitation of the beams high-frequency dynamics¹. Low sampling rate, but strong excitation of high-frequency dynamics causes severe problems with aliasing effects. Increasing the sampling rate not only increases the frequency content of a time signal (Nyquist frequency $f_s/2$), but also reduces the height of a step between consecutive input signal values. This facilitates the subsequent identification task.

¹A flexible structure has an infinite number of natural frequencies.

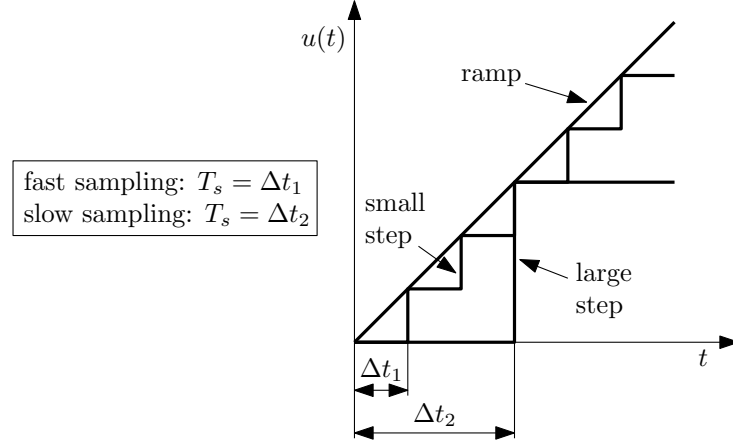


Figure 4.1: Schematic illustration of an input signal of an actuator; quasi-continuous-time signal (stair-case signal)

To improve the resolution of the identification task in the lower frequency range and to ease the identification procedure, the data was down-sampled to 100 Hz. To avoid the effect of aliasing a tenth-order anti-aliasing filter was applied before decimation. Because the anti-aliasing filter causes an edge effect due to rectangular windowing, two percent of the data set at the beginning and at the end of the measured signals were removed. Mean values were subtracted and linear trends removed.

The preprocessed data was imported as a data object in the MATLAB[®] System Identification Toolbox[™], where it was split into about 75% identification data and 25% validation data. The subspace algorithm `n4sid` of the MATLAB[®] System Identification Toolbox[™] was applied on the identification data to identify stable, linear state-space models in discrete-time. On basis of a physical understanding of the test bed, stability of the system is a requirement, while linearity of the system is a hypothesis (an assumption) and necessary for the subsequent controller design.

A fundamental parameter for identifying state-space models is the system order. Models of different system order were identified and compared. As major criteria to decide on a model, the following properties/aspects were considered:

- autocorrelation functions for the residuals² (prediction errors)
- cross correlation functions between inputs and residuals³
- plots visualizing the zeros and poles of a system
- percentage of the measured output that is explained by the simulated output for the validation data (in a so-called cross-validation)
- comparison of the frequency response with a non-parametric (identified), spectral model

²Ideally the autocorrelation function of the residuals is the autocorrelation function of a white noise signal (n), which is $E\{n(k)n(k+\tau)\} = \sigma_n^2\delta(\tau)$ where σ_n^2 is the variance of the white noise signal and

$$\delta(\tau) = \begin{cases} 1 & \text{for } \tau = 0 \\ 0 & \text{for } |\tau| \neq 0 \end{cases}$$

is the Kronecker delta function.

³Ideally the cross correlation functions between inputs and residuals indicate no correlation.

In MATLAB[®] an identified linear discrete-time state-space model is represented by the following discrete-time state (4.1) and output (4.2) equations.

$$\mathbf{x}(k+1) = \mathbf{A}\mathbf{x}(k) + \mathbf{B}\mathbf{u}(k) + \mathbf{K}\mathbf{e}(k) \quad (4.1)$$

$$\mathbf{y}(k) = \mathbf{C}\mathbf{x}(k) + \mathbf{D}\mathbf{u}(k) + \mathbf{e}(k) \quad (4.2)$$

A:	$(n \times n)$	-	state-space system matrix (state matrix)
B:	$(n \times r)$	-	input matrix
K:	$(n \times m)$	-	state disturbance matrix
C:	$(m \times n)$	-	output matrix
D:	$(m \times r)$	-	feed-through matrix
x:	$(n \times 1)$	-	state vector
y:	$(m \times 1)$	-	output vector
e:	$(m \times 1)$	-	model innovations (white, Gaussian noise vector)

The models were directly derived in a modal form via the corresponding option settings of n4sid as of MATLAB[®] release 2012a.

4.2 Extracting the Modes of Interest

In order to speed up time-consuming model-based controller design methods applied in this thesis (see Chapter 8), a model of low order was favored.

Poles of flexible structure dynamics are typically complex-conjugate and low-damped. Each complex-conjugate pair represents a structural mode. The FE model (Chapter 5) reveals that the test bed has five flexible modes with natural frequencies below 50 Hz. With this knowledge a straightforward modal reduction approach was carried out, called “modal truncation”, where all modal dynamics connected to the “masked-out” modes (that is, in the case at hand, the non-structural modes) are neglected. In this manner a tenth-order state-space model in modal form was obtained for the beam with unmounted shaker setup as well as for the beam with mounted shaker setup. The original, unreduced models were used for simulation purposes.

A list of all input-output scaled final models, ready to be used for controller design and simulation purposes, will be given in Section 6.3 (page 70).

In the following sections the derived model for the beam without shaker (Section 4.3) and the model for the beam with mounted shaker (Section 4.4) are discussed, where \mathbf{H}_{c+r} be a model with c complex poles and r real-valued poles directly obtained by the identification procedure, whereas $\mathbf{H}_{c+r}^{r\{c_r+r_r\}}$ be a reduced, tenth-order model obtained by a “modal truncation” of the former model (e.g. $\mathbf{H}_{10+6} \xrightarrow{\text{red.}} \mathbf{H}_{10+6}^{r\{10+0\}}$).

4.3 Model of the Beam without Shaker

In this subsection the identified model of the beam without shaker is presented. Not only the shaker, but also the acceleration and force sensor and all other masses at that attachment position are unmounted. Consequently the beam is only excited by the four piezo patch actuators (inputs u_1^1 to u_4^1) and the only measurements are provided by the four piezo patch sensors (outputs y_1^1 to y_4^1).

In Table 4.1 the cross-validation results achieved by different models are listed. The best model fit was obtained by model \mathbf{H}_{10+6} . It was found that identifying semi-proper system with a non-zero feed-through matrix \mathbf{D} significantly improved the results achieved (see Table 4.1). In MATLAB[®] release 2012a the corresponding option setting of n4sid was activated for each input separately. It turned out that n4sid identified the feed-through matrix \mathbf{D} as a diagonally dominant matrix. The reason for this diagonal dominance in \mathbf{D} can be physically explained by the collocation of actuator j with sensor j (for $j = 1, \dots, 4$), as well as the very fast response of the piezo patch actuators (and piezo patch sensors) compared to the sampling rate. The actual high-frequency dynamics between a collocated actuator and sensor pairing are modelled as large diagonal entries in \mathbf{D} .

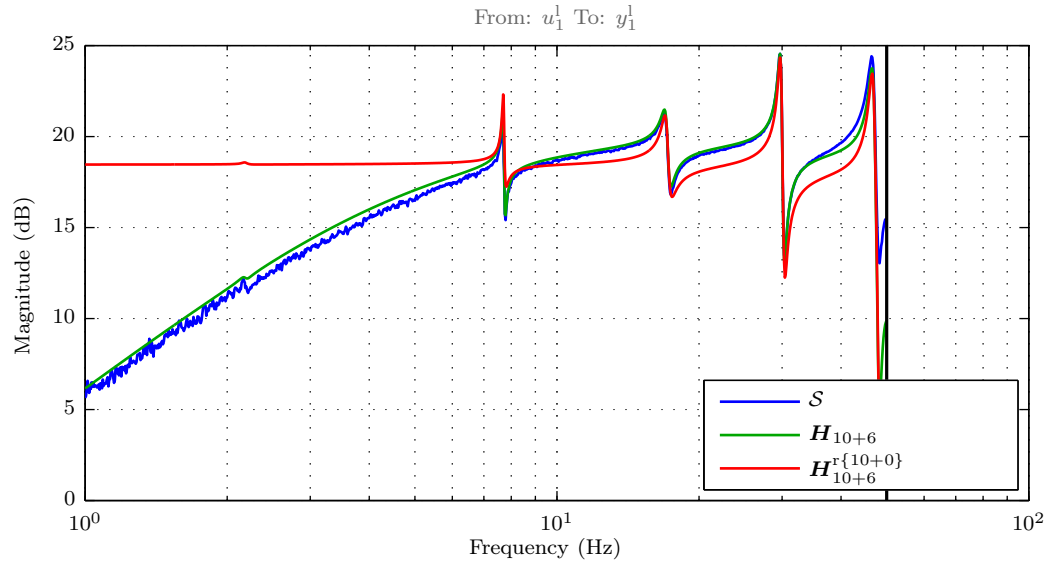
model name	model fit in %			
	y_1^l	y_2^l	y_3^l	y_4^l
\mathbf{H}_{10+6}	88.60	88.19	88.72	89.04
$\mathbf{H}_{10+6}^{r\{10+0\}}$	62.71	78.05	75.57	72.63
\mathbf{H}_{6+4}	79.44	68.14	74.84	68.28
\mathbf{H}_{10+6} with $\mathbf{D} = \mathbf{0}$	9.85	20.87	21.73	11.88

Table 4.1: Cross-validation results for the models of the beam without shaker

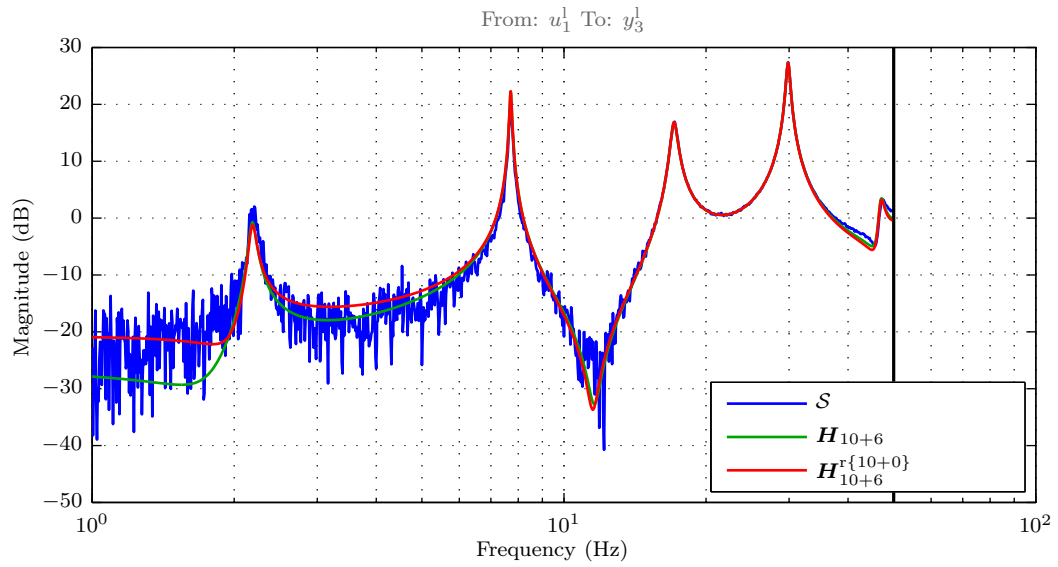
For the identified parametric models and a non-parametric, spectral model (\mathcal{S}) a Bode magnitude plot of a collocated and a non-collocated actuator and sensor pairing is shown in Figure 4.2a respectively 4.2b. As it is typical for a collocated actuator/sensor pairing the Bode plot of Figure 4.2a reveals a dominant constant component whereas the structural modes are only weakly pronounced. Conversely, the Bode plot of Figure 4.2b illustrates that for a non-collocated actuator/sensor pairing the opposite is true. In this case the structural modes are visible as well-pronounced peaks.

The parametric models both show good match (especially for the five structural modes) with the non-parametric spectral model (\mathcal{S}), confirming the high fit of the parametric models achieved in cross-validation (see Table 4.1). Because of the “modal truncation” method, the fit of the model $\mathbf{H}_{10+6}^{r\{10+0\}}$ in the low-frequency range is worse, however, as static actuation is not intended with the piezo patch actuators at hand, this model mismatch is not of major concern.

A plot of the singular values from all inputs to all outputs is depicted in Figure 4.3. The five structural modes can be well spotted as peaks.



(a) collocated actuator and sensor pairing



(b) non-collocated actuator and sensor pairing

Figure 4.2: Bode magnitude plot for parametric and non-parametric (S) identified models of the beam with unmounted shaker

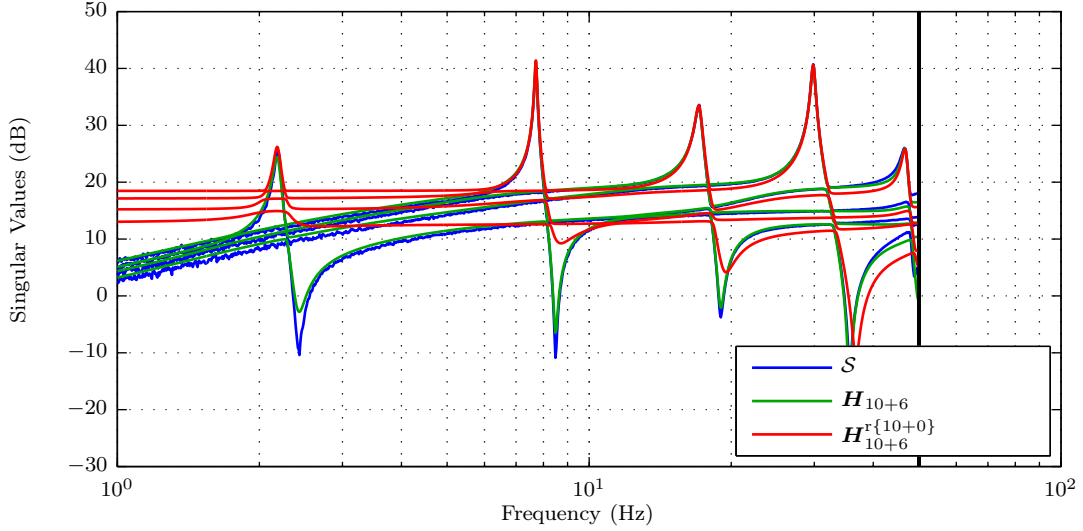


Figure 4.3: Singular values plot for parametric and non-parametric (\mathcal{S}) identified models of the beam without shaker

For each mode the corresponding natural frequency f_i (in Hz) and modal damping coefficient ζ_i (in %), for the beam without shaker model $\mathbf{H}_{10+6}^{r\{10+0\}}$ is shown in Table 4.2. As expected from an investigation of the singular values plot (Figure 4.3), the modes, particularly the second and fourth modes, are only weakly damped.

mode i	natural frequency f_i (in Hz)	modal damping coefficient ζ_i (in %)
1	2.1846	1.67
2	7.7104	0.51
3	17.1042	1.57
4	29.8556	0.93
5	46.8771	1.42

Table 4.2: Natural frequencies of the model $\mathbf{H}_{10+6}^{r\{10+0\}}$ of the beam without shaker

4.4 Model of the Beam with Mounted Shaker

In this subsection the identified model of the beam with mounted shaker is presented. The beam is excited by all four piezo patch actuators (inputs u_1^1 to u_4^1) and the shaker (input u_5^1). The measurements are provided by the four piezo patch sensors (outputs y_1^1 to y_4^1), an acceleration sensor (output y_5^1), and a force sensor (output y_6^1).

In Table 4.3, the cross-validation results achieved by different models for the beam with mounted shaker are listed. The best overall model fit was obtained by model \mathbf{H}_{14+7} . For all outputs except for the acceleration output (y_5^1), model \mathbf{H}_{14+7} has a better model fit than model \mathbf{H}_{10+8} . However, because the overall, average improvement of the cross-validation results is only small the increase in system order (from 18 to 21 states) is not justified. Also due to the fact that the 14 complex poles of \mathbf{H}_{14+7} render its “modal truncation” to a tenth-order model more complicated, model \mathbf{H}_{10+8} was used for the subsequent reduction procedure. However, model \mathbf{H}_{14+7} was intensively used for simulation purposes.

Comparing the cross-validation results for model $\mathbf{H}_{10+8}^{r\{10+0\}}$ and model \mathbf{H}_{10+0} justifies, the approach taken by identifying a system which achieved the best cross-validation results with exactly ten complex poles and all remaining poles real (model: \mathbf{H}_{10+8}) in the first place, and subsequently reducing it by applying “modal truncation” to obtain a model with only five complex pole pairs (model: $\mathbf{H}_{10+8}^{r\{10+0\}}$), instead of restricting the system order used for identification to ten a priori (model: \mathbf{H}_{10+0}). Model $\mathbf{H}_{10+8}^{r\{10+0\}}$ does not fit well in terms of accelerations (output y_5^1) as seen in Table 4.3. However, this is irrelevant for control design which only considers y_1^1, \dots, y_4^1 as measurements.

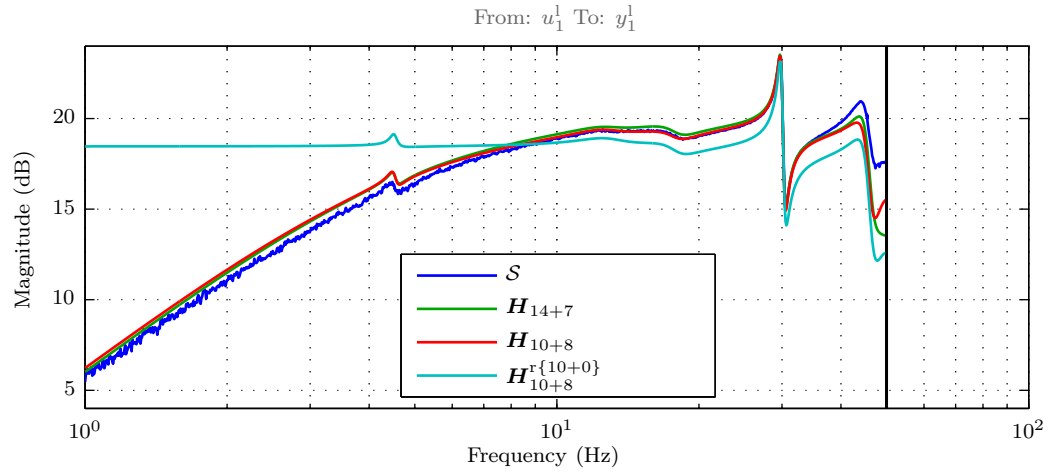
For the same reason as already described in Section 4.3 a non-zero feed-through matrix \mathbf{D} significantly improves the quality of the identified model. Again, collocated actuator and sensor pairings are reflected as dominant entries in \mathbf{D} . Additional feedthrough terms appear which essentially capture the instantaneous collocation feedthrough of the shaker force input to the collocated acceleration and force measurements. The piezo patch actuators 1, 3 and 4 also contribute to dominant entries in \mathbf{D} for the acceleration measurement.

model name	model fit in %					
	y_1^1	y_2^1	y_3^1	y_4^1	y_5^1	y_6^1
\mathbf{H}_{14+7}	88.95	90.28	90.51	91.78	53.75	91.88
\mathbf{H}_{10+8}	88.74	89.79	85.99	91.50	55.87	91.50
$\mathbf{H}_{10+8}^{r\{10+0\}}$	64.77	80.73	78.22	76.33	26.32	90.68
\mathbf{H}_{10+0}	57.79	67.69	73.76	70.85	53.55	73.91
\mathbf{H}_{10+8} with $\mathbf{D} = \mathbf{0}$	20.64	37.13	35.46	40.40	24.47	23.87

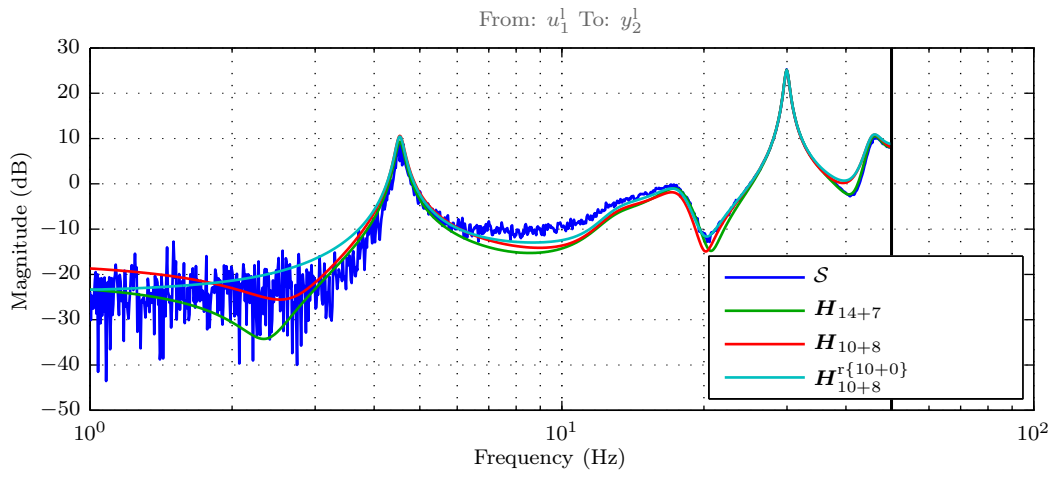
Table 4.3: Cross-validation results for the models of the beam with mounted shaker

For the identified parametric models and a non-parametric, spectral model (\mathcal{S}), a typical Bode magnitude plot of a collocated and a non-collocated actuator and sensor pairing is shown in Figure 4.4a respectively 4.4b. Again, as expected from the lessons learned in Section 4.3, the Bode magnitude plot of the collocated actuator and sensor pairing shows only weakly developed dynamic peaks (structural modes), while for the non-collocated actuator and sensor pairing the dynamic peaks are well-pronounced.

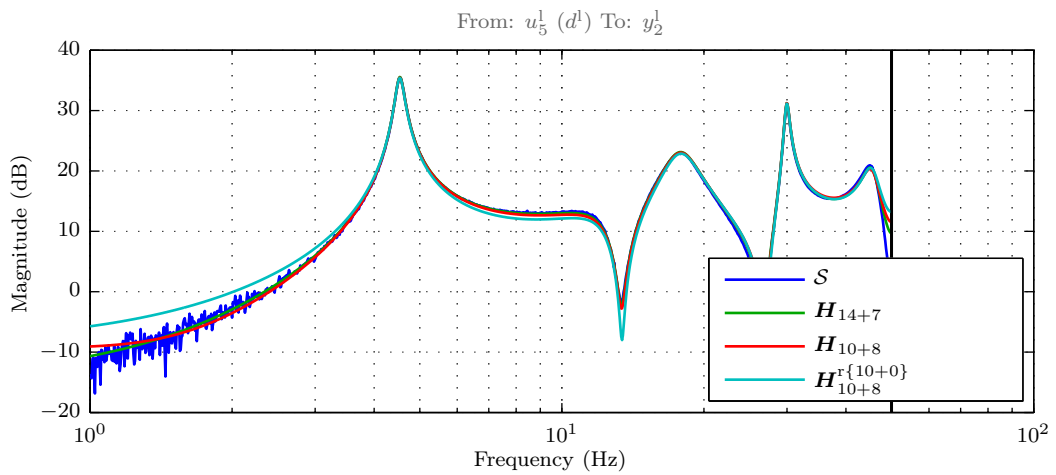
The Bode magnitude plot from the shaker input to a piezo patch sensor is shown in Figure 4.4c and shows the structural modes clearly.



(a) collocated actuator and sensor pairing



(b) non-collocated actuator and sensor pairing



(c) from the shaker input to a piezo patch sensor

Figure 4.4: Bode magnitude plot for parametric and non-parametric (S) identified models of the beam with mounted shaker

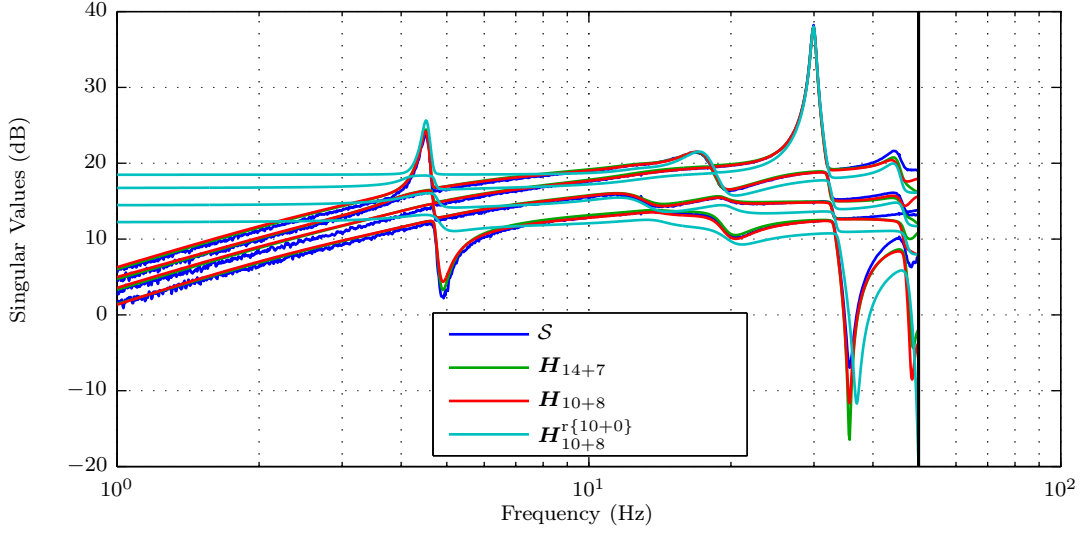
For the parametric and a non-parametric (\mathcal{S}) identified model of the beam with mounted shaker, Figure 4.5a shows a singular values plot from all four piezo patch actuators (inputs u_1^1 to u_4^1) to all four piezo patch sensors (outputs y_1^1 to y_4^1).

Comparing Figure 4.5a with the corresponding singular values plot of the beam with unmounted shaker (Figure 4.3) reveals that the natural frequencies of the first two structural modes have risen significantly and that the beam with mounted shaker, shows smallest damping in the first and fourth structural modes, whereas the other modes have moderate damping, see also Table 4.4. Two counteracting effects contribute to the shift of the natural frequencies: The mounting prisms and the acceleration and force sensor introduce additional mass to the beam which slows down the system, whereas a coupled shaker increases the stiffness of the beam. The latter effect dominates in the lower modes, so their frequencies increase.

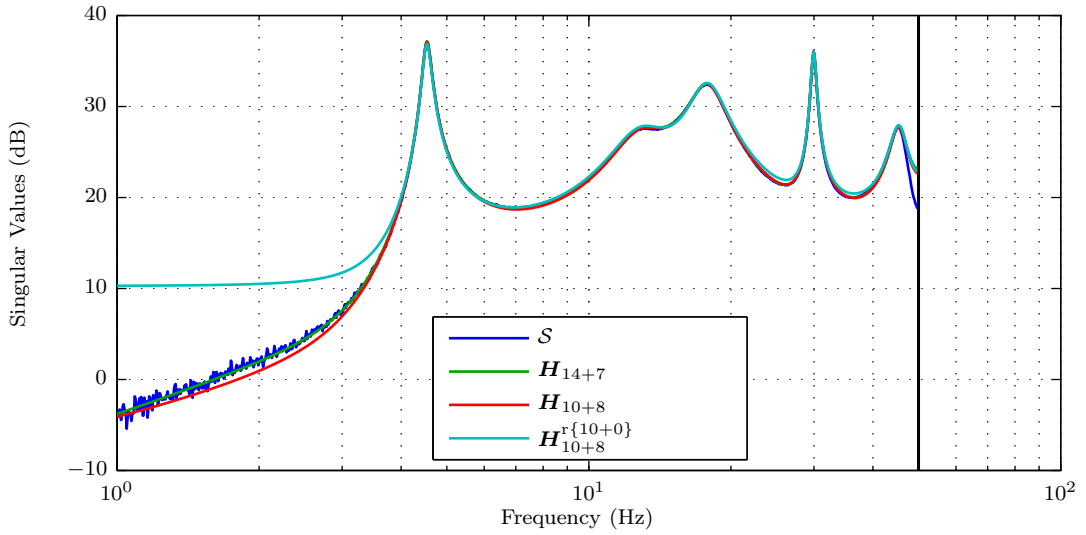
In Figure 4.5b a singular value plot from the shaker (input u_5^1) to all four piezo patch sensors (outputs y_1^1 to y_4^1) is depicted.

The main control goal of this work will be to improve the damping of the low-damped structural modes (especially of structural modes 1 and 4) so that the peaks in Figure 4.5b are flattened, by applying different controller design methods (see Chapters 7 and 8). To do this, the model $\mathbf{H}_{10+6}^{r\{10+0\}}$ used for the subsequent model-based controller designs has to be prepared properly. This will be the task of Chapter 6.

First, however, an analytic modelling onset based on the finite element method (FEM) is outlined in (Chapter 5) as an alternative to the measurement data-based identification approach of this chapter.



(a) from all four piezo patch actuators (inputs u_1 to u_4) to all four piezo patch sensors (outputs y_1 to y_4)



(b) from the shaker (input u_5) to all four piezo patch sensors (outputs y_1 to y_4)

Figure 4.5: Singular values plot for parametric and non-parametric (\mathcal{S}) identified models of the beam with mounted shaker

mode i	natural frequency f_i (in Hz)	modal damping coefficient ζ_i (in %)
1	4.5332	2.12
2	12.8924	14.49
3	17.8445	8.93
4	29.9515	1.23
5	45.4605	4.37

Table 4.4: Natural frequencies of the model $\mathbf{H}_{10+8}^{r{10+0}}$ of the beam with mounted shaker

Chapter 5

Finite Element Model

The subject of this chapter is to derive a structural model using the finite element method (FEM). In order to do this, the bending beam (Figure 2.3) is discretized by “Hermitian beam elements” (i.e. Euler-Bernoulli beams with Hermitian shape functions) (see [3]) introduced in Section 5.1. The finite element (FE) model as a natural consequence results in a nodal model in nodal coordinates represented by the second-order matrix differential equation (5.1) in terms of the nodal displacement vector \mathbf{q} . The task is to derive the required mass matrix \mathbf{M} , damping matrix \mathbf{D} , stiffness matrix \mathbf{K} and input matrix \mathbf{B} , as well as the displacement output matrix \mathbf{C}_q and the velocity output matrix \mathbf{C}_v for these two matrix equations.

$$\begin{aligned} \mathbf{M}\ddot{\mathbf{q}} + \mathbf{D}\dot{\mathbf{q}} + \mathbf{K}\mathbf{q} &= \mathbf{B}\mathbf{u} \\ \mathbf{y} &= \mathbf{C}_q\mathbf{q} + \mathbf{C}_v\dot{\mathbf{q}} \end{aligned} \quad (5.1)$$

Then, the required steps to obtain a modal state-space model with block-diagonal state matrix \mathbf{A}_{mb} (5.2) from (5.1) are described.

$$\begin{aligned} \dot{\mathbf{x}}_{mb} &= \mathbf{A}_{mb}\mathbf{x}_{mb} + \mathbf{B}_{mb}\mathbf{u} \\ \mathbf{y} &= \mathbf{C}_{mb}\mathbf{x}_{mb} + \mathbf{D}_{mb}\mathbf{u} \end{aligned} \quad (5.2)$$

The resulting FE model is validated in terms of its eigenfrequencies, eigenvectors, and the static solution for different clamping conditions against the analytic solution of a uniform beam. Subsequently, utilizing feedback loops in combination with a force input at the shaker position, a model of the beam with mounted shaker is obtained. Again, this model variant is validated (eigenmodes, static solution) for different clamping conditions against the analytic solution of the mounted configuration (where available). Finally, (static) gains are obtained to collectively model the physical systems on the input side of the experimental plant “beam” within the FE models.

5.1 Hermitian Beam Element

One of the simplest structural elements in FEM is the Hermitian beam element. Under the following conditions, bending around a considered principal axis of inertia, longitudinal strain and torsion can be treated separately (decoupled): [3]

- linear elastic material, small deformations
- validity of Bernoulli's hypothesis
- doubly symmetric cross-section being constant within an element (shear center and centroid of an area coincide)
- Saint-Venant's torsion theory, no warping fixity
- local coordinate axes transverse to the beam axis coincide with the principal axes of inertia of the cross section

In Figure 5.1 a Hermitian beam element for bending around the y -axis is depicted. The whole beam consists of several Hermitian beam elements. Each element (e) has four degrees of freedom (DOF): two translational DOF ($q_1^{(e)}, q_3^{(e)}$) and two rotatory DOF ($q_2^{(e)}, q_4^{(e)}$). The length of an element is l .

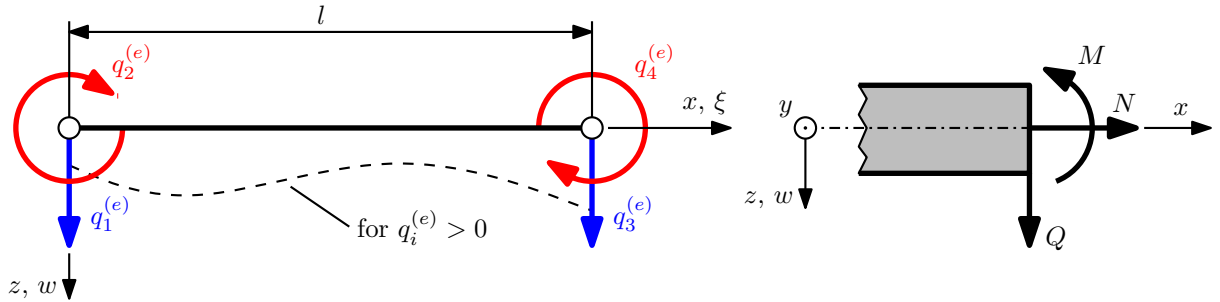


Figure 5.1: Hermitian Beam Element for bending around the (local) y -axis (adopted from [3])

The dimensionless length ξ is defined as:

$$\xi := \frac{x}{l} \quad (5.3)$$

The generalized node displacements of an element e are collected in the element node displacement vector

$$\mathbf{q}^{(e)} = \begin{bmatrix} q_1 \\ q_2 \\ q_3 \\ q_4 \end{bmatrix}^{(e)} = \begin{bmatrix} w|_{\xi=0} \\ \frac{dw}{dx}|_{\xi=0} \\ w|_{\xi=1} \\ \frac{dw}{dx}|_{\xi=1} \end{bmatrix}^{(e)}. \quad (5.4)$$

5.1.1 Shape functions φ_i and element displacement field $w(\xi)$

Equations (3.2) and (3.6) give the relationship between the bending moment M , shear force Q and line load q . Additionally, using (3.8) which is used in the elementary beam theory (Bernoulli hypothesis, linear-elastic material) to specify the relationship between the bending moment and the curvature of the beam axis, it follows for the static case:

$$-\frac{d^2}{dx^2} \left(EJ_y \frac{d^2 w}{dx^2} \right) = \frac{d^2 M}{dx^2} = \frac{dQ}{dx} = -q \quad (5.5)$$

Because EJ_y is constant within an element and only node loads act on the Hermitian beam element (i.e. the external force per unit length $q(x) = 0$)¹ it follows from (5.5) that:

$$\frac{d^4 w}{dx^4} = 0 \quad (5.6)$$

The simplest solution approach which solves the differential equation (5.6) is:

$$w(\xi) = a_0 + a_1 \xi + a_2 \xi^2 + a_3 \xi^3 \quad (5.7)$$

The coefficients a_0, a_1, a_2, a_3 can be expressed by the components of the element node displacement vector $\mathbf{q}^{(e)}$ ($\mathbf{q}^{(e)} = \begin{bmatrix} q_1^{(e)} & q_2^{(e)} & q_3^{(e)} & q_4^{(e)} \end{bmatrix}^T$):

$$\begin{aligned} w(\xi=0) &= a_0 = q_1^{(e)} \\ \frac{dw}{dx}(\xi=0) &= \frac{1}{l} a_1 = q_2^{(e)} \\ w(\xi=1) &= a_0 + a_1 + a_2 + a_3 = q_3^{(e)} \\ \frac{dw}{dx}(\xi=1) &= \frac{1}{l} a_1 + \frac{1}{l} 2a_2 + \frac{1}{l} 3a_3 = q_4^{(e)} \end{aligned} \quad (5.8)$$

From equation (5.8) the displacement w in z -direction follows to:

$$w = (1 - 3\xi^2 + 2\xi^3) \cdot q_1^{(e)} + (\xi - 2\xi^2 + \xi^3) l \cdot q_2^{(e)} + (3\xi^2 - 2\xi^3) \cdot q_3^{(e)} + (-\xi^2 + \xi^3) l \cdot q_4^{(e)} \quad (5.9)$$

Thus the shape functions (φ_i for $i = 1 \dots 4$) concerning the deflection in the x, z -plane are:

$$\boldsymbol{\varphi}(x) = \begin{bmatrix} \varphi_1 \\ \varphi_2 \\ \varphi_3 \\ \varphi_4 \end{bmatrix} = \begin{bmatrix} 1 - 3\xi^2 + 2\xi^3 \\ (\xi - 2\xi^2 + \xi^3) l \\ 3\xi^2 - 2\xi^3 \\ (-\xi^2 + \xi^3) l \end{bmatrix} \Big|_{\xi(x)=\frac{x}{l}} \quad (5.10)$$

A short version for the displacement w in z -direction (5.9) is given by:

$$w = \sum_{i=1}^4 \varphi_i \cdot q_i^{(e)} = \boldsymbol{\varphi}^T \mathbf{q}^{(e)} \quad (5.11)$$

¹Note that $q(x)$ is not to be confused with the element node displacement vector $\mathbf{q}^{(e)}$ or its components $q_i^{(e)}$ (for $i = 1, \dots, 4$).

5.1.2 Element local stiffness matrix $\mathbf{k}^{(e)}$

The element local stiffness matrix (for bending around the y-axis) follows from an energy analysis for bending deformation and is given in equation (5.12). More information on the derivation of the element local stiffness matrix can be found in [3], [4].

$$\mathbf{k}^{\text{by}(e)} = \mathbf{k}^{(e)} = \frac{EJ_y}{l^3} \cdot \begin{bmatrix} 12 & 6l & -12 & 6l \\ & 4l^2 & -6l & 2l^2 \\ & & 12 & -6l \\ \text{symm.} & & & 4l^2 \end{bmatrix} \quad (5.12)$$

5.1.3 Element global stiffness matrix $\mathbf{K}^{(e)}$

In the considered case the local coordinate system for an element is congruent (up to x -translation) with the global coordinate system for the whole beam and therefore the element local stiffness matrix $\mathbf{k}^{(e)}$ is identical with the element stiffness matrix in the global coordinate system $\mathbf{K}^{(e)}$.

$$\mathbf{K}^{(e)} = \mathbf{k}^{(e)} \quad (5.13)$$

5.1.4 Global stiffness matrix \mathbf{K}

In the following the assembly of the global stiffness matrix \mathbf{K} is explained by Example 5.1.

Example 5.1: Assembling the global stiffness matrix \mathbf{K} for a test beam with three elements

Figure 5.2 shows a beam with three Hermitian Beam elements for bending around the y-axis. The numbers in round parentheses are the numbers of the individual elements ((1), (2), (3)). The numbers in curly brackets are the local node numbers ($\{1^{(e)}\}$, $\{2^{(e)}\}$) of an element and the numbers in square brackets are the global node numbers ([1], [2], [3], [4]). Capital L is the length of the whole beam.

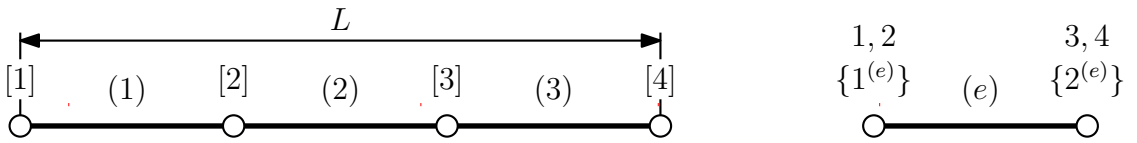


Figure 5.2: Example beam with three Hermitian Beam elements for bending around the y-axis.

Table 5.1 is the corresponding coincidence table for this particular beam. The coincidence table depicts the interrelationship between the element DOF and the global DOF for each element.

element number (e):	(1)		(2)		(3)	
local node number:	$\{1^{(1)}\}$	$\{2^{(1)}\}$	$\{1^{(2)}\}$	$\{2^{(2)}\}$	$\{1^{(3)}\}$	$\{2^{(3)}\}$
element DOF ($i^{(e)}, j^{(e)}$):	1 2	3 4	1 2	3 4	1 2	3 4
global node number:	[1]	[2]	[2]	[3]	[3]	[4]
global DOF (a, b):	1 2	3 4	3 4	5 6	5 6	7 8

Table 5.1: Coincidence table for a beam with three elements.

Figure 5.3 illustrates the assembling of the global stiffness matrix \mathbf{K} via the utilization of the element stiffness matrix in the global coordinate system $\mathbf{K}^{(e)}$ (5.13) and the coincidence table (Table 5.1) for the example beam.

Assembling steps:

1. Assigning each $K_{ij}^{(e)}$ to each $\tilde{K}_{ab}^{(e)}$ via the coincidence table (Table 5.1):

$$K_{ij}^{(e)} \rightarrow \tilde{K}_{ab}^{(e)} \quad (5.14)$$

2. Obtaining an entry K_{ab} of \mathbf{K} via summation of $K_{ab}^{(e)}$ over the elements (e):

$$K_{ab} = \sum_{(e)} \tilde{K}_{ab}^{(e)} \quad (5.15)$$

3. Assembling \mathbf{K} from its entries K_{ab} :

$$K_{ab} \Rightarrow \mathbf{K} \quad (5.16)$$

$$\text{e.g.: } K_{34} = \tilde{K}_{34}^{(1)} + \tilde{K}_{34}^{(2)} = K_{34}^{(1)} + K_{12}^{(2)}$$

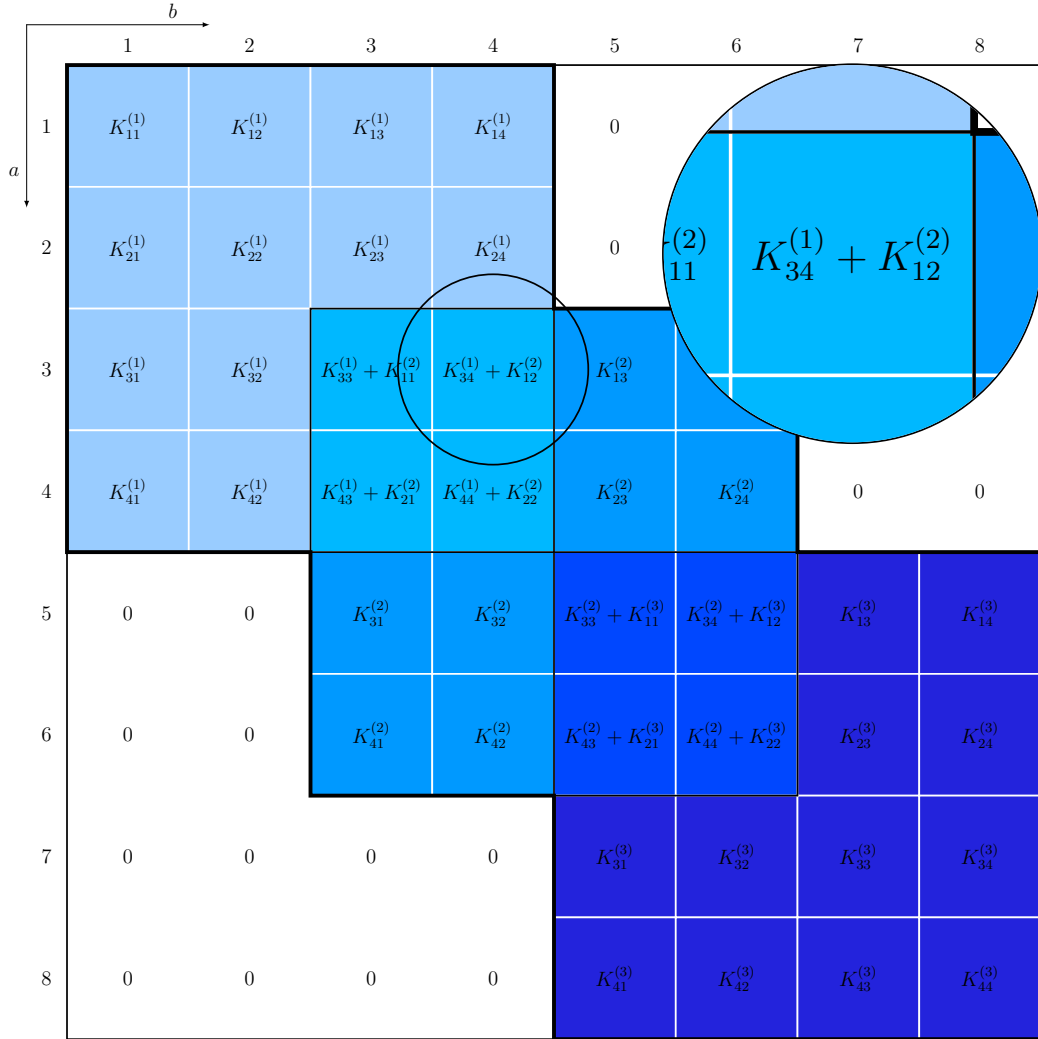


Figure 5.3: Assembling the global stiffness matrix \mathbf{K} for a beam with three elements.

5.1.5 Consistent mass matrix for an element in local coordinates $\mathbf{m}^{(e)}$

The consistent mass matrix for an element in local coordinates ($\mathbf{m}^{(e)}$) is given in (5.18). It is calculated by (5.17). [3, 4]

$$\mathbf{m}^{(e)} = \int_{Vol^{(e)}} \rho \cdot \boldsymbol{\varphi}^{(e)} \boldsymbol{\varphi}^{(e)\top} dVol = \int_0^1 \rho Al \cdot \boldsymbol{\varphi}^{(e)} \boldsymbol{\varphi}^{(e)\top} d\xi \quad (5.17)$$

$$\mathbf{m}^{(e)} = \frac{\rho Al}{420} \cdot \begin{bmatrix} 156 & 22l & 54 & -13l \\ & 4l^2 & 13l & -3l^2 \\ & & 156 & -22l \\ \text{symm.} & & & 4l^2 \end{bmatrix} \quad (5.18)$$

5.1.6 Consistent mass matrix for an element in global coordinates $\mathbf{M}^{(e)}$

As for the stiffness matrix, the consistent mass matrix for an element in local coordinates $\mathbf{m}^{(e)}$ is identical with the consistent mass matrix for an element in global coordinates $\mathbf{M}^{(e)}$.

$$\mathbf{M}^{(e)} = \mathbf{m}^{(e)} \quad (5.19)$$

5.1.7 Global consistent mass matrix \mathbf{M}

The global consistent mass matrix \mathbf{M} is assembled in the same manner as the global stiffness matrix (\mathbf{K}) (see Section 5.1.4, Figure 5.3).²

²The only difference is the usage of capital $M_{ij}^{(e)}$ instead of capital $K_{ij}^{(e)}$ in Example 5.1.

5.1.8 Damping matrix D

The damping matrix is assumed as a Rayleigh Damping (see [3]), where the damping matrix is a linear combination of the stiffness and mass matrices:

$$D = \alpha M + \beta K \quad (5.20)$$

The parameters $\alpha > 0$ and $\beta > 0$ can be computed from (5.21) (see, [3]), where ζ_i is the modal damping coefficient of the i th mode and ω_i is the i th natural angular frequency. If one knows ζ_i and ω_i of at least two (or more, i.e. least squares fit) different modes, a system of linear equations can be solved for α and β .

$$\alpha + \beta\omega_i^2 = 2\omega_i\zeta_i \quad (5.21)$$

In this thesis the information (ω_i, ζ_i) to calculate α and β for the FE model without shaker is taken from the identified model $\mathbf{H}_{10+6}^{r\{10+0\}}$ of the beam without shaker. The values for ζ_1, ω_1 (first mode) and ζ_5, ω_5 (fifth mode) are used to build a system of two linear equations which is solved for α and β . In Figure 5.4,

$$\zeta(\omega) = \frac{\alpha}{2\omega} + \frac{\beta}{2}\omega \quad (5.22)$$

is visualized for the chosen values of α and β . Except for the third structural mode, this choice results in a good agreement with the modal damping coefficients ζ_i of the identified model $\mathbf{H}_{10+6}^{r\{10+0\}}$ of the beam without shaker.³

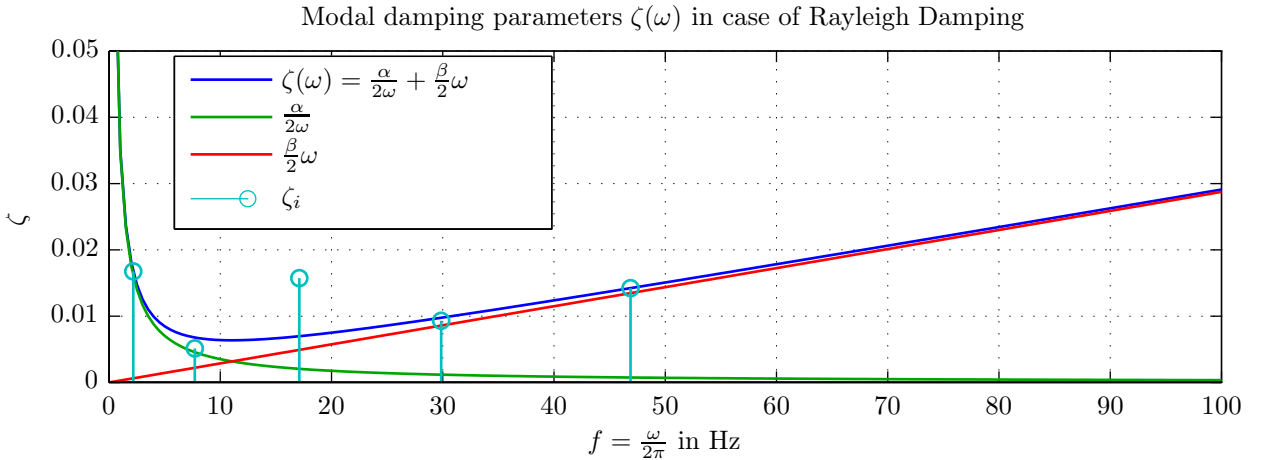


Figure 5.4: Modal damping coefficient $\zeta(\omega)$ in case of Rayleigh Damping and modal damping coefficients ζ_i (for $i = 1, \dots, 5$) of the identified model $\mathbf{H}_{10+6}^{r\{10+0\}}$ of the beam without shaker

Furthermore, the first five modal damping coefficients computed in this manner of the FE model (of the beam without shaker) were replaced by the first five modal damping coefficients ζ_i (for $i = 1, \dots, 5$) of the identified model ($\mathbf{H}_{10+8}^{r\{10+0\}}$) (of the beam without shaker).

³Note that for Rayleigh Damping (see Figure 5.4) the mass proportional damping $\frac{\alpha}{2\omega}$ has a particularly intense effect on the modes with low natural frequency, whereas the stiffness proportional damping $\frac{\beta}{2}\omega$ has a particularly intense effect on the modes with high natural frequency.

5.1.9 Input matrix B and consistent node loads

In the context of the finite element method (FEM), external loads can only act at the element nodes. If distributed loads or concentrated loads act between the nodal positions, they have to be expressed as equivalent nodal loads. This is done by requiring that the resulting node loads in compliance with the shape functions accomplish the same virtual work as the actual (distributed) loads (see [3]).

In the case at hand the equivalent nodal loads for a Hermitian beam element can be computed by

$$\mathbf{F}^{(e)} = \begin{bmatrix} F_{1z} \\ M_{1y} \\ F_{2z} \\ M_{2y} \end{bmatrix}^{(e)} = \int_0^l \boldsymbol{\varphi}^{(e)}(x) \cdot q(x) \cdot dx \quad (5.23)$$

where $q(x)$ is the actual distributed (external) transverse force (or line load).

In Figure 5.5 the positive directions of the (generalized) element node loads are depicted.

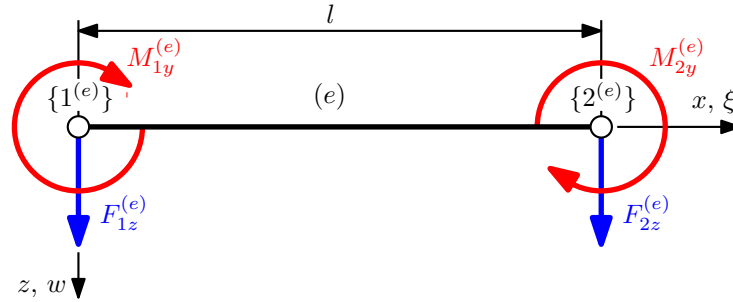


Figure 5.5: Generalized element node loads (positive direction) for a Hermitian beam element

In the FE model the piezo patch actuators are approximated by two opposite single moments, one at each end of a patch. Depending on the discretization of the beam (length of a beam element l), a piezo patch is connected to one⁴ or more⁵ elements in the finite-element model (Figure 5.7). Because the piezo patch actuators and sensors are always collocated pairwise, special care in modeling is required (see Section 5.3.4 for more details).

In the FE model the shaker excitation force is modelled as a single transversal force.

The input vector (load vector) is

$$\mathbf{u} = \begin{bmatrix} M_1 \\ M_2 \\ M_3 \\ M_4 \\ F \end{bmatrix}. \quad (5.24)$$

The consistent node loads for a single force and a single moment, respectively, are given in Figure 5.6.

⁴only two nodes (i.e. four DOF) are influenced

⁵maximum number of influenced nodes is four (i.e. eight DOF)

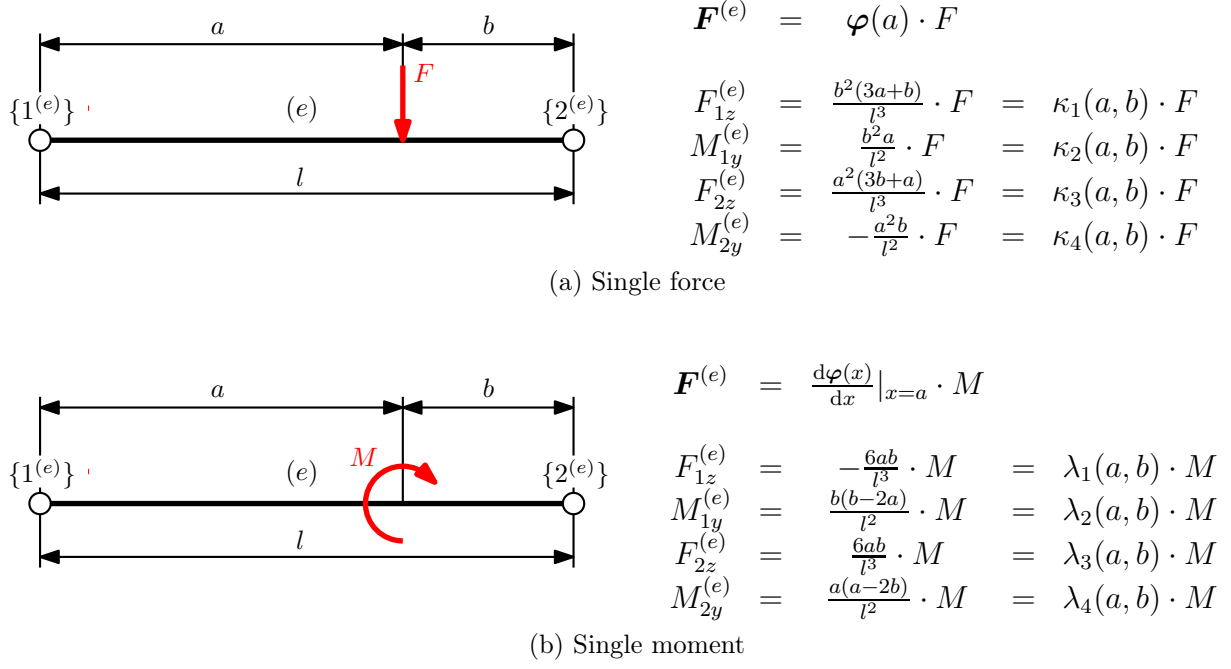


Figure 5.6: Consistent node loads for a Hermitian beam element

In the following, the construction of the input matrix \mathbf{B} is explained by Example 5.2.

Example 5.2: Input matrix B for an example beam with three elements

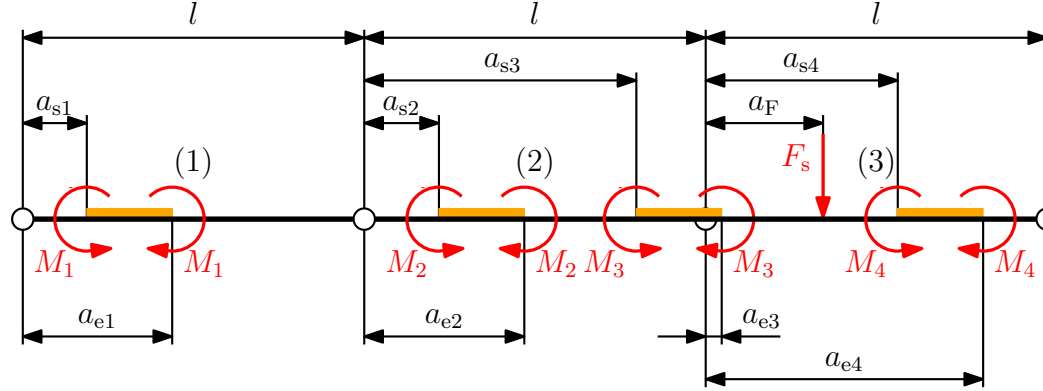


Figure 5.7: Three element beam with four piezo actuators and the shaker force as inputs.

$$b_{si} = l - a_{si}; \quad b_{ei} = l - a_{ei} \quad \text{for } i = 1 \dots 4 \quad (5.25)$$

$$b_F = l - a_F \quad (5.26)$$

$$B = \begin{bmatrix} -\lambda_1(a_{s1}, b_{s1}) + \lambda_1(a_{e1}, b_{e1}) & 0 & 0 & 0 & 0 \\ -\lambda_2(a_{s1}, b_{s1}) + \lambda_2(a_{e1}, b_{e1}) & 0 & 0 & 0 & 0 \\ -\lambda_3(a_{s1}, b_{s1}) + \lambda_3(a_{e1}, b_{e1}) & -\lambda_1(a_{s2}, b_{s2}) + \lambda_1(a_{e2}, b_{e2}) & -\lambda_1(a_{s3}, b_{s3}) & 0 & 0 \\ -\lambda_4(a_{s1}, b_{s1}) + \lambda_4(a_{e1}, b_{e1}) & -\lambda_2(a_{s2}, b_{s2}) + \lambda_2(a_{e2}, b_{e2}) & -\lambda_2(a_{s3}, b_{s3}) & 0 & 0 \\ 0 & -\lambda_3(a_{s2}, b_{s2}) + \lambda_3(a_{e2}, b_{e2}) & -\lambda_3(a_{s3}, b_{s3}) + \lambda_1(a_{e3}, b_{e3}) & -\lambda_1(a_{s4}, b_{s4}) + \lambda_1(a_{e4}, b_{e4}) & \kappa_1(a_F, b_F) \\ 0 & -\lambda_4(a_{s2}, b_{s2}) + \lambda_4(a_{e2}, b_{e2}) & -\lambda_4(a_{s3}, b_{s3}) + \lambda_2(a_{e3}, b_{e3}) & -\lambda_2(a_{s4}, b_{s4}) + \lambda_2(a_{e4}, b_{e4}) & \kappa_2(a_F, b_F) \\ 0 & 0 & \lambda_3(a_{e3}, b_{e3}) & -\lambda_3(a_{s4}, b_{s4}) + \lambda_3(a_{e4}, b_{e4}) & \kappa_3(a_F, b_F) \\ 0 & 0 & \lambda_4(a_{e3}, b_{e3}) & -\lambda_4(a_{s4}, b_{s4}) + \lambda_4(a_{e4}, b_{e4}) & \kappa_4(a_F, b_F) \end{bmatrix} \quad (5.27)$$

5.1.10 Output matrices for displacement (\mathbf{C}_q) and velocity (\mathbf{C}_v)

The four piezo sensors attached to the beam measure the outer fiber strain which is proportional to the curvature of the beam. For this reason the second derivative of the displacement w with respect to the length coordinate x is needed. Thereby, x is the local length within an element. In equation (5.28) only the shape functions φ_i depend on x .

$$w(x) = \sum_{i=1}^4 \varphi_i(x) \cdot q_i = \varphi_1(x) \cdot q_1 + \varphi_2(x) \cdot q_2 + \varphi_3(x) \cdot q_3 + \varphi_4(x) \cdot q_4 \quad (5.28)$$

Inserting (5.3) into (5.10) and calculating the second derivative leads to:

$$\begin{aligned} \frac{d^2 \varphi_1(x)}{dx^2} &= \frac{12}{l^3} \cdot x - \frac{6}{l^2} \\ \frac{d^2 \varphi_2(x)}{dx^2} &= \frac{6}{l^2} \cdot x - \frac{4}{l} \\ \frac{d^2 \varphi_3(x)}{dx^2} &= \frac{6}{l^2} - \frac{12}{l^3} \cdot x \\ \frac{d^2 \varphi_4(x)}{dx^2} &= \frac{6}{l^2} \cdot x - \frac{2}{l} \end{aligned} \quad (5.29)$$

The curvature is calculated by (5.30):

$$\frac{d^2 w(x)}{dx^2} = \sum_{i=1}^4 \frac{d^2 \varphi_i(x)}{dx^2} \cdot q_i = \sum_{i=1}^4 \varphi_i''(x) \cdot q_i \quad (5.30)$$

In the Euler-Bernoulli beam theory the bending strain in the outer fiber $\varepsilon_{\text{bending}}(x)$ is computed by

$$\varepsilon_{\text{bending}}(x) \doteq -\frac{h}{2} \cdot \frac{d^2 w(x)}{dx^2}, \quad (5.31)$$

where h is the thickness of the beam.

An ideal sensor measures the strain in a single point. For this reason in the FE model the curvature is calculated only by the four degrees of freedom from one particular element. Depending on the global position of a sensor on the beam, the local length x within the corresponding element (e) (Figure 5.8) is computed and used in Equations (5.29) and (5.30). A row of the output matrix for displacement (\mathbf{C}_q) contains for each of those four DOF (i.e. for each of those four columns), belonging to that element (e) on which the strain sensor is placed, the twice differentiated shape function ($\frac{d^2 \varphi_i(x)}{dx^2}$ for $i = 1, \dots, 4$) evaluated at the local length x within this element (e), scaled by $-\frac{h}{2}$. The rest of the entries in that row of \mathbf{C}_q are zeros. This is best illustrated by Example 5.3.

Example 5.3: Output matrix for displacement \mathbf{C}_q for an example beam with three elements

For the three element beam in Figure 5.8 the pattern of the output matrix for displacement (\mathbf{C}_q) is given in Equation (5.32).

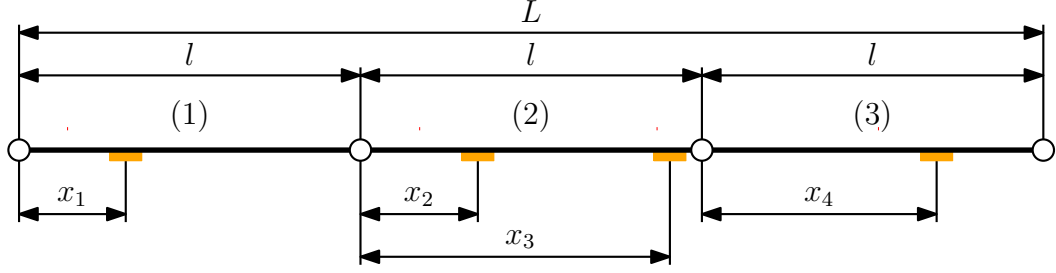


Figure 5.8: Three element beam with four sensors. x_i is the local sensor position within an element.

$$\mathbf{C}_q = -\frac{h}{2} \begin{bmatrix} \varphi_1''(x_1) & \varphi_2''(x_1) & \varphi_3''(x_1) & \varphi_4''(x_1) & 0 & 0 & 0 & 0 \\ 0 & 0 & \varphi_1''(x_2) & \varphi_2''(x_2) & \varphi_3''(x_2) & \varphi_4''(x_2) & 0 & 0 \\ 0 & 0 & \varphi_1''(x_3) & \varphi_2''(x_3) & \varphi_3''(x_3) & \varphi_4''(x_3) & 0 & 0 \\ 0 & 0 & 0 & 0 & \varphi_1''(x_4) & \varphi_2''(x_4) & \varphi_3''(x_4) & \varphi_4''(x_4) \end{bmatrix} \quad (5.32)$$

Because modelled outputs are only displacements, the velocity output matrix \mathbf{C}_v is zero.

5.1.11 Implementation of boundary conditions

Depending on the boundary conditions, zero, one, or two DOF of the first and/or the last node of the beam are locked by simply deleting the row and column corresponding to the individual DOF⁶ in the global stiffness, mass and damping matrices (\mathbf{K} , \mathbf{M} , \mathbf{D}), the row in the input matrix (\mathbf{B}) and the column in the output matrices⁷ for displacement (\mathbf{C}_q) and velocity (\mathbf{C}_v). In MATLAB[®] this is done by just indexing the remaining columns and rows.

The following relationship in terms of the number of degrees of freedom of the beam n_d holds:

$$n_d = (n_e + 1) \cdot d_n - d_l \quad (5.33)$$

n_e : - number of elements

d_n : - number of DOF per node ($d_n = 2$)

d_l : - number of locked DOF (depending on the boundary conditions)

⁶translational or rotatory DOF

⁷as well as for the in Section 5.4.1 described acceleration output matrix \mathbf{C}_a

5.2 Second-Order Structural Model

The system representations of Section 5.2.1 and 5.2.2 are based on the textbook [5].

5.2.1 Nodal model in nodal coordinates

The finite-element model directly results in a nodal model in nodal coordinates represented by the second-order matrix differential equation in terms of nodal displacements \mathbf{q} :

$$\begin{aligned} \mathbf{M}\ddot{\mathbf{q}} + \mathbf{D}\dot{\mathbf{q}} + \mathbf{K}\mathbf{q} &= \mathbf{B}\mathbf{u} \\ \mathbf{y} &= \mathbf{C}_q\mathbf{q} + \mathbf{C}_v\dot{\mathbf{q}} \end{aligned} \quad (5.34)$$

\mathbf{M} :	$(n_d \times n_d)$	-	mass matrix
\mathbf{D} :	$(n_d \times n_d)$	-	damping matrix
\mathbf{K} :	$(n_d \times n_d)$	-	stiffness matrix
\mathbf{B} :	$(n_d \times r)$	-	input matrix
\mathbf{C}_q :	$(m \times n_d)$	-	displacement output matrix
\mathbf{C}_v :	$(m \times n_d)$	-	velocity output matrix
\mathbf{q} :	$(n_d \times 1)$	-	nodal displacement vector
$\dot{\mathbf{q}}$:	$(n_d \times 1)$	-	nodal velocity vector
$\ddot{\mathbf{q}}$:	$(n_d \times 1)$	-	nodal acceleration vector
\mathbf{u} :	$(r \times 1)$	-	input vector
\mathbf{y} :	$(m \times 1)$	-	output vector

n_d : number of degrees of freedom of the beam

r : number of inputs (number of actors + shaker excitation force)

m : number of outputs (number of sensors on the beam)

5.2.2 Modal model in modal coordinates

The solution of the second-order matrix differential equation for a structure (in this case a beam) without external excitation ($\mathbf{u}(t) = \mathbf{0}$ for all t) and zero damping ($\mathbf{D} = \mathbf{0}$),

$$\mathbf{M}\ddot{\mathbf{q}} + \mathbf{K}\mathbf{q} = \mathbf{0}, \quad (5.35)$$

is $\mathbf{q} = \boldsymbol{\phi}_i e^{j\omega_i t}$, which leads to a generalized eigenvalue/eigenvector problem

$$(\mathbf{K} - \omega_i^2 \mathbf{M}) \boldsymbol{\phi}_i e^{j\omega_i t} = \mathbf{0}, \quad (5.36)$$

for which a nontrivial solution exists if

$$\det(\mathbf{K} - \omega_i^2 \mathbf{M}) = 0 \quad (5.37)$$

is true. In this case it is satisfied for a set of n_d generalized eigenvalues ω_i^2 ($i = 1, \dots, n_d$) and ω_i is called the i th natural angular frequency.

The modal model in modal coordinates can be derived by a transformation of the nodal model in nodal coordinates using the modal matrix

$$\Phi = [\phi_1 \quad \phi_2 \quad \dots \quad \phi_i \quad \dots \quad \phi_{n_m}] = \begin{bmatrix} \phi_{11} & \phi_{12} & \dots & \phi_{1i} & \dots & \phi_{1n_m} \\ \phi_{21} & \phi_{22} & \dots & \phi_{2i} & \dots & \phi_{2n_m} \\ \vdots & \vdots & \ddots & & & \vdots \\ \vdots & \vdots & & \phi_{ji} & & \phi_{jn_m} \\ \vdots & \vdots & \ddots & & \ddots & \vdots \\ \phi_{n_d1} & \phi_{n_d2} & \dots & \phi_{n_di} & & \phi_{n_dn_m} \end{bmatrix}, \quad (5.38)$$

whose n_m columns consist of the n_m generalized eigenvectors (“mode shapes”) ϕ_i ($i = 1, \dots, n_m$)⁸, as a transformation matrix.⁹

The modal matrix Φ diagonalizes the mass matrix (M) and the stiffness matrix (K)

$$M_m = \Phi^T M \Phi \quad (5.39)$$

$$K_m = \Phi^T K \Phi \quad (5.40)$$

and, in the case of a Rayleigh damping matrix (see Section 5.1.8), also the damping matrix (D).

$$D_m = \Phi^T D \Phi. \quad (5.41)$$

Introducing the modal displacement vector

$$q = \Phi q_m \quad (5.42)$$

in (5.34) and left-multiplying the resulting equation by Φ^T leads to

$$\begin{aligned} \Phi^T M \Phi \ddot{q}_m + \Phi^T D \Phi \dot{q}_m + \Phi^T K \Phi q_m &= \Phi^T B u \\ y &= C_q \Phi q_m + C_v \Phi \dot{q}_m \end{aligned} \quad (5.43)$$

and subsequently:

$$\begin{aligned} M_m \ddot{q}_m + D_m \dot{q}_m + K_m q_m &= \Phi^T B u \\ y &= C_{mq} q_m + C_{mv} \dot{q}_m \end{aligned} \quad (5.44)$$

$$\begin{aligned} \ddot{q}_m + M_m^{-1} D_m \dot{q}_m + M_m^{-1} K_m q_m &= M_m^{-1} \Phi^T B u \\ y &= C_{mq} q_m + C_{mv} \dot{q}_m \end{aligned} \quad (5.45)$$

$$\begin{aligned} \ddot{q}_m + M_m^{-1} D_m \dot{q}_m + M_m^{-1} K_m q_m &= B_m u \\ y &= C_{mq} q_m + C_{mv} \dot{q}_m \end{aligned} \quad (5.46)$$

where

$$B_m = M_m^{-1} \Phi^T B, \quad (5.47)$$

$$C_{mq} = C_q \Phi \quad \text{and} \quad C_{mv} = C_v \Phi \quad (5.48)$$

⁸Without mode reduction, the number of regarded natural modes n_m is equal to the number of degrees of freedom n_d .

⁹In (5.38) ϕ_{ji} is the j th generalized displacement of the i th mode.

\mathbf{M}_m :	$(n_m \times n_m)$	-	modal mass matrix
\mathbf{D}_m :	$(n_m \times n_m)$	-	modal damping matrix
\mathbf{K}_m :	$(n_m \times n_m)$	-	modal stiffness matrix
\mathbf{B}_m :	$(n_m \times r)$	-	modal input matrix
\mathbf{C}_{mq} :	$(m \times n_m)$	-	modal displacement output matrix
\mathbf{C}_{mv} :	$(m \times n_m)$	-	modal velocity output matrix
\mathbf{q}_m :	$(n_m \times 1)$	-	modal displacement vector
$\dot{\mathbf{q}}_m$:	$(n_m \times 1)$	-	modal velocity vector
\mathbf{u} :	$(r \times 1)$	-	input vector
\mathbf{y} :	$(m \times 1)$	-	output vector

$$\begin{aligned}\ddot{\mathbf{q}}_m + 2\mathbf{Z}\Omega\dot{\mathbf{q}}_m + \Omega^2\mathbf{q}_m &= \mathbf{B}_m\mathbf{u} \\ \mathbf{y} &= \mathbf{C}_{mq}\mathbf{q}_m + \mathbf{C}_{mv}\dot{\mathbf{q}}_m\end{aligned}\quad (5.49)$$

Ω :	$(n_m \times n_m)$	-	diagonal matrix of natural angular frequencies
\mathbf{Z} :	$(n_m \times n_m)$	-	diagonal matrix of modal damping

$$\Omega^2 = \mathbf{M}_m^{-1}\mathbf{K}_m \quad (5.50)$$

$$\Omega = \text{diag}\{\omega_i\} \quad (5.51)$$

$$\mathbf{Z} = 0.5 \cdot \mathbf{M}_m^{-\frac{1}{2}}\mathbf{K}_m^{-\frac{1}{2}}\mathbf{D}_m = \text{diag}\{\zeta_i\} \quad (5.52)$$

Note that a modal representation of a structure (5.49) is a set of uncoupled equations (5.53)

$$\begin{aligned}\ddot{q}_{mi} + 2\zeta_i\omega_i\dot{q}_{mi} + \omega_i^2q_{mi} &= \mathbf{b}_{mi}^T\mathbf{u} \\ \mathbf{y}_i &= \mathbf{c}_{mqi}q_{mi} + \mathbf{c}_{mvi}\dot{q}_{mi}\end{aligned}\quad (5.53)$$

$$\mathbf{y} = \sum_{i=1}^{n_m} \mathbf{y}_i$$

where the structural response \mathbf{y} is the sum of modal responses \mathbf{y}_i . This leads to a number of useful properties that simplify the analysis. [5]

5.2.3 Frequency response matrix of a structure (in modal coordinates) and its distinct modes

From modal coordinates (5.49) the frequency response of a structure is derived by

$$\mathbf{G}(j\omega) = (\mathbf{C}_{mq} + j\omega\mathbf{C}_{mv}) (\Omega^2 - \omega^2\mathbf{I} + 2j\omega\mathbf{Z}\Omega)^{-1} \mathbf{B}_m \quad (5.54)$$

The frequency response of the i th mode is obtained from (5.53) as

$$\mathbf{G}_{mi}(j\omega) = \frac{(\mathbf{c}_{mqi} + j\omega\mathbf{c}_{mvi})\mathbf{b}_{mi}^T}{\omega_i^2 - \omega^2 + 2j\zeta_i\omega_i\omega} \quad (5.55)$$

The structural frequency response is a sum of modal frequency responses

$$\mathbf{G}(\mathrm{j}\omega) = \sum_{i=1}^{n_m} \mathbf{G}_{mi}(\mathrm{j}\omega) \quad (5.56)$$

and the structural frequency response at the i th resonant frequency is approximately equal to the i th modal frequency response at this frequency [5] if ζ_i is small ($\zeta_i \ll 1$)

$$\mathbf{G}(\mathrm{j}\omega_i) \cong \mathbf{G}_{mi}(\mathrm{j}\omega_i) = \frac{(-\mathrm{j}\mathbf{c}_{mqi} + \omega_i \mathbf{c}_{mvi}) \mathbf{b}_{mi}^T}{2\zeta_i \omega_i^2} \quad \text{for } i = 1, \dots, n_m \quad (5.57)$$

5.3 State-Space Structural Model

The state-space representations of Section 5.3.1 and 5.3.2 are based on the textbook [5].

5.3.1 Nodal model in nodal coordinates

The system (5.34) of n_d coupled second-order linear ordinary differential equations (ODEs) of order 2 can be rewritten into a system of $2n_d$ first-order ODEs in state-space form by defining the state-space vector \mathbf{x}_n as a combination of the (structural) nodal displacement vector \mathbf{q} and the (structural) nodal velocity vector $\dot{\mathbf{q}}$: [7]

$$\mathbf{x}_n = \begin{bmatrix} \mathbf{x}_{n1} \\ \mathbf{x}_{n2} \end{bmatrix} = \begin{bmatrix} \mathbf{q} \\ \dot{\mathbf{q}} \end{bmatrix} \quad (5.58)$$

Assuming that the mass matrix \mathbf{M} is non-singular, this choice for \mathbf{x}_n leads to:

$$\mathbf{A}_n = \begin{bmatrix} \mathbf{0} & \mathbf{I} \\ -\mathbf{M}^{-1}\mathbf{K} & -\mathbf{M}^{-1}\mathbf{D} \end{bmatrix} \quad \mathbf{B}_n = \begin{bmatrix} \mathbf{0} \\ \mathbf{M}^{-1}\mathbf{B} \end{bmatrix} \quad \mathbf{C}_n = [\mathbf{C}_q \quad \mathbf{C}_v] \quad (5.59)$$

Thus, the common state-space form is obtained:

$$\dot{\mathbf{x}}_n = \mathbf{A}_n \mathbf{x}_n + \mathbf{B}_n \mathbf{u} \quad (5.60)$$

$$\mathbf{y} = \mathbf{C}_n \mathbf{x}_n + \mathbf{D} \mathbf{u} \quad (5.61)$$

(where $\mathbf{D} = \mathbf{0}$)

5.3.2 Modal model in modal coordinates

Also the system (5.49) of n_m uncoupled second-order ODEs of order 2 can be rewritten into a system of $2n_m$ first-order ODEs in state-space form. The following three state-space models in modal coordinates are derived from (5.49) by choosing three different state vectors \mathbf{x}_m .

One of the main reasons to use a modal instead of a nodal state-space representation is that in case of high-order nodal models (as obtained via FE modeling), the order can easily be reduced in the modal representation by truncating higher modes (“modal truncation”) without significantly changing system behavior. [7]

5.3.2.1 First model

$$\mathbf{x}_m = \begin{bmatrix} \mathbf{x}_{m1} \\ \mathbf{x}_{m2} \end{bmatrix} = \begin{bmatrix} \Omega \mathbf{q}_m \\ \dot{\mathbf{q}}_m \end{bmatrix} \quad (5.62)$$

$$\mathbf{A} = \begin{bmatrix} \mathbf{0} & \Omega \\ -\Omega & -2\mathbf{Z}\Omega \end{bmatrix} \quad \mathbf{B} = \begin{bmatrix} \mathbf{0} \\ \mathbf{B}_m \end{bmatrix} \quad \mathbf{C} = [\mathbf{C}_{mq}\Omega^{-1} \quad \mathbf{C}_{mv}] \quad (5.63)$$

5.3.2.2 Second model

$$\mathbf{x}_m = \begin{bmatrix} \mathbf{x}_{m1} \\ \mathbf{x}_{m2} \end{bmatrix} = \begin{bmatrix} \Omega \mathbf{q}_m \\ \mathbf{Z}\Omega \mathbf{q}_m + \dot{\mathbf{q}}_m \end{bmatrix} \quad (5.64)$$

$$\mathbf{A} = \begin{bmatrix} -\mathbf{Z}\Omega & \Omega \\ -\Omega + \mathbf{Z}^2\Omega & -\mathbf{Z}\Omega \end{bmatrix} \quad \mathbf{B} = \begin{bmatrix} \mathbf{0} \\ \mathbf{B}_m \end{bmatrix} \quad \mathbf{C} = [\mathbf{C}_{mq}\Omega^{-1} - \mathbf{C}_{mv}\mathbf{Z} \quad \mathbf{C}_{mv}] \quad (5.65)$$

For small \mathbf{Z} ($\mathbf{Z}^2 \cong \mathbf{0}$):

$$\mathbf{A} \doteq \begin{bmatrix} -\mathbf{Z}\Omega & \Omega \\ -\Omega & -\mathbf{Z}\Omega \end{bmatrix} \quad \mathbf{B} = \begin{bmatrix} \mathbf{0} \\ \mathbf{B}_m \end{bmatrix} \quad \mathbf{C} = [\mathbf{C}_{mq}\Omega^{-1} - \mathbf{C}_{mv}\mathbf{Z} \quad \mathbf{C}_{mv}] \quad (5.66)$$

5.3.2.3 Third model

$$\mathbf{x}_m = \begin{bmatrix} \mathbf{x}_{m1} \\ \mathbf{x}_{m2} \end{bmatrix} = \begin{bmatrix} \mathbf{q}_m \\ \dot{\mathbf{q}}_m \end{bmatrix} \quad (5.67)$$

$$\mathbf{A} = \begin{bmatrix} \mathbf{0} & \mathbf{I} \\ -\Omega^2 & -2\mathbf{Z}\Omega \end{bmatrix} \quad \mathbf{B} = \begin{bmatrix} \mathbf{0} \\ \mathbf{B}_m \end{bmatrix} \quad \mathbf{C} = [\mathbf{C}_{mq} \quad \mathbf{C}_{mv}] \quad (5.68)$$

5.3.3 Modal form (Modal model with block-diagonal state matrix \mathbf{A}_{mb})

The state vector \mathbf{x}_{mb} (5.71) of a modal state-space representation with block-diagonal state matrix \mathbf{A}_{mb}

$$\dot{\mathbf{x}}_{mb} = \mathbf{A}_{mb}\mathbf{x}_{mb} + \mathbf{B}_{mb}\mathbf{u} \quad (5.69)$$

$$\mathbf{y} = \mathbf{C}_{mb}\mathbf{x}_{mb} + \mathbf{D}_{mb}\mathbf{u} \quad (5.70)$$

consists of n_m independent components \mathbf{x}_{mi} . Hereby, \mathbf{x}_{mi} represents the state vector of the i th mode (modes are usually sorted by their natural frequency ω_i) and consists of two states x_{mi1} and x_{mi2} .

$$\mathbf{x}_{mb} = \begin{bmatrix} \mathbf{x}_{m1} \\ \mathbf{x}_{m2} \\ \vdots \\ \mathbf{x}_{mi} \\ \vdots \\ \mathbf{x}_{mn_m} \end{bmatrix} \quad \mathbf{x}_{mi} = \begin{bmatrix} x_{mi1} \\ x_{mi2} \end{bmatrix} \quad (5.71)$$

Thus, the block-diagonal $(2n_m \times 2n_m)$ state matrix \mathbf{A}_{mb} consists of n_m (2×2) matrices \mathbf{A}_{mi} and the number of states $n = 2n_m$. The input matrix \mathbf{B}_{mb} $(2n_m \times r)$ is filled with n_m $(2 \times r)$ matrices \mathbf{B}_{mi} and the output matrix \mathbf{C}_{mb} $(m \times 2n_m)$ contains n_m $(m \times 2)$ matrices \mathbf{C}_{mi} .

$$\mathbf{A}_{mb} = \text{diag}(\mathbf{A}_{mi}) \quad \mathbf{B}_{mb} = \begin{bmatrix} \mathbf{B}_{m1} \\ \mathbf{B}_{m2} \\ \vdots \\ \mathbf{B}_{mn_m} \end{bmatrix} \quad \mathbf{C}_{mb} = [\mathbf{C}_{m1} \quad \mathbf{C}_{m2} \quad \dots \quad \mathbf{C}_{mn_m}] \quad (5.72)$$

The $(m \times r)$ feed-through matrix of a state-space system is invariant with respect to state transformations, thus $\mathbf{D}_{mb} = \mathbf{D}$.¹⁰

In this work, a modal state-space representation with block-diagonal state matrix \mathbf{A}_{mb} as given in (5.69)-(5.70) is referred to as modal form. The following three modal forms are common in structural analysis:

5.3.3.1 Modal form 1

$$\mathbf{x}_{mi} = \begin{bmatrix} \omega_i q_{mi} \\ \dot{q}_{mi} \end{bmatrix} \quad (5.73)$$

$$\mathbf{A}_{mi} = \begin{bmatrix} 0 & \omega_i \\ -\omega_i & -2\zeta_i \omega_i \end{bmatrix} \quad \mathbf{B}_{mi} = \begin{bmatrix} \mathbf{0}^T \\ \mathbf{b}_{mi}^T \end{bmatrix} \quad \mathbf{C}_{mi} = [\mathbf{c}_{mqi} \frac{1}{\omega_i} \quad \mathbf{c}_{mvi}] \quad (5.74)$$

5.3.3.2 Modal form 2

$$\mathbf{x}_{mi} = \begin{bmatrix} \omega_i q_{mi} \\ \zeta_i \omega_i q_{mi} + \dot{q}_{mi} \end{bmatrix} \quad (5.75)$$

$$\mathbf{A}_{mi} = \begin{bmatrix} -\zeta_i \omega_i & \omega_i \\ -\omega_i & -\zeta_i \omega_i \end{bmatrix} \quad \mathbf{B}_{mi} = \begin{bmatrix} \mathbf{0}^T \\ \mathbf{b}_{mi}^T \end{bmatrix} \quad \mathbf{C}_{mi} = [\mathbf{c}_{mqi} \frac{1}{\omega_i} - \mathbf{c}_{mvi} \zeta_i \quad \mathbf{c}_{mvi}] \quad (5.76)$$

5.3.3.3 Modal form 3

$$\mathbf{x}_{mi} = \begin{bmatrix} q_{mi} \\ \dot{q}_{mi} \end{bmatrix} \quad (5.77)$$

$$\mathbf{A}_{mi} = \begin{bmatrix} 0 & 1 \\ -\omega_i^2 & -2\zeta_i \omega_i \end{bmatrix} \quad \mathbf{B}_{mi} = \begin{bmatrix} \mathbf{0}^T \\ \mathbf{b}_{mi}^T \end{bmatrix} \quad \mathbf{C}_{mi} = [\mathbf{c}_{mqi} \quad \mathbf{c}_{mvi}] \quad (5.78)$$

¹⁰So far \mathbf{D} is a zero matrix, but in Section (5.3.4) this will change, due to the properties of this FE model (no degrees of freedom in longitudinal direction and representation of a piezo actuator as two opposite single moments) and the fact, that a strain sensor and piezo actuator are always located opposite to each other pairwise on the beam.

5.3.4 Introducing a non-zero state-space feed-through matrix D

For the purposes of this thesis it is not of interest to consider any displacements in the beam's longitudinal direction. The respective DOF are therefore neglected in the employed Hermitian beam element formulation (see Figure 5.1 on page 26) which, in turn, reduces the system order of the FE model.

In Figure 5.9 the simplified model concept for representing an input of a piezo patch actuator in the analytical model is depicted.

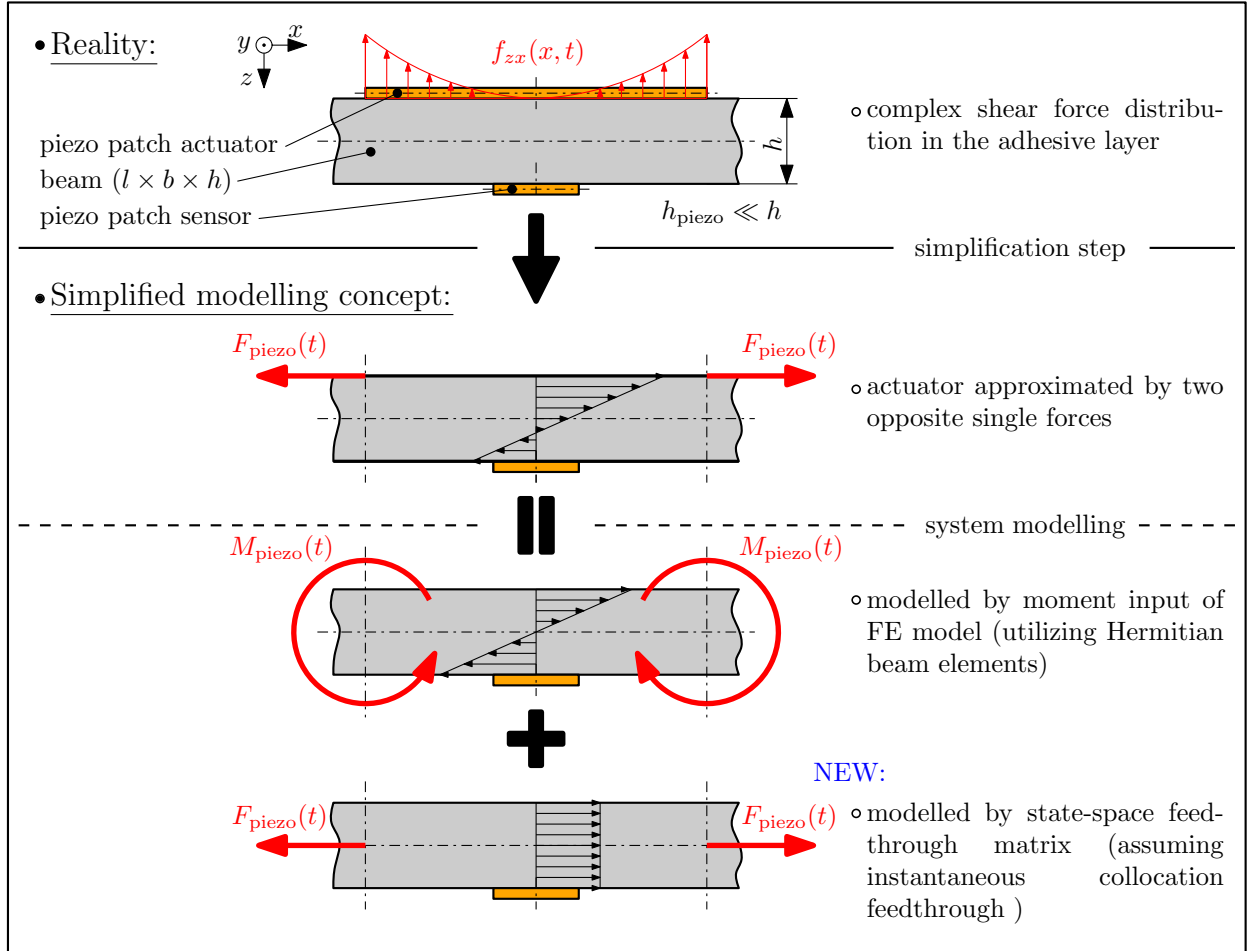


Figure 5.9: Simplified model concept piezo patch actuator (utilizing moment input of FE model and state-space feed-through matrix D)

Note that each sensor measures the outer fiber strain which can be decomposed into the strain $\varepsilon_{bending}$ due to pure bending and the strain $\varepsilon_{tensile}$ due to pure tension.¹¹

While bending strain $\varepsilon_{bending}$ is expressed via $\frac{d^2w}{dx^2}$ and, consequently, via the beam's deformation state, the dynamics in x -direction are neglected (considered instantaneous) and thus $\varepsilon_{tensile}$ can only be modelled by an appropriate feed-through term.

$$\varepsilon_{sensor} = \varepsilon_{bending} + \varepsilon_{tensile} \quad (5.79)$$

$$\varepsilon_{bending} = -\frac{h}{2} \cdot \frac{d^2w}{dx^2} \quad (5.80)$$

¹¹The FE model described in Section (5.1) computes only $\varepsilon_{bending}$.

$$\varepsilon_{\text{tensile}} = \frac{F_{\text{piezo}}}{E \cdot b \cdot h} \quad (5.81)$$

$$F_{\text{piezo}} = \frac{2}{h} \cdot M_{\text{piezo}} \quad (5.82)$$

- $\varepsilon_{\text{sensor}}$: - outer fiber strain measured by an applied piezo patch sensor
- $\varepsilon_{\text{bending}}$: - bending strain computed by the FE model as in Section (5.1.10)
- $\varepsilon_{\text{tensile}}$: - additional tensile strain caused by a piezo actuator
- M_{piezo} : - input to the state-space system (moment M_i)
- F_{piezo} : - force of a piezo patch actuator (normal force in a segment of the beam where a piezo actuator is attached)
- E : - Young's modulus
- b : - width of the beam
- h : - thickness of the beam

$$\mathbf{D}_\varepsilon = \begin{bmatrix} \mathbf{I}_{[4 \times 4]} & \mathbf{0}_{[4 \times 1]} \end{bmatrix} \cdot \frac{1}{E \cdot b \cdot h} \cdot \frac{2}{h} \quad (5.83)$$

Here the input vector \mathbf{u} is defined as $\mathbf{u} = [M_1 \ \dots \ M_4 \ F]^T$.

5.4 Acceleration Output at the Shaker Position \ddot{w}_s

5.4.1 Second-order nodal acceleration output matrix \mathbf{C}_a

The output equation of the nodal second-order matrix differential equation in the case of an acceleration measurement is:

$$\mathbf{y} = \mathbf{C}_a \ddot{\mathbf{q}} \quad (5.84)$$

- \mathbf{C}_a : ($m_a \times n_d$) - nodal acceleration output matrix
- $\ddot{\mathbf{q}}$: ($n_d \times 1$) - nodal acceleration vector
- \mathbf{y} : ($m_a \times 1$) - acceleration output vector

n_d : number of degrees of freedom of the beam

m_a : number of acceleration outputs (number of acceleration sensors on the beam)

The second derivative with respect to time of equation (5.11) is:

$$\ddot{w}(x) = \sum_{i=1}^4 \varphi_i(x) \cdot \ddot{q}_i \quad (5.85)$$

As one can see, the shape functions itself do not change (since they are no function of time). Hence, a row of the second-order nodal acceleration output matrix \mathbf{C}_a ($m_a \times n_d$) contains in each of those four columns belonging to the DOF ($q_1^{(e)}$, $q_2^{(e)}$, $q_3^{(e)}$, $q_4^{(e)}$) of that element (e) on which the acceleration sensor is placed, the shape function $\varphi_i(x)$ ($i = 1, \dots, 4$) belonging to the individual DOF ($q_i^{(e)}$) evaluated at the local length x within this element (e). The rest of the entries in that row of \mathbf{C}_a are zero.

Example 5.4: Nodal acceleration output matrix C_a for an example beam with three elements

For the three element beam with one acceleration sensor in Figure 5.10 the pattern of the nodal acceleration output matrix respectively vector (C_a) is given in Equation (5.86).

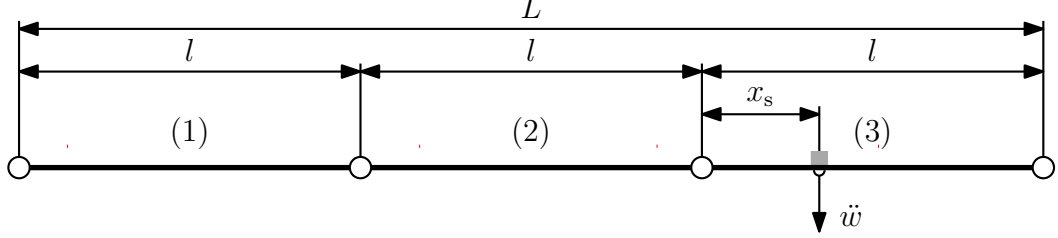


Figure 5.10: Three element beam with one acceleration sensor at the shaker position. x_s is the local length to the acceleration sensor within the third element.

$$C_a = [0 \quad 0 \quad 0 \quad 0 \quad \varphi_1(x_s) \quad \varphi_2(x_s) \quad \varphi_3(x_s) \quad \varphi_4(x_s)] \quad (5.86)$$

5.4.2 Second-order modal acceleration output matrix C_{ma}

The second derivative with respect to time of (5.42) is $\ddot{\mathbf{q}} = \Phi \ddot{\mathbf{q}}_m$. Inserting into (5.84) yields:

$$\mathbf{y} = C_a \Phi \ddot{\mathbf{q}}_m = C_{ma} \ddot{\mathbf{q}}_m \quad (5.87)$$

5.4.3 Provisional modal acceleration output matrix \hat{C}_{ma}

First model:

The first derivative with respect to time of the modal state vector \mathbf{x}_m follows from equation (5.62) to:

$$\dot{\mathbf{x}}_m = \begin{bmatrix} \dot{\mathbf{x}}_{m1} \\ \dot{\mathbf{x}}_{m2} \end{bmatrix} = \begin{bmatrix} \Omega \dot{\mathbf{q}}_m \\ \ddot{\mathbf{q}}_m \end{bmatrix} \quad (5.88)$$

$$\mathbf{y} = C_{ma} \ddot{\mathbf{q}}_m = C_{ma} [\mathbf{0} \quad \mathbf{I}] \dot{\mathbf{x}}_m \quad (5.89)$$

$$\hat{C}_{ma} = [\mathbf{0} \quad C_{ma}] \quad (5.90)$$

Second model: The first derivative with respect to time of the modal state vector \mathbf{x}_m follows from equation 5.64) to:

$$\dot{\mathbf{x}}_m = \begin{bmatrix} \dot{\mathbf{x}}_{m1} \\ \dot{\mathbf{x}}_{m2} \end{bmatrix} = \begin{bmatrix} \Omega \dot{\mathbf{q}}_m \\ \mathbf{Z} \Omega \dot{\mathbf{q}}_m + \ddot{\mathbf{q}}_m \end{bmatrix} \quad (5.91)$$

$$\mathbf{y} = \mathbf{C}_{\text{ma}} \ddot{\mathbf{q}}_{\text{m}} = \mathbf{C}_{\text{ma}} \begin{bmatrix} -\mathbf{Z} & \mathbf{I} \end{bmatrix} \dot{\mathbf{x}}_{\text{m}} \quad (5.92)$$

$$\hat{\mathbf{C}}_{\text{ma}} = \begin{bmatrix} -\mathbf{C}_{\text{ma}} \mathbf{Z} & \mathbf{C}_{\text{ma}} \end{bmatrix} \quad (5.93)$$

Third model: The first derivative with respect to time of the modal state vector \mathbf{x}_{m} follows from equation (5.67) to:

$$\dot{\mathbf{x}}_{\text{m}} = \begin{bmatrix} \dot{\mathbf{x}}_{\text{m}1} \\ \dot{\mathbf{x}}_{\text{m}2} \end{bmatrix} = \begin{bmatrix} \dot{\mathbf{q}}_{\text{m}} \\ \dot{\mathbf{q}}_{\text{m}} \end{bmatrix} \quad (5.94)$$

$$\mathbf{y} = \mathbf{C}_{\text{ma}} \ddot{\mathbf{q}}_{\text{m}} = \mathbf{C}_{\text{ma}} \begin{bmatrix} \mathbf{0} & \mathbf{I} \end{bmatrix} \dot{\mathbf{x}}_{\text{m}} \quad (5.95)$$

$$\hat{\mathbf{C}}_{\text{ma}} = \begin{bmatrix} \mathbf{0} & \mathbf{C}_{\text{ma}} \end{bmatrix} \quad (5.96)$$

5.4.4 Provisional modal acceleration output matrix $\hat{\mathbf{C}}_{\text{mba}}$ (corresponding to the block-diagonal state matrix \mathbf{A}_{mb})

The provisional modal acceleration output matrix $\hat{\mathbf{C}}_{\text{mba}}$ corresponding to a modal model with a block-diagonal state matrix \mathbf{A}_{mb} (modal form) is:

$$\hat{\mathbf{C}}_{\text{mba}} = \begin{bmatrix} \hat{\mathbf{C}}_{\text{ma}1} & \hat{\mathbf{C}}_{\text{ma}2} & \dots & \hat{\mathbf{C}}_{\text{mai}} & \dots & \hat{\mathbf{C}}_{\text{man}_m} \end{bmatrix}$$

Modal form 1:

$$\hat{\mathbf{C}}_{\text{mai}} = \begin{bmatrix} \mathbf{0} & \mathbf{c}_{\text{mai}} \end{bmatrix} \quad (5.97)$$

Modal form 2 :

$$\hat{\mathbf{C}}_{\text{mai}} = \begin{bmatrix} -\mathbf{c}_{\text{mai}} \zeta_i & \mathbf{c}_{\text{mai}} \end{bmatrix} \quad (5.98)$$

Modal form 3:

$$\hat{\mathbf{C}}_{\text{mai}} = \begin{bmatrix} \mathbf{0} & \mathbf{c}_{\text{mai}} \end{bmatrix} \quad (5.99)$$

5.4.5 State-space modal acceleration output matrix \mathbf{C}_{mba} and feed-through matrix \mathbf{D}_{mba} (corresponding to the block-diagonal state matrix \mathbf{A}_{mb})

Inserting (5.100) into (5.101) leads to (5.103).

$$\dot{\mathbf{x}}_{\text{mb}} = \mathbf{A}_{\text{mb}} \mathbf{x}_{\text{mb}} + \mathbf{B}_{\text{mb}} \mathbf{u} \quad (5.100)$$

$$\mathbf{y} = \mathbf{C}_{\text{ma}} \ddot{\mathbf{q}}_{\text{m}} = \hat{\mathbf{C}}_{\text{ma}} \dot{\mathbf{x}}_{\text{m}} = \hat{\mathbf{C}}_{\text{mba}} \dot{\mathbf{x}}_{\text{mb}} \quad (5.101)$$

$$\mathbf{y} = \hat{\mathbf{C}}_{\text{mba}} (\mathbf{A}_{\text{mb}} \mathbf{x}_{\text{mb}} + \mathbf{B}_{\text{mb}} \mathbf{u}) \quad (5.102)$$

$$= \mathbf{C}_{\text{mba}} \mathbf{x}_{\text{mb}} + \mathbf{D}_{\text{mba}} \mathbf{u} \quad (5.103)$$

Thus the state-space modal acceleration output matrix \mathbf{C}_{mba} (in modal form) and feed-through matrix \mathbf{D}_{mba} are obtained by:

$$\mathbf{C}_{\text{mba}} = \hat{\mathbf{C}}_{\text{mba}} \mathbf{A}_{\text{mb}} \quad (5.104)$$

$$\mathbf{D}_{\text{mba}} = \hat{\mathbf{C}}_{\text{mba}} \mathbf{B}_{\text{mb}} \quad (5.105)$$

For reasons of simplification in the following sections the subscript (mb), which stands for “corresponding to a modal model with a block-diagonal state matrix \mathbf{A}_{mb} ” (i.e. modal form) is neglected.

5.5 Validation of the FE Model of the Pure Beam

5.5.1 Natural frequencies (analytical and FE solution)

The natural frequencies of the FE model with unmounted shaker can be calculated directly by solving a generalized eigenvalue/eigenvector problem for the stiffness matrix \mathbf{K} and the mass matrix \mathbf{M} (see (5.36)). The first five analytical and FE natural frequencies f_i (for $i = 1, \dots, 5$) for different boundary conditions are listed in Table 5.3.¹² The equations for computing the analytical natural frequencies for different boundary conditions are given in Table 3.1 on page 14 and the relevant physical parameters of the beam are listed in Table 5.2. As expected, the absolute error between the FE and the analytical natural frequencies is much smaller for the FE model with 200 elements as for the FE model with 5 elements.

bulk material	AlMg3
free length	$L = 1890 \text{ mm}$
beam width	$b = 75 \text{ mm}$
beam thickness	$h = 3 \text{ mm}$
density	$\rho = 2700 \text{ kg/m}^3$
Young’s modulus	$E = 70 \text{ GPa}$

Table 5.2: Required physical parameters of the beam for computing its natural frequencies via analytical equations (see [9]).

¹²In this work a bearing on the left hand side always represents the upper bearing of the experimental setup, whereas a bearing on the right hand side represents the lower bearing of the testbed.

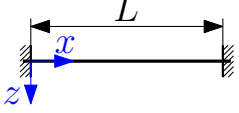
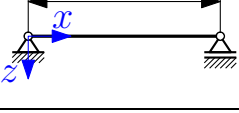
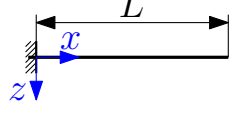
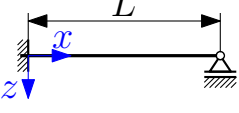
boundary conditions	mode	natural frequency (analytical) f_i^A (in Hz)	natural frequency (FE) (200 el.) f_i^{FE200} (in Hz)	absolute error (200 el.) Δf_i^{FE200} (in 10^{-4} Hz)	natural frequency (FE) (5 el.) f_i^{FE5} (in Hz)	absolute error (5 el.) Δf_i^{FE5} (in Hz)
fixed-fixed 	1	4.3956	4.3957	0.7603	4.3981	0.0025
	2	12.1162	12.1168	6.3159	12.1652	0.0490
	3	23.7555	23.7538	-16.9424	24.0825	0.3270
	4	39.2662	39.2662	-0.0736	40.1230	0.8568
	5	58.6569	58.6569	0.0272	67.3670	8.7100
hinged-hinged 	1	1.9391	1.9391	0.0028	1.9393	0.0002
	2	7.7563	7.7563	0.0011	7.7691	0.0129
	3	17.4517	17.4517	0.0009	17.5902	0.1386
	4	31.0252	31.0252	0.0037	31.7399	0.7147
	5	48.4768	48.4768	0.0129	53.8053	5.3285
fixed-free 	1	0.6907	0.6908	0.7444	0.6908	0.0001
	2	4.3289	4.3291	1.6812	4.3313	0.0023
	3	12.1223	12.1216	-7.4855	12.1651	0.0428
	4	23.7536	23.7535	-1.4480	24.0320	0.2784
	5	39.2662	39.2662	0.0877	39.8872	0.6210
fixed-hinged 	1	3.0298	3.0292	-6.1306	3.0300	0.0002
	2	9.8177	9.8166	-11.5885	9.8425	0.0248
	3	20.4807	20.4815	7.0675	20.7008	0.2201
	4	35.0245	35.0245	0.0051	35.9241	0.8996
	5	53.4457	53.4457	0.0172	59.6274	6.1817

Table 5.3: Comparing analytical and FE solution for the natural frequencies of the pure beam (beam with unmounted shaker) for different boundary conditions.

5.5.2 Eigenmodes of the (pure) beam

Figure 5.11 shows the first five eigenvectors of the translational (left) and rotatory (right) degrees of freedom calculated by the FE model¹³ printed over the length of the whole beam (L). The upper bearing is at $x = 0$ m and the lower bearing is at $x = 1.890$ m.

The eigenvectors were obtained from the generalized eigenvalue/eigenvector problem (5.36). The rows belonging to the eigenvectors of the translational respectively rotatory degrees of freedom are alternating in the modal matrix Φ (5.38).¹⁴

¹³200 elements

¹⁴Depending on the bounding conditions, exceptions of this alternating row order occur. (e.g.: If the lower bearing is a hinged bearing the last two rows of Φ both belong to the eigenvectors of the rotatory degrees of freedom.)

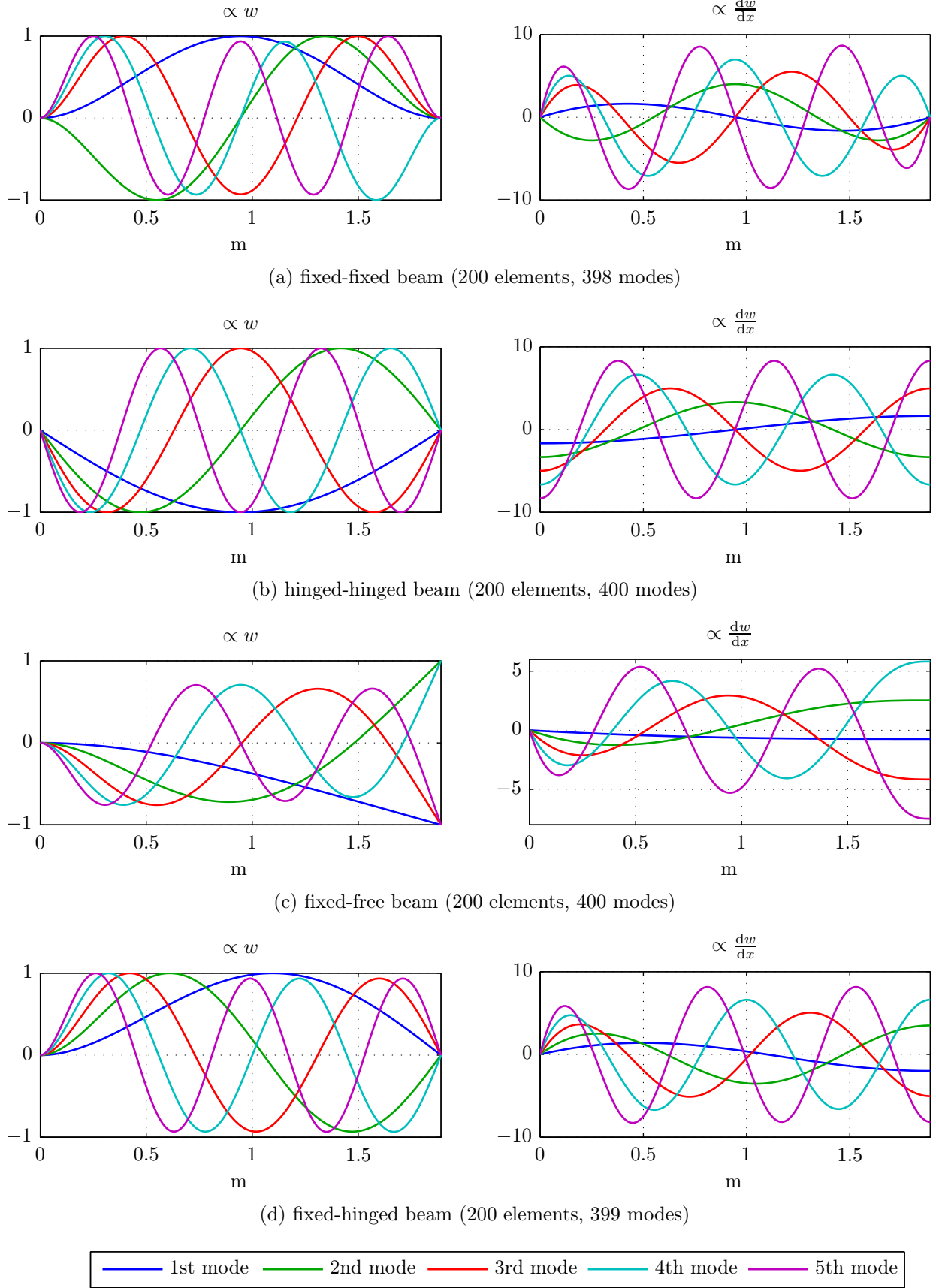


Figure 5.11: Eigenvectors of the first 5 translational (left) / rotatory (right) degrees of freedom (pure beam)

5.5.3 Statical solution of the FE model (pure beam)

The statical model is always included in the dynamic model (5.106) by setting the derivatives to zero. Setting $\dot{\mathbf{x}} = \mathbf{0}$ in the state-space representation

$$\begin{aligned}\dot{\mathbf{x}} &= \mathbf{A}\mathbf{x} + \mathbf{B}\mathbf{u} \\ \mathbf{y} &= \mathbf{C}\mathbf{x} + \mathbf{D}\mathbf{u}\end{aligned}\tag{5.106}$$

leads to:

$$\mathbf{y}_\infty = (-\mathbf{C}\mathbf{A}^{-1}\mathbf{B} + \mathbf{D})\mathbf{u}_\infty\tag{5.107}$$

Remark: The analytical solution was obtained by piecewise integrating the (static) differential equation of the deflection curve (5.108) and considering the boundary/matching conditions.

$$\frac{d^2w(x)}{dx^2} = -\frac{M_y(x)}{EJ_y}\tag{5.108}$$

5.5.3.1 Additional output matrix for displacement, slope, and curvature ($\mathbf{C}_{\text{mbBIG}}$)

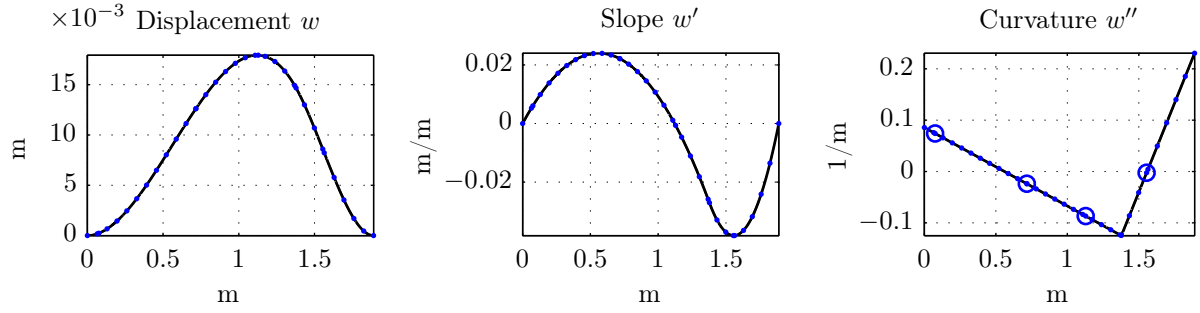
In order to be able to compute the static solution for the displacement w , the slope $\frac{dw}{dx}$ and the curvature $\frac{d^2w}{dx^2}$ along the beam, an additional output matrix called \mathbf{C}_{BIG} was created. Because in the actual experimental setup its corresponding sensors do not exist, they are referred to as “virtual sensors”. The matrix \mathbf{C}_{BIG} ($3m_{\text{BIG}} \times n_d$) computes the outputs of a large number of “virtual sensors” (m_{BIG}) to achieve a good resolution along the beam. In principle the “virtual sensors” are uniformly distributed along the beam. Furthermore, “virtual sensors” are placed at the positions of a “real” sensor and at the shaker attachment point. By using the shape functions for the displacement w (see Section 5.1.1, Equation (5.10)) respectively their first and second derivatives, the first m_{BIG} rows contain the displacement w , the second m_{BIG} the slope $\frac{dw}{dx}$ and the third m_{BIG} rows the curvature $\frac{d^2w}{dx^2}$.

The output matrix \mathbf{C}_{BIG} is transformed analogous to the “normal” output matrix \mathbf{C} (see Sections 5.2 and 5.3). The result is a modal output matrix called $\mathbf{C}_{\text{mbBIG}}$, which corresponds to the same state-space representation with block-diagonal state matrix \mathbf{A}_{mb} as \mathbf{C}_{mb} . It is used for an additional FE model (named “Big FE model”) with the state-space representation of equation (5.109) to compute the static solution of the FE model along the beam.

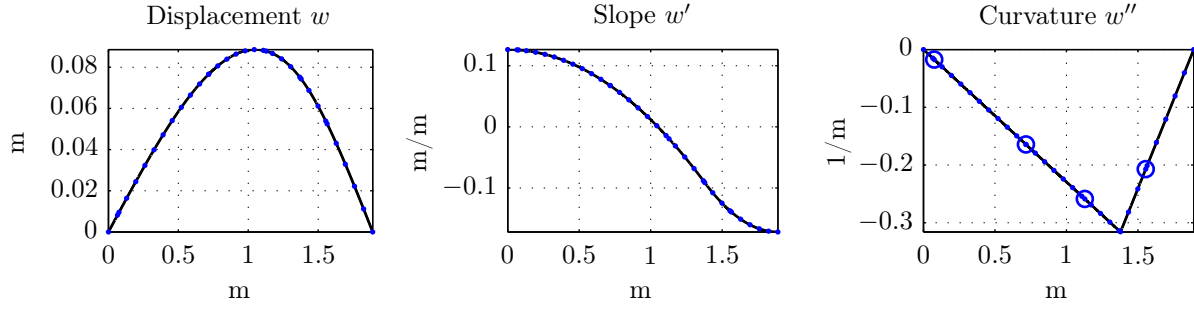
$$\begin{aligned}\mathbf{x}_{\text{mb}} &= \mathbf{A}_{\text{mb}}\mathbf{x}_{\text{mb}} + \mathbf{B}_{\text{mb}}\mathbf{u} \\ \mathbf{y}_{\text{BIG}} &= \mathbf{C}_{\text{mbBIG}}\mathbf{x}_{\text{mb}}\end{aligned}\tag{5.109}$$

5.5.3.2 Statical deformation by a single force

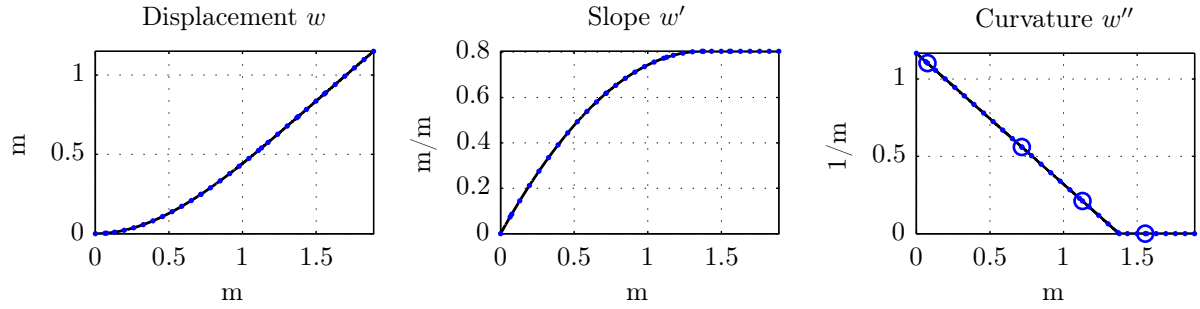
Figure 5.12 illustrates displacement w , slope w' and curvature w'' for different boundary conditions, when a single force $F_s = 10\text{ N}$ acts on the pure beam at $l_s = 1.378\text{ m}$. In the plots the number of “virtual sensors” is $m_{\text{BIG}} = 35$. The number of elements is $n_e = 200$ and all possible modes are considered. The blue circles in the curvature plots show the value of w'' (calculated by the FE model) at the actual position of the “real” sensors, which because of (5.31) is assumed proportional to the bending strain.



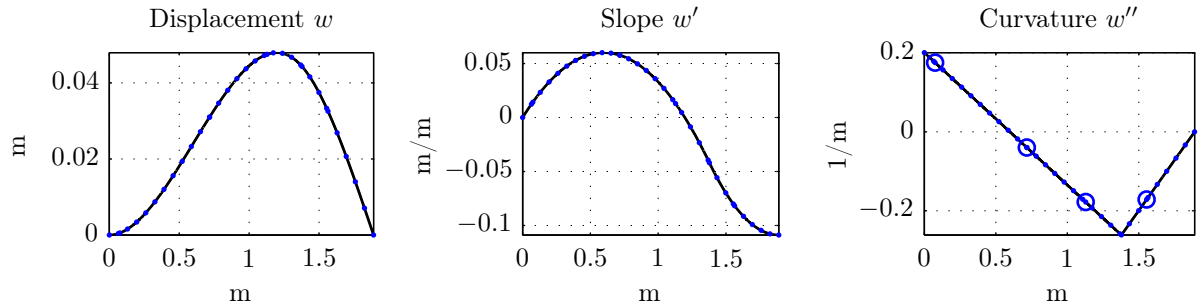
(a) fixed-fixed beam (200 elements, 398 modes)



(b) hinged-hinged beam (200 elements, 400 modes)



(c) fixed-free beam (200 elements, 400 modes)



(d) fixed-hinged beam (200 elements, 399 modes)

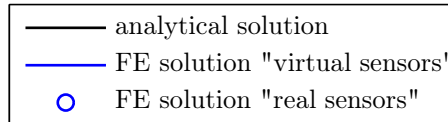
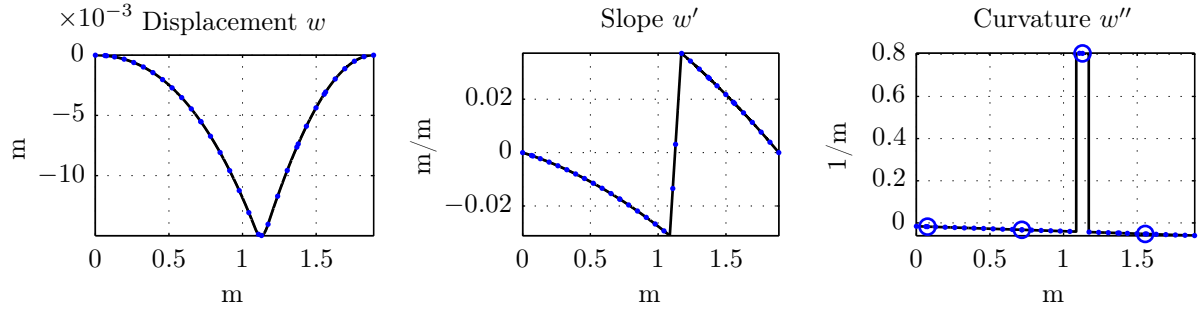


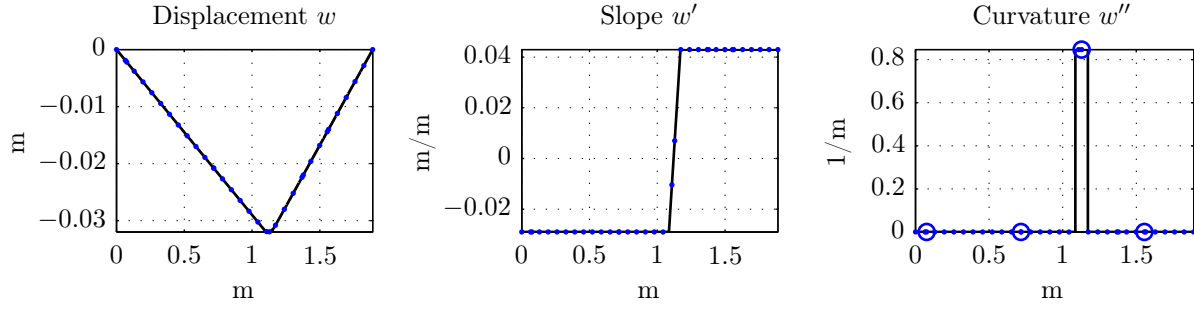
Figure 5.12: Statical deformation of the pure beam, when a single force $F_d = 10$ N is applied at $l_s = 1.378$ m.

5.5.3.3 Statical deformation by two opposite single moments

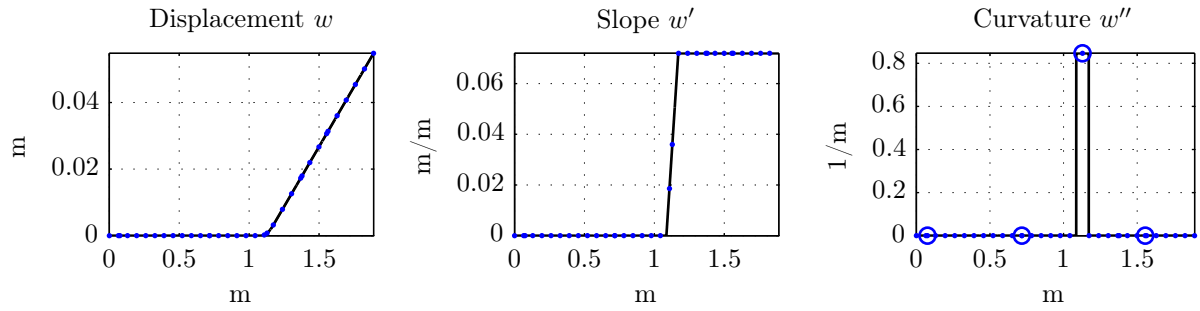
The plots ($m_{\text{BIG}} = 35$, $n_e = 200$) in Figure 5.13 show w , w' , and w'' for different boundary conditions, when two opposite single moments (same value: $M = 10 \text{ Nm}$) initiated by piezo actuator number three act on the pure beam. The distance to the upper bearing (l_3) and the length of a piezo patch actuator (l_A) as depicted in Figure 2.3 are given in Table 2.1 on page 7.



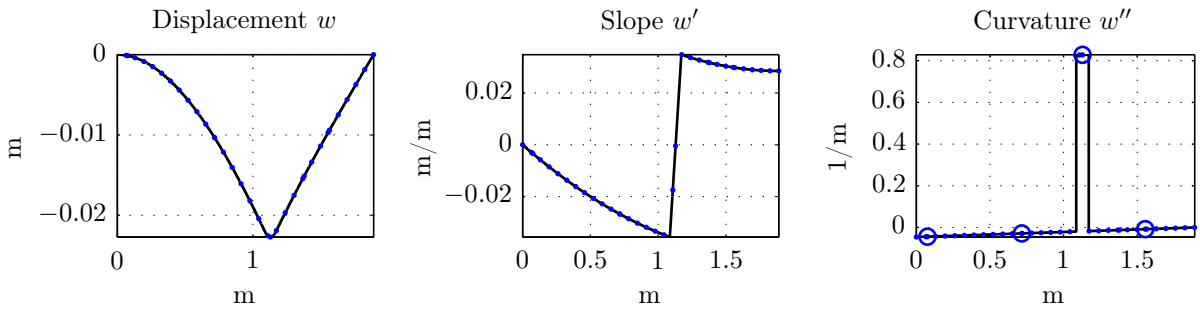
(a) fixed-fixed beam (200 elements, 398 modes)



(b) hinged-hinged beam (200 elements, 400 modes)



(c) fixed-free beam (200 elements, 400 modes)



(d) fixed-hinged beam (200 elements, 399 modes)

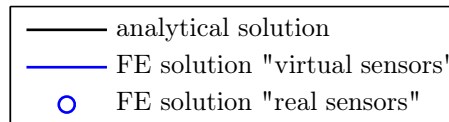


Figure 5.13: Static deformation of the pure beam, when two opposite single moments (same value: $M = 10 \text{ Nm}$) are applied via piezo actuator number three.

5.5.3.4 Convergence study of the statical FE solution

Displacement oriented finite element method (FEM) discretize the field of displacement. Because slope w' and curvature w'' (respectively bending strain $\varepsilon_{\text{bending}}$) are computed by differentiating approximations of displacements w , they can be expected to be even less precise than the displacements. In order to keep the error of the curvature approximations acceptably low, the resolution of spatial discretization must be sufficiently high. [3]

In Figure 5.14 the convergence of the FE solution for different resolutions of spatial discretization for a hinged-hinged beam is depicted. The spacing of the x -grid in all plots of Figure 5.14 was set to the length of an element as used for the lowest depicted resolution of spatial discretization (5 elements) to indicate the nodes of this particular FE model.

For the displacement w Figure 5.14a indicates that even with the lowest resolution of spatial discretization the FE solution yields good results compared to the analytical solution. As expected, by increasing the resolution of spatial discretization the FE solution converges to the analytical solution. At the highest chosen resolution of spatial discretization in Figure 5.14a the deflection curves of the FE solution and the analytical solution are indistinguishable.

For applied external moments, the resulting analytical solution for the slope w' is not continuously differentiable (Figure 5.14b): It has kinks at those positions where the moments are initiated. The shape functions used by the FE model to compute the slope are the differentiated shape functions originally designed for calculating the displacements and thus are only quadratic instead of cubic. In order to achieve a good match for the FE solution at the kinks of the analytical solution a low resolution of spatial discretization is inappropriate. (see blue dots in Figure 5.14b).

Finally the shape functions used by the FE model to compute the curvature w'' are only polynomials of first order. In Figure 5.14c the convergence of the curvature w'' is illustrated. By taking a look at the curve of the FE model with the lowest resolution of spatial discretization, it can easily be seen that between two nodes (visualized by the x -grid), the FE solution approximates the curvature by straight lines. Although at the border of an element the displacements w proceed continuously to the adjoining element, the curvatures w'' (and in the further the distortions) at the border of an element have discontinuities, in particular leaps. Even with the highest depicted resolution of spatial discretization the FE model is not capable to match the analytical solution well around the positions where the moments are initiated (points of discontinuity), but in the middle of a piezo actuator respectively sensor the FE model with the highest resolution of spatial discretization achieves quite good results for w'' , which validates this resolution of spatial discretization.

In this work the beam was discretized by Hermitian beam elements all of the same length l . In order to improve the FE model at those positions where the external loads are initiated, by maintaining a reasonably small overall element number, the length of an element could be reduced only in regions around these load initiation positions (h-refinement method, see [3]). Moreover, utilizing a structural element as the Hermitian beam element for spatial discretization the accuracy of the FE solution can be increased, when external loads are applied only to nodes and not in between two nodes. [3]

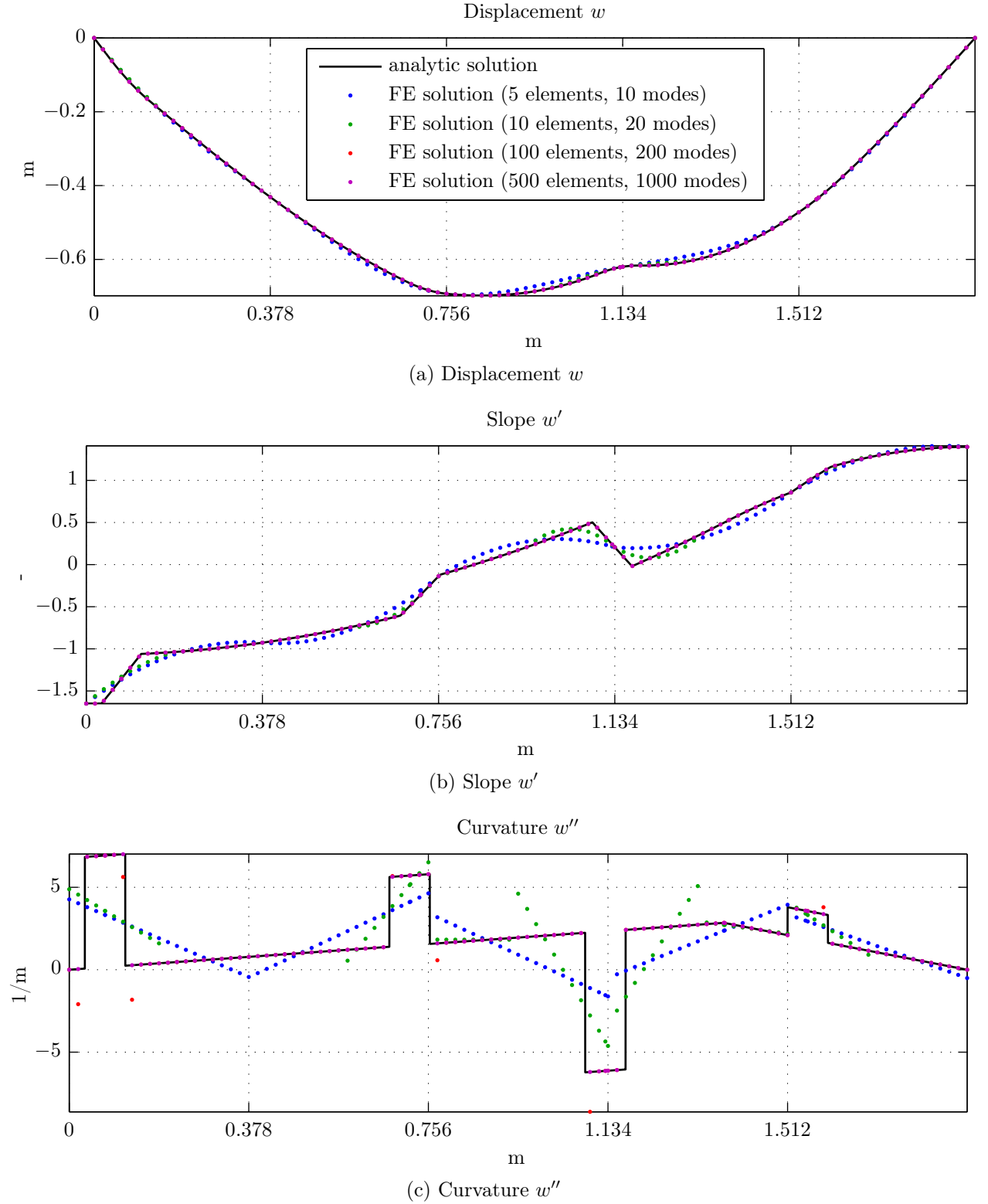


Figure 5.14: Convergence of the FE solution for different resolutions of the spatial discretization (hinged-hinged supported pure beam)
 $M_1 = 80 \text{ Nm}$, $M_2 = 50 \text{ Nm}$, $M_3 = -100 \text{ Nm}$, $M_4 = 20 \text{ Nm}$, $F_s = -90 \text{ N}$
 (Loads as depicted in Figure 5.7 on page 34)

5.5.4 Statical solution for the outer fiber strain

For the outer fiber strain Figure 5.15 shows the difference between disregarding ($\varepsilon_{\text{bending}}$) and considering ($\varepsilon_{\text{overall}}$) the non-zero state-space feed-through matrix \mathbf{D} , as derived in Section 5.3.4.

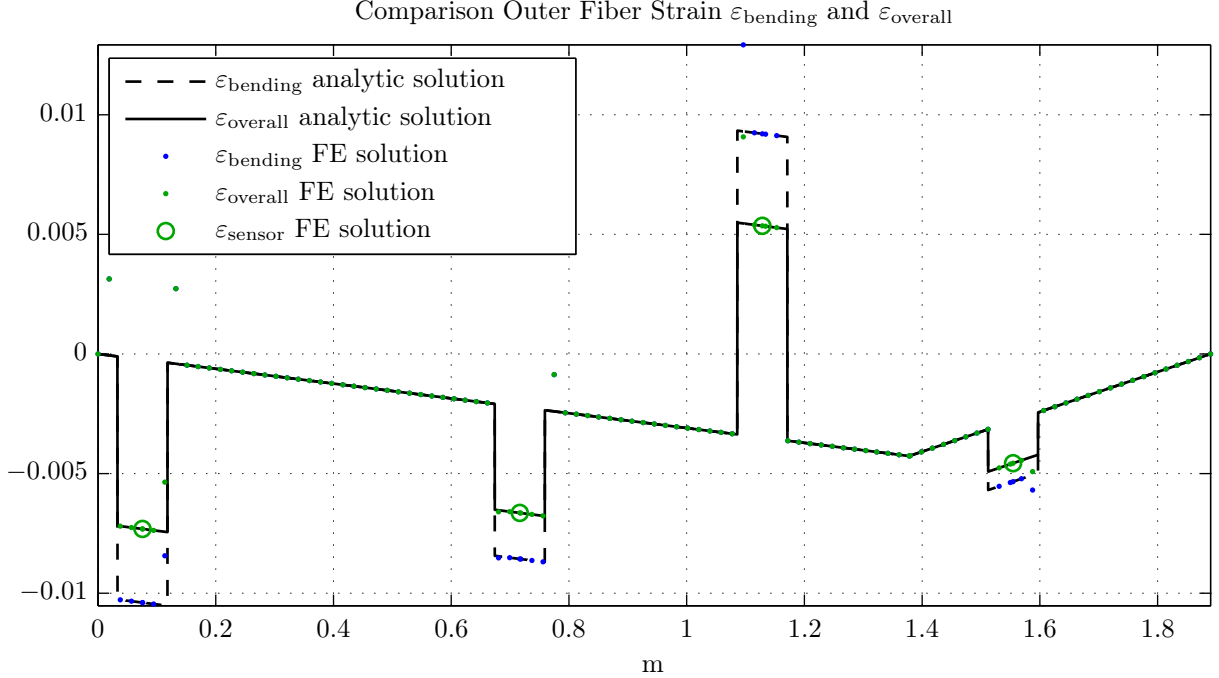


Figure 5.15: Comparison between $\varepsilon_{\text{bending}}$ and $\varepsilon_{\text{overall}}$ (hinged-hinged supported pure beam with 100 elements and 200 modes)
 $M_1 = 80 \text{ Nm}$, $M_2 = 50 \text{ Nm}$, $M_3 = -100 \text{ Nm}$, $M_4 = 20 \text{ Nm}$, $F_s = -90 \text{ N}$
 (Loads as depicted in Figure 5.7 on page 34)

It can be concluded that the consideration of tensile strain (and thus, the feed-through term) is relevant.

5.6 Beam with Mounted Shaker

In Figure 5.16 the model concept as used for the FE model for taking a mounted shaker into account is depicted. The mass m_1 (0.0242 kg) is the mass of both mounting prisms. For simplification only one mounting prism is drawn in Figure 5.16. The mass m_2 (0.0292 kg) is the mass of the acceleration and force sensor (0.0192 kg) plus the half mass of the nylon stinger (0.010 kg). The mass m_3 (0.055 kg) is composed of the other half of the nylon stinger plus the moving parts of the shaker (0.045 kg), denoted as armature mass in the data sheet. The nylon stinger is modelled as a parallel combination of a spring (k_1) and a velocity-proportional damper (c_1). Also, the suspension of the mass m_3 inside the shaker is modelled as a parallel combination of a spring ($k_2 = 2630 \text{ N/m}$, given in the data sheet of the shaker) and a velocity-proportional damper with a (fully unknown, positive) damping coefficient (c_2).

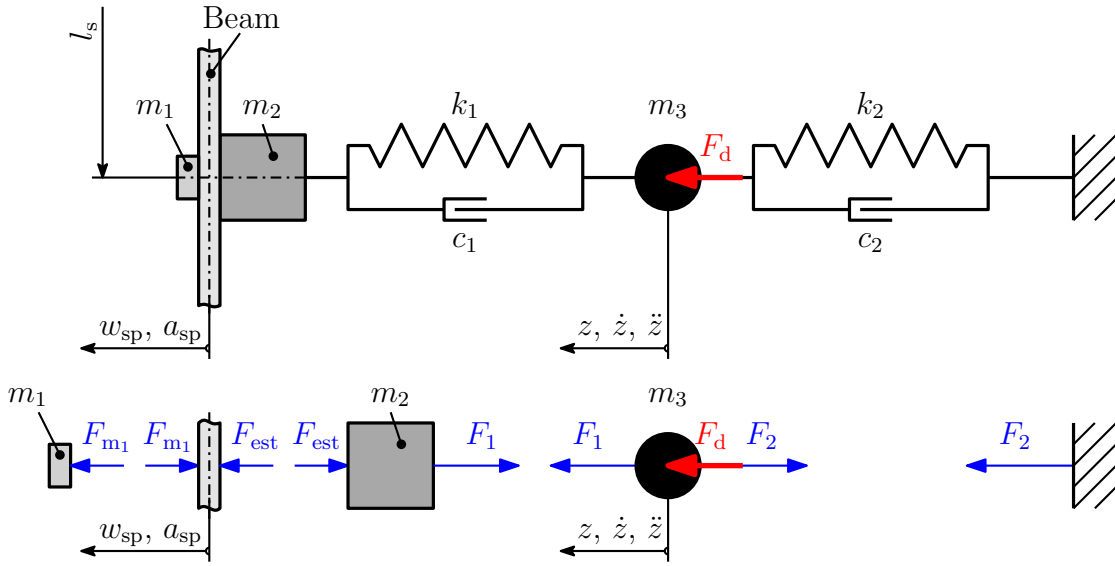


Figure 5.16: Model concept used for the shaker mounting. (m_1 is the mass of both mounting prisms. For simplification only one prism is drawn.)

Applying the center-of-mass theorem on the masses m_1 , m_2 , and m_3 yields Equations (5.110) to (5.112).

$$m_1 a_{sp} = F_{m1} \quad (5.110)$$

$$m_2 a_{sp} = -F_{est} - F_1 \quad (5.111)$$

$$m_3 \ddot{z} = F_1 - F_2 + F_d \quad (5.112)$$

In Figure 5.16, F_d is the electrodynamic force acting on the moving parts of the shaker. The dynamic force F_1 of the nylon stinger is computed by Equation (5.113) and the dynamic force F_2 of the suspension inside the shaker on the shaker's moving parts is computed by Equation (5.114).

$$F_1 = c_1 \cdot (\dot{w}_{sp} - \dot{z}) + k_1 \cdot (w_{sp} - z) \quad (5.113)$$

The system order of the FE beam model with mounted shaker is larger by four than the system order of the FE beam model without shaker.¹⁵

It turned out that the presumed high, but unknown stiffness of the nylon stinger (k_1) has a negligible influence on the system's first eigenfrequencies. Therefore choosing k_1 as infinitely stiff is a reasonable choice, simplifying the following transfer functions:

$$\lim_{k_1 \rightarrow \infty} G_{zw_{sp}}(s) = 1 \quad (5.121)$$

$$\lim_{k_1 \rightarrow \infty} G_{zF_d}(s) = 0 \quad (5.122)$$

$$\lim_{k_1 \rightarrow \infty} G_{F_1 w_{sp}}(s) = m_3 \cdot s^2 + c_2 \cdot s + k_2 \quad (5.123)$$

$$\lim_{k_1 \rightarrow \infty} G_{F_1 F_d}(s) = 1 \quad (5.124)$$

Of course, equations (5.121) to (5.124) exhibit that by letting k_1 approach infinity, the damping coefficient of the stinger (c_1) has no influence on the system at all and that in this case the disturbance force F_d directly acts on the beam (see (5.124)). This way, only c_2 remained as unknown parameter which had to be found by tuning. By comparing the absolute difference of the first five natural frequencies of the identified model with mounted shaker ($\mathbf{H}_{10+8}^{r\{10+0\}}$) with those of the FE model with mounted shaker when varying c_2 it turned out that $c_2 = 15.8 \text{ N/m/s}$ was a good choice.

Comparing the FE and the identified models will be the main subject of Chapter 6.

5.7 Validation of the FE Model of the Beam with Mounted Shaker

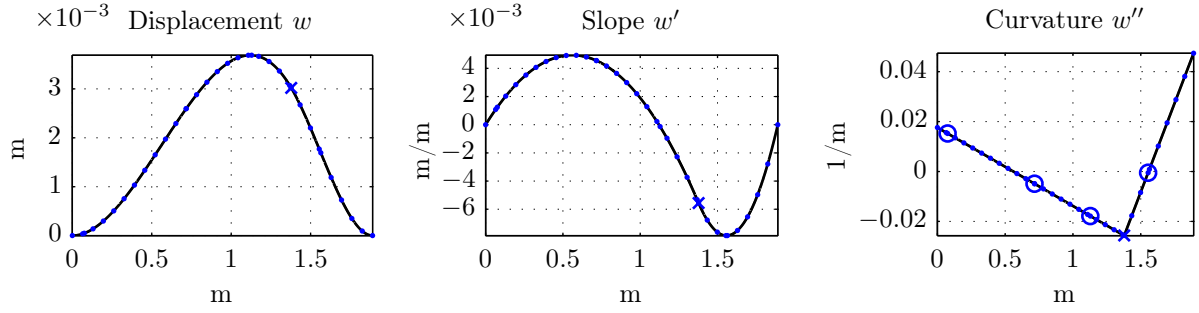
5.7.1 Statical deformation by a single force

Figure 5.18 illustrates the displacement w , slope w' , and curvature w'' for different boundary conditions when a single force $F_d = 10 \text{ N}$ (see Figure 5.16) is applied to the beam with mounted shaker. Again, the analytical solution was obtained by solving the differential equation of the deflection curve. In Table 5.4 the static solution(s) for F_{est} and w_{sp} for this load case are shown. The analytical and the FE solution match very well.

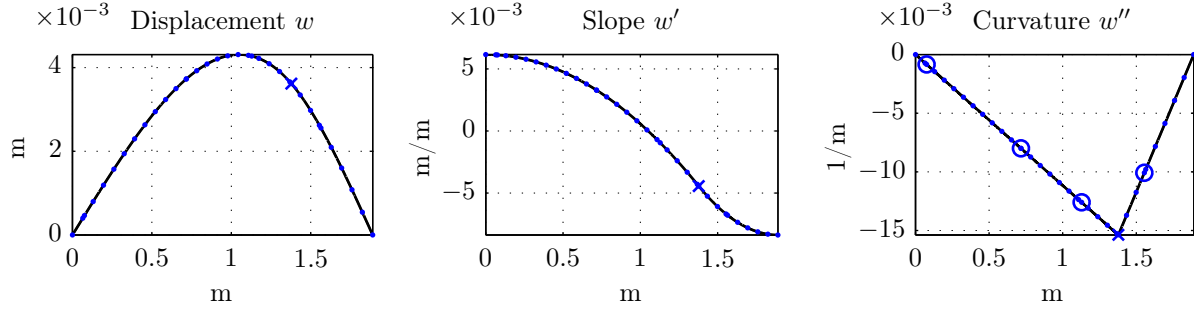
beam with mounted shaker boundary conditions	analytical solution F_{est}	FE solution (200 elements)	
		F_{est}	w_{sp}
fixed-fixed	2.0573 N	2.0573 N	0.0030 m
hinged-hinged	0.4867 N	0.4867 N	0.0036 m
fixed-free	0.0512 N	0.0512 N	0.0038 m
fixed-hinged	0.7903 N	0.7903 N	0.0035 m

Table 5.4: Statical solution for F_{est} and w_{sp} (see Figure 5.16) when a single force $F_d = 10 \text{ N}$ is applied to the beam with mounted shaker

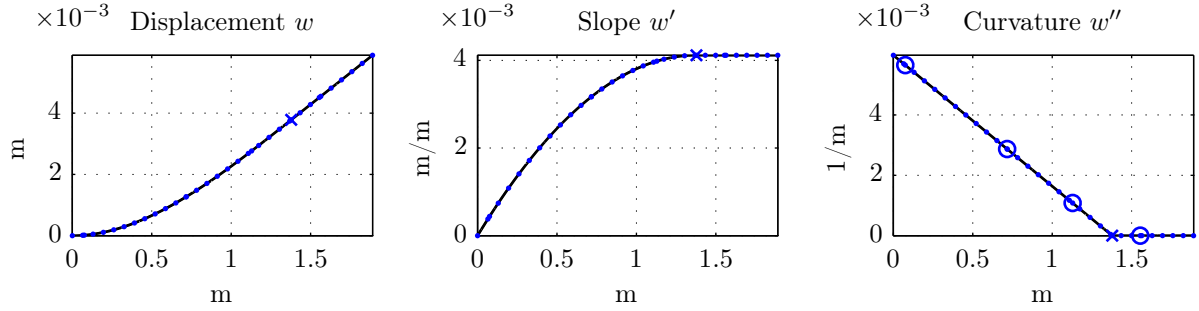
¹⁵When in Figure 5.17 $G_{F_1 F_d}(s)$ is set to the static gain $G_{F_1 F_d}(s) = 1$, the disturbance force input F_d in Figure 5.16 acts directly on the beam. In this case the system order of the FE beam model with mounted shaker would be only two more than the system order of the FE beam model without shaker.



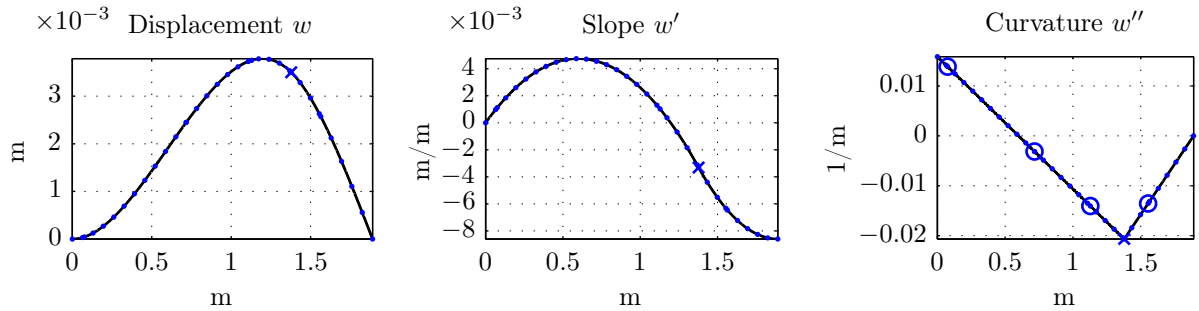
(a) fixed-fixed beam with mounted shaker (200 elements, 398 modes)



(b) hinged-hinged beam with mounted shaker (200 elements, 400 modes)



(c) fixed-free beam with mounted shaker (200 elements, 400 modes)



(d) fixed-hinged beam with mounted shaker (200 elements, 399 modes)

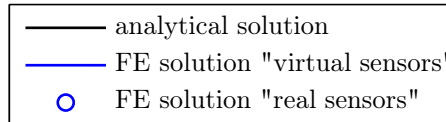


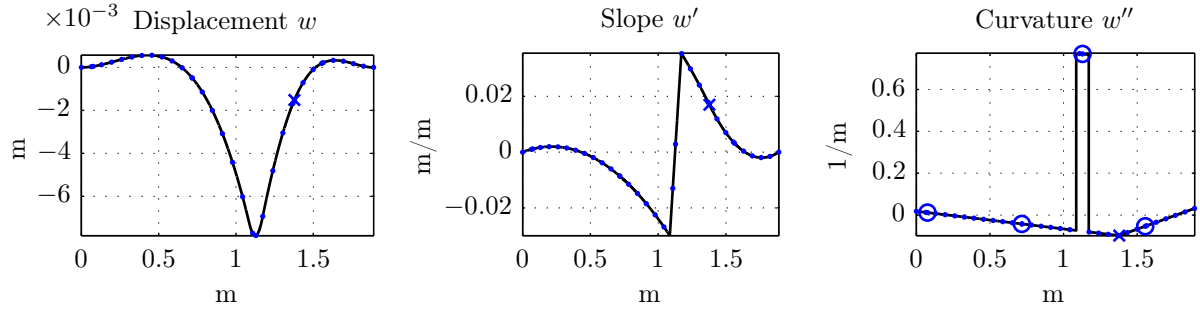
Figure 5.18: Static deformation of the beam with mounted shaker, when a single force $F_d = 10$ N is applied at the shaker position $l_s = 1.378$ m. A cross is used to mark the position of the shaker coupling point.

5.7.2 Statical deformation by two opposite single moments

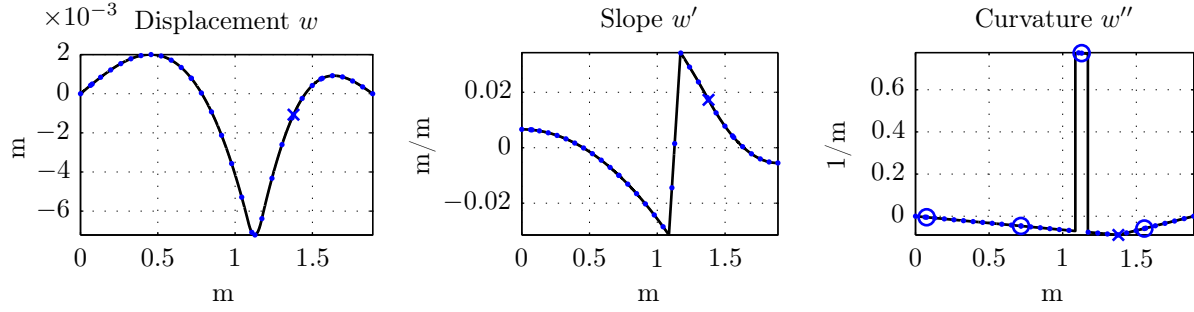
Figure 5.18 illustrates the displacement w , slope w' , and curvature w'' for different boundary conditions, when two opposite single moments (same value: $M = 10 \text{ Nm}$) are applied to the beam with mounted shaker via piezo actuator number three. In Table 5.5 the static solution(s) for F_{est} and w_{sp} for this load case are shown. The analytical and the FE solution match very well.

beam with mounted shaker boundary conditions	analytical solution F_{est}	FE solution (200 elements)	
		F_{est}	w_{sp}
fixed-fixed	3.9890 N	3.9890 N	-0.0015 m
hinged-hinged	2.8158 N	2.8158 N	-0.0011 m
fixed-free	-0.2419 N	-0.2419 N	$9.1977 \cdot 10^{-5} \text{ m}$
fixed-hinged	3.1428 N	3.1428 N	-0.0012 m

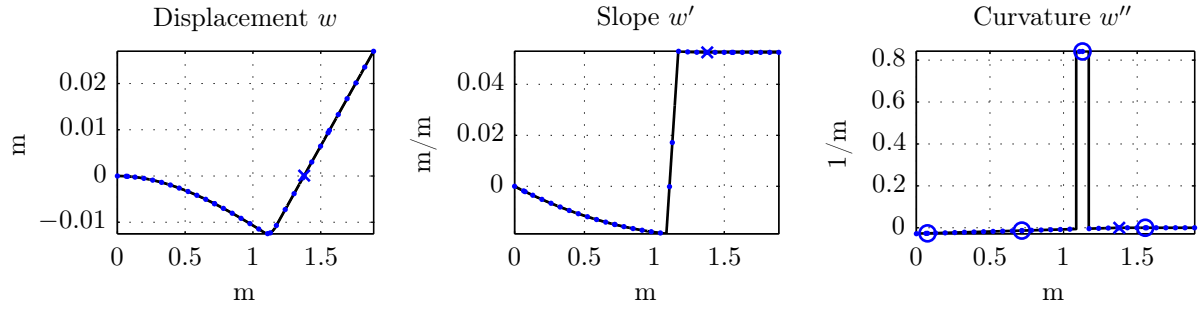
Table 5.5: Statical solution for F_{est} and w_{sp} (see Figure 5.16) when two opposite single moments (same value: $M = 10 \text{ Nm}$) are applied to the beam with mounted shaker via piezo actuator number three.



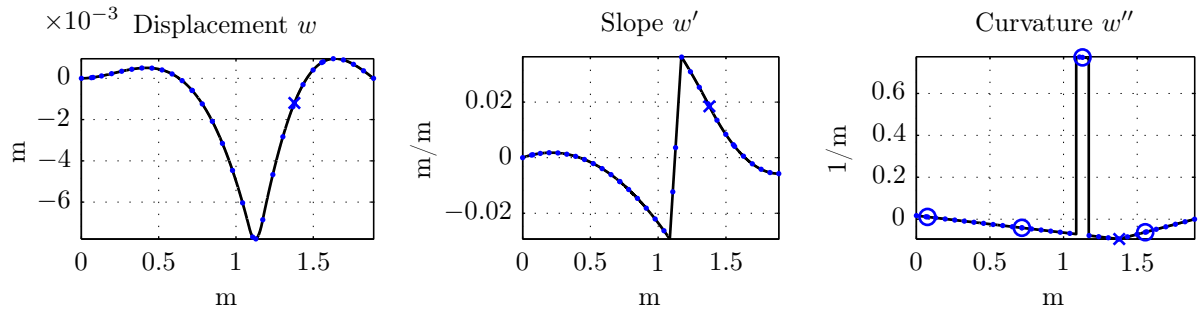
(a) fixed-fixed beam with mounted shaker (200 elements, 398 modes)



(b) hinged-hinged beam with mounted shaker (200 elements, 400 modes)



(c) fixed-free beam with mounted shaker (200 elements, 400 modes)



(d) fixed-hinged beam with mounted shaker (200 elements, 399 modes)

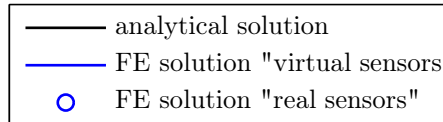


Figure 5.19: Statical deformation of the beam with mounted shaker, when two opposite single moments (same value: $M = 10 \text{ Nm}$) are applied via piezo actuator number three. A cross is used to mark the position of the shaker coupling point.

5.7.3 Eigenmodes

The eigenmodes (mode shapes) of the beam with mounted shaker were computed by utilizing the eigenvectors of the state matrix of the beam with mounted shaker state-space model (see Section 5.6).

Consider the homogeneous system ($\mathbf{u} = \mathbf{0}$) with state-equation (5.125) and output-equation (5.126).

$$\dot{\mathbf{x}} = \mathbf{A}\mathbf{x} \quad (5.125)$$

$$\mathbf{y} = \mathbf{C}\mathbf{x} \quad (5.126)$$

For a complex conjugate eigenvalue pair $\lambda_i = \mu_i \pm j\nu_i$ of the state matrix \mathbf{A} the eigenvalue/eigenvector problem follows to

$$\mathbf{A}(\mathbf{u}_i \pm j\mathbf{v}_i) = (\mu_i \pm j\nu_i) \cdot (\mathbf{u}_i \pm j\mathbf{v}_i) \quad (5.127)$$

or (rearranged)

$$(\mathbf{A} - (\mu_i \pm j\nu_i)\mathbf{I})(\mathbf{u}_i \pm j\mathbf{v}_i) = \mathbf{0}, \quad (5.128)$$

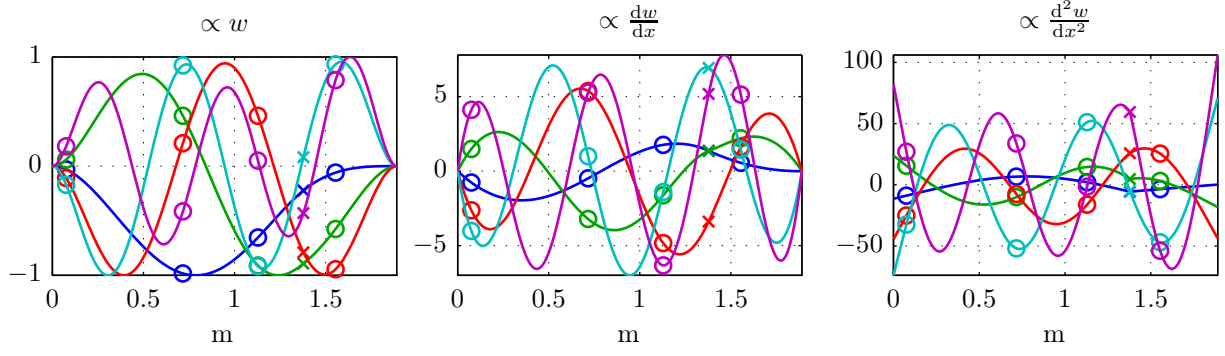
where the vectors \mathbf{u}_i and \mathbf{v}_i span the mode's oscillation plane.¹⁶ [13]

By choosing the projection on the real axis (\mathbf{u}_i) of the complex-valued eigenvector ($\mathbf{u}_i \pm j\mathbf{v}_i$) as state vector \mathbf{x} in (5.126) the i th mode shape $\mathbf{y}_{\text{mode}i}$ of the output vector \mathbf{y} was obtained by:

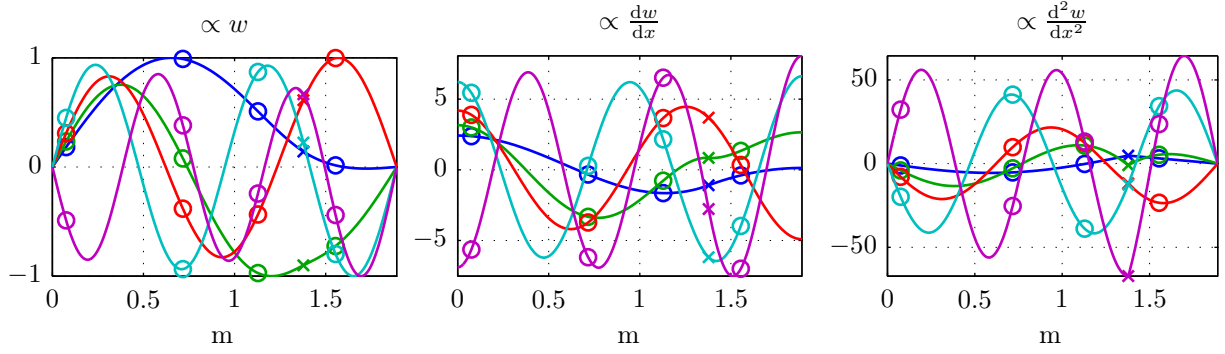
$$\mathbf{y}_{\text{mode}i} = \mathbf{C}\mathbf{u}_i \quad (5.129)$$

In order to get a good resolution along the beam the output matrix of “virtual sensors” (of the beam with mounted shaker state-space model) was used in (5.129). For different clamping conditions the first five displacement- (w), slope- ($\frac{dw}{dx}$), and curvature- ($\frac{d^2w}{dx^2}$) proportional mode shapes of the FE beam with mounted shaker are depicted in Figure 5.20. The bending strain ($\varepsilon_{\text{bending}}$) proportional mode shapes look like the curvature ($\frac{d^2w}{dx^2}$) proportional mode shapes because in linear elastic bending theory $\varepsilon_{\text{bending}} \propto \frac{d^2w}{dx^2}$ (see (5.31)). In Figure 5.20, circles mark the positions of the “real sensors” and a cross is used to mark the position of the shaker coupling point.

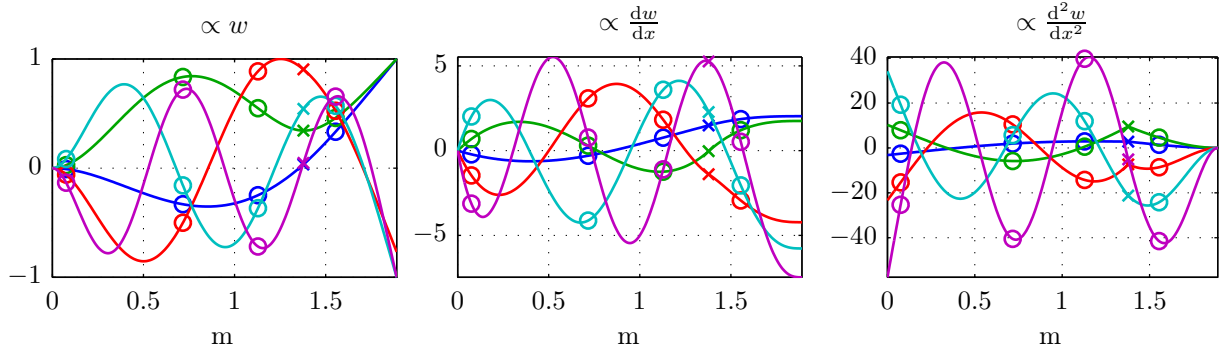
¹⁶Once the state vector $\mathbf{x}(t)$ of the homogeneous system (5.125) lies within this plane it remains in it as it spirally moves around the origin. For $\mu_i < 0$ the trajectory approaches the origin asymptotically, for $\mu_i > 0$ the trajectory moves away from the origin exponentially and for $\mu_i = 0$ the trajectory stays at the same orbit for all time. [13]



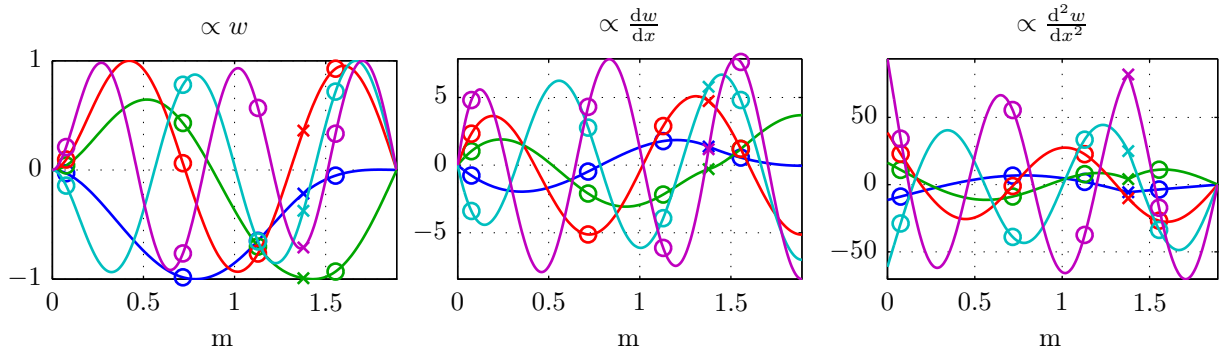
(a) fixed-fixed beam with mounted shaker (200 elements, 398 modes)



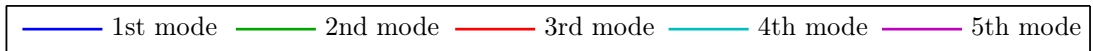
(b) hinged-hinged beam with mounted shaker (200 elements, 400 modes)



(c) fixed-free beam with mounted shaker (200 elements, 400 modes)



(d) fixed-hinged beam with mounted shaker (200 elements, 399 modes)

Figure 5.20: First five displacement- (w), slope- ($\frac{dw}{dx}$), and curvature- ($\frac{d^2w}{dx^2}$) proportional mode shapes of the FE beam with mounted shaker

5.8 Modeling a Piezo Patch Actuator as a Static Gain and Regarding its Amplifiers

So far, the input of a piezo patch actuator is modelled as a moment input. Modeling a piezo patch actuator as a static gain and including a simple amplifier model in the FE model will be the purpose of this section.

An additional state-space system was created which computes the strain of the piezo patch actuators (and not the sensors). This model(s) (FE model with/without mounted shaker) was built by multiplying those rows of the output matrix \mathbf{C} which correspond to the strain computations of the sensors by the factor $-(h+h_p)/h$ and is called “FE model with ε_a output” ($h_p = 0.3 \text{ mm}$ is the thickness of a piezo patch actuator). Let $\mathbf{G}_{\varepsilon_a M}(s)$ be its MIMO transfer function matrix with elements $G_{\varepsilon_a Mij}(s)$. Its diagonal elements are $G_{\varepsilon_a Mii}(s)$.

Figure 5.21 visualizes the characteristic equation of piezo patch actuator i (5.130) (see also Section 2.1).

$$F_i(\varepsilon_{ai}, U_i) = F_B \cdot \left(1 - \frac{\varepsilon_{ai}}{\varepsilon_0}\right) \cdot \frac{U_i}{U_{\max}} \quad (5.130)$$

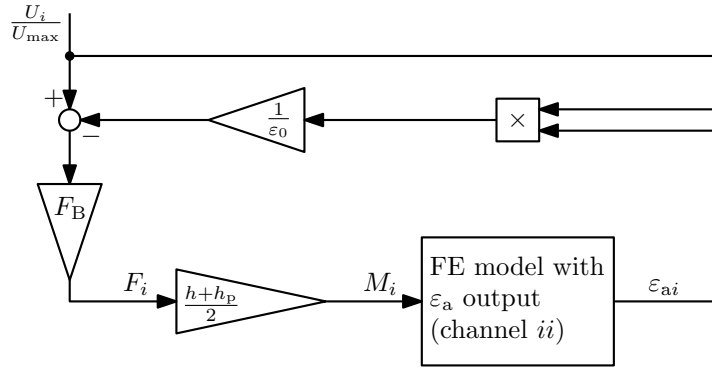


Figure 5.21: Non-linear function of the force exerted by a piezo patch actuator to a structure (due to an applied voltage input signal) of the own elongation

In order to simplify the computation, the static solution, the constant gain $K_{\varepsilon_a Mii}$ (5.131) was computed and used for the further computations. (A bar “-” indicates a static solution.)

$$K_{\varepsilon_a Mii} = \lim_{s \rightarrow 0} G_{\varepsilon_a Mii}(s) \quad (5.131)$$

$$\bar{\varepsilon}_{ai} = K_{\varepsilon_a Mii} \cdot \frac{h+h_p}{2} \cdot F_B \cdot \left(1 - \frac{\bar{\varepsilon}_{ai}}{\varepsilon_0}\right) \cdot \frac{U_i}{U_{\max}} \quad (5.132)$$

$$\bar{\varepsilon}_{ai}(U_i) = \frac{K_{\varepsilon_a Mii} \cdot \frac{h+h_p}{2} \cdot F_B \cdot U_i}{U_{\max} + K_{\varepsilon_a Mii} \cdot \frac{h+h_p}{2} \cdot F_B \cdot \frac{1}{\varepsilon_0} \cdot U_i} \quad (5.133)$$

Equation (5.133) exhibits the nonlinear dependency of $\bar{\varepsilon}_{ai}$ on the applied voltage input signal U_i . By setting $U_i = U_{\max}$ a working point was chosen (indicated with a hat “^”).

$$\hat{\bar{\varepsilon}}_{ai} = \bar{\varepsilon}_{ai}(U_i = U_{\max}) \quad (5.134)$$

$$\hat{\bar{F}}_i = F_B \cdot \left(1 - \frac{\hat{\bar{\varepsilon}}_{ai}}{\varepsilon_0}\right) \quad (5.135)$$

$$R_i = \frac{\hat{F}_i}{F_B} \quad (5.136)$$

$$M_i = \underbrace{\frac{h + h_p}{2} \cdot F_B \cdot R_i \cdot \frac{1}{U_{\max}}}_{K_{\text{MU}i}} \cdot U_i \quad (5.137)$$

$$M_i = \underbrace{K_{\text{MU}i} \cdot K_{\text{higV}} \cdot K_{\text{dSPACE}}}_{K_{\text{Mui}}} \cdot u_i \quad (5.138)$$

- U_i : - voltage input piezo actuator i (for $i = 1, \dots, 4$)
- u_i : - equivalent input signal to a logged input signal u_i^l (for $i = 1, \dots, 4$) of the experimental setup (see Figure 2.4)
- $\hat{\varepsilon}_{ai}$: - max. strain in piezo patch actuator i (computed by the statical FE model)
- \hat{F}_i : - max. force applied by piezo patch actuator i (computed by the statical FE model)
- R_i : - ratio between max. applied force \hat{F}_i and blocking force
- $K_{\text{MU}i}$: - gain from voltage input piezo actuator U_i to moment M_i (FE input)
- K_{higV} : - gain of the piezo actuator amplifier (high voltage amplifier)
 $K_{\text{higV}} = 200 \text{ V/V}$
- K_{dSPACE} : - gain of the DAC (see Figure 2.4) $K_{\text{dSPACE}} = 10 \text{ V}$
- K_{Mui} : - overall gain at the input side from u_i to moment M_i (as static gain computed)

In Table 5.6 the computed values for R_i are listed (hinged-hinged beam). For a hinged-hinged beam with unmounted shaker the values of R_i have to be all the same, because the curvature is zero along the beam (see Figure 5.13b) except in the regions of the piezo patch actuators, where the curvature (and in the further the outer fiber strain) is of the same value, when $M_i = M$ (for $i = 1, \dots, 4$). For a hinged-hinged beam with mounted shaker the values of R_i are different, because of the additional bearing introduced by the shaker spring k_2 (see Figure 5.16), the curvature (and in the further the outer fiber strain) varies along the beam (see Figure 5.19b on page 62).

	FE model beam with unmounted shaker (hinged-hinged beam, 200 elements)	FE model beam with mounted shaker (hinged-hinged beam, 200 elements)
R_1 :	0.8690	0.8703
R_2 :	0.8690	0.8814
R_3 :	0.8690	0.8887
R_4 :	0.8690	0.8847

Table 5.6: Computed ratio between max. applied force and blocking force for a hinged-hinged beam

5.9 Shaker Gain $K_{F_{dd}}$

The shaker gain $K_{F_{dd}} = 1.2713 \text{ N/V} \cdot 10 \text{ V}$ was obtained by a separate identification utilizing the measured force and acceleration signals of the impedance head, but this was not part of this work.

5.10 Discussion of unmodelled effects/behaviour

The absence of degrees of freedom in the x -direction is regarded as entirely appropriate. While it would be possible to model with additional degrees of freedom in the x -direction the normal forces introduced by the actuators (in the respective sections of the beam) directly, this would increase the system order unnecessarily, since the influence on a collocated sensor can be considered as instantaneous and thus in a state-space representation can be easily regarded by a non-zero feed-through matrix. Furthermore, an increased effort in modeling the shear stress in the adhesive layer is not considered appropriate, since the piezo patch actuators (as well as the sensors) exhibit hysteresis behavior anyway and improvement measures should focus on that area.

Moreover, it is assumed that bearing friction and additional stiffness, damping, and mass introduced via measurement and control cabling should be taken into account rather, possibly by using feedback loops utilizing slope/slope rate outputs and moment inputs respectively acceleration outputs and force inputs.

Also the dynamics of physical system (e.g. amplifiers) on the plants input- respectively output-side were not modelled. Assuming linearity, these neglected dynamics can be explicitly taken into account in a DK control design by utilizing an adequate multiplicative input respectively output uncertainty description, see Section 8.6.2.2.

Chapter 6

Preparing and Comparing the Derived Models

6.1 Physical Calibration of the Piezo Patch Sensors

In order to compare the two kinds of models (the FE model and the identified model), the inputs and outputs of both types of models have to be expressed in the same physical units. In Section 5.8 and 5.9 the inputs of the FE model(s) were adapted to match the physical units of the identified model(s).

By using the conversion factors for the acceleration and force signals, documented in the data sheet of the acceleration and force sensors, the Simulink[®] subsystem “MIMO beam” (see Figure 2.4) directly yields these output signals in their mechanical units.

To obtain the outputs of the piezo patch sensors in their mechanical units (i.e. the outer fiber strain), the static conversion factors $K_{\text{ey}^1 i}$ (for $i = 1, \dots, 4$) are obtained as follows. Linearity is assumed.

The experimental beam is excited by applying a sine signal to the shaker (forced oscillation) of a frequency of $f_{\text{excite}} = 5.5 \text{ Hz}$. This frequency lies far away from the beam’s (beam with unmounted shaker) natural frequencies (between its first and second natural frequency), in a region where all four frequency responses from the shaker to the piezo patch sensors are relatively flat and by this means insensible to a small frequency variation. This choice of f_{excite} improves the accuracy of the following procedure:

After the beam’s transient behaviour has decayed, the harmonic system responses of the four piezo patch sensors (with amplitudes \bar{y}_1^1 to \bar{y}_4^1) and the force sensor (with amplitude \bar{y}_6^1) are logged. The logged output signals $y_i^1(t)$ (indicated by the letter “1”) are the input signals to the output ports of the Simulink[®] subsystem “MIMO beam” (see Figure 2.4).

Let $G_{\text{di}}^{\text{FEb}}(s)$ be the transfer function from the force input to the strain output i (at the position of piezo patch sensor i) of the FE model of the beam with unmounted shaker. Then, the resulting amplitude (at steady state) of the strain signal (of sensor i), when a sinusoidal force signal $d(t)$ (6.1) of amplitude \bar{y}_6^1 and frequency f_{excite} is applied to the FE model, is obtained by using Equation (6.2).

$$d(t) = \bar{y}_6^1 \cdot \sin(2\pi f_{\text{excite}} t) \quad (6.1)$$

$$\bar{y}_i^{\text{FEb}} = |G_{\text{di}}^{\text{FEb}}(j2\pi f_{\text{excite}})| \bar{y}_6^1 \quad (6.2)$$

Finally, the conversion factor $K_{\varepsilon y^l i}$ for piezo patch sensor i is computed as the ratio between the simulated output \bar{y}_i^{FEb} of the FE model (beam with unmounted shaker) and the measured outputs \bar{y}_i^l (for $i = 1, \dots, 4$).

$$K_{\varepsilon y^l i} = \frac{\bar{y}_i^{\text{FEb}}}{\bar{y}_i^l}$$

For simplicity (and because the measurement lines of all piezo patch sensors are identical) their mean value was used.

$$K_{\varepsilon y^l} = \frac{1}{4} \sum_{i=1}^4 K_{\varepsilon y^l i} = 1.9321 \cdot 10^{-5} \quad (6.3)$$

6.2 Input/Output Scaling

Applying input/output-scaling to a MIMO transfer system by utilizing knowledge about maximum signal amplitudes allows to compare the relative importance of different transfer paths. Moreover, input/output-scaling is essential in order to apply the definitions of the control goals in optimal and robust \mathcal{H}_∞ control (see Chapter 8). [6]

Let the unscaled (or originally scaled) MIMO system obtained in the previous sections be

$$\hat{\mathbf{y}} = \hat{\mathbf{G}}\hat{\mathbf{u}} + \hat{\mathbf{G}}_d\hat{\mathbf{d}} \quad \hat{\mathbf{e}} = \hat{\mathbf{y}} - \hat{\mathbf{r}} \quad (6.4)$$

where a hat (“ $\hat{}$ ”) is used to indicate signals in unscaled, physical units. The scaling is done with the diagonal scaling matrices (\mathbf{D}_d , \mathbf{D}_u , \mathbf{D}_e) whose diagonal elements (ii) contain the largest allowed (or expected) value ($\hat{d}_{i\max}$, $\hat{u}_{i\max}$, $\hat{e}_{i\max}$) of the associated signal magnitude in the corresponding signal vector ($\hat{\mathbf{d}}$, $\hat{\mathbf{u}}$, $\hat{\mathbf{e}}$).

The scaled variables are:

$$\mathbf{d} = \mathbf{D}_d^{-1}\hat{\mathbf{d}} \quad \mathbf{u} = \mathbf{D}_u^{-1}\hat{\mathbf{u}} \quad \mathbf{y} = \mathbf{D}_e^{-1}\hat{\mathbf{y}} \quad \mathbf{e} = \mathbf{D}_e^{-1}\hat{\mathbf{e}} \quad \mathbf{r} = \mathbf{D}_e^{-1}\hat{\mathbf{r}}. \quad (6.5)$$

This leads to the scaled transfer function matrices:

$$\mathbf{G} = \mathbf{D}_e^{-1}\hat{\mathbf{G}}\mathbf{D}_u \quad (6.6)$$

$$\mathbf{G}_d = \mathbf{D}_e^{-1}\hat{\mathbf{G}}_d\mathbf{D}_d \quad (6.7)$$

The model in terms of scaled variables is:

$$\mathbf{y} = \mathbf{G}\mathbf{u} + \mathbf{G}_d\mathbf{d} \quad \mathbf{e} = \mathbf{y} - \mathbf{r} \quad (6.8)$$

The following scaling matrices were used to scale the FE and identified models:

$$\mathbf{D}_d = 0.3 \quad \mathbf{D}_u = \mathbf{I}_{[4 \times 4]} \cdot 0.5 \quad \mathbf{D}_e = \begin{bmatrix} \mathbf{D}_{e\epsilon} & \mathbf{0} & \mathbf{0} \\ \mathbf{0} & D_{ea} & 0 \\ \mathbf{0} & 0 & D_{eF} \end{bmatrix} \quad (6.9)$$

with

$$\mathbf{D}_{\text{e}\varepsilon} = K_{\varepsilon\text{y}^1} \cdot 7.6 \cdot \mathbf{I}_{[4 \times 4]} \quad D_{\text{ea}} = 27.2 \text{ m/s}^2 \quad D_{\text{eF}} = 6.5 \text{ N} \quad (6.10)$$

All numerical values in (6.9) and (6.10) were chosen according to the largest measured or applied absolute values occurred during the identification procedure.

6.3 Final Models

The input-output scaled final models for controller design and simulation are listed in Table 6.1 (hinged-hinged beam with unmounted shaker) respectively Table 6.2 (hinged-hinged beam with mounted shaker).

The notation “ID” is used to indicate a (discrete-time) model ($T_s = 0.01 \text{ s}$) which originates from an identification procedure (see Chapter 4), whereas “FE” is used to indicate a (continuous-time) model which originates from the finite element method (FEM) (see Chapter 5). “b” is used to denote a model of the beam with unmounted shaker, while “bs” is used to denote a model of the beam with mounted shaker. An additional “(ho)” is used to denote a model of “high order”.

model name	available models	model order	model origin (description)
IDb(ho)	$\mathbf{G}^{\text{IDb(ho)}}$	16	identified system of the beam with unmounted shaker \mathbf{H}_{10+6} (see Section 4.3)
IDb	\mathbf{G}^{IDb}	10	identified system of the beam with unmounted shaker $\mathbf{H}_{10+6}^{\text{r}\{10+0\}}$ (see Section 4.3)
FEb(ho)	$\mathbf{G}^{\text{FEb(ho)}}, \mathbf{G}_{\text{d}}^{\text{FEb(ho)}}$	400	FEmodel of the beam with unmounted shaker (100 elements, 200 modes)
FEb	$\mathbf{G}^{\text{FEb}}, \mathbf{G}_{\text{d}}^{\text{FEb}}$	10	“modally truncated” (modes with natural frequencies below 50 Hz) “FEb(ho)-model”

Table 6.1: Model origin of input-output scaled final models of the hinged-hinged beam with unmounted shaker

model name	available models	model order	model origin (description)
IDbs(ho)	$\mathbf{G}^{\text{IDbs(ho)}}, \mathbf{G}_{\text{d}}^{\text{IDbs(ho)}}$	21	identified system of the beam with mounted shaker \mathbf{H}_{14+7} (see Section 4.4)
IDbs	$\mathbf{G}^{\text{IDbs}}, \mathbf{G}_{\text{d}}^{\text{IDbs}}$	10	identified system of the beam with mounted shaker $\mathbf{H}_{10+8}^{\text{r}\{10+0\}}$ (see Section 4.4)
FEbs(ho)	$\mathbf{G}^{\text{FEbs(ho)}}, \mathbf{G}_{\text{d}}^{\text{FEbs(ho)}}$	400	FEmodel of the beam with mounted shaker (100 elements, 200 modes)
FEbs	$\mathbf{G}^{\text{FEbs}}, \mathbf{G}_{\text{d}}^{\text{FEbs}}$	10	“modally truncated” (modes with natural frequencies below 50 Hz) “FEbs(ho)-model”

Table 6.2: Model origin of input-output scaled final models of the hinged-hinged beam with mounted shaker

In Chapter 9 feedback controllers will be designed on the basis of the “IDbs-model” as well as on the “FEbs-model”.

Remark: Because in Section 5.6 the stiffness of the nylon stinger k_1 was chosen as infinite ($k_1 \rightarrow \infty$) the FE model of the (hinged-hinged) beam with unmounted shaker (“FEb(ho)-model”) and the FE model of the (hinged-hinged) beam with mounted shaker (“FEbs(ho)-model”) have the same number of modes (100 elements \Rightarrow 200 modes).

6.4 Comparing the Identified and FE Models for the Beam without Shaker

Figure 6.1 compares the input-output scaled continuous-time FE and discrete-time ($T_s = 0.01$ s) ID (“high order”) models of the beam with unmounted shaker in a Bode magnitude plot. The inputs u_1 to u_4 are associated with the piezo patch actuators and the outputs y_1 to y_4 are associated with the piezo patch sensors.

In the lower frequency range, the magnitude of the ID model is lower than the magnitude of the FE model because the actual transfer function of a piezo patch sensor has globally derivative behavior, which is not contained in the FE model. Nevertheless, the Bode magnitude plot of the FE and ID models of the beam with unmounted shaker indicate a good match in the depicted frequency range of interest, i.e. below 50 Hz. Note that, compared to the other modes, the first mode shows a higher relative mismatch, whereas, as evident in Table 6.3, its absolute frequency deviation is of similar size.

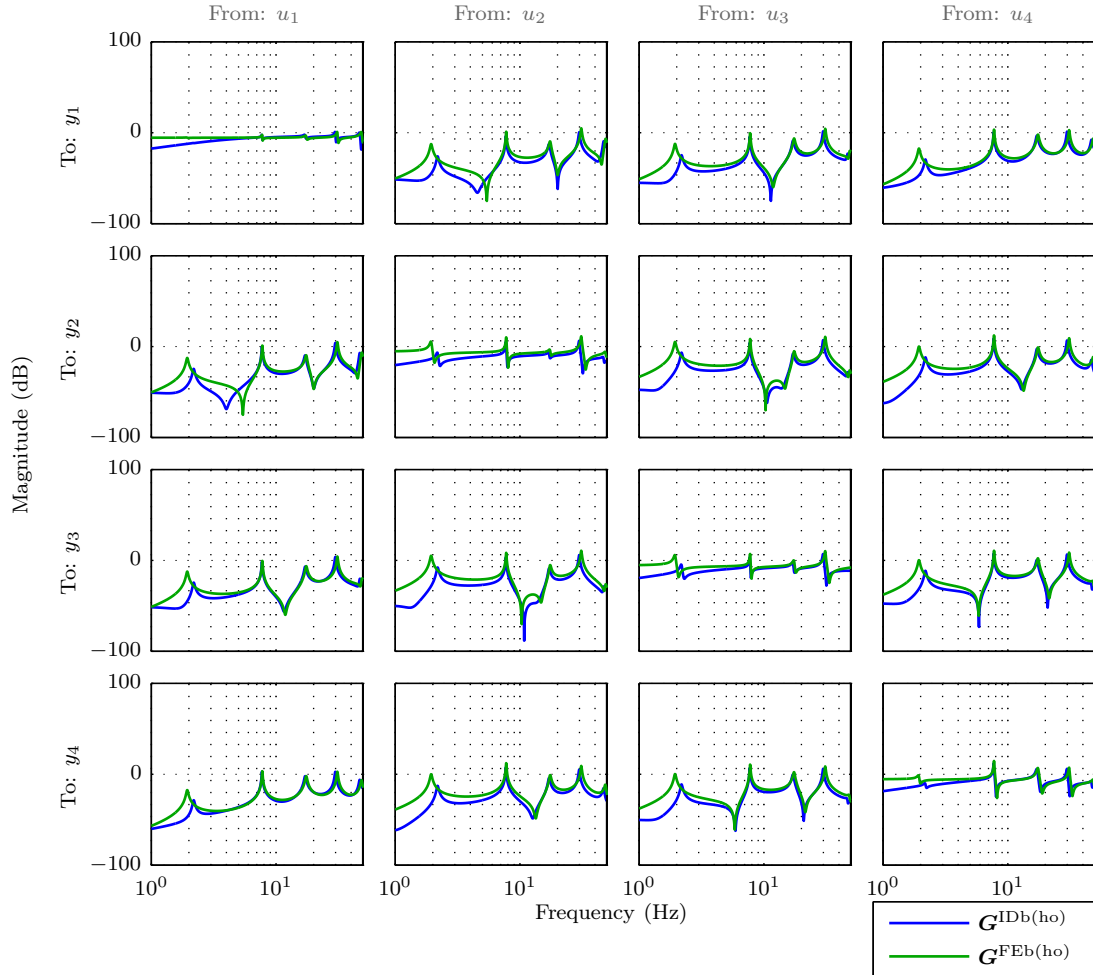


Figure 6.1: Comparing FE and ID (“high order”) models of the beam with unmounted shaker in a Bode magnitude plot

The natural frequencies and modal damping coefficients of the two different kinds of tenth-order models (“FEb-model”, “IDb-model”) are compared in Table 6.3. Because the FE

model of the beam with unmounted shaker uses for its first five modal damping coefficients ζ_i^{FEb} (for $i = 1, \dots, 5$) the values ζ_i^{IDb} of the identified beam with unmounted shaker model (see Section 5.1.8), in Table 6.3 $\Delta\zeta_i^{\text{b}} = 0$ (for $i = 1, \dots, 5$).

mode	f_i^{FEb} (in Hz)	f_i^{IDb} (in Hz)	Δf_i^{b} $= f_i^{\text{FEb}} - f_i^{\text{IDb}}$ (in Hz)	ζ_i^{FEb} (in %)	ζ_i^{IDb} (in %)	$\Delta\zeta_i^{\text{b}}$ $= \zeta_i^{\text{FEb}} - \zeta_i^{\text{IDb}}$ (in %)
1	1.9391	2.1846	-0.2455	1.6749	1.6749	0
2	7.7563	7.7104	0.0459	0.5142	0.5142	0
3	17.4517	17.1042	0.3474	1.5735	1.5735	0
4	31.0252	29.8556	1.1696	0.9300	0.9300	0
5	48.4768	46.8771	1.5997	1.4229	1.4229	0

Table 6.3: Comparing natural frequencies and modal damping coefficients between FE and identified models of the beam with unmounted shakers (“FEb-model”, “IDb-model”)

6.5 Comparing the Identified and FE Models for the Beam with Mounted Shaker

Figure 6.2 compares the input-output scaled continuous-time FE and discrete-time ($T_s = 0.01$ s) ID (“high order”) models of the beam with mounted shaker in a Bode magnitude plot. As before, the inputs u_1 to u_4 are associated with the piezo patch actuators and the outputs y_1 to y_4 are associated with the piezo patch sensors. The outputs y_5 and y_6 are associated with the acceleration, and force, respectively (acceleration and force sensor at the shaker position).

Again, as expected, the effect of the globally derivative behavior of the piezo patch sensors is visible in the identified model.

An other difference between the Bode magnitude plot of the FE and ID models, especially in the lower frequency range, is evident in the acceleration signal (output y_5): The globally derivative behavior ($\lim_{s \rightarrow 0} a_{\text{sp}}(s) = 0$) of all transfer-function matrix elements associated with this output (y_5) is not correctly modelled by the identified model. In general, because of the relatively bad results achieved in the cross-validation (see Section 4.4, Table 4.3) the acceleration output of the identified model should be treated with caution.

It should be pointed out that in order to obtain a good matching FE model of the beam with mounted shaker as shown in Section 5.6 (see Figure 5.17), it was necessary to use high resolution in spatial discretization (100 elements 200 modes) for the beam with unmounted shaker in the first place. A reduction by “modal truncation” (should be and) was carried out not until then (“FEbs-model”).

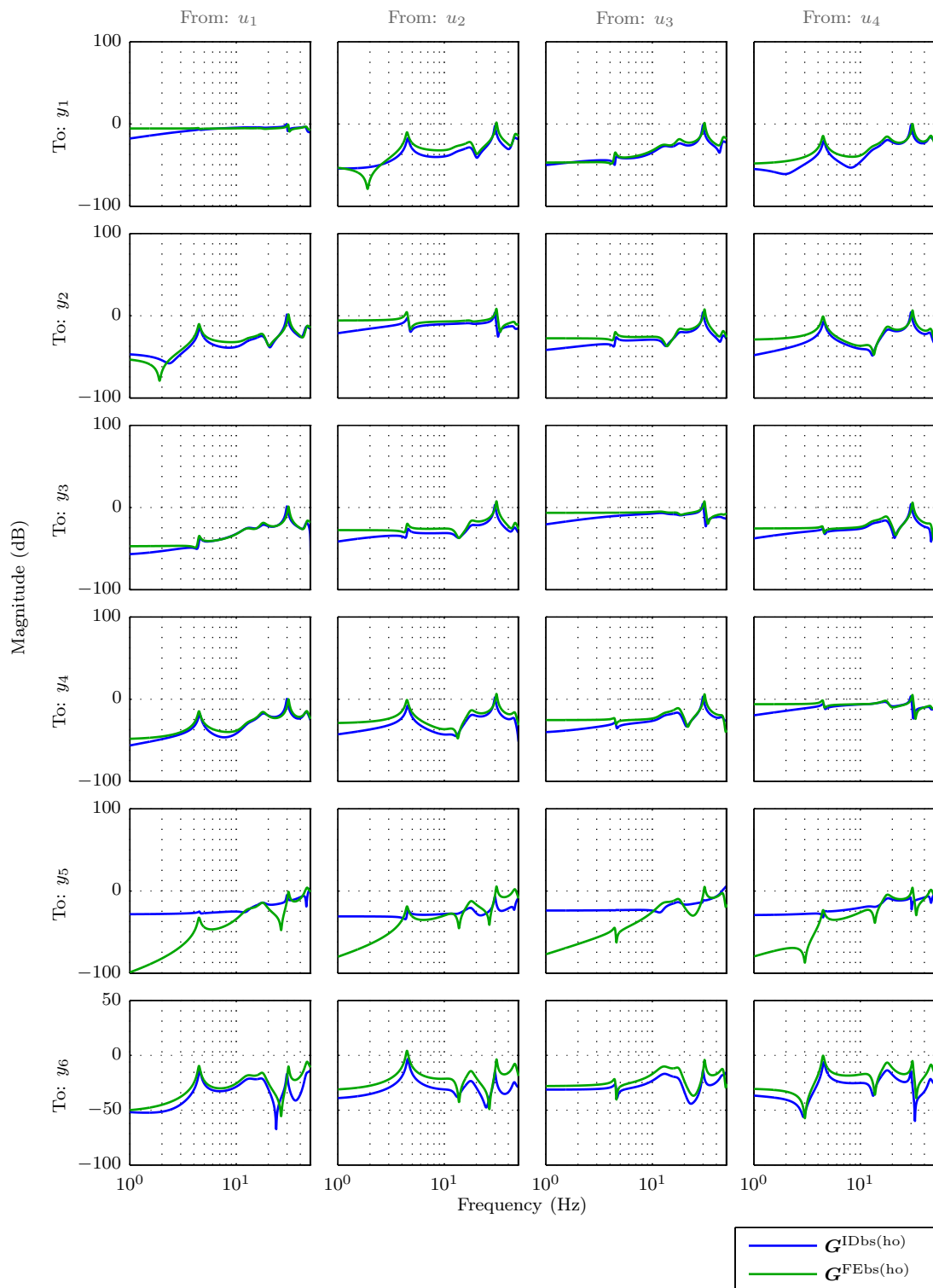


Figure 6.2: Comparing FE and ID (“high order”) models of the beam with mounted shaker in a Bode magnitude plot

Figure 6.3 compares the input-output scaled continuous-time FE and discrete-time ($T_s = 0.01$ s) ID (“high order”) disturbance models of the beam with mounted shaker in a Bode magnitude plot. The disturbance input d is associated with the excitation signal of the shaker which introduces a force in direction of oscillation.

Note that the Bode magnitude plot associated with the force output (y_6) show particularly the low-frequency modes of the beam with mounted shaker.

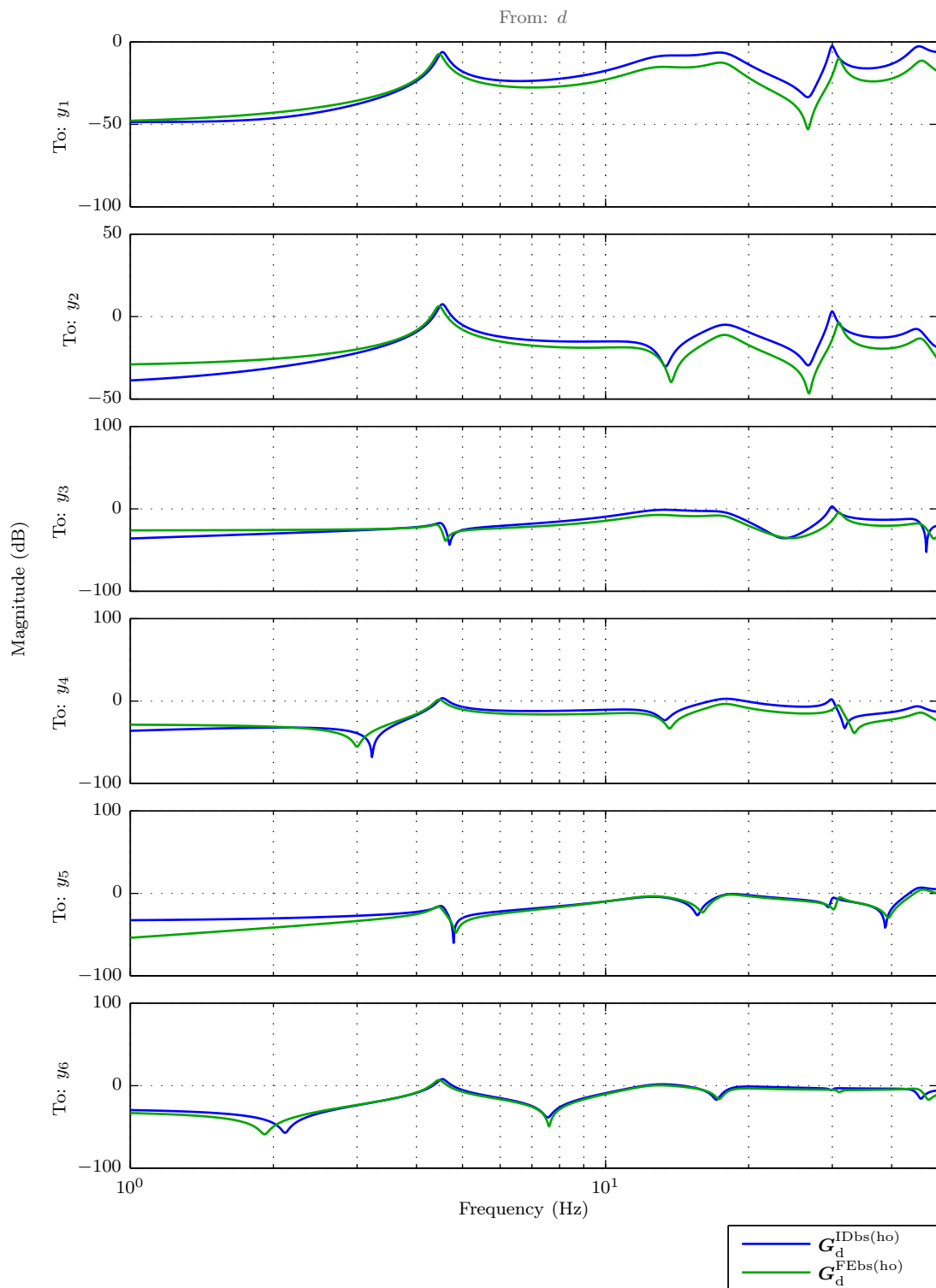


Figure 6.3: Comparing FE and ID (“high order”) disturbance models of the beam with mounted shaker in a Bode magnitude plot

Figure 6.4 shows a good match for the phase plot of output y_6 , validating that in the FE model the signs for the shaker mounting have been set correctly.

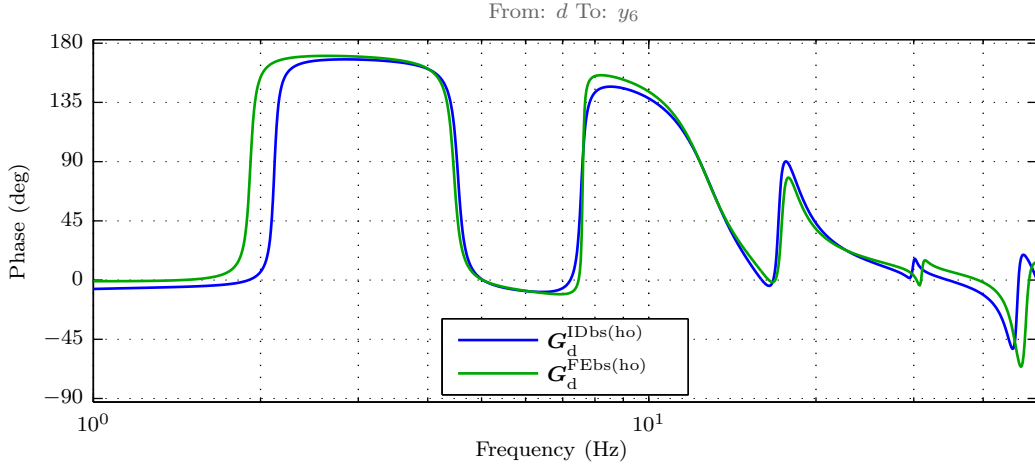


Figure 6.4: Comparing FE and ID (“high order”) disturbance models of the beam with mounted shaker in a phase plot for output y_6 (associated with the force sensor)

The natural frequencies and modal damping coefficients of the two different kinds of tenth-order models (“FEbs-model”, “IDbs-model”) are compared in Table 6.4.

The fact that for the FE model with mounted shaker the natural frequency of the lowest-damped, fourth mode (sharp peek) shows a large deviation Δf_4^{bs} (when comparing it to the identified model), leads to difficulties when designing controllers (based on the FE model) to improve the damping of the fourth mode in the experiment, see Section 9.3.

mode	f_i^{FEbs} (in Hz)	f_i^{IDbs} (in Hz)	Δf_i^{bs} $= f_i^{\text{FEbs}} - f_i^{\text{IDbs}}$ (in Hz)	ζ_i^{FEbs} (in %)	ζ_i^{IDbs} (in %)	$\Delta \zeta_i^{\text{bs}}$ $= \zeta_i^{\text{FEbs}} - \zeta_i^{\text{IDbs}}$ (in %)
1	4.4601	4.5332	-0.0731	2.1346	2.1192	0.0153
2	12.6525	12.8924	-0.2400	14.0135	14.4887	-0.4752
3	17.7772	17.8445	-0.0673	7.1113	8.9303	-1.8190
4	30.9467	29.9515	0.9952	1.2924	1.2332	0.0592
5	46.2427	45.4605	0.7822	3.8049	4.3655	-0.5606

Table 6.4: Comparing natural frequencies and modal damping coefficients between FE and identified models of the beam with mounted shakers (“FEbs-model”, “IDbs-model”)

Figure 6.5 compares the input-output scaled tenth-order models (\mathbf{G}^{IDbs} , \mathbf{G}^{FEbs}) in a singular values plot.

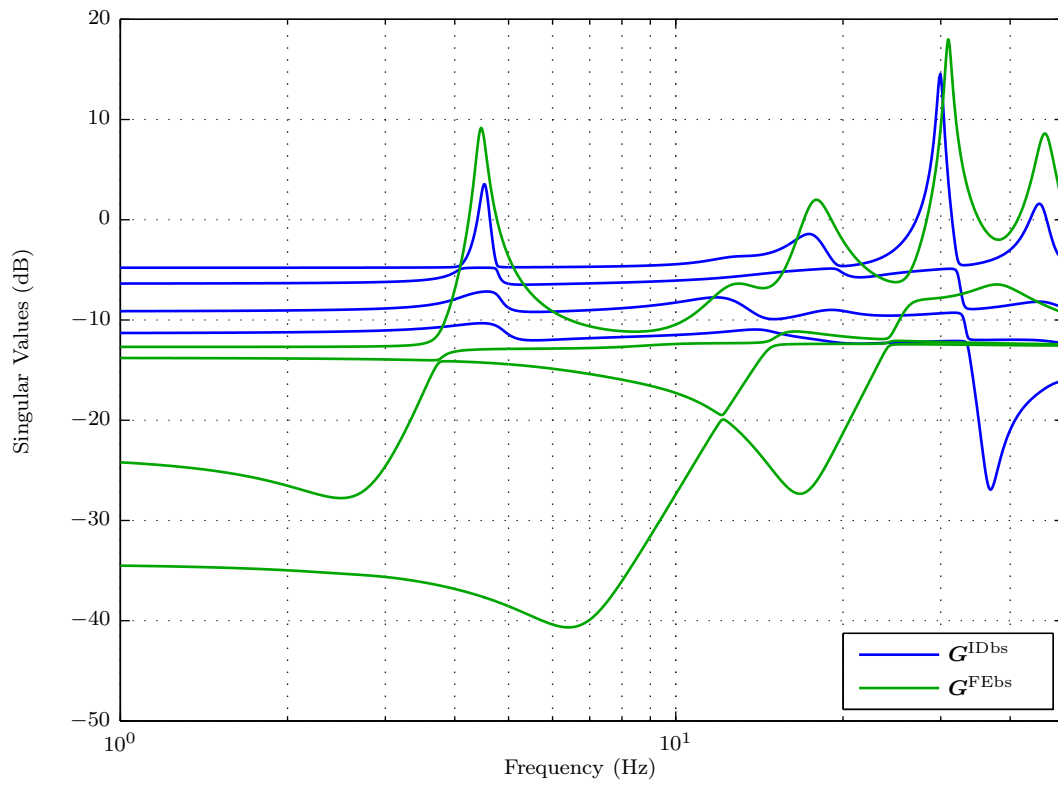


Figure 6.5: Comparing FE and ID models of the beam with mounted shaker in a singular values plot (inputs u_1 to u_4 ; outputs y_1 to y_4)

Chapter 7

Modally Weighted LQG Design

7.1 The LQG Problem

Linear Quadratic Gaussian (LQG) control assumes the plant dynamics linear and known with stochastic noise excitation of known statistical properties

$$\dot{\mathbf{x}} = \mathbf{A}\mathbf{x} + \mathbf{B}\mathbf{u} + \mathbf{w} \quad (7.1)$$

$$\mathbf{y} = \mathbf{C}\mathbf{x} + \mathbf{D}\mathbf{u} + \mathbf{v} \quad (7.2)$$

where the process noise signal \mathbf{w} and measurement noise signal \mathbf{v} are usually assumed to be uncorrelated¹ zero-mean Gaussian stochastic processes (i.e. \mathbf{w} and \mathbf{v} are white noise processes) with constant power spectral density matrices \mathbf{W} and \mathbf{V} respectively. [6, 7]

$$\mathbb{E} \{ \mathbf{w}(t) \mathbf{w}(\tau)^T \} = \mathbf{W} \delta(t - \tau) \quad (7.3)$$

$$\mathbb{E} \{ \mathbf{v}(t) \mathbf{v}(\tau)^T \} = \mathbf{V} \delta(t - \tau) \quad (7.4)$$

Given the noisy system in (7.1) - (7.2) the LQG control problem is to find the optimal control $\mathbf{u}(t)$ which minimizes

$$J = \mathbb{E} \left\{ \lim_{T \rightarrow \infty} \frac{1}{T} \int_0^T [\mathbf{x}(t)^T \mathbf{Q} \mathbf{x}(t) + \mathbf{u}(t)^T \mathbf{R} \mathbf{u}(t)] dt \right\}, \quad (7.5)$$

where \mathbf{Q} and \mathbf{R} are appropriately chosen constant real weighting matrices for the states $\mathbf{x}(t)$ respectively the input $\mathbf{u}(t)$ such that $\mathbf{Q} = \mathbf{Q}^T \geq 0$ (\mathbf{Q} symmetric and positive semi-definite) and $\mathbf{R} = \mathbf{R}^T > 0$ (\mathbf{R} symmetric and positive definite).

Because of the so-called separation theorem, the optimal solution of the LQG problem (7.5) can be decomposed into finding the optimal constant state vector feedback gain \mathbf{K}_{LQR} via the associated deterministic Linear Quadratic Regulator (LQR) problem and computing a dynamic Kalman state estimator (observer) $\mathbf{K}_{\text{est}}(s)$, which has the same system order n as the plant. [7] Instead of the usually non-(fully)-measurable state vector \mathbf{x} , the estimated state vector $\hat{\mathbf{x}}$ of the Kalman observer is fed to the state feedback controller \mathbf{K}_{LQR} (Figure 7.1).

¹ $\mathbb{E} \{ \mathbf{w}(t) \mathbf{v}(\tau)^T \} = \mathbf{0}$; $\mathbb{E} \{ \mathbf{v}(t) \mathbf{w}(\tau)^T \} = \mathbf{0}$

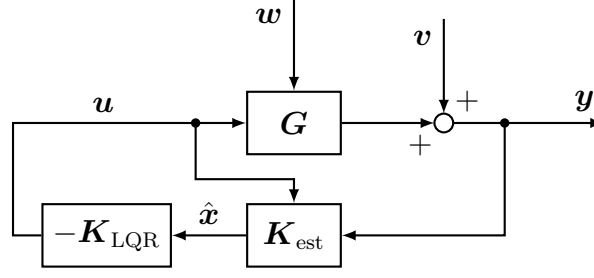


Figure 7.1: LQG architecture

7.2 The LQR Problem

The Linear Quadratic Regulator (LQR) problem is to find the optimal control $\mathbf{u}(t)$ which minimizes the deterministic cost function (in $\mathbf{x}(t)$ and $\mathbf{u}(t)$)

$$J_{\text{LQR}} = \int_0^\infty [\mathbf{x}(t)^\top \mathbf{Q} \mathbf{x}(t) + \mathbf{u}(t)^\top \mathbf{R} \mathbf{u}(t)] dt, \quad (7.6)$$

where \mathbf{Q} and \mathbf{R} are appropriately chosen constant real weighting matrices for the states $\mathbf{x}(t)$ respectively the input $\mathbf{u}(t)$ such that $\mathbf{Q} = \mathbf{Q}^\top \geq 0$ (\mathbf{Q} symmetric and positive semi-definite) and $\mathbf{R} = \mathbf{R}^\top > 0$ (\mathbf{R} symmetric and positive definite).

The optimal solution for any initial state $\mathbf{x}_0 = \mathbf{x}(0)$ is

$$\mathbf{u}(t) = -\mathbf{K}_{\text{LQR}} \mathbf{x}(t) \quad (7.7)$$

$$\mathbf{K}_{\text{LQR}} = \mathbf{R}^{-1} \mathbf{B}^\top \mathbf{X} \quad (7.8)$$

where $\mathbf{X} = \mathbf{X}^\top \geq 0$ is the unique symmetric and positive semi-definite solution of the controller algebraic Riccati equation (CARE).

$$\mathbf{A}^\top \mathbf{X} + \mathbf{X} \mathbf{A} - \mathbf{X} \mathbf{B} \mathbf{R}^{-1} \mathbf{B}^\top \mathbf{X} + \mathbf{Q} = \mathbf{0} \quad (7.9)$$

The closed-loop system with the state feedback controller \mathbf{K}_{LQR} is guaranteed to be asymptotically stable if the matrix pair (\mathbf{A}, \mathbf{B}) is stabilizable and (\mathbf{A}, \mathbf{Q}) is detectable.

7.3 Kalman Filter

The Kalman filter (Figure 7.2) has the structure of a Luenberger state estimator (or observer) with the dynamics

$$\dot{\hat{\mathbf{x}}} = \mathbf{A} \hat{\mathbf{x}} + \mathbf{B} \mathbf{u} + \mathbf{H}(\mathbf{y} - \mathbf{C} \hat{\mathbf{x}} - \mathbf{D} \mathbf{u}) \quad (7.10)$$

The optimal filter gain \mathbf{H} , which minimizes the steady-state error covariance (see [14])

$$\mathbf{Y} = \lim_{t \rightarrow \infty} \mathbb{E} \{ [\mathbf{x} - \hat{\mathbf{x}}][\mathbf{x} - \hat{\mathbf{x}}]^\top \}$$

is given by

$$\mathbf{H} = \mathbf{Y} \mathbf{C}^\top \mathbf{V}^{-1} \quad (7.11)$$

where the matrix $\mathbf{Y} = \mathbf{Y}^T \geq 0$ is computed as the unique symmetric and positive semi-definite solution of the associated filter algebraic Riccati equation (FARE):

$$\mathbf{Y}\mathbf{A}^T + \mathbf{A}\mathbf{Y} - \mathbf{Y}\mathbf{C}^T\mathbf{V}^{-1}\mathbf{C}\mathbf{Y} + \mathbf{W} = 0 \quad (7.12)$$

The solutions to the CARE (7.9) and FARE (7.12), and thus the optimal gain matrices \mathbf{K}_{LQR} respectively \mathbf{H} exist, and the LQG-controlled system is internally stable, provided the systems with state-space realizations $(\mathbf{A}, \mathbf{B}, \mathbf{Q}^{\frac{1}{2}})$ and $(\mathbf{A}, \mathbf{W}^{\frac{1}{2}}, \mathbf{C})$ are stabilizable and detectable. Thereby $\mathbf{Q}^{\frac{1}{2}}$ ($\mathbf{W}^{\frac{1}{2}}$) denotes the matrix square root of the positive semi-definite matrix \mathbf{Q} (\mathbf{W}).

The overall LQG controller ($\mathbf{u}(s) = \mathbf{K}_{\text{LQG}}(s)\mathbf{y}(s)$), which is of the same system order as the plant is given by

$$\mathbf{K}_{\text{LQG}}(s) \stackrel{\text{ss}}{=} \left[\frac{\mathbf{A} - \mathbf{B}\mathbf{K}_{\text{LQR}} - \mathbf{H}\mathbf{C} + \mathbf{H}\mathbf{D}\mathbf{K}_{\text{LQR}}}{-\mathbf{K}_{\text{LQR}}} \middle| \frac{\mathbf{H}}{0} \right] \quad (7.13)$$

Note that positive feedback is used to connect the controller $\mathbf{K}_{\text{LQG}}(s)$ to the plant output \mathbf{y} .

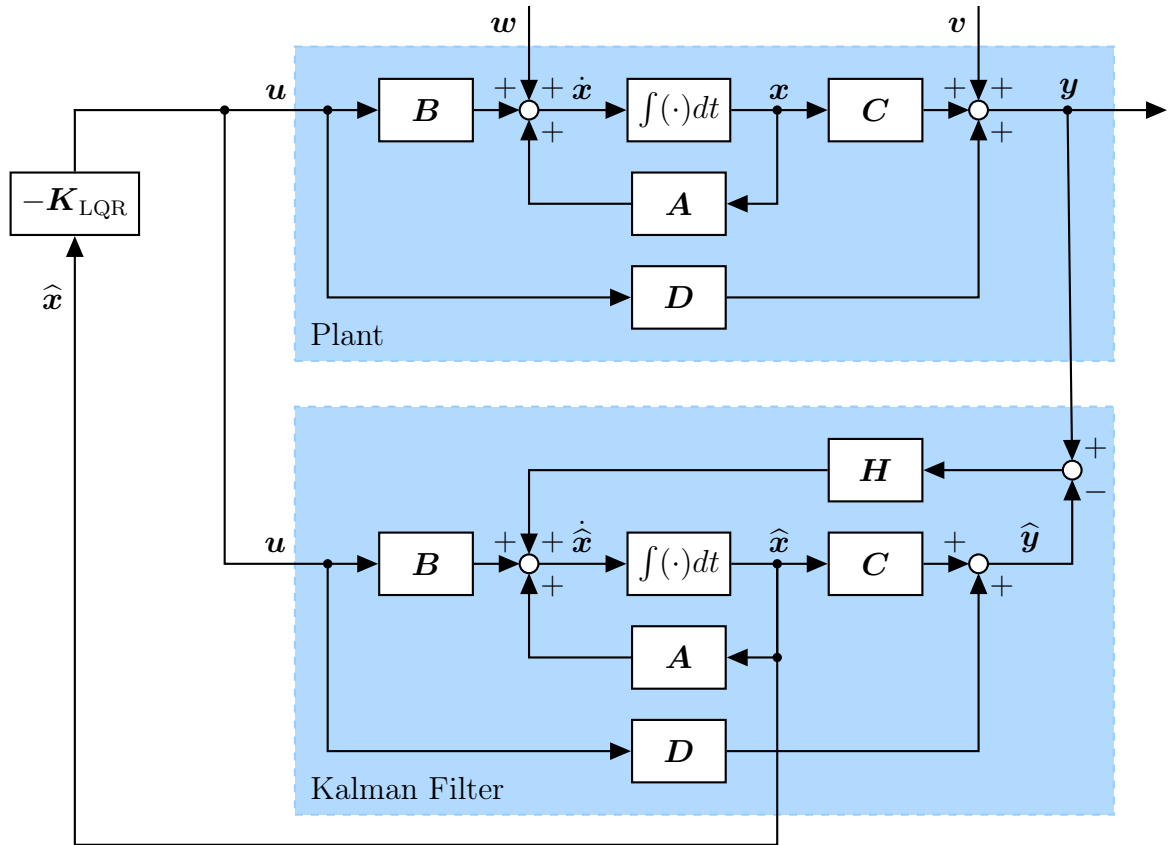


Figure 7.2: LQG controller and noisy plant

7.4 Modal Weighting Matrix \mathbf{Q}_m

Modal weighting is appropriate for cases in which certain undesirable eigenmodes of the plant

$$\mathbf{G}(s) \stackrel{\text{ss}}{=} \left[\begin{array}{c|c} \mathbf{A} & \mathbf{B} \\ \hline \mathbf{C} & \mathbf{D} \end{array} \right] \quad (7.14)$$

shall be weighted. This is of special interest for active damping of flexible structures (such as the beam investigated in this thesis), where each mode is excited almost independently and the total structural response is the sum of modal responses (see, Equation 5.56 on page 40). [5] For flexible structures it might be desirable to avoid critical resonances or because of some performance criteria guarantee high damping within a certain frequency range of interest. [13]

For each eigenvector \mathbf{s}_k of the state matrix \mathbf{A} it is required that the auxiliary weighting matrix $\hat{\mathbf{Q}}$ fulfills

$$\hat{\mathbf{Q}}\mathbf{s}_k = \mathbf{s}_k m_k \quad \text{for } k = 1, \dots, n, \quad (7.15)$$

where $m_k \geq 0$ is a scalar weighting factor and n is the number of states of the plant. Collecting all scalar weighting factors m_k in the diagonal matrix \mathbf{M} and all eigenvectors \mathbf{s}_k in the matrix \mathbf{S} leads to:

$$\hat{\mathbf{Q}}\mathbf{S} = \mathbf{S}\mathbf{M}, \quad (7.16)$$

so the auxiliary matrix $\hat{\mathbf{Q}}$ reads

$$\hat{\mathbf{Q}} = \mathbf{S}\mathbf{M}\mathbf{S}^{-1}. \quad (7.17)$$

Finally, the symmetric state weighting matrix \mathbf{Q}_m for modal weighting is obtained as:

$$\mathbf{Q}_m = \hat{\mathbf{Q}}^T \hat{\mathbf{Q}}$$

Equation (7.18) reveals that the k th eigenmode \mathbf{s}_k is weighted by the value of m_k^2 if \mathbf{Q}_m is used as weighting \mathbf{Q} in the deterministic cost function (7.6).

$$\mathbf{s}_k^T \mathbf{Q}_m \mathbf{s}_k = \mathbf{s}_k^T \hat{\mathbf{Q}}^T \hat{\mathbf{Q}} \mathbf{s}_k = m_k \mathbf{s}_k^T \mathbf{s}_k m_k = m_k^2 \quad \text{with } \|\mathbf{s}_k\|_2 = 1 \quad (7.18)$$

Because of (7.18) it is ensured that the matrix pair $(\mathbf{A}, \mathbf{Q}_m)$ is detectable, if for all eigenvalues of the state matrix \mathbf{A} with $\Re\{\lambda_k(\mathbf{A})\} > 0$ for the scalar weighting factor $m_k > 0$ holds.

Chapter 8

Optimal & Robust \mathcal{H}_∞ Control Design Methods

This chapter is mainly based on [6, 7].

8.1 General Control Problem Formulation for \mathcal{H}_∞ Optimization

Many linear control problems¹ can be formulated as shown in the block diagram in Figure 8.1. [6] Then, the overall control objective is to find an internally stabilizing (see Definition 8.2 on page 99) controller \mathbf{K} which based on the information in \mathbf{v} , generates a control signal \mathbf{u} that counteracts the influence of \mathbf{w} on \mathbf{z} , thereby minimizing some system norm (here, the \mathcal{H}_∞ norm) of the closed-loop transfer function from \mathbf{w} to \mathbf{z} . [6]

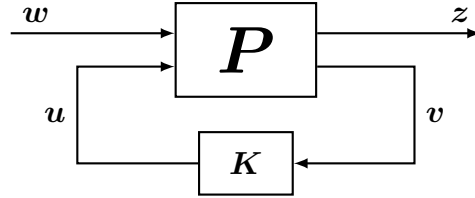


Figure 8.1: General control configuration (for controller synthesis)

The generalized plant \mathbf{P} and controller \mathbf{K} of Figure 8.1 are described by

$$\begin{bmatrix} \mathbf{z} \\ \mathbf{v} \end{bmatrix} = \underbrace{\begin{bmatrix} \mathbf{P}_{11}(s) & \mathbf{P}_{12}(s) \\ \mathbf{P}_{21}(s) & \mathbf{P}_{22}(s) \end{bmatrix}}_{\mathbf{P}(s)} \begin{bmatrix} \mathbf{w} \\ \mathbf{u} \end{bmatrix} \quad (8.1)$$

$$\mathbf{u} = \mathbf{K}(s)\mathbf{v}, \quad (8.2)$$

where a state-space realization of \mathbf{P} is given by

$$\mathbf{P}(s) \stackrel{\text{ss}}{=} \left[\begin{array}{c|cc} \mathbf{A} & \mathbf{B}_1 & \mathbf{B}_2 \\ \hline \mathbf{C}_1 & \mathbf{D}_{11} & \mathbf{D}_{12} \\ \mathbf{C}_2 & \mathbf{D}_{21} & \mathbf{D}_{22} \end{array} \right]. \quad (8.3)$$

¹If control design with respect to model uncertainty is an issue, an additional perturbation block $\mathbf{\Delta}$ is added to the block diagram. More on that in Section 8.6.3 (see Figure 8.9 on page 96)

The signals are generally multivariate (i.e., vectors): \mathbf{u} are the control variables, \mathbf{v} are the measured variables, \mathbf{w} are the exogenous signals such as disturbances \mathbf{d} and reference commands \mathbf{r} , and \mathbf{z} are the exogenous outputs which are to be minimized. The latter signal, $\mathbf{z} = [\mathbf{z}_1^T \quad \mathbf{z}_2^T \quad \dots]^T$, is usually a vector of frequency-weighted signals (e.g. $\mathbf{z}_1(s) = \mathbf{W}_1(s)\mathbf{y}(s)$ or $\mathbf{z}_1(s) = \mathbf{W}_1(s)\mathbf{e}(s)$ and $\mathbf{z}_2(s) = \mathbf{W}_2(s)\mathbf{u}(s)$).

The closed-loop transfer function from \mathbf{w} on \mathbf{z} is obtained by a lower linear fractional transformation (LFT)

$$\mathbf{z} = \mathcal{F}_l(\mathbf{P}, \mathbf{K})\mathbf{w} \quad (8.4)$$

where

$$\mathcal{F}_l(\mathbf{P}, \mathbf{K}) = \mathbf{P}_{11} + \mathbf{P}_{12}\mathbf{K}(\mathbf{I} - \mathbf{P}_{22}\mathbf{K})^{-1}\mathbf{P}_{21}. \quad (8.5)$$

8.2 Prerequisites for Standard \mathcal{H}_∞ Design

The central prerequisites to apply the standard methods for \mathcal{H}_∞ (sub-)optimal control design are outlined in the following (based on [7, 6]).

Definition 8.1: Assumptions for \mathcal{H}_2 and \mathcal{H}_∞ standard design problems [7]

The following set of assumptions is posed on the standard feedback design problem statement for \mathcal{H}_2 and \mathcal{H}_∞ optimization, see [6]. Of these, A1-A4 are required and A5-A8 can (partially) be relaxed (in exchange for more complex solutions which are available in specialized literature but which are omitted here).

Assumption	Comment
A1.: $(\mathbf{A}, \mathbf{B}_2, \mathbf{C}_2)$ is stabilizable and detectable	required for the existence of a stabilizing \mathbf{K}
A2.: \mathbf{D}_{12} and \mathbf{D}_{21} have full rank	sufficient to ensure that \mathbf{K} is proper (i.e. realizable)
A3.: $\begin{bmatrix} \mathbf{A} - j\omega\mathbf{I} & \mathbf{B}_2 \\ \mathbf{C}_1 & \mathbf{D}_{12} \end{bmatrix}$ has full column rank for all ω	A.3 and A.4 ensure that \mathbf{K} does not try to cancel poles or zeros on the imaginary axis which would result in closed-loop instability
A4.: $\begin{bmatrix} \mathbf{A} - j\omega\mathbf{I} & \mathbf{B}_1 \\ \mathbf{C}_2 & \mathbf{D}_{21} \end{bmatrix}$ has full row rank for all ω	
A5.: $\mathbf{D}_{11} = \mathbf{0}$ and $\mathbf{D}_{22} = \mathbf{0}$	necessary for \mathcal{H}_2 case (strictly proper plants), simplifying the solution in the \mathcal{H}_∞ case (if not fulfilled, an equivalent problem in which A5 holds can be stated, see [6])
A6.: $\mathbf{D}_{12} = \begin{bmatrix} \mathbf{0} \\ \mathbf{I} \end{bmatrix}$ and $\mathbf{D}_{21} = \begin{bmatrix} \mathbf{0} & \mathbf{I} \end{bmatrix}$	simplifies the solution, by scaling \mathbf{u} and \mathbf{v} and by a unitary transformation of \mathbf{w} and \mathbf{z} , this can always be obtained
A7.: $\mathbf{D}_{12}^T \mathbf{C}_1 = \mathbf{0}$ and $\mathbf{B}_1 \mathbf{D}_{21}^T = \mathbf{0}$	common for LQG control which can be cast as \mathcal{H}_2 optimization problem (see [6])
A8.: $(\mathbf{A}, \mathbf{B}_1)$ is stabilizable and $(\mathbf{A}, \mathbf{C}_1)$ is detectable	If A7 is true, A8 replaces A3 and A4.

8.3 \mathcal{H}_∞ (Sub-)Optimal Control

In the following the standard solution for the \mathcal{H}_∞ suboptimal controller design problem is presented. The solution includes the central controller and the parametrization of all stabilizing suboptimal controllers (adopted from [7]).

Given a generalized plant $\mathbf{P}(s)$ as in (8.3) which satisfies the assumptions A1-A8 in Definition 8.1, all stabilizing controllers $\mathbf{K}(s)$ that satisfy

$$\|\mathcal{F}_1(\mathbf{P}, \mathbf{K})\|_\infty < \gamma \quad (8.6)$$

for a suboptimal bound $\gamma > \gamma_{\min}$ are obtained as follows:

1. Let $\mathbf{X}_\infty = \mathbf{X}_\infty^T \geq 0$ be a symmetric, positive semi-definite solution of the algebraic Riccati equation (ARE)

$$\mathbf{A}^T \mathbf{X}_\infty + \mathbf{X}_\infty \mathbf{A} + \mathbf{C}_1^T \mathbf{C}_1 + \mathbf{X}_\infty (\gamma^{-2} \mathbf{B}_1 \mathbf{B}_1^T - \mathbf{B}_2 \mathbf{B}_2^T) \mathbf{X}_\infty = \mathbf{0} \quad (8.7)$$

such that $\Re \{ \lambda_i [\mathbf{A} + (\gamma^{-2} \mathbf{B}_1 \mathbf{B}_1^T - \mathbf{B}_2 \mathbf{B}_2^T) \mathbf{X}_\infty] \} < 0 \ \forall i$ (called “stabilizing solution” of (8.7));

2. let $\mathbf{Y}_\infty = \mathbf{Y}_\infty^T \geq 0$ be a symmetric, positive semi-definite solution of the ARE

$$\mathbf{A} \mathbf{Y}_\infty + \mathbf{Y}_\infty \mathbf{A}^T + \mathbf{B}_1 \mathbf{B}_1^T + \mathbf{Y}_\infty (\gamma^{-2} \mathbf{C}_1^T \mathbf{C}_1 - \mathbf{C}_2^T \mathbf{C}_2) \mathbf{Y}_\infty = \mathbf{0} \quad (8.8)$$

such that $\Re \{ \lambda_i [\mathbf{A} + \mathbf{Y}_\infty (\gamma^{-2} \mathbf{C}_1^T \mathbf{C}_1 - \mathbf{C}_2^T \mathbf{C}_2)] \} < 0 \ \forall i$ (called “stabilizing solution” of (8.8)); and

3. let $\rho(\mathbf{X}_\infty \mathbf{Y}_\infty) < \gamma^2$ be fulfilled.

Then, all controllers $\mathbf{K}(s)$ are given by $\mathbf{K} = \mathcal{F}_1(\mathbf{K}_{\text{cent}}, \mathbf{Q})$ where the “central controller” \mathbf{K}_{cent} is of the same order as \mathbf{P} and is given by

$$\mathbf{K}_{\text{cent}}(s) \stackrel{\text{ss}}{=} \left[\begin{array}{c|cc} \mathbf{A}_\infty & -\mathbf{Z}_\infty \mathbf{L}_\infty & \mathbf{Z}_\infty \mathbf{B}_2 \\ \hline \mathbf{F}_\infty & \mathbf{0} & \mathbf{I} \\ -\mathbf{C}_2 & \mathbf{I} & \mathbf{0} \end{array} \right] \quad (8.9)$$

$$\mathbf{A}_\infty = \mathbf{A} + \gamma^{-2} \mathbf{B}_1 \mathbf{B}_1^T \mathbf{X}_\infty + \mathbf{B}_2 \mathbf{F}_\infty + \mathbf{Z}_\infty \mathbf{L}_\infty \mathbf{C}_2 \quad (8.10)$$

$$\mathbf{Z}_\infty = (\mathbf{I} - \gamma^{-2} \mathbf{Y}_\infty \mathbf{X}_\infty)^{-1} \quad (8.11)$$

$$\mathbf{L}_\infty = -\mathbf{Y}_\infty \mathbf{C}_2^T \quad (8.12)$$

$$\mathbf{F}_\infty = -\mathbf{B}_2^T \mathbf{X}_\infty \quad (8.13)$$

and $\mathbf{Q}(s)$ is any stable proper transfer function such that $\|\mathbf{Q}\|_\infty < \gamma$ holds.

If the stated conditions on the Riccati equations listed above (items 1–3) are not fulfilled, the tested value of γ is too small and hence infeasible. This is utilized to formulate a bisection algorithm, called γ -iteration, to search for a feasible value $\gamma \geq \gamma_{\min}$ close to the optimum to within a tolerance ε such that $\gamma - \gamma_{\min} < \varepsilon$ holds. The MATLAB® Robust Control Toolbox algorithm `hinfscn` implements this procedure (γ -iteration and the solution to the suboptimal \mathcal{H}_∞ design problem with relaxed conditions). Therein, several methods to compute the solutions \mathbf{X}_∞ , \mathbf{Y}_∞ are implemented. Also, assumption A2 in Definition 8.1 may be violated and a realizable controller for slightly perturbed entries in \mathbf{D} is computed in this case.[7]

8.4 Frequency-Dependent Weighting Functions for \mathcal{H}_∞ Control Design

This section is based on [7].

Given a scalar stable transfer function (weighting function) $W(s)$ and a stable (MIMO) transfer function matrix, for example the sensitivity function $\mathbf{S}(s)$, the following holds:

$$\bar{\sigma}(W(j\omega) \cdot \mathbf{S}(j\omega)) = \bar{\sigma}(W(j\omega)) \cdot \bar{\sigma}(\mathbf{S}(j\omega)) = |W(j\omega)| \cdot \bar{\sigma}(\mathbf{S}(j\omega)) \quad \forall \omega \in \mathbb{R} \quad (8.14)$$

Note that the first equality follows from the fact that the multiplicative matrix norm inequality (A.29) is fulfilled with equality because the product is a scalar product.

Consider that as a result of an \mathcal{H}_∞ control design, the weighted sensitivity function $W\mathbf{S}$ fulfills

$$\|W\mathbf{S}\|_\infty < 1 \Leftrightarrow |W(j\omega)| \cdot \bar{\sigma}(\mathbf{S}(j\omega)) < 1 \quad \forall \omega \in \mathbb{R}. \quad (8.15)$$

Then, this is equivalent to

$$\bar{\sigma}(\mathbf{S}(j\omega)) < \frac{1}{|W(j\omega)|} = |W^{-1}(j\omega)| \quad \forall \omega \in \mathbb{R}, \quad (8.16)$$

so, in this example the inverse weight magnitude $|W^{-1}(j\omega)|$ is a valid upper bound for the maximum singular value of $\mathbf{S}(j\omega)$ at all frequencies.

A case where $\bar{\sigma}(\mathbf{S}(j\omega))$ exceeds its upper bound $|W^{-1}(j\omega)|$, resulting in $\|W\mathbf{S}\|_\infty > 1$, is depicted in Figure 8.2.

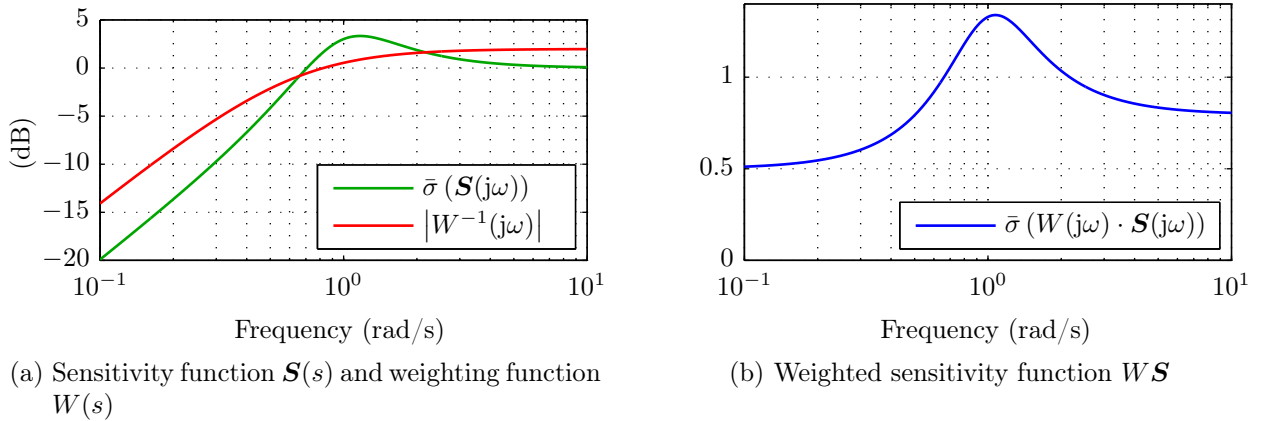


Figure 8.2: Case where $\bar{\sigma}(\mathbf{S}(j\omega))$ exceeds its upper bound $|W^{-1}(j\omega)|$, resulting in $\|W\mathbf{S}\|_\infty > 1$ (adopted from [6])

Equation (8.16) sketches the following weight selection procedure to construct weights for (closed-loop) transfer functions $\mathbf{X}(s)$: [7]

1. Define a desired upper bound on $\bar{\sigma}(\mathbf{X}(j\omega)) \quad \forall \omega \in \mathbb{R}$.
2. Shape a suitable scalar, minimum-phase, stable, invertible, and bi-proper transfer function $V(s)$ as an approximation from above to this upper bound.

3. Obtain the design weighting function by inversion: $W(s) = V^{-1}(s)$.
4. Perform the corresponding \mathcal{H}_∞ controller design and try to achieve $\|W\mathbf{X}\|_\infty < 1$ (i.e. Nominal Performance (NP)). If successful, it is guaranteed that the desired upper bound

$$\bar{\sigma}(\mathbf{X}(j\omega)) < \frac{1}{|W(j\omega)|} = |W^{-1}(j\omega)| \quad \forall \omega \in \mathbb{R}$$

is fulfilled.

Note that these relations do not hold if the weighting function $\mathbf{W}(s)$ is a transfer function matrix (MIMO), even if it is only chosen diagonally with different entries along the diagonal, because then the multiplicative matrix norm property (8.17),

$$\bar{\sigma}(\mathbf{W}(j\omega)\mathbf{X}(j\omega)) \leq \bar{\sigma}(\mathbf{W}(j\omega)) \cdot \bar{\sigma}(\mathbf{X}(j\omega)) \quad \forall \omega \in \mathbb{R}, \quad (8.17)$$

is in general NOT fulfilled with equality. Thus, if $\|\mathbf{W}\mathbf{X}\|_\infty < 1$ is fulfilled (i.e. NP is satisfied), $1/\bar{\sigma}(\mathbf{W}(j\omega)) = \underline{\sigma}(\mathbf{W}^{-1}(j\omega))$ can in general not be interpreted as an upper bound on $\bar{\sigma}(\mathbf{X}(j\omega))$ if $\mathbf{W}(s)$ is a transfer function matrix (MIMO).

$$\|\mathbf{W}\mathbf{X}\|_\infty < 1 \Leftrightarrow \bar{\sigma}(\mathbf{W}(j\omega)\mathbf{X}(j\omega)) < 1 \quad \forall \omega \in \mathbb{R} \Leftrightarrow \bar{\sigma}(\mathbf{W}(j\omega)) \cdot \bar{\sigma}(\mathbf{X}(j\omega)) < 1 \quad \forall \omega \in \mathbb{R} \quad (8.18)$$

In order to fulfill the set of prerequisites or assumptions on the augmented plant \mathbf{P} (see Definition 8.1) used to formulate and solve standard \mathcal{H}_∞ design problems, the following restrictions on weighting functions are usually made. [7, 6]

- strictly stable²
- proper³
- minimum-phase

The most common weighting function shapes are high- and low-pass functions given by

$$W(s) = K \cdot \left(\frac{\frac{s}{\omega_1} + 1}{\frac{s}{\omega_2} + 1} \right)^n \quad (8.19)$$

where, if $\omega_1 < \omega_2$ holds, $W(s)$ is a high-pass filter, whereas for $\omega_1 > \omega_2$ it is a low-pass filter. It is often beneficial to use simple bandpass and bandstop filters given by

$$W(s) = K \cdot \left(\frac{(\frac{s}{\omega_1} + 1)(\frac{s}{\omega_4} + 1)}{(\frac{s}{\omega_2} + 1)(\frac{s}{\omega_3} + 1)} \right)^n \quad (8.20)$$

instead. If in (8.20) $\omega_1 < \omega_2 < \omega_3 < \omega_4$ holds, $W(s)$ is a bandpass filter, whereas for $\omega_2 < \omega_1 < \omega_4 < \omega_3$ it is a bandstop filter.

To shape the damping of low-damped structural modes, it is convenient to use weighting function shapes with sharp peaks at specific frequencies of interest. A single peak (see Figure 8.3a) is created by

²Pure integrators have to be replaced by “quasi-integrators”: $\frac{1}{s} \xrightarrow{\text{repl.}} \frac{1}{s+\epsilon}$ with $\epsilon > 0$, ϵ small

³Replace terms which make $W(s)$ non-proper as follows: $(1 + \tau_1 s) \xrightarrow{\text{repl.}} (1 + \tau_1 s)/(1 + \tau_2 s)$ with $\tau_2 \ll \tau_1$

$$W_{\text{peak}}(s) = \frac{\omega_1^2}{\omega_2^2} \cdot \frac{s^2 + 2\zeta_2\omega_2 \cdot s + \omega_2^2}{s^2 + 2\zeta_1\omega_1 \cdot s + \omega_1^2} \quad (8.21)$$

where usually $\omega_1 = \omega_2 = \omega_{\text{peak}}$ is chosen, so that

$$\lim_{\omega \rightarrow 0} W_{\text{peak}}(j\omega) = 1 \quad \text{and} \quad \lim_{\omega \rightarrow \infty} W_{\text{peak}}(j\omega) = 1 \quad (8.22)$$

Thus, when such a peak is combined (multiplied) with one of the aforementioned filters, it affects the original shape only at a close region around ω_{peak} (see Figure 8.3b). If $\zeta_1 < \zeta_2$ holds, $W_{\text{peak}}(s)$ is an anti-notch filter, whereas for $\zeta_1 > \zeta_2$ it is a notch filter.

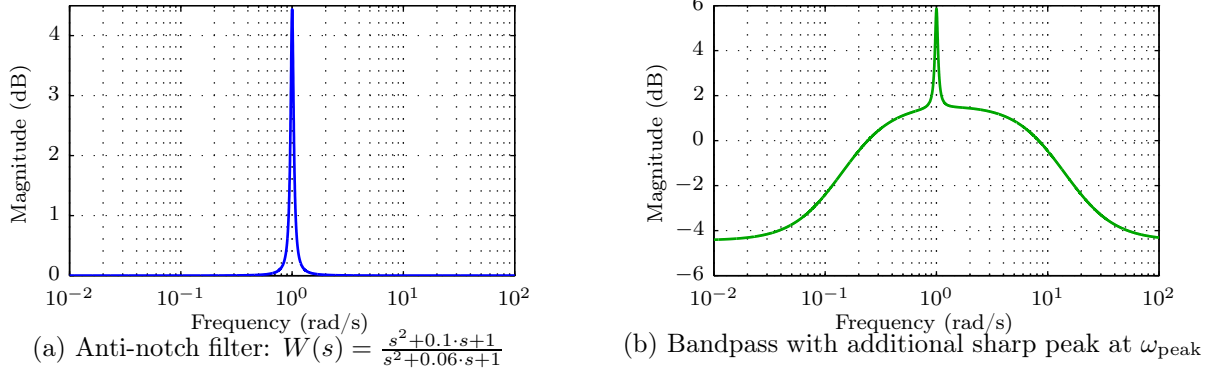


Figure 8.3: Exemplary weighting function $W(s)$ for damping of low-damped structural modes

8.5 Mixed-Sensitivity \mathcal{H}_∞ Optimal Control

The name mixed-sensitivity \mathcal{H}_∞ control is given to transfer function shaping problems in which (utilizing frequency-dependent weights) the sensitivity function $\mathbf{S} = (\mathbf{I} + \mathbf{G}\mathbf{K})^{-1}$ is shaped along with one or more other closed-loop transfer functions by stacking them on top of each other in an overall closed-loop performance transfer function matrix \mathbf{N} and minimizing its \mathcal{H}_∞ norm with respect to \mathbf{K} . Thus the \mathcal{H}_∞ optimal controller for this stacked formulation is obtained by solving the problem

$$\min_{\mathbf{K}} \|\mathbf{N}(\mathbf{K})\|_\infty \quad (8.23)$$

where \mathbf{K} is an internally stabilizing controller. The design specifications are fulfilled (i.e. Nominal Performance (NP) is achieved) if

$$\|\mathbf{N}\|_\infty = \max_{\omega} \bar{\sigma}(\mathbf{N}(j\omega)) < 1. \quad (8.24)$$

In this work, the regulation (disturbance rejection) problem depicted in Figure 8.4 is investigated⁴. In this case the exogenous input signal \mathbf{w} entering the generalized plant \mathbf{P} is

⁴Because in Figure 8.4 the disturbance transfer function matrix \mathbf{G}_d is included in the generalized plant \mathbf{P} , the regulation problem is in a non-standard formulation. Other, typical mixed-sensitivity \mathcal{H}_∞ control problems (in standard form) are found in [6].

the disturbance \mathbf{d} .⁵ In Figure 8.4 \mathbf{u} are the control inputs and \mathbf{v} are the measured outputs fed back to the controller \mathbf{K} .

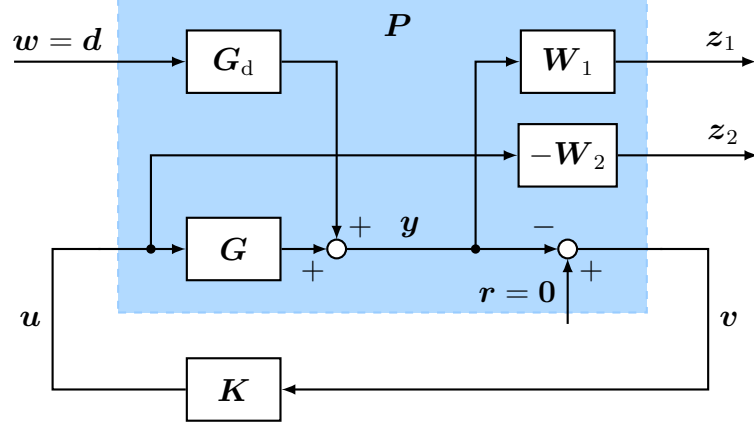


Figure 8.4: $\mathbf{S}\mathbf{G}_d/\mathbf{K}\mathbf{S}\mathbf{G}_d$ mixed-sensitivity optimization (regulation)

Utilizing a frequency-dependent performance weight $\mathbf{W}_1(s)$ and an input weight $\mathbf{W}_2(s)$, the exogenous output signal $\mathbf{z} = \begin{bmatrix} z_1^T & z_2^T \end{bmatrix}^T$, where $z_1 = \mathbf{W}_1 \mathbf{y}$ and $z_2 = -\mathbf{W}_2 \mathbf{u}$ is defined and the generalized plant \mathbf{P} is given by

$$\begin{bmatrix} z_1 \\ z_2 \\ \mathbf{v} \end{bmatrix} = \underbrace{\begin{bmatrix} \mathbf{W}_1 \mathbf{G}_d & \mathbf{W}_1 \mathbf{G} \\ 0 & -\mathbf{W}_2 \\ -\mathbf{G}_d & -\mathbf{G} \end{bmatrix}}_{\mathbf{P}} \begin{bmatrix} \mathbf{w} \\ \mathbf{u} \end{bmatrix} \quad (8.25)$$

Closing the lower feedback loop with the controller \mathbf{K} yields the closed-loop performance transfer function matrix \mathbf{N} :

$$\begin{bmatrix} z_1 \\ z_2 \end{bmatrix} = \underbrace{\begin{bmatrix} \mathbf{W}_1 \mathbf{S} \mathbf{G}_d \\ \mathbf{W}_2 \mathbf{K} \mathbf{S} \mathbf{G}_d \end{bmatrix}}_{\mathbf{N}} \mathbf{w} \quad (8.26)$$

\mathbf{N} can be either derived directly by an investigation of the block diagram of Figure 8.4 (without breaking the loop before and after \mathbf{K}) or by solving the lower linear fractional transformation (LFT)

$$\mathbf{N} = \mathcal{F}_l(\mathbf{P}, \mathbf{K}) = \mathbf{P}_{11} + \mathbf{P}_{12} \mathbf{K} (\mathbf{I} - \mathbf{P}_{22} \mathbf{K})^{-1} \mathbf{P}_{21}, \quad (8.27)$$

where \mathbf{P} is partitioned to be compatible with \mathbf{K} .

In equation (8.26) $\mathbf{S}\mathbf{G}_d$ is the transfer function between \mathbf{d} and the output \mathbf{y} , and $-\mathbf{K}\mathbf{S}\mathbf{G}_d$ is the transfer function between \mathbf{d} and the control signals \mathbf{u} .⁶ Because the disturbance transfer function \mathbf{G}_d is given, \mathbf{S} and $\mathbf{K}\mathbf{S}$ are the only adjustable transfer functions, which, in order to meet the design specifications have to be shaped properly.

The disturbance \mathbf{d} is typically a low-frequency signal, and hence it will be successfully rejected if the maximum singular value of \mathbf{S} is made small over the same low frequencies. [6] This is obtained by selecting \mathbf{W}_1 (typically chosen scalar or diagonal) as a low-pass filter.

⁵In this work the disturbance is actually a scalar signal d associated with the shaker force.

⁶Because only the magnitude of $-\mathbf{K}\mathbf{S}\mathbf{G}_d$ matters here, the negative sign is neglected in the following.

Weighting \mathbf{KS} with a high-pass filter \mathbf{W}_2 , which penalizes large high-frequency magnitudes in \mathbf{u} , while allowing low-frequency control action, works as a mechanism for limiting the control input magnitude and the bandwidth of the controller. Small $\bar{\sigma}(\mathbf{K}(j\omega)\mathbf{S}(j\omega))$ is also important for robust stability with respect to additive uncertainty (see Section 8.6.2) at ω . [7, 6]

Since the particularly applied piezo patch sensors have a lower frequency limit (i.e. static measurement is not possible), \mathbf{W}_1 and \mathbf{W}_2 were actually chosen as a bandpass respectively bandstop.

Because the largest singular value (for each frequency $s = j\omega$) of a stacked matrix $\begin{bmatrix} \mathbf{A} \\ \mathbf{B} \end{bmatrix}$ is bounded by

$$\max\{\bar{\sigma}(\mathbf{A}), \bar{\sigma}(\mathbf{B})\} \leq \bar{\sigma}\left(\begin{bmatrix} \mathbf{A} \\ \mathbf{B} \end{bmatrix}\right) \leq \sqrt{2} \max\{\bar{\sigma}(\mathbf{A}), \bar{\sigma}(\mathbf{B})\} \quad (8.28)$$

the fulfillment of

$$\bar{\sigma}\left(\begin{bmatrix} \mathbf{W}_1\mathbf{S}\mathbf{G}_d(j\omega) \\ \mathbf{W}_2\mathbf{K}\mathbf{S}\mathbf{G}_d(j\omega) \end{bmatrix}\right) < 1 \quad \forall \omega \in \mathbb{R} \quad \Leftrightarrow \quad \left\| \begin{bmatrix} \mathbf{W}_1\mathbf{S}\mathbf{G}_d \\ \mathbf{W}_2\mathbf{K}\mathbf{S}\mathbf{G}_d \end{bmatrix} \right\|_{\infty} < 1 \quad (8.29)$$

implies that

$$\|\mathbf{W}_1\mathbf{S}\mathbf{G}_d\|_{\infty} < 1 \quad \text{and} \quad \|\mathbf{W}_2\mathbf{K}\mathbf{S}\mathbf{G}_d\|_{\infty} < 1 \quad (8.30)$$

both hold. Note that the converse implication, however, is not true, but from (8.28) it is evident that the conservativeness is at most $\sqrt{2}$: [7]

$$\|\mathbf{W}_1\mathbf{S}\mathbf{G}_d\|_{\infty} < 1 \quad \text{and} \quad \|\mathbf{W}_2\mathbf{K}\mathbf{S}\mathbf{G}_d\|_{\infty} < 1 \quad \Rightarrow \quad \left\| \begin{bmatrix} \mathbf{W}_1\mathbf{S}\mathbf{G}_d \\ \mathbf{W}_2\mathbf{K}\mathbf{S}\mathbf{G}_d \end{bmatrix} \right\|_{\infty} < \sqrt{2} \quad (8.31)$$

8.6 Fundamentals of Robust Control

The principle of robust control is used for the problem, that the models for \mathbf{G} and \mathbf{G}_d in equation (8.32) may be inaccurate or may change slowly with time.

$$\mathbf{y}(s) = \mathbf{G}(s)\mathbf{u}(s) + \mathbf{G}_d(s)\mathbf{d}(s) \quad (8.32)$$

In particular, inaccuracies in \mathbf{G} can cause severe problems due to the fact that model uncertainty combined with feedback may easily create instability. Note that \mathbf{G} is part of the feedback loop where the control signal \mathbf{u} depends on the (controlled) output signal \mathbf{y} .

To deal with such problems robust control makes use of the concept of model uncertainty. Instead of a single model \mathbf{G} the behavior of a set of possible perturbed plant models \mathbf{G}_p is investigated.⁷ In order to account for the actual model uncertainty well suitable uncertainty modeling is of major importance in robust control. Typical uncertainty descriptions are presented in Section 8.6.2 (uncertainty is explicitly modelled by the designer) and 8.8.2 (uncertainty is not explicitly modelled).

⁷The subscript “p” stands for “perturbed”.

8.6.1 Control objectives in robust control

The concept of robust control distinguishes between the following control objectives: [6]

Nominal stability (NS): The closed-loop system is internally stable with no model uncertainty.

Nominal performance (NP): The closed-loop system satisfies the performance specifications with no model uncertainty.

Robust stability (RS): The closed-loop system is stable for all perturbed plants about the nominal model up to the worst-case model uncertainty.

Robust performance (RP): The closed-loop system satisfies the performance specifications for all perturbed plants about the nominal model up to the worst-case model uncertainty.

8.6.2 Uncertainty modeling

In the following the two main classes of modeling uncertainty are described generally. Subsequently the uncertainty models applied in this work are given in detail.

8.6.2.1 Parametric (real) uncertainty

When it comes to parametric (real) uncertainty, the structure of the model including the system order is considered known. However, some of the system parameters are assumed to be uncertain. [6]

By postulating that each uncertain parameter α_p is bounded to within an interval $\alpha_{\min} \leq \alpha_p \leq \alpha_{\max}$, a parameter set

$$\alpha_p = \bar{\alpha} \cdot (1 + w_\alpha \delta_\alpha) \quad (8.33)$$

is defined. Here $\bar{\alpha} = \frac{\alpha_{\max} + \alpha_{\min}}{2}$ is the mean parameter value, $w_\alpha = \frac{\alpha_{\max} - \alpha_{\min}}{\alpha_{\max} + \alpha_{\min}}$ is the relative uncertainty in the parameter, and δ_α is any real scalar satisfying $-1 \leq \delta_\alpha \leq 1$, but otherwise unknown.

Parametric state-space uncertainties

In this section, which is based on [7, 12], a method is presented to model parametric uncertainty in the state matrix \mathbf{A} .

While multiplicative and additive uncertainties (see Section 8.6.2.2 on page 94) are defined in the frequency domain and are complex-valued, the uncertainties in the parameters of a dynamic system (natural angular frequencies, modal damping coefficients, etc.) are real-valued uncertainties. [12]

The state matrix (block) \mathbf{A} for a single structural mode i with natural angular frequency ω_i and modal damping coefficient ζ_i is depicted in (8.34) (i is the first and only mode in this case, thus $i = 1$).⁸

$$\mathbf{A} = \begin{bmatrix} 0 & 1 \\ -\omega_i^2 & -2\zeta_i\omega_i \end{bmatrix} \quad (8.34)$$

⁸The system is in the third modal state-space representation (modal model 3) with block-diagonal state matrix $\mathbf{A} = \text{diag}\{\mathbf{A}_i\}$ (see Section 5.3.3).

Appropriate uncertainty descriptions, if the uncertain parameters are the natural angular frequency ω_i and the modal damping coefficient ζ_i are

$$\omega_{ip}(\delta_{i\omega}) = \omega_i(1 + w_{i\omega}\delta_{i\omega}) \quad (8.35)$$

$$\zeta_{ip}(\delta_{i\zeta}) = \zeta_i(1 + w_{i\zeta}\delta_{i\zeta}), \quad (8.36)$$

where $w_{i\omega}$ is the relative magnitude of the (symmetric) uncertainty of ω_i and $w_{i\zeta}$ is the relative magnitude of the (symmetric) uncertainty of ζ_i . The real-valued uncertain parameters are $\delta_{i\omega}$ and $\delta_{i\zeta}$ ($\delta_{i\omega}, \delta_{i\zeta} \in \mathbb{R}, |\delta_{i\omega}| \leq 1, |\delta_{i\zeta}| \leq 1$).

Then, according to Morton's method [15], the perturbed state matrix $\mathbf{A}_p(\delta_{i\omega}, \delta_{i\zeta})$ (2×2) of an uncertain structural mode i is given by

$$\mathbf{A}_p = \begin{bmatrix} 0 & 1 \\ -\omega_{ip}^2(\delta_{i\omega}) & -2\zeta_{ip}(\delta_{i\zeta})\omega_{ip}(\delta_{i\omega}) \end{bmatrix} \quad (8.37)$$

where the polynomials ω_{ip} and ζ_{ip} in $\delta_{i\omega}$ and $\delta_{i\zeta}$ can be realized by a LFT ([7]) of the system

$$\mathbf{H}(s) \stackrel{\text{ss}}{=} \left[\begin{array}{c|cc} \mathbf{A} & \mathbf{B}_{\text{par}} & \mathbf{B} \\ \hline \mathbf{C}_{\text{par}} & \mathbf{D}_{\text{par}} & \mathbf{0} \\ \mathbf{C} & \mathbf{0} & \mathbf{D} \end{array} \right] \quad (8.38)$$

with inputs $[\mathbf{u}_\Delta^T \quad \mathbf{u}^T]^T$ and outputs $[\mathbf{y}_\Delta^T \quad \mathbf{y}^T]^T$, where

$$\left[\begin{array}{c|cc} \mathbf{A} & \mathbf{B}_{\text{par}} & \mathbf{B} \\ \hline \mathbf{C}_{\text{par}} & \mathbf{D}_{\text{par}} & \mathbf{0} \\ \mathbf{C} & \mathbf{0} & \mathbf{D} \end{array} \right] = \left[\begin{array}{cc|cc} 0 & 1 & 0 & -\omega_i w_{i\omega} & 1 & 1 \\ -\omega_i^2 & -2\zeta_i \omega_i & -\omega_i^2 w_{i\omega} & 2\zeta_i \omega_i^2 w_{i\omega} & -2\zeta_i \omega_i & -2\zeta_i \omega_i \\ \hline 1 & 0 & 0 & 0 & 0 & 0 \\ -2\zeta_i & -\frac{1}{\omega_i} & 0 & 0 & 0 & 0 \\ -2\zeta_i \omega_i w_{i\omega} & 0 & 0 & 0 & 0 & w_{i\omega} \\ -2\zeta_i \omega_i w_{i\zeta} & 0 & 0 & 0 & 0 & 0 \end{array} \right] \quad (8.39)$$

and with the diagonal real-valued uncertainty block

$$\mathbf{\Delta}_{\text{par}} = \begin{bmatrix} \delta_{i\omega} & & & \\ & \delta_{i\omega} & & \\ & & \delta_{i\omega} & \\ & & & \delta_{i\zeta} \end{bmatrix}. \quad (8.40)$$

Because the parameter $\delta_{i\omega}$, associated with the natural angular frequency ω_i , occurs three times in the \mathbf{A} matrix, it is repeated three times in the $\mathbf{\Delta}_{\text{par}}$ -block. The parameter $\delta_{i\zeta}$, associated with the modal damping coefficient ζ_i , occurs only once as its influence on \mathbf{A} is only linear and only in a single matrix element. [7] This highlights the importance of choosing a state-space representation where the uncertain parameters occur as seldomly as possible. Consequently, representing the system in the second modal form (5.76) can be thought of as a negative example, because ω_i and ζ_i occur four respectively two times in the \mathbf{A} matrix. Moreover, in order to account for the same extent of parametric uncertainty for an (uncertain) structural mode, one would also have to perturb the output matrix \mathbf{C} if the system would be represented in the second (or first) modal form (see (5.76) and (5.74)). Thus the third modal form might be a good choice.⁹

⁹The simplification algorithms implemented in MATLAB[®] achieve a better representation where the parameter $\delta_{i\omega}$ occurs always only twice (and $\delta_{i\zeta}$ occurs once).

By utilizing the system interconnection structure $\mathbf{H}(s)$ and the diagonal real-valued uncertainty block Δ_{par} the perturbed system \mathbf{G}_p is computed by

$$\mathbf{G}_p(s) = \mathcal{F}_u(\mathbf{H}(s), \Delta_{\text{par}}) \quad (8.41)$$

$$= \mathbf{H}_{22} + \mathbf{H}_{21}\Delta_{\text{par}}(\mathbf{I} - \mathbf{H}_{11}\Delta_{\text{par}})^{-1}\mathbf{H}_{12}. \quad (8.42)$$

where $\mathbf{H}(s)$ is partitioned to be compatible with Δ_{par} (see Figure 8.5) and $\mathbf{G}(s) = \mathbf{H}_{22}(s)$ is the nominal plant model.

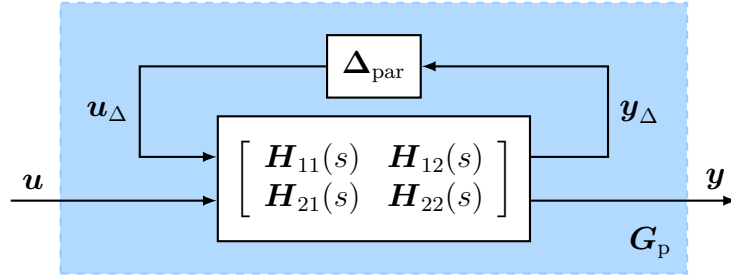


Figure 8.5: Uncertain plant, $\mathbf{y} = \mathbf{G}_p \mathbf{u}$, represented by LFT (\mathbf{H} - Δ_{par} -structure)

Example 8.1: Interconnection structure $\mathbf{H}(s)$ for parametric uncertainty in the state matrix \mathbf{A} for a system in modal form with three structural modes

For a state-space system in modal form with three structural modes the block-diagonal state matrix \mathbf{A} is given schematically by:

$$\mathbf{A} = \begin{bmatrix} \mathbf{A}_1 & \mathbf{0} & \mathbf{0} \\ \mathbf{0} & \mathbf{A}_2 & \mathbf{0} \\ \mathbf{0} & \mathbf{0} & \mathbf{A}_3 \end{bmatrix} \quad (8.43)$$

In this example parametric uncertainty (of ω and ζ) shall be only considered in the \mathbf{A}_i -blocks (2×2) corresponding to the first and third structural mode. In this case, the input, output, and feed-through matrices \mathbf{B}_{par} , \mathbf{C}_{par} and \mathbf{D}_{par} for the interconnection with the uncertainty block (diagonal matrix of real-valued uncertain parameters)

$$\Delta_{\text{par}} = \begin{bmatrix} \Delta_{\text{par1}} & \mathbf{0} \\ \mathbf{0} & \Delta_{\text{par3}} \end{bmatrix} \quad (8.44)$$

is

$$\mathbf{B}_{\text{par}} = \begin{bmatrix} \mathbf{B}_{\text{par1}} & \mathbf{0} \\ \mathbf{0} & \mathbf{0} \\ \mathbf{0} & \mathbf{B}_{\text{par3}} \end{bmatrix} \quad \mathbf{C}_{\text{par}} = \begin{bmatrix} \mathbf{C}_{\text{par1}} & \mathbf{0} & \mathbf{0} \\ \mathbf{0} & \mathbf{0} & \mathbf{C}_{\text{par3}} \end{bmatrix} \quad \mathbf{D}_{\text{par}} = \begin{bmatrix} \mathbf{D}_{\text{par1}} & \mathbf{0} \\ \mathbf{0} & \mathbf{D}_{\text{par3}} \end{bmatrix}. \quad (8.45)$$

The matrices \mathbf{B}_{par} , \mathbf{C}_{par} and \mathbf{D}_{par} are then used in the state-space representation of the system interconnection structure $\mathbf{H}(s)$ as given in (8.38), together with the matrices (\mathbf{A} , \mathbf{B} , \mathbf{C} , \mathbf{D}) of the modal state-space representation of $\mathbf{G}(s)$.

By using the Robust Control Toolbox of MATLAB[®] a perturbed state matrix \mathbf{A}_p was designed and used to replace the nominal state matrix \mathbf{A} . More information about this kind of uncertainty can be found in [12, 7].

8.6.2.2 Dynamic (frequency-dependent) uncertainty (complex uncertainties)

Dynamic (frequency-dependent) uncertainty modeling is used to model uncertainty caused by missing dynamics, usually at high frequencies, either through deliberate neglect (neglected dynamics) or because of a lack of understanding of the physical process (unmodelled dynamics). [6]

For example a class of models is defined by using an additive (subscript A) uncertainty description $\mathbf{G}_p(s) = \mathbf{G}(s) + \mathbf{E}_A(s)$, where $\mathbf{G}(s)$ is the nominal model and $\mathbf{E}_A(s)$ is the unknown but bounded (non-normalized) additive model “uncertainty” or “perturbation”. Usually a (non-normalized) perturbation $\mathbf{E}(s)$ (8.47) is modelled as an unknown but normalized, stable perturbation $\Delta(s)$ (complex-valued LTI dynamics), where the \mathcal{H}_∞ norm of Δ is

$$\|\Delta(s)\|_\infty \leq 1, \quad (8.46)$$

pre- and post-multiplied by dynamic weights (stable and minimum-phase LTI systems) $\mathbf{W}_1(s)$ and $\mathbf{W}_2(s)$ (design parameters representing the frequency-dependent uncertainty).

$$\mathbf{E}(s) = \mathbf{W}_2(s)\Delta(s)\mathbf{W}_1(s) \quad (8.47)$$

Additive uncertainty

In Figure 8.6 a system with additive uncertainty is shown. The corresponding transfer function matrix of the uncertain system \mathbf{G}_p is given by (8.48).

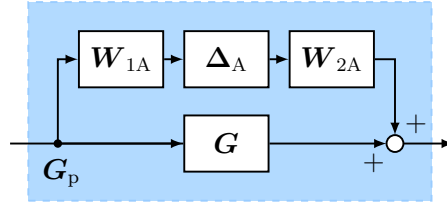


Figure 8.6: Additive uncertainty

$$\mathbf{G}_p(s) = \mathbf{G}(s) + \mathbf{W}_{2A}(s)\Delta_A(s)\mathbf{W}_{1A}(s) \quad \|\Delta_A(s)\|_\infty \leq 1 \quad (8.48)$$

Usually $\Delta_A(s)$ is considered as a full complex perturbation matrix, where any coupling from its inputs to its outputs are possible, and phase relations are unknown. [7]

Commonly the dimensions of $\Delta_A(s)$ are chosen to be compatible with those of the nominal plant $\mathbf{G}(s)$ ($m \times r$), resulting in square weights $\mathbf{W}_{1A}(s)$ ($r \times r$) and $\mathbf{W}_{2A}(s)$ ($m \times m$). Typically it is sufficient to choose the weights diagonal, populated with simple transfer functions. [7]

Additive uncertainty is commonly used to model neglected or unknown system dynamics in a simplified manner by increasing the magnitude of the uncertainty weight(s) in those frequency regions where the nominal plant can not be trusted. [7]

Multiplicative uncertainty

In Figure 8.7a a system with multiplicative input uncertainty and in Figure 8.7b a system with multiplicative output uncertainty is depicted. The uncertain plant $\mathbf{G}_p(s)$ is given by (8.49) respectively (8.50).

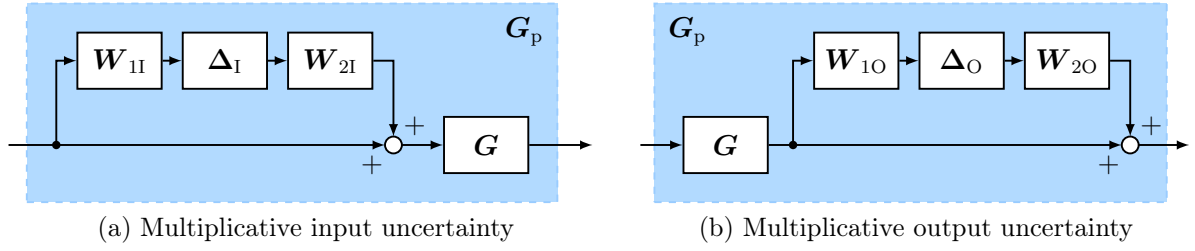


Figure 8.7: Multiplicative uncertainty

$$\mathbf{G}_p(s) = \mathbf{G}(s) (\mathbf{I} + \mathbf{W}_{2I}(s)\Delta_I(s)\mathbf{W}_{1I}(s)) \quad \|\Delta_I(s)\|_\infty \leq 1 \quad (8.49)$$

$$\mathbf{G}_p(s) = (\mathbf{I} + \mathbf{W}_{2O}(s)\Delta_O(s)\mathbf{W}_{1O}(s)) \mathbf{G}(s) \quad \|\Delta_O(s)\|_\infty \leq 1 \quad (8.50)$$

Multiplicative input (respectively output) uncertainty is frequently used to model actuator (respectively sensor) magnitude and phase uncertainty over frequency. In that case, the perturbation $\Delta_I(s)$ ($r \times r$) (respectively $\Delta_O(s)$ ($m \times m$)) is a complex diagonal matrix

$$\Delta(s) = \text{diag}\{\Delta_i(s)\}; \quad |\Delta_i(j\omega)| \leq 1, \forall \omega, \forall i \quad (8.51)$$

This circumstance is clarified in the following by considering uncertainty in the individual input channels i (for $i = 1, \dots, r$).

Associated with each input u_i there is a separate physical system (amplifier, signal converter, actuator, valve, etc.) which, based on the controller output signal u_i , generates a physical plant input m_i . [6]

$$m_i = h_i(s)u_i \quad (8.52)$$

Usually the SISO system $h_i(s)$ is absorbed into the plant model $\mathbf{G}(s)$, but for representing the uncertainty it is essential to note that $h_i(s)$ originates at the input. For SISO systems, it is often beneficial to lump multiple sources of parametric real uncertainty into a single complex perturbation, because in the Nyquist locus the true uncertainty region at a particular frequency ω (created by this multiple real perturbations) is often almost “disc-shaped” and may be more efficiently represented by a single complex perturbation. [6] A simpler uncertainty description for a SISO system $h_i(s)$ with a single complex perturbation could be in a multiplicative form (8.53).

$$h_{pi}(s) = h_i(s) (1 + w_i(s)\Delta_i(s)) \quad |\Delta_i(j\omega)| \leq 1, \forall \omega \quad (8.53)$$

Of course, by choosing $w_i(s)$ properly one can also consider neglected and/or unmodelled dynamics in the uncertainty description of equation (8.53).

At frequencies where $|\Delta_i(j\omega)| > 1$ the uncertainty exceeds 100 % and the Nyquist curve of $h_{pi}(j\omega)$ may pass through the origin (see Figure 8.8), thus the phase is unknown, and zeros can cross from the left half plane (LHP) to the right half plane (RHP). [6]

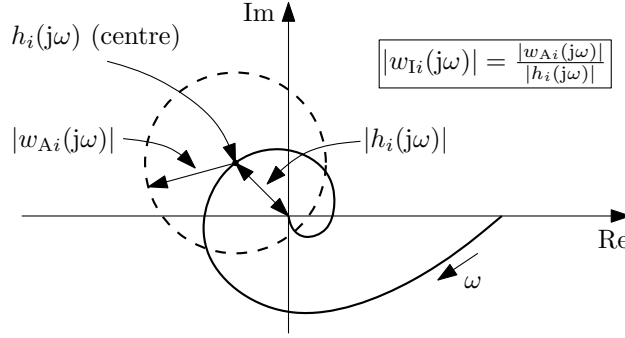


Figure 8.8: Exemplary Nyquist plot of $h_i(j\omega)$ and disc-shaped uncertainty region (at a given frequency ω) generated by complex additive uncertainty $h_{pi}(s) = h_i(s) + w_{Ai}(s)\Delta_{Ai}(s)$ with $|\Delta_{Ai}(j\omega)| \leq 1$ (SISO case!). The set of possible plants $h_{pi}(s)$ includes the origin at frequencies ω where $|w_{Ai}(j\omega)| \geq |h_i(j\omega)|$, or equivalently $|w_{Ii}(j\omega)| \geq 1$ (adopted from [6])

After combining all input channels i (for $i = 1, \dots, r$), a complex diagonal input uncertainty for the plant (8.54) is found [6]:

$$\mathbf{G}_p(s) = \mathbf{G}(\mathbf{I} + \mathbf{W}_I\Delta_I); \quad \Delta_I(s) = \text{diag}\{\Delta_{Ii}(s)\}, \quad \mathbf{W}_I(s) = \text{diag}\{w_{Ii}(s)\} \quad (8.54)$$

8.6.3 General control configuration with uncertainty (The P - K - Δ -structure)

Figure 8.9 shows the general control configuration (standard form of the robust control design problem) with uncertainty (P - K - Δ -structure), which, if model uncertainty is considered in the design process is used for controller synthesis.

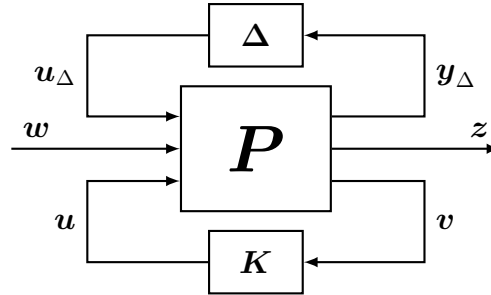


Figure 8.9: General control configuration with uncertainty (for controller synthesis)

The normalized ($\|\Delta\|_\infty \leq 1$), stable, block-diagonal LTI perturbation matrix $\Delta \in \Delta_B$ (8.55), which is only known in terms of its qualitative structure¹⁰, is derived by “pulling out” all the uncertain perturbations (Figure 8.10b) from the uncertain closed-loop transfer function \mathbf{F} (Figure 8.10a).

$$\Delta \in \Delta_B \Leftrightarrow \|\Delta\|_\infty \leq 1, \Delta \text{ LTI, structured, and stable} \quad (8.55)$$

¹⁰The linear time-invariant (LTI) system $\Delta(s)$ (see (8.56)) is a block-diagonal matrix ($\Delta \in \Delta_B$), where evaluating $\Delta_i(s)$ at $s = j\omega$ is either allowed to be a full complex matrix ($\Delta_i = \Delta_i(j\omega)$) or only a complex diagonal matrix ($\Delta_i = \text{diag}\{\Delta_j(j\omega)\}$), or it is only allowed to be a constant matrix Δ_i of a diagonally repeated real scalar ($\Delta_i = \delta_i \cdot \mathbf{I}_{[r_i \times r_i]}$). The cases where the i th perturbation Δ_i is a complex scalar $\Delta_i(j\omega)$ respectively real scalar δ_i follow as a special case. The actual values of Δ are **unknown**!

$$\Delta = \begin{bmatrix} \Delta_1 & 0 & 0 & 0 \\ 0 & \ddots & 0 & 0 \\ 0 & 0 & \Delta_i & 0 \\ 0 & 0 & 0 & \ddots \end{bmatrix} \quad (8.56)$$

Each individual perturbation Δ_i (8.56), which represents a specific source of uncertainty¹¹, is assumed to be stable and is normalized by:

$$\bar{\sigma}(\Delta_i(j\omega)) \leq 1 \quad \forall \omega \in \mathbb{R} \quad (8.57)$$

In the case of a complex scalar perturbation the condition for the maximum singular value $\bar{\sigma}$ yields $|\Delta_i(j\omega)| \leq 1 \quad \forall \omega$ and in the case of a real scalar perturbation $-1 \leq \delta_i \leq 1$ holds. A Δ which is allowed to be any (full) complex matrix is also called unstructured uncertainty or full-block complex perturbation uncertainty.

An important fact is derived from the circumstance that the maximum singular value of a block-diagonal matrix is equal to the largest maximum singular value of its individual blocks (8.58).

$$\bar{\sigma} \left(\begin{bmatrix} \mathbf{A} & \mathbf{0} \\ \mathbf{0} & \mathbf{B} \end{bmatrix} \right) = \max \{ \bar{\sigma}(\mathbf{A}), \bar{\sigma}(\mathbf{B}) \} \quad (8.58)$$

For the block-diagonal perturbation matrix Δ follows from equation (8.58):

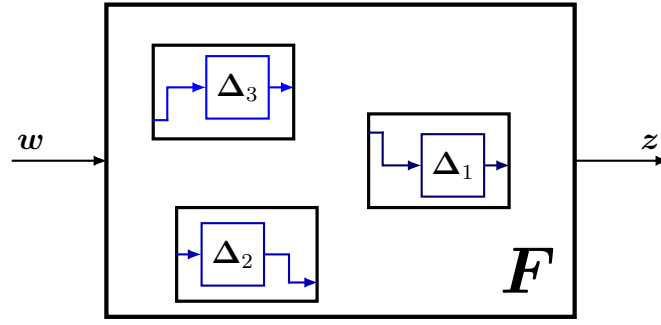
$$\bar{\sigma}(\Delta_i(j\omega)) \leq 1 \quad \forall \omega \in \mathbb{R}, \forall i \Leftrightarrow \boxed{\|\Delta\|_\infty \leq 1} \quad (8.59)$$

The generalized plant \mathbf{P} represents the interconnection between the nominal plant model \mathbf{G} (and eventually the disturbance model \mathbf{G}_d , a matrix weight for performance \mathbf{W}_p , a matrix weight for input usage \mathbf{W}_u) and several uncertainty matrix weights for the different kinds of used uncertainty descriptions (see Section 8.6.2). The inputs to \mathbf{P} are \mathbf{u}_Δ (output vector of the normalized perturbation matrix Δ), \mathbf{w} (exogenous input signals: commands \mathbf{r} and/or disturbances \mathbf{d}), and \mathbf{u} (control signals). The outputs of \mathbf{P} are \mathbf{y}_Δ (input vector of the normalized perturbation matrix Δ), \mathbf{z} (exogenous or performance outputs), and \mathbf{v} (measured outputs). The generalized plant \mathbf{P} is partitioned accordingly to be compatible with the controller \mathbf{K} (8.60).

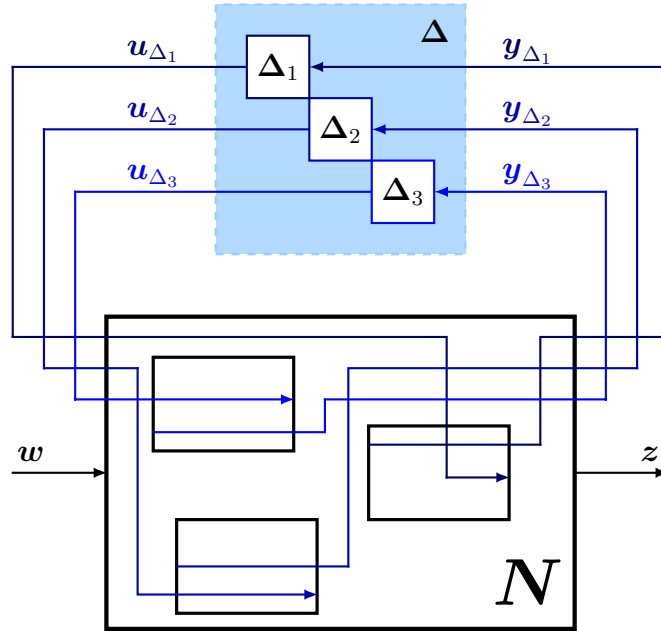
$$\begin{bmatrix} \mathbf{y}_\Delta \\ \mathbf{z} \\ \mathbf{v} \end{bmatrix} = \underbrace{\begin{bmatrix} \mathbf{P}_{11} & \mathbf{P}_{12} \\ \mathbf{P}_{21} & \mathbf{P}_{22} \end{bmatrix}}_{\mathbf{P}} \begin{bmatrix} \mathbf{u}_\Delta \\ \mathbf{w} \\ \mathbf{u} \end{bmatrix} \quad (8.60)$$

The generalized controller \mathbf{K} , which is used in a positive feedback loop with the generalized plant \mathbf{P} , has the overall control objective to generate a control signal \mathbf{u} , based on the measured information in \mathbf{v} , that counteracts the influence of \mathbf{w} on \mathbf{z} , hence minimizing the \mathcal{H}_∞ norm of the uncertain closed-loop transfer function \mathbf{F} (Figures 8.10a, 8.12) from \mathbf{w} to \mathbf{z} , thereby ensuring internal stability (see, Definition 8.2 on page 99) of the nominal closed-loop system \mathbf{N} .

¹¹For example Δ_i represents a complex diagonal input uncertainty ($\Delta_i = \Delta_I(s) = \text{diag}\{\Delta_{Ij}(s)\}$), a full complex additive uncertainty ($\Delta_i = \Delta_A(s)$), a parametric uncertainty ($\Delta_i = \delta_i \cdot \mathbf{I}$, where δ_i is a real scalar), etc..



(a) Uncertain closed-loop transfer function F from the exogenous inputs w to exogenous outputs with multiple perturbations (original system)



(b) Pulling out the perturbations

Figure 8.10: Rearranging an uncertain system into the N - Δ -structure (adopted from [6])

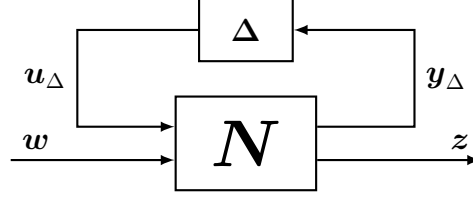
8.6.4 The N - Δ -structure (for robust performance analysis)

The nominal closed-loop system N (Figure 8.11) is derived by closing the lower feedback loop between P and K (see Figure 8.9) by a lower linear fractional transformation (LFT):

$$N = \mathcal{F}_l(P, K) = P_{11} + P_{12}K(I - P_{22}K)^{-1}P_{21} \quad (8.61)$$

The N - Δ -structure is used for robust performance analysis (see Definition 8.9) and N is partitioned accordingly to be compatible with Δ :

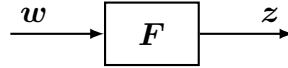
$$\begin{bmatrix} y_\Delta \\ z \end{bmatrix} = \underbrace{\begin{bmatrix} N_{11} & N_{12} \\ N_{21} & N_{22} \end{bmatrix}}_N \begin{bmatrix} u_\Delta \\ w \end{bmatrix} \quad (8.62)$$

Figure 8.11: N - Δ -structure for robust performance analysis

8.6.5 The uncertain closed-loop transfer function matrix F

The uncertain closed-loop transfer function matrix F from w to z (Figure 8.12) is related to N and Δ by an upper linear fractional transformation (LFT):

$$F = \mathcal{F}_u(N, \Delta) = N_{22} + N_{21}\Delta(\mathbf{I} - N_{11}\Delta)^{-1}N_{12} \quad (8.63)$$

Figure 8.12: Uncertain closed-loop transfer function F

8.6.6 Definitions for the control objectives in robust control with respect to the \mathcal{H}_∞ norm

As a major prerequisite for nominal performance (NP), robust stability (RS) and robust performance (RP), nominal stability (NS) has to be satisfied. Only then, the \mathcal{H}_∞ system norm is related to the maximum singular value.

Definition 8.2: Nominal Stability (NS)

A system N as given in Figure 8.11 is nominally stable (NS) if it is internally stable, that is, if none of its components contain hidden unstable modes (see Definition 8.3) and if the injection of bounded input signals at any place in the system result in bounded output signals measured anywhere in the system. [7, 6]

Definition 8.3: Stabilizable, detectable and hidden unstable modes. [6]

A system is stabilizable if all unstable modes are state controllable. A system is detectable if all unstable modes are state observable. A system with unstabilizable or undetectable modes is said to contain hidden unstable modes.[6]

In terms of the \mathbf{N} - Δ -structure in Figure 8.11, the requirements for stability and performance can be summarized as follows:

$$\text{NS : } \mathbf{N} \text{ is internally stable} \quad (8.64)$$

$$\text{NP : } \|\mathbf{N}_{22}\|_\infty < 1; \text{ and NS} \quad (8.65)$$

$$\text{RS : } \mathbf{F} = \mathcal{F}_u(\mathbf{N}, \Delta) \text{ is stable } \forall \Delta, \|\Delta\|_\infty \leq 1; \text{ and NS} \quad (8.66)$$

$$\text{RP : } \|\mathbf{F}\|_\infty < 1, \forall \Delta, \|\Delta\|_\infty \leq 1; \text{ and NS} \quad (8.67)$$

Note that the \mathcal{H}_∞ norm is used to define nominal performance¹² (8.65) and robust performance (8.67) and that for RP it is required, that $\|\mathbf{F}(\Delta)\|_\infty < 1$ for all allowed perturbations Δ with $\|\Delta\|_\infty \leq 1$. The main problem with the definitions for RS and RP as defined in (8.66) and (8.67) is that in order to test these conditions they have to be tested for an infinite set of allowable (possible) perturbations Δ , which can not be done directly. To overcome this problem the so-called structured singular value structured singular value (SSV) μ was defined, addressing the worst case, see Section 8.6.8.

8.6.7 The \mathbf{M} - Δ -structure for robust stability analysis

When \mathbf{N} in Figure 8.11 is nominally stable (8.64) and Δ is also stable, then the only possible source of instability in the upper LFT for the closed-loop system \mathbf{F} in (8.63), is the feedback term $(\mathbf{I} - \mathbf{N}_{11}\Delta)^{-1}$. Hence in this case, the stability of the system in Figure 8.11 is equivalent to the stability of the \mathbf{M} - Δ -structure in Figure 8.13, with $\mathbf{M} = \mathbf{N}_{11}$.

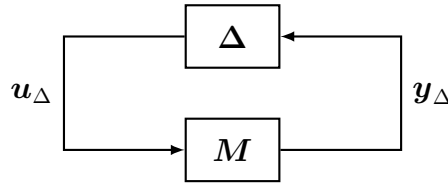


Figure 8.13: \mathbf{M} - Δ -structure for robust stability analysis

Definition 8.4: Small gain theorem [6]

Given a stable open-loop transfer function $\mathbf{L}(s)$, the closed-loop system is stable if

$$\|\mathbf{L}(j\omega)\| < 1 \quad \forall \omega \in \mathbb{R} \quad (8.68)$$

where $\|\cdot\|$ is any matrix norm (see Definition A.6).

Because the open-loop transfer function $\mathbf{M}\Delta(s)$ is considered stable, the closed-loop system is stable (i.e. RS is fulfilled) if

$$\bar{\sigma}(\mathbf{M}\Delta(j\omega)) < 1 \quad \forall \omega \in \mathbb{R} \quad (8.69)$$

¹² $\mathbf{N}_{22} = \mathcal{F}_u(\mathbf{N}, \Delta = \mathbf{0})$, see (8.63)

where the spectral norm was used (see Section A.6.1). Because a matrix norm such as the spectral norm satisfies the multiplicative property

$$\|\mathbf{A}\mathbf{B}\| \leq \|\mathbf{A}\| \cdot \|\mathbf{B}\|, \quad (8.70)$$

respectively

$$\bar{\sigma}(\mathbf{M}\Delta(j\omega)) \leq \bar{\sigma}(\mathbf{M}(j\omega)) \cdot \bar{\sigma}(\Delta(j\omega)) \quad \forall \omega \in \mathbb{R} \quad (8.71)$$

at each frequency ω the following is true:

$$\bar{\sigma}(\mathbf{M}(j\omega)) \cdot \bar{\sigma}(\Delta(j\omega)) < 1 \Rightarrow \bar{\sigma}(\mathbf{M}\Delta(j\omega)) < 1 \Rightarrow \text{RS}$$

Let Δ be the set of all complex matrices of any structure (i.e. $\Delta(j\omega)$ can also be a full complex matrix) such that

$$\bar{\sigma}(\Delta(j\omega)) \leq 1 \quad \forall \omega \in \mathbb{R} \quad (8.72)$$

Then the following holds:

$$\max_{\Delta(j\omega)} \bar{\sigma}(\mathbf{M}\Delta(j\omega)) = \bar{\sigma}(\mathbf{M}(j\omega)) \cdot \underbrace{\max_{\Delta(j\omega)} \bar{\sigma}(\Delta(j\omega))}_{=1} \quad \forall \omega \in \mathbb{R} \quad (8.73)$$

By maximizing at each frequency ω both sides of the inequality (8.71) (multiplicative property of a matrix norm)

$$\max_{\Delta(j\omega)} \bar{\sigma}(\mathbf{M}\Delta(j\omega)) \leq \bar{\sigma}(\mathbf{M}(j\omega)) \cdot \max_{\Delta(j\omega)} \bar{\sigma}(\Delta(j\omega)) \quad \forall \omega \in \mathbb{R} \quad (8.74)$$

with respect to a perturbation $\Delta(j\omega)$, which (at each frequency ω) is allowed to be a full complex matrix, it turns out that for any $\mathbf{M}(j\omega)$ at each frequency ω the inequality (8.74) is actually an equality.

In the following, this is proved for a square $\mathbf{M}(j\omega)$ by choosing an allowed $\Delta'(j\omega) = \mathbf{V}\mathbf{U}^H$ ($\bar{\sigma}(\Delta'(j\omega)) = 1 \quad \forall \omega$), where $\mathbf{U}(j\omega)$ and $\mathbf{V}(j\omega)$ are (at each frequency ω) matrices of the left and right singular vectors (singular value decomposition, see Definition A.4) of $\mathbf{M}(j\omega) = \mathbf{U}\Sigma\mathbf{V}^H$ ($\mathbf{V}^H = \mathbf{V}^{-1}$ and $\mathbf{U}^H = \mathbf{U}^{-1}$):

$$\bar{\sigma}(\mathbf{M}\Delta'(j\omega)) = \bar{\sigma}(\mathbf{U}\Sigma\mathbf{V}^H\mathbf{V}\mathbf{U}^H(j\omega)) = \bar{\sigma}(\mathbf{U}\Sigma\mathbf{U}^H(j\omega)) = \bar{\sigma}(\Sigma(j\omega)) = \bar{\sigma}(\mathbf{M}(j\omega)) \quad (8.75)$$

By combining (8.69) and (8.73), the robust stability condition in case of a full complex perturbation matrix $\Delta(s)$ is derived.

Definition 8.5: Robust stability (RS) theorem for full complex (unstructured) perturbations Δ [6]

Assume that the nominal system $\mathbf{M}(s)$ is stable ($\mathbf{N}(s)$ is NS) and that the perturbations $\Delta(s)$ are stable. Then the \mathbf{M} - Δ -structure in Figure 8.13 is stable for all perturbations Δ satisfying $\|\Delta\|_\infty < 1$ (i.e. RS is fulfilled) if and only if

$$\bar{\sigma}(\mathbf{M}(j\omega)) < 1 \quad \forall \omega \in \mathbb{R}, \text{ and NS} \Leftrightarrow \|\mathbf{M}\|_\infty < 1 \text{ and NS} \quad (8.76)$$

Remark: Condition (8.76) for full complex (unstructured) perturbations $\Delta(s)$ (Δ LTI and stable) may be rewritten as

$$\bar{\sigma}(\mathbf{M}(j\omega)) \cdot \bar{\sigma}(\Delta(j\omega)) < 1 \quad \forall \omega \in \mathbb{R}, \forall \Delta. \quad (8.77)$$

In the case of a structured Δ (block-diagonal perturbation matrix $\Delta \in \Delta_B$) the above RS condition (8.76) is often conservative. This motivated the definition of the structured singular value μ .

8.6.8 The structured singular value μ

The structured singular value μ is a concept which provides a generalization of the maximum singular value $\bar{\sigma}$, see [6].

Definition 8.6: Structured Singular Value μ [7, 6]

Consider a system interconnection as in Figure 8.13. The structured singular value μ of the complex-valued matrix $\mathbf{M}(j\omega)$ ($\mathbf{M}(s)$ evaluated at $s = j\omega$) is the real non-negative scalar function

$$\mu_{\Delta}(\mathbf{M}(j\omega)) = \frac{1}{\min_{\Delta \in \Delta_B} \{k_m \mid \det(\mathbf{I} - k_m \mathbf{M}(j\omega) \Delta) = 0\}}, \quad (8.78)$$

where

$$\Delta \in \Delta_B \Leftrightarrow \|\Delta\|_{\infty} \leq 1, \Delta \text{ LTI, structured, and stable} \quad (8.79)$$

is structured in a known block-diagonal real or complex form and at each frequency ω satisfies the norm bound $\bar{\sigma}(\Delta(j\omega)) \leq 1$.

If no such structured $\Delta \in \Delta_B$ exists then $\mu_{\Delta}(\mathbf{M}) = 0$.

The structured singular value μ for complex perturbations is bounded by the spectral radius ρ (see Definition A.8) and the maximum singular value $\bar{\sigma}$: [6]

$$\boxed{\rho(\mathbf{M}) \leq \mu_{\Delta}(\mathbf{M}) \leq \bar{\sigma}(\mathbf{M})} \quad (8.80)$$

The first inequality is an equality if Δ is a complex diagonal matrix with a repeated scalar complex perturbation $\Delta(j\omega)$ ($\Delta = \Delta(j\omega) \cdot \mathbf{I}$). The second inequality is an equality if Δ is a full-block complex perturbation matrix.

8.6.9 Control objectives in robust control with respect to μ

Definition 8.7: Nominal Performance (NP)

The \mathbf{N} - Δ system in Figure 8.11 with $\Delta = \mathbf{0}$ is said to achieve nominal performance (NP) if \mathbf{N} is nominally stable (NS) and if and only if

$$\bar{\sigma}(\mathbf{N}_{22}(j\omega)) < 1 \quad \forall \omega \in \mathbb{R}, \text{ and NS} \Leftrightarrow \|\mathbf{N}_{22}\|_{\infty} < 1 \text{ and NS} \quad (8.81)$$

holds. [7]

In terms of the structured singular value^a μ nominal performance is achieved if \mathbf{N} is nominally stable and if and only if

$$\mu_{\Delta_P}(\mathbf{N}_{22}(j\omega)) < 1, \quad \forall \omega \in \mathbb{R}, \text{ and NS} \quad (8.82)$$

holds. Thereby μ_{Δ_P} is calculated with respect to a full complex^b “artificial” perturbation matrix for performance Δ_P . (for Δ_P see also Definition 8.9)

^aIn practice the SSV is not used for NP analysis, because equation (8.81) is much easier to check than (8.82).

^bIn this case the second inequality in (8.80) is an equality ($\mu_{\Delta_P}(\mathbf{N}_{22}(j\omega)) = \bar{\sigma}(\mathbf{N}_{22}(j\omega))$).

Definition 8.8: Robust Stability (RS)

The stability of the \mathbf{N} - Δ -structure in Figure 8.11 is equivalent to the stability of the \mathbf{M} - Δ -structure in Figure 8.13 with $\mathbf{M} = \mathbf{N}_{11}$ if \mathbf{N} is NS and Δ is stable (see Section. 8.6.7). The uncertain closed-loop system $\mathbf{F} = \mathcal{F}_u(\mathbf{N}, \Delta)$ from \mathbf{w} to \mathbf{z} is stable (robustly stable) for all allowed stable perturbations $\Delta \in \Delta_B$ with $\|\Delta\|_{\infty} \leq 1$, if and only if

$$\mathbf{F} = \mathcal{F}_u(\mathbf{N}, \Delta) \text{ is stable } \forall \Delta \in \Delta_B \text{ with } \|\Delta\|_{\infty} \leq 1, \text{ and NS} \quad (8.83)$$

$$\Leftrightarrow \mu_{\Delta}(\mathbf{M}(j\omega)) < 1, \quad \forall \omega \in \mathbb{R}, \forall \Delta \in \Delta_B \text{ with } \|\Delta\|_{\infty} \leq 1, \text{ and NS} \quad (8.84)$$

Note that Nominal Stability, Internal Stability (NS) is a prerequisite and must be verified separately because the frequency-wise evaluation of μ does not contain this information. [7, 6]

Definition 8.9: Robust Performance (RP)

For the uncertain closed-loop system $\mathbf{F} = \mathcal{F}_u(\mathbf{N}, \mathbf{\Delta})$ robust performance (RP) is achieved with respect to all allowed stable perturbations $\mathbf{\Delta} \in \mathbf{\Delta}_B$ with $\|\mathbf{\Delta}\|_\infty \leq 1$, if and only if

$$\|\mathbf{F}\|_\infty = \|\mathcal{F}_u(\mathbf{N}, \mathbf{\Delta})\|_\infty < 1, \quad \forall \mathbf{\Delta} \in \mathbf{\Delta}_B \text{ with } \|\mathbf{\Delta}\|_\infty \leq 1, \text{ and NS} \quad (8.85)$$

$$\Leftrightarrow \mu_{\hat{\Delta}}(\mathbf{N}(j\omega)) < 1, \quad \forall \omega \in \mathbb{R}, \forall \hat{\Delta} \in \hat{\Delta}_B \text{ with } \|\hat{\Delta}\|_\infty \leq 1, \text{ and NS} \quad (8.86)$$

where

$$\hat{\Delta} = \begin{bmatrix} \mathbf{\Delta} & \mathbf{0} \\ \mathbf{0} & \mathbf{\Delta}_P \end{bmatrix}, \quad (8.87)$$

and $\mathbf{\Delta}_P$ is a full complex “artificial” perturbation matrix for performance^a, a stable LTI system with its actual values unknown, compatible with the dimension of \mathbf{F} in Figure 8.12 and norm-bounded by $\|\mathbf{\Delta}_P\|_\infty \leq 1$, whereas $\mathbf{\Delta}$ represents the “true” uncertainty. [7, 6]

^a $\mathbf{\Delta}_P$ is a full complex “artificial” perturbation matrix stemming from the \mathcal{H}_∞ norm performance specification (this will be shown in Section 8.6.10). [6]

In terms of the \mathbf{N} - $\mathbf{\Delta}$ -structure in Figure (8.11), the requirements for stability and performance with respect to the structured singular value μ can be summarized as follows:

$$\text{NS} \Leftrightarrow \mathbf{N} \text{ (internally) stable} \quad (8.88)$$

$$\text{NP} \Leftrightarrow \bar{\sigma}(\mathbf{N}_{22}(j\omega)) = \mu_{\Delta_P}(\mathbf{N}_{22}(j\omega)) < 1, \quad \forall \omega \in \mathbb{R}, \text{ and NS} \quad (8.89)$$

$$\text{RS} \Leftrightarrow \mu_{\Delta}(\mathbf{N}_{11}(j\omega)) < 1, \quad \forall \omega \in \mathbb{R}, \forall \mathbf{\Delta} \in \mathbf{\Delta}_B, \text{ and NS} \quad (8.90)$$

$$\text{RP} \Leftrightarrow \mu_{\hat{\Delta}}(\mathbf{N}(j\omega)) < 1, \quad \forall \omega \in \mathbb{R}, \forall \hat{\Delta} = \begin{bmatrix} \mathbf{\Delta} & \mathbf{0} \\ \mathbf{0} & \mathbf{\Delta}_P \end{bmatrix} \in \hat{\Delta}_B, \text{ and NS} \quad (8.91)$$

Condition (8.92) implies that, provided NS is satisfied, RS and NP are automatically satisfied if RP is satisfied. The reverse is not true.

$$\underbrace{\mu_{\hat{\Delta}}(\mathbf{N})}_{\text{RP}} \geq \max\{\underbrace{\mu_{\Delta}(\mathbf{N}_{11})}_{\text{RS}}, \underbrace{\mu_{\Delta_P}(\mathbf{N}_{22})}_{\text{NP}}\} \quad (8.92)$$

8.6.10 Block diagram proof of the robust performance (RP) definition with respect to μ

The RP definition with respect to μ (Definition 8.9) is proved by the equivalence between the various block diagrams in Figure 8.14, where **STEP B** is the key step to this proof. This section is based on [6].

- STEP A:** Is the definition of RP.
- STEP B:** The stability of the \mathbf{M} - Δ -structure (i.e. RS) in Figure 8.13, when Δ is a full complex matrix is equivalent to $\|\mathbf{M}\|_\infty < 1$ (see Definition 8.5). Thus the RP condition $\|\mathbf{F}\|_\infty < 1$ is equivalent to RS of the \mathbf{F} - Δ_P -structure, where Δ_P is a full complex matrix.
- STEP C:** Introduce the \mathbf{N} - Δ -structure ($\mathbf{F} = \mathcal{F}_u(\mathbf{N}, \Delta)$) from Figure 8.11.
- STEP D:** Collect Δ and Δ_P into the block-diagonal matrix $\hat{\Delta} = \begin{bmatrix} \Delta & \mathbf{0} \\ \mathbf{0} & \Delta_P \end{bmatrix}$. Thus the original RP problem is equivalent to RS of the \mathbf{N} - $\hat{\Delta}$ -structure, which from Definition 8.8 is equivalent to $\mu_{\hat{\Delta}}(\mathbf{N}(j\omega)) < 1, \forall \omega \in \mathbb{R}, \forall \hat{\Delta} \in \hat{\Delta}_B$.

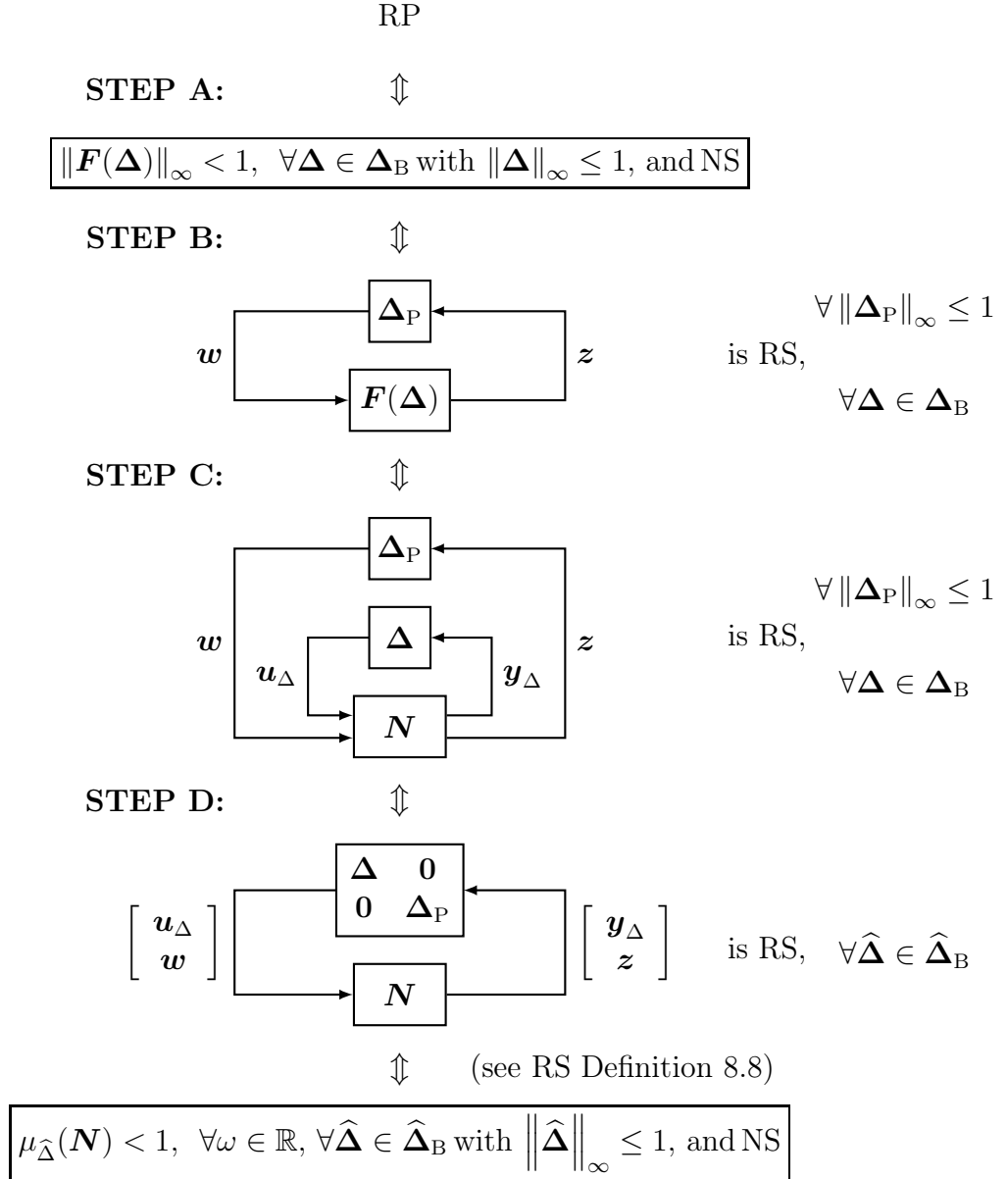


Figure 8.14: RP as a special case of RS with a block-diagonal $\hat{\Delta} = \begin{bmatrix} \Delta & 0 \\ 0 & \Delta_P \end{bmatrix}$. As always NS has to be verified separately! (adopted from [6])

8.6.11 Worst-case gain and skewed- μ value

The RP μ -value, i.e. $\mu_{\hat{\Delta}}(N(j\omega))$ (Definition 8.9) considers that **both** uncertainty blocks, Δ and Δ_P , are scaled by the common factor $k_m = 1/\mu_{\hat{\Delta}}(N(j\omega))$. Thus, if the RP μ -value at a given frequency is different from 1, then the interpretation is that at this frequency the design can tolerate up to $1/\mu_{\hat{\Delta}}(N(j\omega))$ -times the modelled uncertainty and satisfy the performance objective with a margin of $1/\mu_{\hat{\Delta}}(N(j\omega))$. [6] Consequently $\mu_{\hat{\Delta}}(N(j\omega))$ does not, as one might expect, state the worst-case gain, i.e. $\max_{\Delta \in \Delta_B} \bar{\sigma}(F(\Delta(j\omega)))$, of the uncertain closed-loop system $F = \mathcal{F}_u(N, \Delta)$ (Figure 8.12) in the presence of the uncertainty Δ .

To find the worst-case gain for a given uncertainty, the uncertainty Δ has to be left unscaled. This onset is denoted skewed- μ analysis.

Definition 8.10: Skewed- μ [6, 7]

The skewed- μ value of a complex transfer matrix $N(j\omega)$ is defined as

$$\mu_{\hat{\Delta}}^s(N(j\omega)) = \frac{1}{\min_{\hat{\Delta} \in \hat{\Delta}_B} \{k_m | \det(\mathbf{I} - \mathbf{K}_m N(j\omega) \hat{\Delta}) = 0\}} \quad (8.93)$$

where $\hat{\Delta} = \begin{bmatrix} \Delta & \mathbf{0} \\ \mathbf{0} & \Delta_P \end{bmatrix}$, $\mathbf{K}_m = \begin{bmatrix} \mathbf{I} & \mathbf{0} \\ \mathbf{0} & k_m \mathbf{I} \end{bmatrix}$ is partitioned compatibly to $\hat{\Delta}$, so that only Δ_P is scaled.

It turns out that μ^s is always farther from 1 than μ , i.e. $\mu^s \geq \mu$ for $\mu > 1$, $\mu^s = \mu$ for $\mu = 1$ and $\mu^s \leq \mu$ for $\mu < 1$.

The value of μ^s can be interpreted as the worst-case gain, i.e. $\max_{\Delta \in \Delta_B} \bar{\sigma}(\mathcal{F}_u(N, \Delta)(j\omega)) = \mu_{\hat{\Delta}}^s(N(j\omega))$.

8.6.12 DK-iteration

Currently there is no direct method to synthesize a μ -optimal controller, that minimizes a given μ -condition for a general uncertainty structure.

Nevertheless, in most cases good results are attained by splitting the μ -synthesis problem into the two subproblems μ -analysis and \mathcal{H}_∞ controller synthesis, which are solved in an alternating, iterative fashion. [7] For problems with only complex perturbations an algorithm named DK-iteration is available. Its extension, called DGK-iteration (also referred to as mixed- μ -synthesis) addresses problems with mixed (i.e., real and complex) structured perturbations. [7] The basic structure of the DK-iteration algorithm is outlined in the following.

For complex perturbations, an upper bound on μ is given in terms of the scaled singular value

$$\mu_{\hat{\Delta}}(N(j\omega)) \leq \min_{D(j\omega) \in \mathcal{D}} \bar{\sigma}(D(j\omega)N(j\omega)D^{-1}(j\omega)), \quad (8.94)$$

where (assuming $\hat{\Delta}$ square) $\mathcal{D} = \{D : D\hat{\Delta} = \hat{\Delta}D\}$ is the set of all matrices that commute with the enlarged perturbation $\hat{\Delta} = \begin{bmatrix} \Delta & \mathbf{0} \\ \mathbf{0} & \Delta_P \end{bmatrix}$. The structures of $\hat{\Delta}$ and D are “opposites” (e.g. $\hat{\Delta} = \text{diag}\{\Delta_1(\text{full}), \Delta_2\mathbf{I}, \Delta_3, \Delta_4, \Delta_P\} : D = \text{diag}\{d_1\mathbf{I}, D_2(\text{full}), d_3, d_4, d_P\mathbf{I}\}$). [6] For non-square uncertainties $\hat{\Delta}$ the scaling matrices $D_l^{-1}(s)$ and $D_r(s)$ (left and right of N , see Figure 8.15) have to be used instead of $D^{-1}(s)$ and $D(s)$ (i.e. $\mathcal{D} = \{D : D_l\hat{\Delta} = \hat{\Delta}D_r\}$). [12] For simplicity $\hat{\Delta}$ is assumed square in the following.

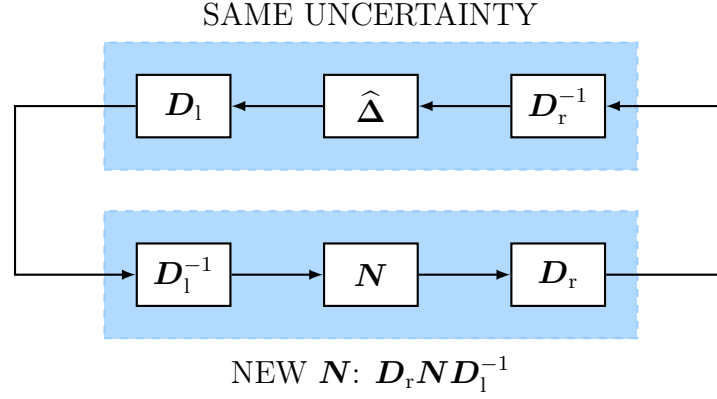


Figure 8.15: Use of block-diagonal scalings, $\hat{\Delta} = D_1 \hat{\Delta} D_r^{-1}$ (adopted from [6])

The basic idea of DK-iteration is to find the controller \mathbf{K} that minimizes the peak of this upper bound on μ (8.94) over all frequencies by alternately optimizing over the set of stabilizing \mathcal{H}_∞ sub-optimal controllers $\mathbf{K}(s)$ and over the set of (approximated dynamic) scalings $\mathbf{D}(s)$, expressed as: [7]

$$\min_{\mathbf{K}} \min_{\mathbf{D}(s) \in \mathcal{D}(s)} \|\mathbf{D} \mathbf{N} \mathbf{D}^{-1}\|_\infty$$

The DK-iteration algorithm proceeds as follows [7, 6]:

1. Initialize scalings $\mathbf{D}(s)$, typically with the identity \mathbf{I} (provided that the problem is reasonably scaled)
2. K-step: Synthesize an internally stabilizing controller $\mathbf{K}(s)$ for the scaled plant, by solving the \mathcal{H}_∞ (sub-)optimal controller design problem $\min_{\mathbf{K}} \|\mathbf{D} \mathbf{N}(\mathbf{K}) \mathbf{D}^{-1}\|_\infty$ with fixed $\mathbf{D}(s)$.
3. D-step: Find $\tilde{\mathbf{D}}(j\omega)$ that minimizes $\bar{\sigma}(\tilde{\mathbf{D}}(j\omega) \mathbf{N}(j\omega) \tilde{\mathbf{D}}^{-1}(j\omega))$ at each frequency in a predefined frequency gridding, where $\mathbf{N} = \mathcal{F}_l(\mathbf{P}, \mathbf{K})$ is kept fixed. If μ -based termination criterion is fulfilled, stop.
4. Approximate the magnitude of each element in $\tilde{\mathbf{D}}(j\omega)$ by a stable and minimum-phase transfer function to obtain the dynamic scaling transfer function matrix $\mathbf{D}(s)$ and go to step 2.

One fundamental problem of DK iteration is that the combined optimization problem is not guaranteed to be convex, although each of its minimization steps (K-step and D-step) are convex. As a consequence, the iterations may not converge to a unique global optimum but to one of potentially many local optima. Also convergence is not guaranteed, hence an actual increase in the μ value from one iteration to the next can occur. [7, 6] Another disadvantage is the possibly high system order of the resulting controller \mathbf{K} . Since the \mathcal{H}_∞ controller is designed upon the dynamically scaled plant

$$\check{\mathbf{P}}(s) = \underbrace{\begin{bmatrix} \mathbf{D}_r(s) & \mathbf{0} \\ \mathbf{0} & \mathbf{I}_{[m \times m]} \end{bmatrix}}_{\check{\mathbf{D}}_r(s)} \mathbf{P}(s) \underbrace{\begin{bmatrix} \mathbf{D}_1^{-1}(s) & \mathbf{0} \\ \mathbf{0} & \mathbf{I}_{[r \times r]} \end{bmatrix}}_{\check{\mathbf{D}}_1(s)} \quad (8.95)$$

(where $\mathbf{I}_{[m \times m]}$ is associated with the inputs and $\mathbf{I}_{[r \times r]}$ is associated with the outputs of the controller \mathbf{K}), its order is $n_K = n_P + n_{\check{D}_r} + n_{\check{D}_l}$ where n_P is the order of the augmented plant (that is, the order of the plant and the order of all dynamic weightings in the augmented plant interconnection \mathbf{P}) and $n_{\check{D}_r}$, $n_{\check{D}_l}$ are the dynamic orders of the scaling transfer function $\check{\mathbf{D}}_r(s)$ respectively $\check{\mathbf{D}}_l(s)$. Therefore, a subsequent order reduction of the synthesized controller might be necessary before implementation in a real time environment is feasible.

Nevertheless, DK-iteration is usually a well-performing algorithm if the problem is carefully formulated and well-scaled. [7]

8.7 DK-synthesized μ -“optimal” Controller Design

In Figure 8.16 a system with multiplicative input uncertainty, additive uncertainty, and multiplicative output uncertainty is depicted, where $\mathbf{G}(s)$ ($m \times r$) is the nominal plant model. For this case, the set of possible perturbed plants $\mathbf{G}_p(s)$ ($m \times r$) is defined by

$$\mathbf{G}_p = (\mathbf{I} + \mathbf{W}_{2O}\Delta_O\mathbf{W}_{1O})(\mathbf{G} + \mathbf{W}_{2A}\Delta_A\mathbf{W}_{1A})(\mathbf{I} + \mathbf{W}_{2I}\Delta_I\mathbf{W}_{1I}) \quad (8.96)$$

where $\Delta_I(s)$ ($r \times r$) and $\Delta_O(s)$ ($m \times m$) are considered as unknown but norm-bounded ($\|\Delta_I\|_\infty \leq 1$ and $\|\Delta_O\|_\infty \leq 1$) complex diagonal matrices, whereas $\Delta_A(s)$ ($m \times r$) is contemplated as an unknown but norm-bounded ($\|\Delta_A\|_\infty \leq 1$) full complex matrix.

$$\Delta_I(s) = \text{diag}\{\Delta_{I1}(s), \dots, \Delta_{Ij}(s), \dots, \Delta_{Ir}(s)\}, \quad |\Delta_{Ij}(j\omega)| \leq 1 \quad \forall \omega, \forall j \quad (8.97)$$

$$\Delta_O(s) = \text{diag}\{\Delta_{O1}(s), \dots, \Delta_{Oi}(s), \dots, \Delta_{Om}(s)\}, \quad |\Delta_{Oi}(j\omega)| \leq 1 \quad \forall \omega, \forall i \quad (8.98)$$

$$\Delta_A(s) = \begin{bmatrix} \Delta_{A11}(s) & \Delta_{A12}(s) & \dots & \Delta_{A1r}(s) \\ \Delta_{A21}(s) & \Delta_{A22}(s) & \dots & \Delta_{A2r}(s) \\ \vdots & \vdots & \ddots & \vdots \\ \Delta_{Am1}(s) & \Delta_{Am2}(s) & \dots & \Delta_{Amr}(s) \end{bmatrix} \quad (8.99)$$

In the case at hand, the overall, block-diagonal, norm-bounded perturbation matrix used to represent the uncertainty in terms of the \mathbf{P} - \mathbf{K} - Δ - and \mathbf{N} - Δ -structure is

$$\Delta = \begin{bmatrix} \Delta_I & \mathbf{0} & \mathbf{0} \\ \mathbf{0} & \Delta_A & \mathbf{0} \\ \mathbf{0} & \mathbf{0} & \Delta_O \end{bmatrix}, \quad \|\Delta\|_\infty \leq 1 \quad (8.100)$$

Performance is measured in terms of the frequency-weighted error signal

$$\mathbf{z}_1(s) = \mathbf{W}_P(s)(\mathbf{y}(s) - \mathbf{r}(s)). \quad (8.101)$$

By choosing

$$\mathbf{z}_2(s) = \mathbf{W}_u(s)\mathbf{u}(s) \quad (8.102)$$

control energy is directly limited by the design. The exogenous inputs are the disturbance $\mathbf{w}_1 = \mathbf{d}$ (in this work $w_1 = d$ is scalar), the reference commands $\mathbf{w}_2 = \mathbf{r}$ (in this work $\mathbf{r} = \mathbf{0}$) and the measurement noise $\mathbf{w}_3 = \mathbf{n}$.

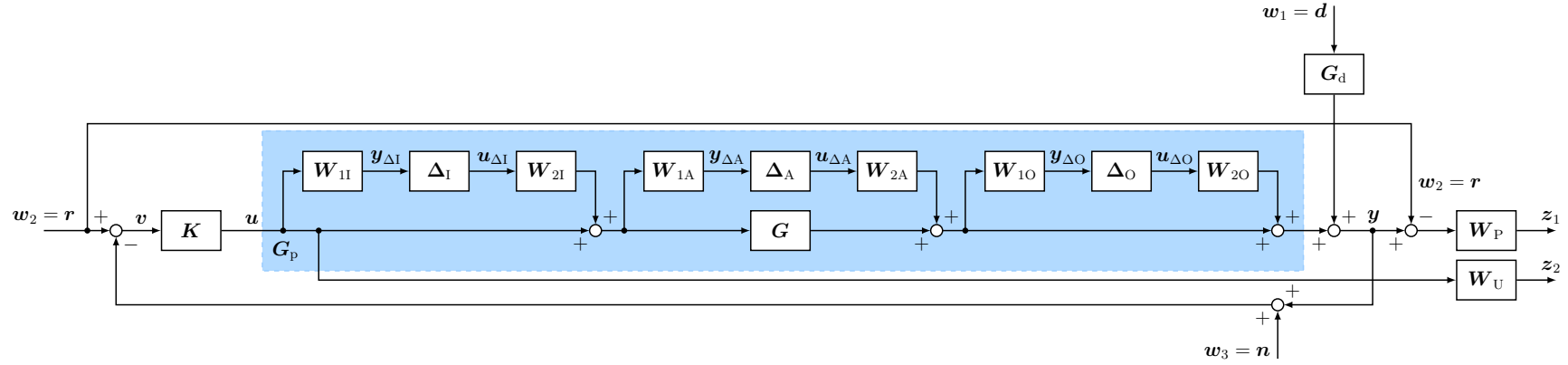


Figure 8.16: Augmented plant interconnection with with multiplicative input uncertainty, additive uncertainty, and multiplicative output uncertainty

$$\begin{bmatrix} y_{\Delta I} \\ y_{\Delta A} \\ y_{\Delta O} \\ z_1 \\ z_2 \\ v \end{bmatrix} = \underbrace{\begin{bmatrix} 0 & 0 & 0 & 0 & 0 & 0 & W_{1I} \\ W_{1A}W_{2I} & 0 & 0 & 0 & 0 & 0 & W_{1A} \\ W_{1O}GW_{2I} & W_{1O}W_{2A} & 0 & 0 & 0 & 0 & W_{1O}G \\ W_PGW_{2I} & W_PW_{2A} & W_PW_{2O} & W_PG_d & -W_P & 0 & W_PG \\ 0 & 0 & 0 & 0 & 0 & 0 & W_U \\ -GW_{2I} & -W_{2A} & -W_{2O} & -G_d & I & -I & -G \end{bmatrix}}_P \begin{bmatrix} u_{\Delta I} \\ u_{\Delta A} \\ u_{\Delta O} \\ w_1 \\ w_2 \\ w_3 \\ u \end{bmatrix} \quad (8.103)$$

$$\begin{bmatrix} y_{\Delta I} \\ y_{\Delta A} \\ y_{\Delta O} \\ z_1 \\ z_2 \end{bmatrix} = \underbrace{\begin{bmatrix} -W_{1I}KSGW_{2I} & -W_{1I}KSW_{2A} & -W_{1I}KSW_{2O} & -W_{1I}KSG_d & W_{1I}KS & -W_{1I}KS \\ W_{1A}S_1W_{2I} & -W_{1A}KSW_{2A} & -W_{1A}KSW_{2O} & -W_{1A}KSG_d & W_{1A}KS & -W_{1A}KS \\ W_{1O}SGW_{2I} & W_{1O}SW_{2A} & -W_{1O}TW_{2O} & -W_{1O}TG_d & W_{1O}T & -W_{1O}T \\ W_PSGW_{2I} & W_PSW_{2A} & W_PSW_{2O} & W_PSG_d & -W_PS & -W_PT \\ -W_UKSGW_{2I} & -W_UKSW_{2A} & -W_UKSW_{2O} & -W_UKSG_d & W_UKS & -W_UKS \end{bmatrix}}_N \begin{bmatrix} u_{\Delta I} \\ u_{\Delta A} \\ u_{\Delta O} \\ w_1 \\ w_2 \\ w_3 \end{bmatrix} \quad (8.104)$$

The generalized plant \mathbf{P} for this control configuration is given in equation (8.103). The nominal closed loop system \mathbf{N} is given in equation (8.104)

The uncertain closed-loop transfer function matrix \mathbf{F} from \mathbf{w} to \mathbf{z} is

$$\begin{bmatrix} z_1 \\ z_2 \end{bmatrix} = \underbrace{\begin{bmatrix} \mathbf{W}_P \mathbf{S}_p \mathbf{G}_d & -\mathbf{W}_P \mathbf{S}_p & -\mathbf{W}_P \mathbf{T}_p \\ -\mathbf{W}_U \mathbf{K} \mathbf{S}_p \mathbf{G}_d & \mathbf{W}_U \mathbf{K} \mathbf{S}_p & -\mathbf{W}_U \mathbf{K} \mathbf{S}_p \end{bmatrix}}_{\mathbf{F}} \begin{bmatrix} w_1 \\ w_2 \\ w_3 \end{bmatrix} \quad (8.105)$$

where

$$\mathbf{S}_p = (\mathbf{I} + \mathbf{G}_p \mathbf{K})^{-1} \quad (8.106)$$

is the perturbed sensitivity function and

$$\mathbf{T}_p = \mathbf{I} - \mathbf{S}_p = \mathbf{G}_p \mathbf{K} \mathbf{S}_p \quad (8.107)$$

is the perturbed complementary sensitivity function.

Because the numerous cost functions included in \mathbf{F} increase the complexity of achieving robust performance (see Definition 8.9), in this work only $w_1 = d$ was considered as exogenous input. The columns associated with w_2 and w_3 in \mathbf{P} , \mathbf{N} and \mathbf{F} were removed.¹³ In MATLAB[®] also the possibility to use extra measurements (e.g. acceleration and force measurements), which are fed back to the (feedback) controller \mathbf{K} , but are not considered as outputs to be controlled, was implemented. However, this was not used.

¹³It should be pointed out that when it comes to the implementation in MATLAB[®] canceling of columns associated with inputs (or rows associated with outputs) of a state-space model, does not effect the state matrix \mathbf{A} and thus leaves it (\mathbf{A}) unnecessarily large, which slows down the algorithms used for controller synthesis. The MATLAB[®] command `sminreal`, which eliminates the states of state-space models that do not affect the input/output response, can solve this problem. In order to avoid this problem at the outset and decrease interconnection complexity, the MATLAB[®] command `sysic` was found helpful.

8.8 \mathcal{H}_∞ Loop-Shaping Design Considering Coprime Factor Uncertainty

The intention of \mathcal{H}_∞ loop-shaping is to apply the classical loop-shaping ideas of feedback control for SISO plants - shaping the open-loop SISO transfer function $L = GK$ to attain the desired closed-loop characteristics - on MIMO plants. In principle \mathcal{H}_∞ loop-shaping is a two-stage design process: [6]

- First, the open-loop plant $\mathbf{G}(s)$ is augmented by pre- and post-compensators $\mathbf{W}_1(s)$ and $\mathbf{W}_2(s)$ to give a desired shape to the singular values of the so-called shaped plant (or initial/desired loop-shape) $\mathbf{G}_s = \mathbf{W}_2 \mathbf{G} \mathbf{W}_1$.
- Then this resulting shaped plant \mathbf{G}_s is robustly stabilized (“robustified”) with respect to the general class of normalized coprime factor uncertainty¹⁴ using \mathcal{H}_∞ optimization.

This section is based on the textbook [6], where further information can be found.

8.8.1 Applying the ideas of classical loop shaping to multivariable systems

In classical loop shaping, it is the magnitude of the open-loop transfer function $L = GK$ which is shaped, whereas for multivariable systems the requirements are usually all postulated in terms of closed-loop transfer functions, which to a certain degree can be obtained by an investigation of (A.7) and (A.8). In the following it is shown how closed-loop equivalent open-loop requirements can be obtained.

The underlying equations justifying this approach arise from the inequality

$$\underline{\sigma}(\mathbf{L}(j\omega)) - 1 \leq \frac{1}{\bar{\sigma}(\mathbf{S}(j\omega))} \leq \underline{\sigma}(\mathbf{L}(j\omega)) + 1 \quad (8.108)$$

for which if $\underline{\sigma}(\mathbf{L}(j\omega)) \gg 1$ the following holds

$$\bar{\sigma}(\mathbf{S}(j\omega)) \approx \frac{1}{\underline{\sigma}(\mathbf{L}(j\omega))} \quad \text{if } \underline{\sigma}(\mathbf{L}(j\omega)) \gg 1 \quad (8.109)$$

and from the fact that if $\bar{\sigma}(\mathbf{L}(j\omega)) \ll 1$, the maximum singular value of the complementary sensitivity function

$$\mathbf{T} = \mathbf{L}(\mathbf{I} - \mathbf{L})^{-1} \quad (8.110)$$

(positive feedback control system) can be approximated by

$$\bar{\sigma}(\mathbf{T}(j\omega)) \approx \bar{\sigma}(\mathbf{L}(j\omega)) \quad \text{if } \bar{\sigma}(\mathbf{L}(j\omega)) \ll 1. \quad (8.111)$$

Thus, utilizing (8.109) and (8.111), it is relatively easy to approximate closed-loop requirements by open-loop objectives over a specified frequency range (Table 8.1):

¹⁴For SISO systems the classical gain and phase margins provide useful general robustness measures. However, for multivariable systems, classical gain and phase margins are unreliable indicators of RS when defined for each channel (or loop), taken one at a time, because simultaneous perturbations in more than one loop are not catered for. [6] For MIMO systems, normalized coprime factor uncertainty (which allows for zeros and poles to cross into the RHP) provides a useful general class of uncertainty. [6]

control objective	typical frequency range	closed-loop requirement	open-loop requirement
disturbance rejection	ω low $\omega \leq \omega_1 \leq \omega_B$	$\bar{\sigma}(\mathbf{S}(j\omega))$ small	$\underline{\sigma}(\mathbf{L}(j\omega))$ large; valid if $\underline{\sigma}(\mathbf{L}(j\omega)) \gg 1$
reference tracking	ω low $\omega \leq \omega_1 \leq \omega_B$	$\bar{\sigma}(\mathbf{T}(j\omega)) \approx \underline{\sigma}(\mathbf{T}(j\omega)) \approx 1$	$\underline{\sigma}(\mathbf{L}(j\omega))$ large; valid if $\underline{\sigma}(\mathbf{L}(j\omega)) \gg 1$
noise attenuation	ω high $\omega_B \leq \omega_h \leq \omega$	$\bar{\sigma}(\mathbf{T}(j\omega))$ small	$\bar{\sigma}(\mathbf{L}(j\omega))$ small; valid if $\bar{\sigma}(\mathbf{L}(j\omega)) \ll 1$
input usage (control energy) reduction	ω high $\omega_B \leq \omega_h \leq \omega$	$\bar{\sigma}(\mathbf{KS}(j\omega))$ small	$\bar{\sigma}(\mathbf{K}(j\omega))$ small; valid if $\bar{\sigma}(\mathbf{L}(j\omega)) \ll 1$
robust stability to an additive perturbation	ω high $\omega_B \leq \omega_h \leq \omega$	$\bar{\sigma}(\mathbf{KS}(j\omega))$ small	$\bar{\sigma}(\mathbf{K}(j\omega))$ small; valid if $\bar{\sigma}(\mathbf{L}(j\omega)) \ll 1$
robust stability to a multiplicative output perturbation	ω high $\omega_B \leq \omega_h \leq \omega$	$\bar{\sigma}(\mathbf{T}(j\omega))$ small	$\bar{\sigma}(\mathbf{L}(j\omega))$ small; valid if $\bar{\sigma}(\mathbf{L}(j\omega)) \ll 1$

Table 8.1: Closed-loop equivalent open-loop requirements (in addition to the requirement that \mathbf{K} stabilizes \mathbf{G}) [6], ω_B is the bandwidth frequency ($\bar{\sigma}(\mathbf{S}(j\omega_B)) = \frac{1}{\sqrt{2}}$)

At a given frequency ω , the requirements in Table 8.1 cannot be all satisfied simultaneously. Feedback design is therefore a trade-off over frequency of conflicting objectives. [6] In terms of the open-loop requirements of Table 8.1, this is summarized graphically in Figure 8.17.

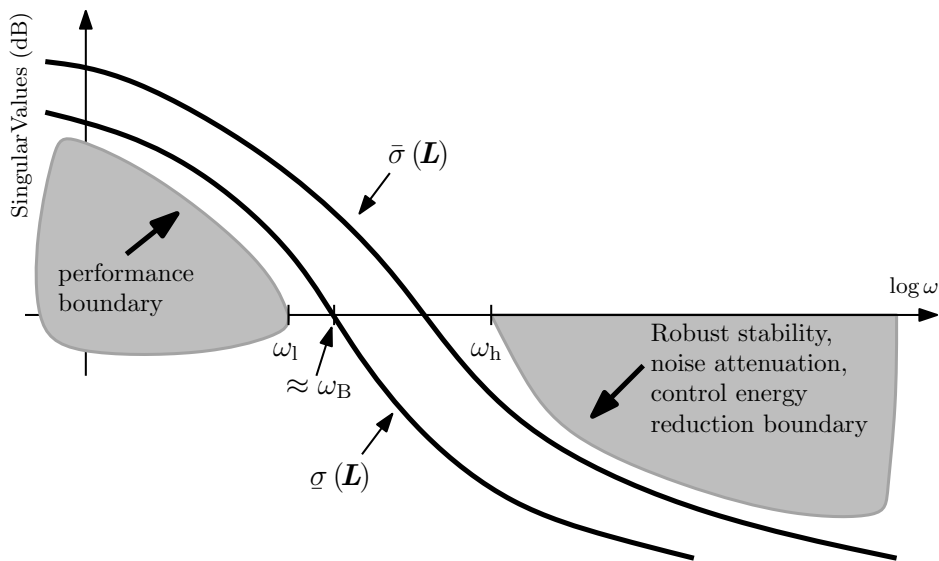


Figure 8.17: Design trade-offs for the multivariable loop transfer function $\mathbf{L} = \mathbf{G}\mathbf{K}$ (adopted from [6])

8.8.2 Robust stabilization with respect to coprime factor uncertainty

Figure 8.18 shows the perturbed (positive) feedback system in terms of so-called coprime factor uncertainty, which shall be robustly stabilized. The coprime factor uncertainty description for the set of perturbed plants \mathbf{G}_p is

$$\mathbf{G}_p = (\mathbf{M}_1 + \Delta_M)^{-1}(\mathbf{N}_1 + \Delta_N), \quad \left\| \begin{bmatrix} \Delta_N & \Delta_M \end{bmatrix} \right\|_\infty < \epsilon \quad (8.112)$$

where $\mathbf{G} = \mathbf{M}_1^{-1}\mathbf{N}_1$ is the normalized left coprime factorization of the nominal plant \mathbf{G} . The stable unknown transfer functions Δ_M and Δ_N represent the uncertainty and $\epsilon > 0$ is the stability margin. This uncertainty description allows for zeros and poles to cross into the RHP while being comprised of stable components $\mathbf{M}_1(s)$, $\mathbf{N}_1(s)$, $\Delta_M(s)$ and $\Delta_N(s)$. [6]

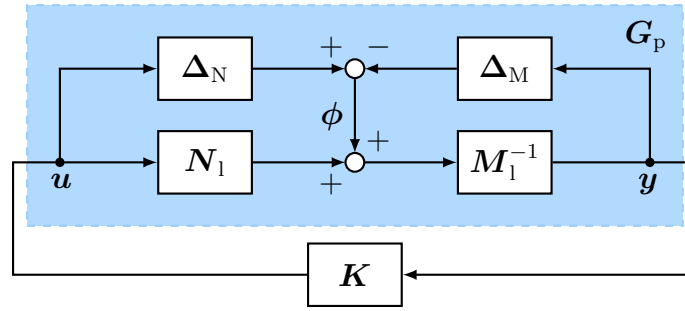


Figure 8.18: \mathcal{H}_∞ robust stabilization problem for coprime factor uncertainty

Arranging the block diagram of Figure 8.18 into the \mathbf{M} - Δ -structure for robust stability analysis (see Figure 8.13 on page 100), where in this case \mathbf{M} is the transfer function matrix from ϕ to $\begin{bmatrix} u \\ y \end{bmatrix}$ yields:

$$\Delta = \begin{bmatrix} \Delta_N & \Delta_M \end{bmatrix} \quad \text{and} \quad \mathbf{M} = \begin{bmatrix} \mathbf{K} \\ \mathbf{I} \end{bmatrix} (\mathbf{I} - \mathbf{G}\mathbf{K})^{-1} \mathbf{M}_1^{-1} \quad (8.113)$$

Note that because the output vectors of the uncertainty blocks Δ_N and Δ_M enter at the same location in the block diagram, the perturbations can be stacked side by side forming an overall full complex perturbation matrix Δ .

Consequently (see (8.77)) the perturbed (positive) feedback system of Figure 8.18 is robustly stable (RS) for all stable perturbations Δ_N and Δ_M satisfying $\left\| \begin{bmatrix} \Delta_N & \Delta_M \end{bmatrix} \right\|_\infty < \epsilon$ if and only if the nominal feedback system is stable (NS) and

$$\gamma_K \triangleq \underbrace{\left\| \begin{bmatrix} \mathbf{K} \\ \mathbf{I} \end{bmatrix} (\mathbf{I} - \mathbf{G}\mathbf{K})^{-1} \mathbf{M}_1^{-1} \right\|_\infty}_{\|\mathbf{M}\|_\infty} \leq \frac{1}{\epsilon} = \gamma. \quad (8.114)$$

As stated by Glover and McFarlane [16] the lowest achievable value of γ_K denoted as γ_{\min} corresponding to the maximum stability margin ϵ_{\max} is given by equation (8.115), where $\|\cdot\|_H$ denotes the Hankel-norm and ρ is the spectral radius.

$$\gamma_{\min} = \frac{1}{\epsilon_{\max}} = \left\{ 1 - \left\| \begin{bmatrix} \mathbf{N}_1 & \mathbf{M}_1 \end{bmatrix} \right\|_H^2 \right\}^{-\frac{1}{2}} = (1 + \rho(\mathbf{X}\mathbf{Z}))^{\frac{1}{2}} \quad (8.115)$$

For a minimal state-space realization of $\mathbf{G} \stackrel{ss}{=} \left[\begin{array}{c|c} \mathbf{A} & \mathbf{B} \\ \hline \mathbf{C} & \mathbf{D} \end{array} \right]$, $\mathbf{Z} > 0$ (\mathbf{Z} positive definite) is the unique solution to the algebraic Riccati equation (8.116)

$$(\mathbf{A} - \mathbf{B}\mathbf{S}^{-1}\mathbf{D}^T\mathbf{C})\mathbf{Z} + \mathbf{Z}(\mathbf{A} - \mathbf{B}\mathbf{S}^{-1}\mathbf{D}^T\mathbf{C})^T - \mathbf{Z}\mathbf{C}^T\mathbf{R}^{-1}\mathbf{C}\mathbf{Z} + \mathbf{B}\mathbf{S}^{-1}\mathbf{B}^T = \mathbf{0} \quad (8.116)$$

where

$$\mathbf{R} = \mathbf{I} + \mathbf{D}\mathbf{D}^T \quad (8.117)$$

$$\mathbf{S} = \mathbf{I} + \mathbf{D}^T\mathbf{D} \quad (8.118)$$

and $\mathbf{X} > 0$ (\mathbf{X} positive definite) is the unique solution to the algebraic Riccati equation (8.119).

$$(\mathbf{A} - \mathbf{B}\mathbf{S}^{-1}\mathbf{D}^T\mathbf{C})^T\mathbf{X} + \mathbf{X}(\mathbf{A} - \mathbf{B}\mathbf{S}^{-1}\mathbf{D}^T\mathbf{C}) - \mathbf{X}\mathbf{B}\mathbf{S}^{-1}\mathbf{B}^T\mathbf{X} + \mathbf{C}^T\mathbf{R}^{-1}\mathbf{C} = \mathbf{0} \quad (8.119)$$

By solving the two Riccati equations (8.116) and (8.119) it is possible to calculate the exact γ_{\min} directly from (8.115) and hence avoid the γ -iteration needed to solve the general \mathcal{H}_∞ problem. [6]

A controller which guarantees for a certain $\gamma > \gamma_{\min}$ that

$$\left\| \left[\begin{array}{c} \mathbf{K} \\ \mathbf{I} \end{array} \right] (\mathbf{I} - \mathbf{G}\mathbf{K})^{-1}\mathbf{M}_1^{-1} \right\|_\infty \leq \gamma \quad (8.120)$$

is given by the following state-space realization:

$$\begin{aligned} \mathbf{K} &\stackrel{ss}{=} \left[\begin{array}{c|c} \mathbf{A}_K & \mathbf{B}_K \\ \hline \mathbf{C}_K & \mathbf{D}_K \end{array} \right] \\ &= \left[\begin{array}{c|c} \mathbf{A} + \mathbf{B}\mathbf{F} + \gamma^2(\mathbf{L}^T)^{-1}\mathbf{Z}\mathbf{C}^T(\mathbf{C} + \mathbf{D}\mathbf{F}) & \gamma^2(\mathbf{L}^T)^{-1}\mathbf{Z}\mathbf{C}^T \\ \hline \mathbf{B}^T\mathbf{X} & -\mathbf{D}^T \end{array} \right] \end{aligned} \quad (8.121)$$

$$\mathbf{F} = -\mathbf{S}^{-1}(\mathbf{D}^T\mathbf{C} + \mathbf{B}^T\mathbf{X}) \quad (8.122)$$

$$\mathbf{L} = (1 - \gamma^2)\mathbf{I} + \mathbf{X}\mathbf{Z} \quad (8.123)$$

8.8.3 Regarding performance requirements in the design

To meet the performance specifications, McFarlane and Glover suggested to pre- and post-multiply the plant $\mathbf{G}(s)$ by two weighting matrices (compensators) $\mathbf{W}_1(s)$ and $\mathbf{W}_2(s)$ (8.124) to shape the open-loop singular values (Figure 8.19) prior to robust stabilization of the “shaped” plant $\mathbf{G}_s(s)$. [6]

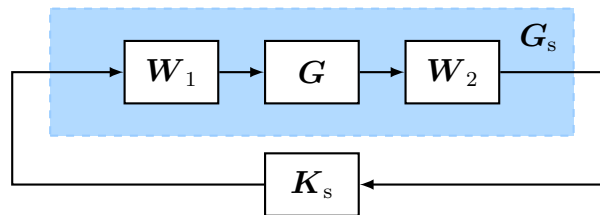


Figure 8.19: The shaped plant and controller

Then this shaped plant

$$\mathbf{G}_s(s) = \mathbf{W}_2(s)\mathbf{G}(s)\mathbf{W}_1(s) \quad (8.124)$$

with state-space representation

$$\mathbf{G}_s \stackrel{ss}{=} \left[\begin{array}{c|c} \mathbf{A}_s & \mathbf{B}_s \\ \hline \mathbf{C}_s & \mathbf{D}_s \end{array} \right] \quad (8.125)$$

is robustly stabilized by the feedback controller \mathbf{K}_s using equations (8.112) to (8.123), where $\mathbf{G}_s = \mathbf{M}_{ls}^{-1}\mathbf{N}_{ls}$ is the normalized left coprime factorization of the shaped plant. The feedback controller for the plant \mathbf{G} is then $\mathbf{K} = \mathbf{W}_1\mathbf{K}_s\mathbf{W}_2$. [6]

It is desirable to achieve γ_{\min} ($\gamma_{\min} \geq 1$) as small as possible, where the usual requirement is $\gamma_{\min} < 4$, corresponding to at least 25% allowed coprime uncertainty ($\epsilon_{\max} = \frac{1}{\gamma_{\min}}$).

If γ is sufficiently small then the following holds: [16]

- At frequencies where $\underline{\sigma}(\mathbf{G}_s)$ is sufficiently large, also (as desired) $\underline{\sigma}(\mathbf{L})$ will be large.
- At frequencies where $\bar{\sigma}(\mathbf{G}_s)$ is sufficiently small, also (as desired) $\bar{\sigma}(\mathbf{L})$ will be small.

8.8.4 Deriving a reasonable weight (compensator) $\mathbf{W}_1(s)$ for shaping the open-loop plant

When the control objective is disturbance rejection, in a closed-loop shaping approach (see Section 8.5) the \mathcal{H}_∞ norm of $\mathbf{S}\mathbf{G}_d$ (usually weighted and combined in a stack together with other closed loop functions) is bounded by

$$\|\mathbf{S}\mathbf{G}_d\|_\infty < 1 \Leftrightarrow \bar{\sigma}(\mathbf{S}\mathbf{G}_d(j\omega)) < 1 \quad \forall \omega \in \mathbb{R}. \quad (8.126)$$

Now it is shown that at frequencies ω where $\underline{\sigma}(\mathbf{L}(j\omega)) \approx \underline{\sigma}(\mathbf{G}_s(j\omega))$ and $\underline{\sigma}(\mathbf{L}(j\omega)) \gg 1$ hold, the postulation (\dagger denotes the pseudo-inverse, see Section A.5)

$$\bar{\sigma}(\mathbf{W}_1^\dagger(j\omega)) \cdot \bar{\sigma}(\mathbf{G}^\dagger(j\omega)) \cdot \bar{\sigma}(\mathbf{W}_2^\dagger(j\omega)) \cdot \bar{\sigma}(\mathbf{G}_d(j\omega)) < 1 \quad (8.127)$$

because of the multiplicative matrix norm property (see A.29) implies $\bar{\sigma}(\mathbf{S}\mathbf{G}_d(j\omega)) < 1$:

$$1 > \bar{\sigma}(\mathbf{W}_1^\dagger(j\omega)) \cdot \bar{\sigma}(\mathbf{G}^\dagger(j\omega)) \cdot \bar{\sigma}(\mathbf{W}_2^\dagger(j\omega)) \cdot \bar{\sigma}(\mathbf{G}_d(j\omega)) \geq \underbrace{\bar{\sigma}(\mathbf{W}_1^\dagger \mathbf{G}^\dagger \mathbf{W}_2^\dagger(j\omega))}_{\bar{\sigma}(\mathbf{G}_s^\dagger(j\omega))} \cdot \bar{\sigma}(\mathbf{G}_d(j\omega)) \quad (8.128)$$

$$1 > \bar{\sigma}(\mathbf{G}_s^\dagger(j\omega)) \cdot \bar{\sigma}(\mathbf{G}_d(j\omega)) = \frac{1}{\underline{\sigma}(\mathbf{G}_s(j\omega))} \cdot \bar{\sigma}(\mathbf{G}_d(j\omega)) \quad (8.129)$$

Considering the loop transfer function \mathbf{L} instead of the desired loop shape or shaped plant $\mathbf{G}_s(s) = \mathbf{W}_2(s)\mathbf{G}(s)\mathbf{W}_1(s)$ in (8.129) yields:¹⁵

$$1 > \frac{1}{\underline{\sigma}(\mathbf{L}(j\omega))} \cdot \bar{\sigma}(\mathbf{G}_d(j\omega)) \stackrel{(8.109)}{\approx} \bar{\sigma}(\mathbf{S}(j\omega)) \cdot \bar{\sigma}(\mathbf{G}_d(j\omega)) \geq \bar{\sigma}(\mathbf{S}\mathbf{G}_d(j\omega)) \quad (8.130)$$

¹⁵If the achieved γ is small (i.e. $\gamma < 4$) the shape of the open-loop singular values will not have changed significantly after robust stabilization [6], i.e., if γ is small (i.e. $\gamma < 4$) then $\underline{\sigma}(\mathbf{L}(j\omega)) \approx \underline{\sigma}(\mathbf{G}_s(j\omega))$ if $\underline{\sigma}(\mathbf{G}_s(j\omega))$ is sufficiently large.

In the following (8.127) is utilized to derive a reasonable weight $\mathbf{W}_1(s)$ for the \mathcal{H}_∞ loop shaping problem at hand (disturbance rejection). Thus, an adequately shaped plant $\mathbf{G}_s = \mathbf{G}\mathbf{W}_1$ ($\mathbf{W}_2 = \mathbf{I}$) is obtained:

$$1 > \bar{\sigma}(\mathbf{W}_1^\dagger(j\omega)) \cdot \bar{\sigma}(\mathbf{G}^\dagger(j\omega)) \cdot \bar{\sigma}(\mathbf{G}_d(j\omega)) = \frac{1}{\underline{\sigma}(\mathbf{W}_1(j\omega))} \cdot \frac{1}{\underline{\sigma}(\mathbf{G}(j\omega))} \cdot \bar{\sigma}(\mathbf{G}_d(j\omega)) \quad (8.131)$$

$$\underline{\sigma}(\mathbf{W}_1(j\omega)) > \frac{\bar{\sigma}(\mathbf{G}_d(j\omega))}{\underline{\sigma}(\mathbf{G}(j\omega))} = \bar{\sigma}(\mathbf{G}^\dagger(j\omega)) \cdot \bar{\sigma}(\mathbf{G}_d(j\omega)) \geq \bar{\sigma}(\mathbf{G}^\dagger \mathbf{G}_d(j\omega)) \quad (8.132)$$

However, in order to minimize the input signals \mathbf{u} and to avoid stability problems, $\underline{\sigma}(\mathbf{W}_1(j\omega))$ should not be larger than necessary. Thus, a more conservative choice could be

$$\underline{\sigma}(\mathbf{W}_1(j\omega)) \approx \bar{\sigma}(\mathbf{G}^\dagger \mathbf{G}_d(j\omega)). \quad (8.133)$$

As outlined in Figure 8.17 $\bar{\sigma}(\mathbf{L}(j\omega))$ and thus $\bar{\sigma}(\mathbf{G}_s(j\omega))$ should be small at those typically high frequencies, where noise attenuation, input usage and/or robust stability (with respect to additive and/or multiplicative output uncertainty) might be an issue. This has to be regarded when to decide on the shape of $\mathbf{W}_1(s)$ in the high frequency range.

Another possibility to decide on a desired loop shape, or rather shaped plant $\mathbf{G}_s(s)$, and thus a way to derive a reasonable weight(s) $\mathbf{W}_1(s)$ (and $\mathbf{W}_2(s)$) for shaping the plant \mathbf{G} (in the case of disturbance rejection also applicable if the disturbance transfer function \mathbf{G}_d is unknown) is described in the following. The following suggestion was inspired by [6].

- Design an initial controller based on LQG¹⁶ (which may use modal weighting), and validate its stability and performance (e.g. disturbance rejection performance) in an experiment.
- If the outcome is satisfying, use its loop transfer function matrix \mathbf{L}_{LQG} as a provisionally shaped plant $\tilde{\mathbf{G}}_s(s) = \tilde{\mathbf{W}}_2(s)\mathbf{G}(s)\tilde{\mathbf{W}}_1(s)$.
- For simplicity choose $\tilde{\mathbf{W}}_2 = \mathbf{I}$. Thus, the preliminary weight $\tilde{\mathbf{W}}_1(s)$ is computed by

$$\tilde{\mathbf{W}}_1(s) = \mathbf{G}^\dagger \mathbf{L}_{\text{LQG}}. \quad (8.134)$$

In general the weight $\tilde{\mathbf{W}}_1(s)$ may not be minimum phase or even stable, and thus inapplicable. On one hand, an all-pass factorization in terms of RHP zeros as well as RHP poles of $\tilde{\mathbf{W}}_1(s)$, $\tilde{\mathbf{W}}_{\text{sm1}}(s)$ (stable and minimum phase) can be used. The mathematical background on all-pass factorization can be found in [6]. Still, the weight $\tilde{\mathbf{W}}_{\text{sm1}}(s)$ might be inappropriate because of its complexity and usually high system order so further simplification might be needed.

On the other hand, one can simply investigate the singular values of $\tilde{\mathbf{W}}_1(j\omega)$ in a plot. This might give an idea of how to choose a simple diagonal weight \mathbf{W}_1 , for example by reasonably approximating the shape of the maximum singular value $\bar{\sigma}(\tilde{\mathbf{W}}_1(j\omega))$ over frequency with a relatively simple, stable, and minimum phase SISO weight $W_1(s)$ and letting $\mathbf{W}_1 = W_1(s) \cdot \mathbf{I}$ (see Figures 9.13 and 9.30).

¹⁶ \mathbf{G}_d is not needed

Instead of using the loop transfer function matrix of a LQG based design, one can try to use \mathbf{L} of a different, successfully validated controller design (method), for example the loop shape $\mathbf{L}_{\text{mixedS}}$, obtained by the mixed-sensitivity \mathcal{H}_∞ regulation (disturbance rejection) problem¹⁷ which was described in Section 8.5.

$$\widetilde{\mathbf{W}}_1(s) = \mathbf{G}^\dagger \mathbf{L}_{\text{mixedS}} \quad (8.135)$$

¹⁷ \mathbf{G}_d is needed

Chapter 9

Simulation and Validation of Control Performance

Improving disturbance rejection (the disturbance signal d is associated with the shaker force) of the experimental plant “beam with mounted shaker” by applying the feedback control design methods described in Chapters 7 and 8 will be shown in this chapter. Here the measured outputs \mathbf{y} are the strain signals of the four piezo patch sensors (i.e. the acceleration and force measurements will be omitted in the following) and all four outputs are fed back to the feedback controller \mathbf{K} (i.e. $\mathbf{u} = \mathbf{K}\mathbf{y}$ or $\mathbf{u} = -\mathbf{K}\mathbf{y}$). The four different feedback controllers,

- modally weighted LQG (see Chapter 7, page 79),
- mixed-sensitivity \mathcal{H}_∞ optimal design (see Section 8.5, page 88),
- \mathcal{H}_∞ loop-shaping design (see Section 8.8, page 112) and
- D(G)K¹ synthesized μ -“optimal” design (see Section 8.7, page 109)

will be designed on the basis of the “IDbs-model” as well as on the “FEbs-model”. The origin of the input-output scaled final models, ready to be used for controller design and simulation purposes was described in Table 6.2 on page 70.

9.1 Disturbance Signal(s) and Identification of Spectral “Experimental Validation Models”

In order to be able to compare the experimental validated closed-loop (disturbance rejection) performance achieved by a certain controller with the experimental open-loop (disturbance) performance, and among one another (and with simulated closed-loop performance (i.e. $\mathbf{S}\mathbf{G}_d$)), over a wide frequency range, spectral, non-parametric models (from d to \mathbf{y}) were identified. These identified spectral models from validation at the experiment (actual hardware experiment) are referred to as closed-loop experimental validation model(s) ($\mathcal{S}^{\text{CL-EV}}$) respectively open-loop experimental validation model ($\mathcal{S}^{\text{OL-EV}}$). The identification procedure carried out to obtain these spectral models is described in the following.

¹In section 9.3.5 parametric real uncertainty (see Section 8.6.2.1 on page 91) in the natural angular frequency ω_i will be considered, thus DGK-iteration is used. For information about DGK-iteration see [7].

To concentrate the excitation on the modes below 50 Hz and to avoid ringing in the frequency domain, a discrete white noise signal (i.e. Gaussian random amplitude at the chosen sampling frequency of 1000 Hz) with a variance of 0.36 was fed to five first-order low pass filters in series all with a cutoff frequency of 100 Hz. This disturbance signal $d(kT_s)$ was scaled by the disturbance scaling gain D_d (see Section 6.2) and fed to the shaker input of the Simulink[®] subsystem “MIMO beam”.²

For each experimental validation of a controller and for the experimental open-loop case data sets of about $1.2 \cdot 10^6$ samples were recorded using a sampling time $T_s = 0.001$ s. The signals d^l and \mathbf{y}^l were recorded (see Section 2.2, Figure 2.4).

It should be pointed out that the applied disturbance signal $d^l(kT_s)$ was exactly the same for all identifications with closed-loop (different controllers) and for the one (new) open-loop identification and that in this chapter for each plot comparing a closed-loop experimental validation model ($\mathcal{S}^{\text{CL-EV}}$) with an open-loop experimental validation model ($\mathcal{S}^{\text{OL-EV}}$) both of these spectral models were identified with the same amount of data (i.e. the shorter signal length of both was used).

Because the input signal is the generated disturbance signal d^l , it is not an identification in the closed loop, when the feedback loop is closed with the (feedback) controller \mathbf{K} , but only an identification with closed loop. Thus, it is simply an identification of a different system. For the generated (disturbance) input signal d^l the (identification) requirement that it is uncorrelated with the measurement noise (of \mathbf{y}^l) is fulfilled.

For better comparability of (singular value and Bode) plots of simulated performance ($\mathbf{S}\mathbf{G}_d$) and plots of experimental validated closed-loop performance in terms of spectral models ($\mathcal{S}^{\text{CL-EV}}$ -model(s)), the logged signals d^l and \mathbf{y}^l were input- respectively output-scaled.³

The data was down-sampled to 100 Hz to improve the resolution of the identification task in the lower frequency range. Where a tenth-order anti-aliasing filter was applied before decimation and two percent at the beginning and at the end of the signal were skipped. Mean values were subtracted and linear trends removed.

Then the preprocessed data was used to identify a spectral model⁴ (non-parametric model) from d to \mathbf{y} by using the MATLAB[®] algorithm `spafdr`.

In addition to this excitation by a noise signal, each controller was validated by applying five different sine signals ($d(t) = 1/4 \cdot \sin(2\pi f_i^{\text{IDbs}} t)$ for $i = 1, \dots, 5$) and five different pairs of subtended step signals (same step size, but different sign) with temporal difference $\Delta t_i = 1/(2 \cdot f_i^{\text{IDbs}})$ ($d(t) = \sigma(t) - \sigma(t - \Delta t_i)$ for $i = 1, \dots, 5$), where Δt was rounded down to be an integer multiple of the sampling time T_s (for f_i^{IDbs} see Table 6.4 on page 77).

²For the controller validation the inputs and outputs of the Simulink[®] subsystem “MIMO beam” had to be scaled as follows:

The inputs associated with the piezo patch actuators had to be scaled with \mathbf{D}_u ($\mathbf{u}^l = \mathbf{D}_u \mathbf{u} + \mathbf{u}_{\text{offset}}$).

The input associated with the shaker had to be scaled with D_d ($d^l = D_d d + d_{\text{offset}}$).

The outputs associated with the piezo patch sensors had to be scaled with $K_{\varepsilon y^l} \mathbf{D}_{\varepsilon \varepsilon}^{-1}$ ($\mathbf{y} = K_{\varepsilon y^l} \mathbf{D}_{\varepsilon \varepsilon}^{-1} \mathbf{y}^l$).

³Thus, by applying a spectral analysis to this scaled input and output data, the non-parametric (spectral) models ($\mathcal{S}^{\text{OL-EV}}$ and $\mathcal{S}^{\text{CL-EV}}$) were directly obtained in input- and output-scaled form as outlined in Section 6.2.

⁴The only structural assumption to be made for identifying a spectral model is the linearity of the system. [17]

9.2 Controller Designs Based on the Identified (ID) Model

In this section all discrete-time controller designs are based on the discrete-time ($T_s = 0.01$ s) “IDbs-model” as design plant. For simplicity, the notation \mathbf{G} instead of \mathbf{G}^{IDbs} and \mathbf{G}_d instead of $\mathbf{G}_d^{\text{IDbs}}$ is used to denote the nominal plant respectively disturbance model in the following.

9.2.1 Mixed-sensitivity \mathcal{H}_∞ control

The scalar performance weight $W_1(s)$ was chosen as a bandpass with two additional peaks. These two extra peaks were utilized to put strong weight on the low-damped first and fourth modes. Thus, by design of $W_1(s)$, performance is not an issue at low and high frequencies, where actuation is not desired with the applied piezo patch actuators, respectively where the system is simply unknown. The scalar input weight $W_2(s)$ was selected as a bandstop, thus input usage is highly penalized outside the frequency range of interest spanned by the natural frequencies of the first five (structural) modes of the beam with mounted shaker.

As already mentioned, the size of \mathbf{KS} (in \mathbf{N} , see (9.5)) is also important for robust stability with respect to additive plant uncertainty (see equation (8.48) on page 94), where Δ_A is usually considered as a full complex perturbation matrix and thus the (frequency-wise) requirement for robustly stability (see Definition 8.5 on page 101) is

$$\|\mathbf{M}\|_\infty < 1. \quad (9.1)$$

where $\mathbf{M} = -\mathbf{W}_{1A}\mathbf{K}\mathbf{S}\mathbf{W}_{2A}$. The negative sign in front of \mathbf{M} is irrelevant in the following.

By considering $\mathbf{W}_{1A}(s) = W_{1A}(s) \cdot \mathbf{I}$ and $\mathbf{W}_{2A} = \mathbf{I}$ from (9.1) follows that, although uncertainty is not explicitly modelled by this mixed-sensitivity \mathcal{H}_∞ design, it is robustly stable for all perturbed plants \mathbf{G}_p with

$$\bar{\sigma}(\mathbf{G}_p(j\omega) - \mathbf{G}(j\omega)) = \bar{\sigma}(W_{1A}\Delta_A(j\omega)) = |W_{1A}(j\omega)| \cdot \underbrace{\bar{\sigma}(\Delta_A(j\omega))}_{\leq 1} \leq |W_{1A}(j\omega)| \quad \forall \omega \in \mathbb{R} \quad (9.2)$$

where

$$|W_{1A}(j\omega)| < \frac{1}{\bar{\sigma}(\mathbf{KS}(j\omega))} = \underline{\sigma}((\mathbf{KS}(j\omega))^\dagger) \quad \forall \omega \in \mathbb{R} \quad (9.3)$$

if additionally to \mathbf{N} ($\mathbf{z} = \mathbf{N}w$, see Equation (8.26)), which by the (mixed-sensitivity) \mathcal{H}_∞ design is guaranteed to be stable, the transfer function matrices

$$\mathbf{M} = -\mathbf{W}_{1A}\mathbf{K}\mathbf{S}\mathbf{W}_{2A}, \quad \widetilde{\mathbf{N}}_{12} = -\mathbf{W}_{1A}\mathbf{K}\mathbf{S}\mathbf{G}_d \quad \text{and} \quad \widetilde{\mathbf{N}}_{21} = \begin{bmatrix} \mathbf{W}_{1A}\mathbf{S}\mathbf{W}_{2A} \\ \mathbf{W}_{2A}\mathbf{K}\mathbf{S}\mathbf{W}_{2A} \end{bmatrix} \quad (9.4)$$

are stable.⁵ Because \mathbf{W}_{1A} and \mathbf{W}_{2A} are assumed stable, and

$$\mathbf{N} = \begin{bmatrix} \mathbf{W}_{1A}\mathbf{S}\mathbf{G}_d \\ \mathbf{W}_{2A}\mathbf{K}\mathbf{S}\mathbf{G}_d \end{bmatrix} \quad (9.5)$$

⁵i.e. If $\widetilde{\mathbf{N}} = \begin{bmatrix} \mathbf{M} & \widetilde{\mathbf{N}}_{12} \\ \widetilde{\mathbf{N}}_{21} & \mathbf{N} \end{bmatrix}$ is internally stable (NS) the mixed-sensitivity \mathcal{H}_∞ design at hand is robustly stable (RS) for all perturbed plants \mathbf{G}_p with: $\bar{\sigma}(\mathbf{G}_p(j\omega) - \mathbf{G}(j\omega)) < \frac{1}{\bar{\sigma}(\mathbf{KS}(j\omega))} \quad \forall \omega \in \mathbb{R}$

is stable also \mathbf{S} , \mathbf{KS} and \mathbf{KSG}_d are stable.⁶ Thus the mixed-sensitivity \mathcal{H}_∞ design at hand fulfills the nominal stability (NS) condition with respect to additive plant uncertainty. Because in this mixed-sensitivity \mathcal{H}_∞ design \mathbf{KS} is shaped by $\mathbf{W}_2(s)$, the shape of $\mathbf{W}_2(s)$ has direct influence on robust stability with respect to additive plant uncertainty.

A singular value plot of the discretized weights (zero-pole matching method; $T_s = 0.01$ s) $\mathbf{W}_1(z)$ and $\mathbf{W}_2(z)$ is depicted in Figure 9.1.

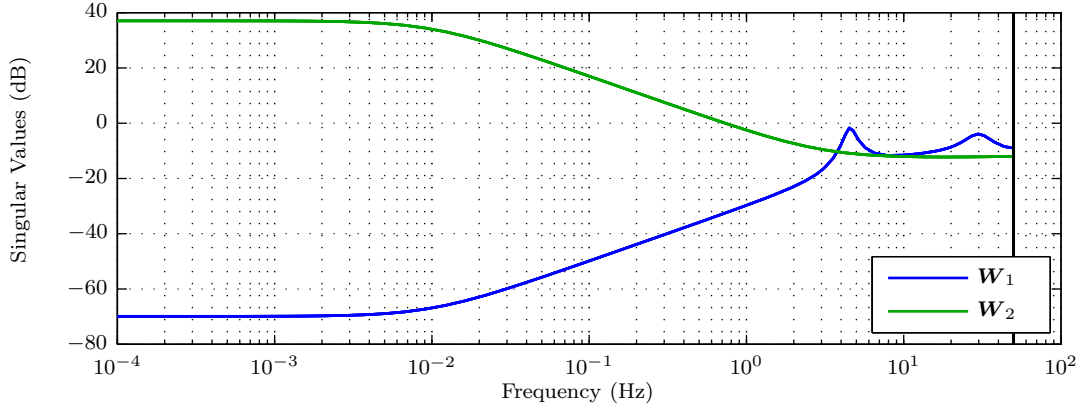


Figure 9.1: Singular values of performance weight $\mathbf{W}_1(z) = W_1(z) \cdot \mathbf{I}$ and input weight $\mathbf{W}_2(z) = W_2(z) \cdot \mathbf{I}$

By applying the MATLAB[®] algorithm `hinfsv` on the generalized plant \mathbf{P} (8.25), a stabilizing, stable feedback controller \mathbf{K} (with 42 states) was obtained. As desired, the singular values of \mathbf{K} (Figure 9.2) (especially the maximum singular value $\bar{\sigma}(\mathbf{K}(e^{j\omega T_s}))$) are high around the natural frequencies of the first and fourth (structural) modes, thus considerable damping improvements of these particularly low damped modes are expected when the loop is closed.

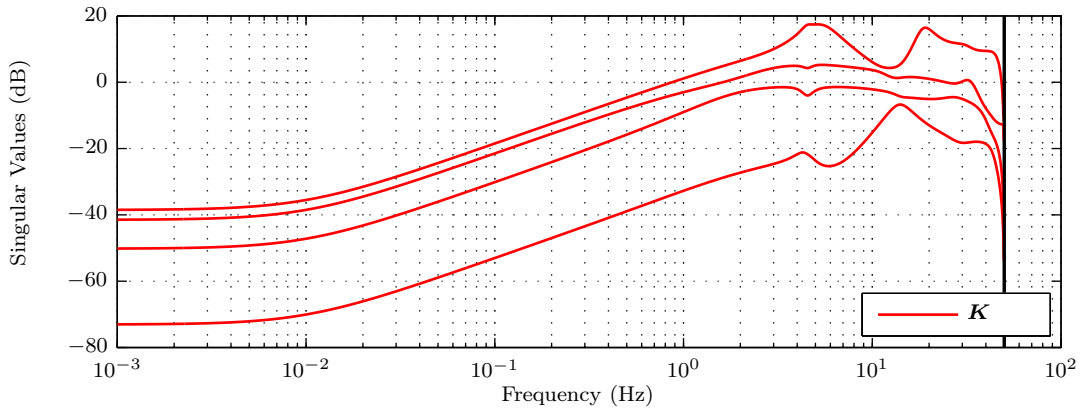


Figure 9.2: Singular values of the feedback controller \mathbf{K}

⁶In a case where \mathbf{K} itself is unstable, \mathbf{S} has RHP zeros (all-pass behavior) which cancel these RHP poles (unstable poles) of \mathbf{K} . When it comes to implementation of an itself unstable controller \mathbf{K} , special techniques have to be applied in order to guard against the case when the loop transfer function \mathbf{L} is opened and thus the control signal \mathbf{u} would increase boundlessly. If \mathbf{G}_d would be unstable, which is not the case (flexible structure), its RHP poles would be also canceled by corresponding RHP zeros in \mathbf{S} .

In Figure 9.3 the maximum singular value of the closed-loop performance transfer function matrix \mathbf{N} ($\mathbf{N} = \mathcal{F}_1(\mathbf{P}, \mathbf{K})$) is shown. The nominal performance (NP) requirement

$$\|\mathbf{N}\|_\infty < 1 \Leftrightarrow \bar{\sigma}(\mathbf{N}(e^{j\omega T_s})) < 1 \quad \forall \omega \in \mathbb{R}$$

(i.e. the design) is most critical ($\|\mathbf{N}\|_\infty = \gamma = 0.7018$) around the natural frequency of the first (structural) mode ($f_1^{\text{IDbs}} = 4.5332 \text{ Hz}$), but nevertheless is easily satisfied. Also the other modes can be easily spotted in the maximum singular value plot of \mathbf{N} , but are even less problematic for the design. As expected, at low frequencies, where by the shape of the performance weight $\mathbf{W}_1(z)$ the demand on the design is vanishing, the maximum singular value of \mathbf{N} drops down to an insignificantly low level.

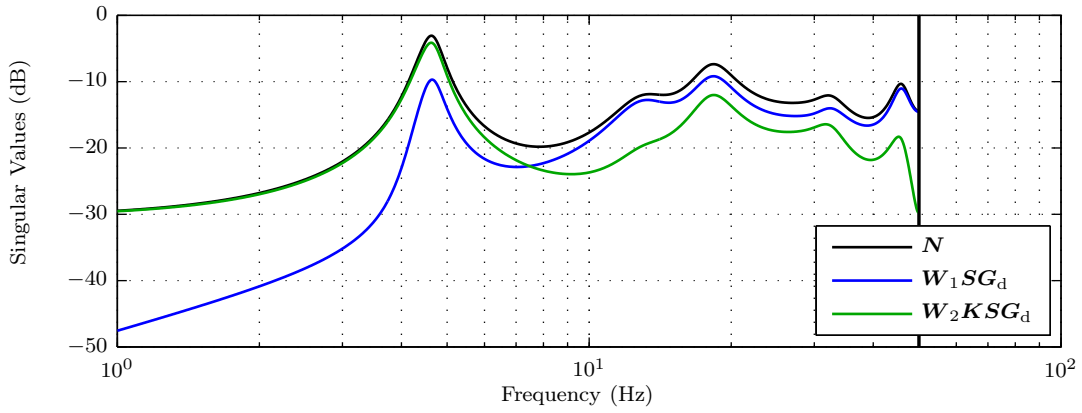


Figure 9.3: Singular values plot of the closed-loop performance transfer function (vector) \mathbf{N} ($\mathbf{z} = \mathbf{N}w$, where $w = d$) and its individual stacked components

The singular value plot (Figure 9.4a) of the simulated (nominal) closed-loop behavior ($\mathbf{y} = \mathbf{S}\mathbf{G}_d d$) looks promising when compared to the simulated (nominal) open-loop behavior ($\mathbf{y} = \mathbf{G}_d d$). The first and the fourth modes are highly damped by the feedback controller \mathbf{K} , and also the damping of all other modes is improved significantly. By applying the controller \mathbf{K} on the “IDbs(ho)-model”, the feedback system is also stable and the improvement of mode damping (Figure 9.4b) is quite similar.

However, because for the two models (“IDbs-model” and “IDbs(ho)-model”) the first peak (corresponding to the first structural mode), which is rather sharp, appears at a slightly different frequency (barely noticeably in Figures 4.5a and 4.5b on page 24), the controller \mathbf{K} “splits” the first peak of the “IDbs(ho)-model” in two. This effect is also seen in Figure 9.5, which plots the singular values of the open-loop experimental validation model ($\mathcal{S}^{\text{OL-EV}}$) and those of the closed-loop experimental validation model ($\mathcal{S}^{\text{CL-EV}}$). The slight shift of the third and fourth modes to higher frequencies in the simulation can also be seen in the experimental closed-loop validation ($\mathcal{S}^{\text{CL-EV}}$). The improvement in mode damping is excellent in the experimental closed-loop validation. The first mode is reduced by 9.3 dB and the fourth is reduced by more than 14 dB. Also the damping of the second, third and fifth structural modes is improved (reductions of 1 dB, 1.6 dB and 1.4 dB, respectively). In general the experimental validated closed-loop behavior ($\mathcal{S}^{\text{CL-EV}}$) is in good accordance to the simulation on the “IDbs(ho)-model”.

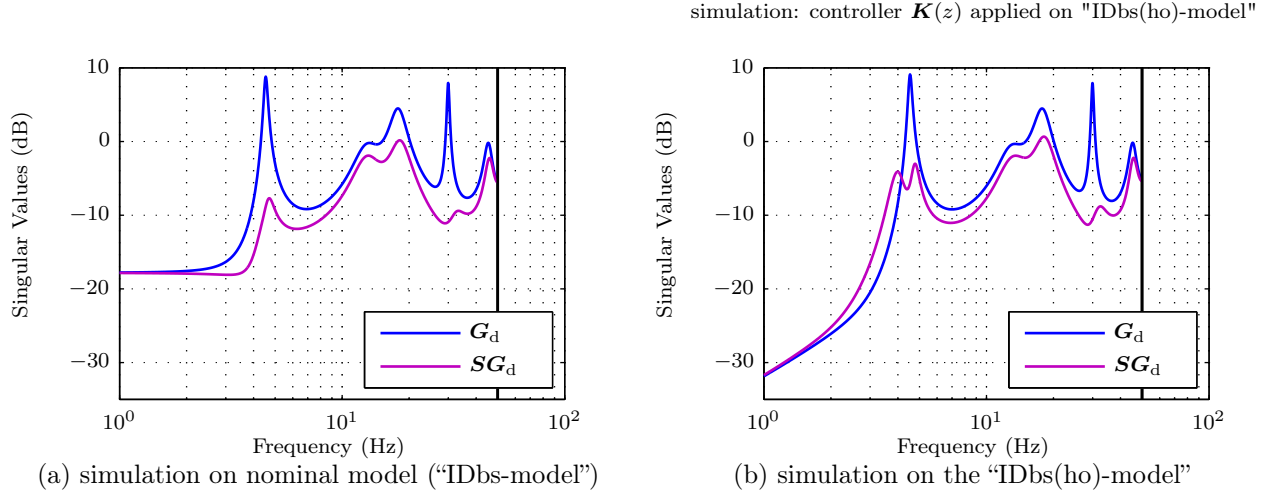


Figure 9.4: Singular values of simulated open-loop and closed-loop behavior (from d to y)

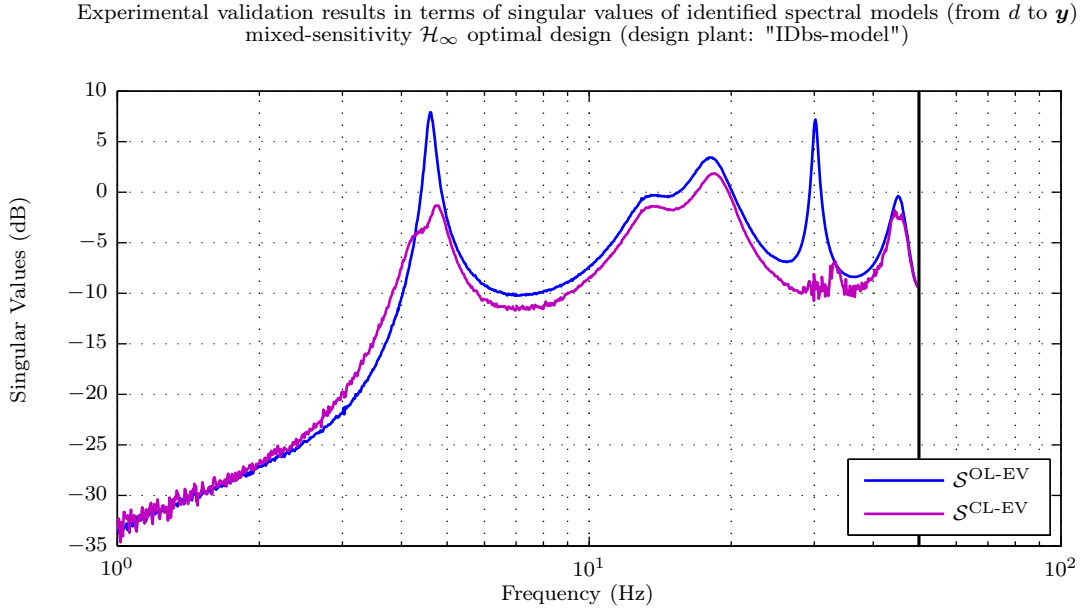


Figure 9.5: Experimental validation results in terms of singular values (from d to y) of open-loop ($\mathcal{S}^{\text{OL-EV}}$) and closed-loop ($\mathcal{S}^{\text{CL-EV}}$) identified spectral models (mixed-sensitivity \mathcal{H}_∞ optimal design based on the "IDbs-model")

In Figure 9.6 Bode magnitude plots of the open-loop ($\mathcal{S}^{\text{OL-EV}}$) and closed-loop experimental validation models ($\mathcal{S}^{\text{CL-EV}}$) are shown. For the fourth structural mode the magnitude reduction is excellent for all outputs y_i ($i = 1, \dots, 4$), whereas for the first structural mode the reduction in magnitude of output y_3 is negligible compared to the other outputs. The magnitude of the open-loop experimental validation model ($\mathcal{S}^{\text{OL-EV}}$) is much lower around the first structural mode (at about 4.53 Hz) for y_3 , because (for a hinged-hinged beam with mounted shaker) the third piezo patch sensor lies quite close to the node of oscillation of the first bending strain mode shape. This is shown by the third blue circle (piezo patch sensor number three) in the right picture of Figure 5.20b on page 64, which shows the first five mode

shapes proportional to the curvature respectively bending strain (assuming $\varepsilon_{\text{bending}} \propto \frac{d^2 w}{dx^2}$) of the FE beam with mounted shaker.

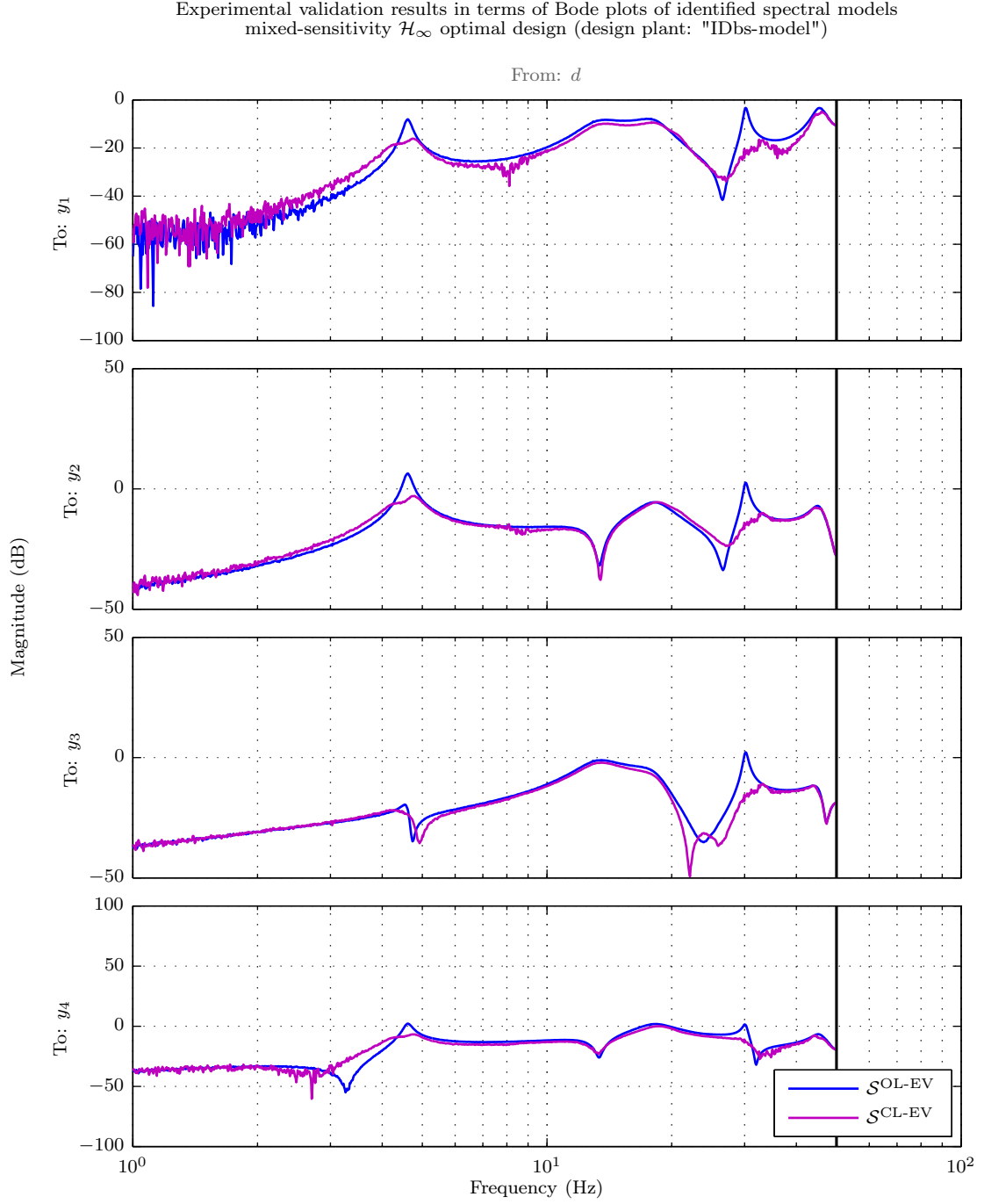


Figure 9.6: Experimental validation results in terms of (disturbance path) Bode plots of open-loop ($\mathcal{S}^{\text{OL-EV}}$) and closed-loop ($\mathcal{S}^{\text{CL-EV}}$) identified spectral models (mixed-sensitivity \mathcal{H}_∞ optimal design based on the "IDbs-model")

In terms of the scaled outputs \mathbf{y} , Figure 9.7b depicts the actual open-loop and closed-loop responses to a persistent sine signal (scaled disturbance signal $d(t) = 1/4 \cdot \sin(2\pi f_1^{\text{IDbs}} t)$) of frequency $f_1^{\text{IDbs}} = 4.53$ Hz (Figure 9.7a). At times $t < 0$ measurement noise and the effects of unmeasured process noise (crosstalk/noise) on actuator lines are clearly (but indistinguishable) visible in Figure 9.7b. After a short period of transient behavior the system response is more or less sinusoidal. For this (scaled) disturbance signal d , the ratio of the open-loop and closed-loop amplitudes is about the same for all outputs, except for output y_3 , where the open-loop and closed-loop amplitudes are inherently both significantly lower (spatial proximity to the node of oscillation for bending strain). This behavior was also revealed by the Bode magnitude plots of Figure 9.6.

As seen from Figure 9.7c damping of the first structural mode is mostly accomplished by the second and fourth piezo patch actuators (u_2 and u_4), which collocated piezo patch sensors (y_2 and y_4) measure the highest amplitudes (see Figure 9.7b and blue circles in the right picture of Figure 5.20b on page 64). As expected, here the third piezo patch actuator (u_3) has only a minor part.

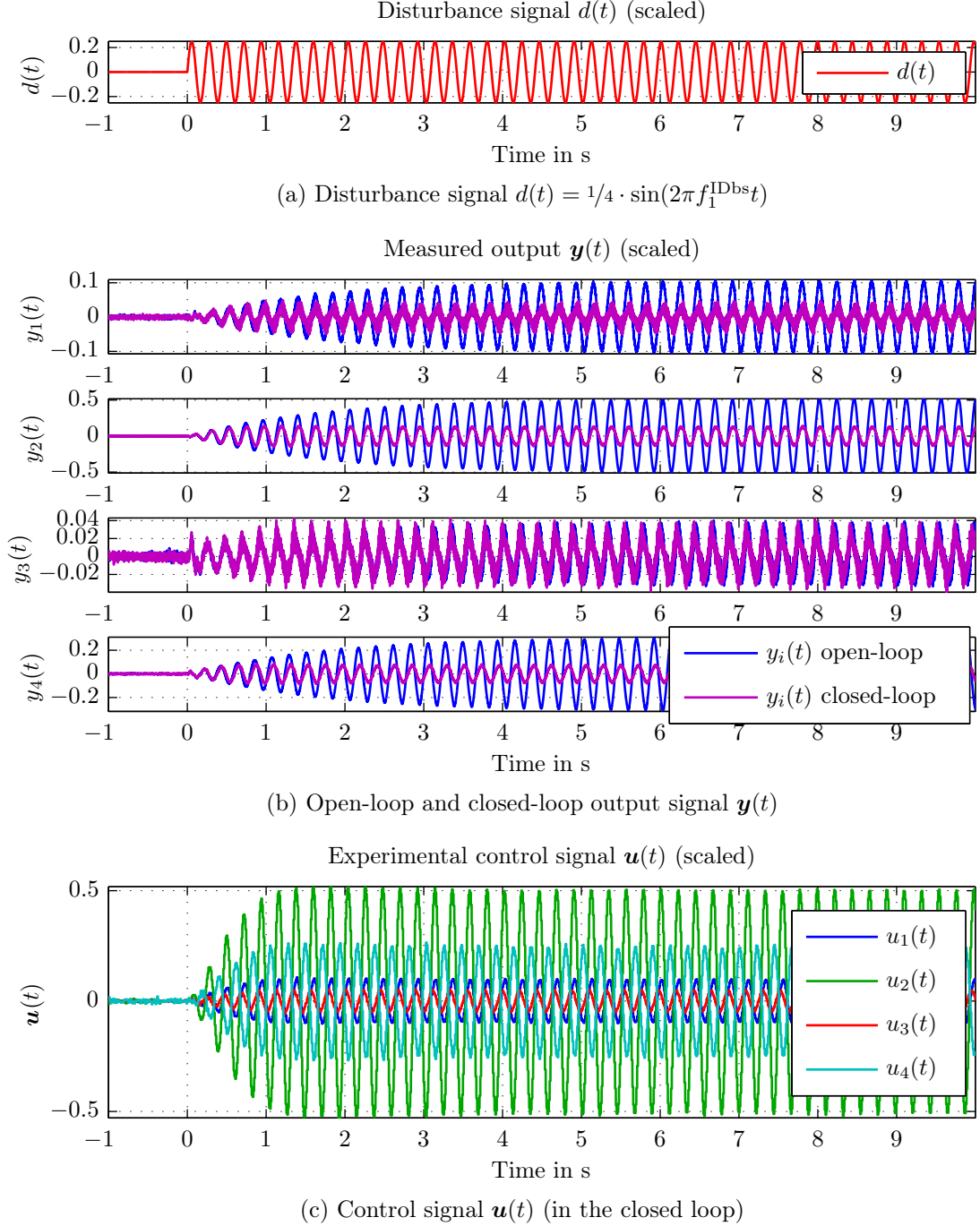
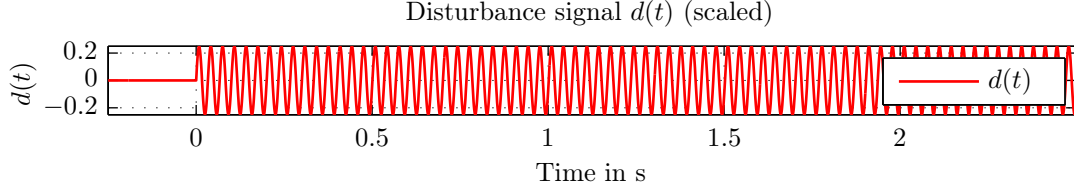
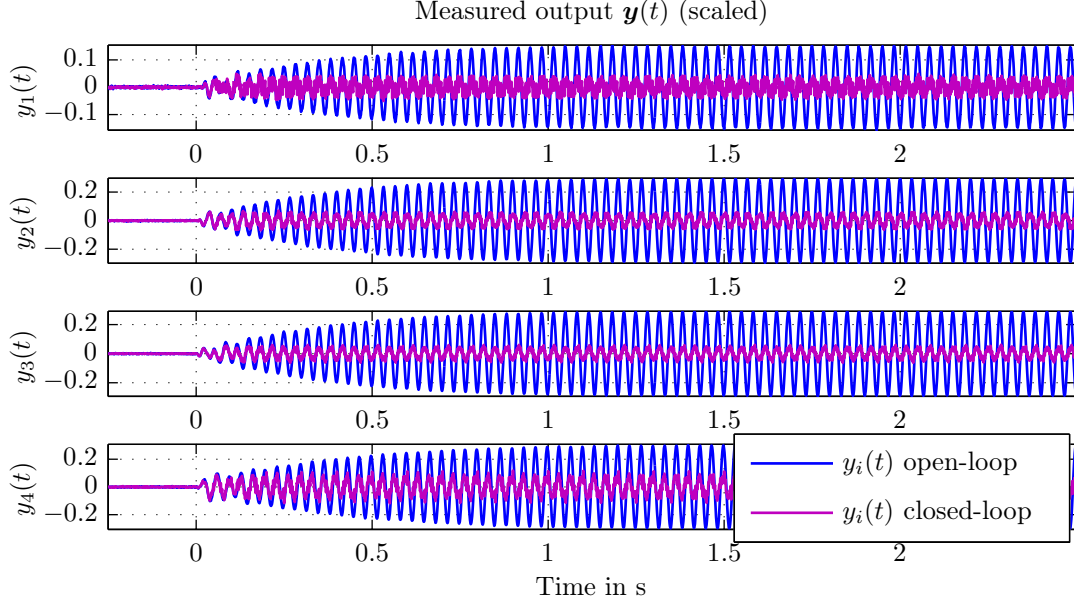
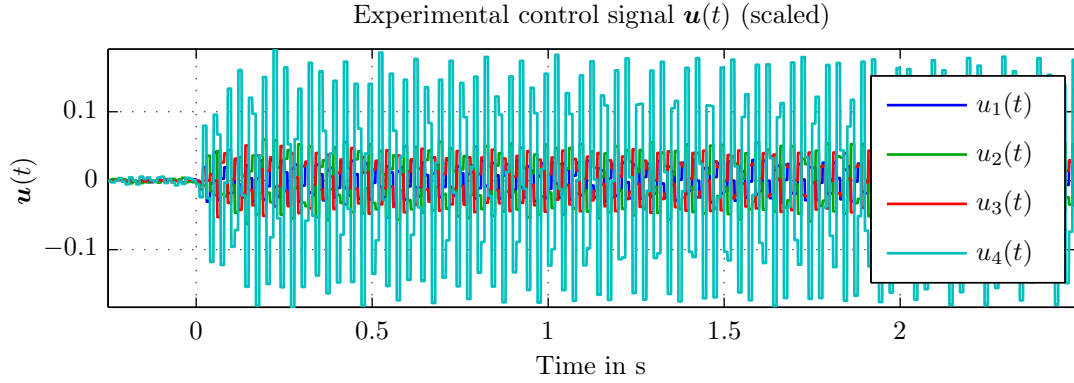


Figure 9.7: Measured open-loop and closed-loop output signal $y(t)$ and control signal $u(t)$ (disturbance excitation $d(t) = 1/4 \cdot \sin(2\pi f_1^{\text{IDbs}} t)$)

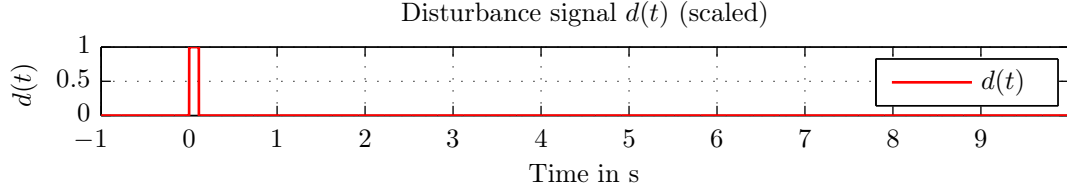
The case when a persistent sine signal ($d(t) = 1/4 \cdot \sin(2\pi f_4^{\text{IDbs}} t)$) of frequency $f_4^{\text{IDbs}} = 29.95 \text{ Hz}$ is applied as disturbance d (Figure 9.8a) is depicted in Figure 9.8b. The ratio of the open-loop and closed-loop amplitudes confirm the excellent damping improvement seen in the Bode magnitude plots of Figure 9.6.

Figure 9.8c reveals that the amplitude of the control signal u_4 is considerably larger than all others, possibly due to the fact that the (collocated) piezo patch sensor number four is closer to the shaker coupling point than the others.

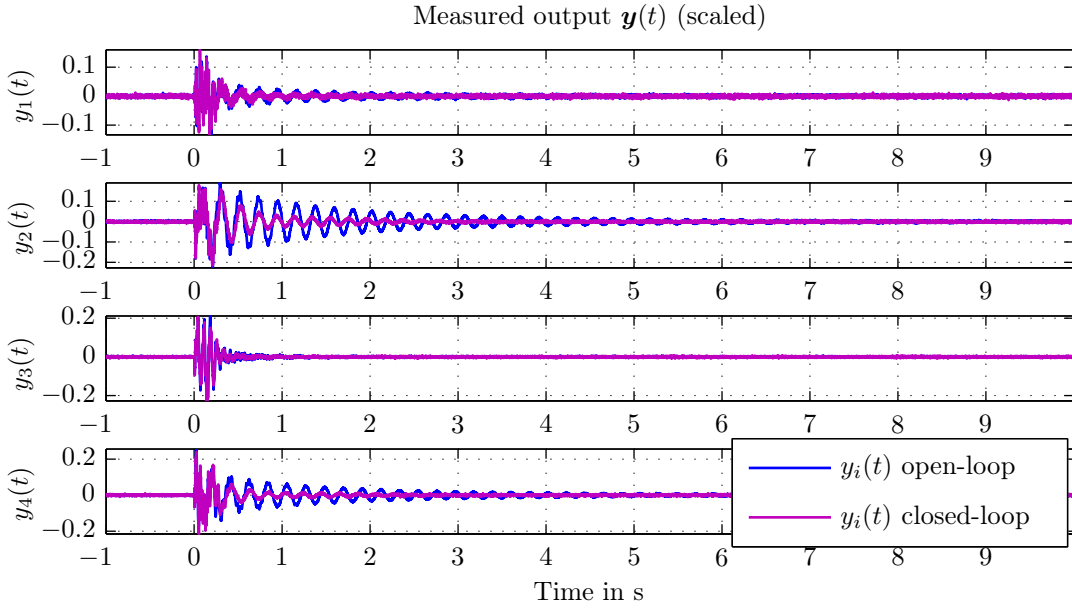
(a) Disturbance signal $d(t) = 1/4 \cdot \sin(2\pi f_4^{\text{IDbs}} t)$ (b) Open-loop and closed-loop output signal $\mathbf{y}(t)$ (c) Control signal $\mathbf{u}(t)$ (in the closed loop)Figure 9.8: Measured open-loop and closed-loop output signal $\mathbf{y}(t)$ and control signal $\mathbf{u}(t)$ (disturbance excitation $d(t) = 1/4 \cdot \sin(2\pi f_4^{\text{IDbs}} t)$)

The open-loop and closed-loop response to a rectangular pulse signal ($d(t) = \sigma(t) - \sigma(t - \Delta t_1)$) is presented in Figure 9.9b. The intention by choosing $\Delta t_1 = 1/(2 \cdot f_1^{\text{IDbs}})$ ($\Delta t_1 = 0.11$ s) was to cause a strong excitation of the first structural mode. After a short transient behavior the open-loop and closed-loop responses decay with the natural frequency of the first structural mode, whereas because the third piezo patch sensor lies in close vicinity to the node of oscillation for bending strain the output y_3 drops down immediately as soon as the transient response is over. The other outputs show that the closed-loop response decays faster.

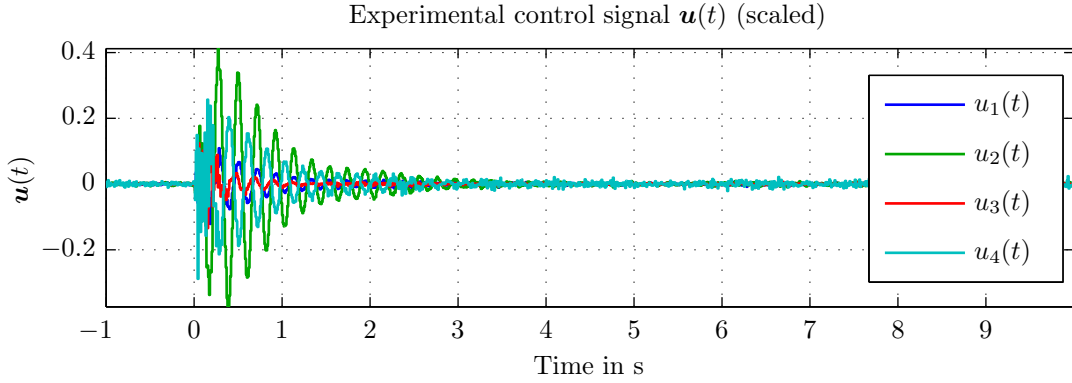
As expected for this desired strong excitation of the first structural mode, the \mathcal{H}_∞ controller makes again (compare with Figure 9.7c) intense use of actuators two and four (u_2 and u_4), while the third actuator (u_3) is used least of all.



(a) Disturbance signal $d(t) = \sigma(t) - \sigma(t - \Delta t_1)$



(b) Open-loop and closed-loop output signal $\mathbf{y}(t)$



(c) Control signal $\mathbf{u}(t)$ (in the closed loop)

Figure 9.9: Measured open-loop and closed-loop output signal $\mathbf{y}(t)$ and control signal $\mathbf{u}(t)$ (disturbance excitation $d(t) = \sigma(t) - \sigma(t - \Delta t_1)$)

Although uncertainty is not explicitly modelled by this mixed-sensitivity \mathcal{H}_∞ design, it is robustly stable for all perturbed plants \mathbf{G}_p with

$$\bar{\sigma}(\mathbf{G}_p(e^{j\omega T_s}) - \mathbf{G}(e^{j\omega T_s})) \leq |W_{1A}(e^{j\omega T_s})| \quad \forall \omega \in \mathbb{R} \quad (9.6)$$

where the singular values of $\mathbf{W}_{1A}(e^{j\omega T_s}) = W_{1A}(e^{j\omega T_s}) \cdot \mathbf{I}(\bar{\sigma}(\mathbf{W}_{1A}(e^{j\omega T_s}))) = \underline{\sigma}(\mathbf{W}_{1A}(e^{j\omega T_s}))$ are depicted in Figure 9.10. At low frequencies the high value of $\frac{1}{\bar{\sigma}(\mathbf{K}\mathbf{S}(e^{j\omega T_s}))}$ allows for large additive uncertainty. In terms of the structural modes additive uncertainty is allowed to be largest around the first structural mode.

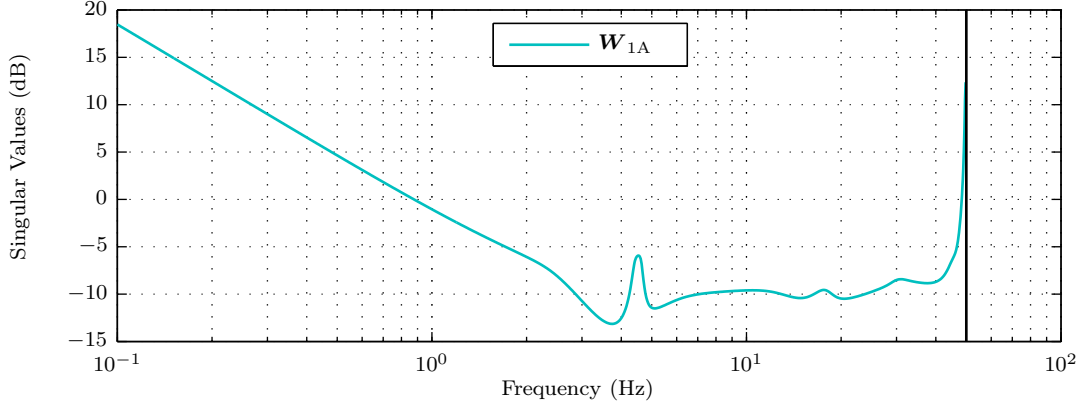


Figure 9.10: Singular values of $\mathbf{W}_{1A}(e^{j\omega T_s}) = W_{1A}(e^{j\omega T_s}) \cdot \mathbf{I}(|W_{1A}(e^{j\omega T_s})|) = \frac{(1-\epsilon)}{\bar{\sigma}(\mathbf{K}\mathbf{S}(e^{j\omega T_s}))}$ with an infinitesimally small $\epsilon \in \mathbb{R}^+$

9.2.2 Modally weighted LQG design

Because the plant is (strictly) stable (i.e. $|\lambda_i(\mathbf{A})| < 1$ for $i = 1, \dots, n$), the closed loop system with state feedback controller \mathbf{K}_{LQR} is guaranteed to be asymptotically stable.⁷ And because \mathbf{A} and \mathbf{A}^T have the same eigenvalues (i.e. for a strictly stable plant $|\lambda_i(\mathbf{A}^T)| < 1$ for $i = 1, \dots, n$) it is guaranteed that the solution \mathbf{Y} of the filter algebraic Riccati equation (7.12 on page 81), and thus the optimal filter gain matrix \mathbf{H} exists.⁸ Thus for this (strictly) stable (nominal) plant at hand the LQG-controlled system is guaranteed to be internally stable independent of the chosen (but valid) LQG design parameters.

In MATLAB[®] the command `eig` was used to compute eigenvectors of the state matrix \mathbf{A} . Then according to the natural angular frequency ω_i each eigenvector \mathbf{s}_i was sorted in ascending order of ω_i yielding a matrix of eigenvectors \mathbf{S} (see Example 9.1). Because \mathbf{A} has complex-conjugate eigenvalues (i.e. complex-conjugate eigenvectors) in the diagonal matrix of weighting factors \mathbf{M} (9.7) the weighting factors m_i appear in pairs. Thus, the first two diagonal elements of \mathbf{M} are utilized for weighting the first structural mode, the next two diagonal elements of \mathbf{M} for weighting the second structural mode, and so on. A high value m_i means that the corresponding eigenmode \mathbf{s}_i is weighted strongly in the state weighting matrix \mathbf{Q} (by m_i^2) and thus the improvement of damping of this eigenmode \mathbf{s}_i is important.

$$\mathbf{M} = \begin{bmatrix} 120 \cdot \mathbf{I}_{[2 \times 2]} & \mathbf{0} & \mathbf{0} & \mathbf{0} & \mathbf{0} \\ \mathbf{0} & 30 \cdot \mathbf{I}_{[2 \times 2]} & \mathbf{0} & \mathbf{0} & \mathbf{0} \\ \mathbf{0} & \mathbf{0} & 50 \cdot \mathbf{I}_{[2 \times 2]} & \mathbf{0} & \mathbf{0} \\ \mathbf{0} & \mathbf{0} & \mathbf{0} & 100 \cdot \mathbf{I}_{[2 \times 2]} & \mathbf{0} \\ \mathbf{0} & \mathbf{0} & \mathbf{0} & \mathbf{0} & 50 \cdot \mathbf{I}_{[2 \times 2]} \end{bmatrix} \quad (9.7)$$

⁷This is, because independent of \mathbf{B} and $\mathbf{Q}(\mathbf{A}, \mathbf{B})$ is stabilizable and (\mathbf{A}, \mathbf{Q}) is detectable.

⁸This is, because independent of \mathbf{C} and $\mathbf{W}(\mathbf{A}^T, \mathbf{C}^T)$ is stabilizable and $(\mathbf{A}^T, \mathbf{W})$ is detectable.

Because \mathbf{Q} has to be a real-valued matrix, in MATLAB® the following code was used:

Example 9.1: Deriving the state weighting matrix \mathbf{Q} for modal weighting using MATLAB®

```

1 % given:
2 % G ... plant (minimal state-space realization)
3 % M ... diagonal matrix of weighting factors (design param.; 1. mode ...
   first)
4
5 [S,EW] = eig(G.A);
6 EW = diag(EW);
7 if G.Ts == 0                % continuous-time:
8     omega = abs(EW);        % natural angular frequency
9 else                        % discrete-time:
10    omega = abs(log(EW))/G.Ts; % natural angular frequency
11 end
12 [dummy,ind] = sort(omega,'ascend'); % 1. mode first
13 S = S(:,ind);               % matrix of eigenvectors of A sorted by omega
14 Q_hat = S*M/S;             % auxiliary matrix
15 Q = real(Q_hat'*Q_hat); % state weighting matrix for modal weighting

```

The input weighting matrix \mathbf{R} is usually considered as a diagonal matrix, where a high diagonal entry R_{ii} penalizes input usage of the associated actuator i strongly. Because all four piezo patch actuators are the same, the input weighting matrix \mathbf{R} was chosen as a matrix of diagonally repeated values.

$$\mathbf{R} = 2000 \cdot \mathbf{I}_{[4 \times 4]} \quad (9.8)$$

With the state feedback controller \mathbf{K}_{LQR} and preamplifier matrix \mathbf{K}_r (only meaningful for reference tracking) the (discrete-time) closed-loop state-equation (9.9) and output-equation (9.10) for the state feedback control configuration (with control law $\mathbf{u} = \mathbf{K}_r \mathbf{r} - \mathbf{K}_{\text{LQR}} \mathbf{x}$) is given by:⁹

$$\mathbf{x}(k+1) = (\mathbf{A} - \mathbf{BK}_{\text{LQR}})\mathbf{x}(k) + \mathbf{BK}_r \mathbf{r}(k) + \mathbf{B}_d \mathbf{d}(k) \quad (9.9)$$

$$\mathbf{y} = (\mathbf{C} - \mathbf{DK}_{\text{LQR}})\mathbf{x}(k) + \mathbf{DK}_r \mathbf{r}(k) + \mathbf{D}_d \mathbf{d}(k) \quad (9.10)$$

Next, a motivation is presented how to derive reasonable weights \mathbf{W} and \mathbf{V} for designing a Kalman filter by utilizing information of the `idss` MATLAB® object (identified state-space model represented by (9.11)-(9.12))

$$\mathbf{x}(k+1) = \mathbf{A}\mathbf{x}(k) + \mathbf{B}\mathbf{u}(k) + \mathbf{K}\mathbf{e}(k) \quad (9.11)$$

$$\mathbf{y}(k) = \mathbf{C}\mathbf{x}(k) + \mathbf{D}\mathbf{u}(k) + \mathbf{e}(k) \quad (9.12)$$

on the estimated process noise model

$$\tilde{\mathbf{w}}(k) = \mathbf{K}\mathbf{e}(k) \quad (9.13)$$

⁹In MATLAB® the command `dlqr` can be used to compute a linear-quadratic state-feedback regulator for a discrete-time state-space system.

and measurement noise (in MATLAB[®] $\mathbf{e}(k)$ is called model innovations, see MATLAB[®] documentation `doc idss`)

$$\tilde{\mathbf{v}}(k) = \mathbf{e}(k) \quad (9.14)$$

Ideally the model innovation $\tilde{\mathbf{v}}(k) = \mathbf{e}(k)$ is a signal vector of uncorrelated white, Gaussian noise signals. It turned out that indeed its covariance matrix¹⁰

$$\tilde{\mathbf{V}} = \mathbb{E}\{\tilde{\mathbf{v}}(k)\tilde{\mathbf{v}}^T(k)\} \quad (9.15)$$

is a diagonal dominant matrix.¹¹

$$\tilde{\mathbf{V}} = \begin{bmatrix} 13,69 & -1,57 & 0,46 & 2,27 \\ -1,57 & 9,56 & -4,03 & -1,04 \\ 0,46 & -4,03 & 9,88 & -0,45 \\ 2,27 & -1,04 & -0,45 & 8,44 \end{bmatrix} \cdot 10^{-5} \quad (9.16)$$

The covariance matrix $\tilde{\mathbf{W}}$ of the estimated (white) process noise $\tilde{\mathbf{w}}(k)$ is computed by:

$$\tilde{\mathbf{W}} = \mathbb{E}\{\tilde{\mathbf{w}}(k)\tilde{\mathbf{w}}^T(k)\} = \mathbb{E}\{\mathbf{K}\mathbf{e}(k)\mathbf{e}^T(k)\mathbf{K}^T\} = \mathbf{K}\mathbb{E}\{\mathbf{e}(k)\mathbf{e}^T(k)\}\mathbf{K}^T = \mathbf{K}\tilde{\mathbf{V}}\mathbf{K}^T \quad (9.17)$$

Because in LQG the (white) process noise signal \mathbf{w} and (white) measurement noise signal \mathbf{v} are usually assumed to be uncorrelated (i.e. $\mathbb{E}\{\mathbf{w}(t)\mathbf{v}(t)^T\} = \mathbf{0}$; $\mathbb{E}\{\mathbf{v}(t)\mathbf{w}(t)^T\} = \mathbf{0}$) the diagonal values of $\tilde{\mathbf{V}}$ and $\tilde{\mathbf{W}}$ were chosen.

$$\mathbf{V} = \begin{bmatrix} \tilde{V}_{11} & 0 & 0 & 0 \\ 0 & \tilde{V}_{22} & 0 & 0 \\ 0 & 0 & \tilde{V}_{33} & 0 \\ 0 & 0 & 0 & \tilde{V}_{44} \end{bmatrix} \quad \mathbf{W} = \begin{bmatrix} \tilde{W}_{11} & 0 & \dots & 0 \\ 0 & \ddots & \ddots & \vdots \\ \vdots & \ddots & \ddots & 0 \\ 0 & \dots & 0 & \tilde{W}_{nn} \end{bmatrix} \quad (9.18)$$

In MATLAB[®] the command `kalman` was used to design a delayed Kalman state estimator $\mathbf{K}_{\text{est}}(z)$.¹² Then the command `lqgreg` was used to form the Linear Quadratic Gaussian (LQG) regulator $\mathbf{K}(z)$, which is of the same system order as the plant (i.e. same system order

¹⁰Given a measurement matrix $\mathbf{x}(k) = [x_1(k), \dots, x_i(k), \dots, x_n(k)]^T$ its empirical covariance matrix $\hat{\mathbf{C}}(\mathbf{x}) = \hat{\mathbf{C}}^T(\mathbf{x}) \geq 0$ (symmetric and positive semi-definite) is computed by:

$\hat{\mathbf{C}}(\mathbf{x}) = \mathbb{E}\{[\mathbf{x}(k) - \hat{\boldsymbol{\mu}}_x][\mathbf{x}(k) - \hat{\boldsymbol{\mu}}_x]^T\}$, where $\hat{\boldsymbol{\mu}}_x = [\hat{\mu}_1, \dots, \hat{\mu}_i, \dots, \hat{\mu}_n]^T$ and $\hat{\mu}_i$ is the empirical mean of the scalar signal $x_i(k)$.

Because a white noise signal $n_i(k)$ is zero-mean, for a vector of white noise signals $\mathbf{n}(k) = [n_1(k), \dots, n_i(k), \dots, n_n(k)]^T$

$\hat{\mathbf{C}}(\mathbf{n}) = \mathbb{E}\{\mathbf{n}(k)\mathbf{n}^T(k)\}$.

¹¹In MATLAB[®] the covariance matrix of the white, Gaussian noise component $\mathbf{e}(k)$ is obtained by: `idss_object.NoiseVariance`

Attention! The “`idss_object`” has to be the same state-space system with matrices $(\mathbf{A}, \mathbf{B}, \mathbf{C}, \mathbf{D})$ as $\mathbf{G}^{\text{SS}} = \begin{bmatrix} \mathbf{A} & \mathbf{B} \\ \mathbf{C} & \mathbf{D} \end{bmatrix}$ (same input-output scaling, same states).

¹²In MATLAB[®] the command `kalman` can be used to design a Kalman state estimator \mathbf{K}_{est} (dynamic system) for continuous- or discrete-time estimation problems, where in the later case a decision on the type of Kalman estimator (“current” or “delayed” estimator) has to be made.

as the Kalman estimator), by connecting the Kalman estimator $\mathbf{K}_{\text{est}}(z)$ and the optimal state-feedback gain \mathbf{K}_{LQR} .¹³

As desired (by the chosen values of the modal weighting factors m_i), the first and fourth modes are highly damped in the singular value plot of the simulated (nominal) closed-loop behavior (from d to \mathbf{y}) (Figure 9.11a). By applying the tenth order controller $\mathbf{K}(z)$ on the “IDbs(ho)-model”, the feedback system is also stable and the improvement of mode damping (Figure 9.11b) is quite similar. However, because of some model mismatch between the nominal (“IDbs-model”) and the “IDbs(ho)-model” around the first structural mode, the controller $\mathbf{K}(z)$ “splits” the first peak of the “IDbs(ho)-model” in two. This behavior of “splitting” the first peak of the “IDbs(ho)-model” was already seen for the mixed-sensitivity \mathcal{H}_∞ design of Section 9.2.1 (see Figure 9.4b). However, unlike in Section 9.2.1 here this behavior is not seen in Figure 9.12 which plots the singular values of the open-loop experimental validation model ($\mathcal{S}^{\text{OL-EV}}$) and those of the closed-loop experimental validation model ($\mathcal{S}^{\text{CL-EV}}$). For the closed-loop experimental validation model ($\mathcal{S}^{\text{CL-EV}}$) the improvement of damping of the first, third, fourth and fifth structural modes are about 9.15 dB, 0.65 dB, 5.66 dB and 0.9 dB, while the second structural mode remains unchanged in damping. The improvement in performance by the LQG controller is considered good, but especially for the fourth structural mode considerably less convincing than the performance achieved by the mixed-sensitivity \mathcal{H}_∞ design (see Figure 9.5 on page 124).

Again (as well as for the mixed-sensitivity \mathcal{H}_∞ design of Section 9.2.1) the experimental validated closed-loop behavior ($\mathcal{S}^{\text{CL-EV}}$) is in good accordance to the simulation on the “IDbs(ho)-model” confirming the latter as an accurate model, well suited for simulation purposes.

Because unlike computational sophisticated (time-consuming) design methods used in this work (especially D(G)K synthesized designs) where a plant of low order might significantly speed up the algorithms, for LQG a low plant order is not as crucial and the fact that LQG controllers have the same (in the case at hand relatively low) order as the plant might give rise to use the “IDbs(ho)-model” as a design plant. However, for reasons of better comparability among the different design methods the “IDbs-model” was used.

¹³The MATLAB[®] command `lqg`, which handles both continuous- and discrete-time plants (in the discrete case a “delayed” Kalman estimator is used) can be used to derive the LQG regulator \mathbf{K} in one call (e.g. `K_LQG = lqg(G,blkdiag(Q,R),blkdiag(W,V));`).

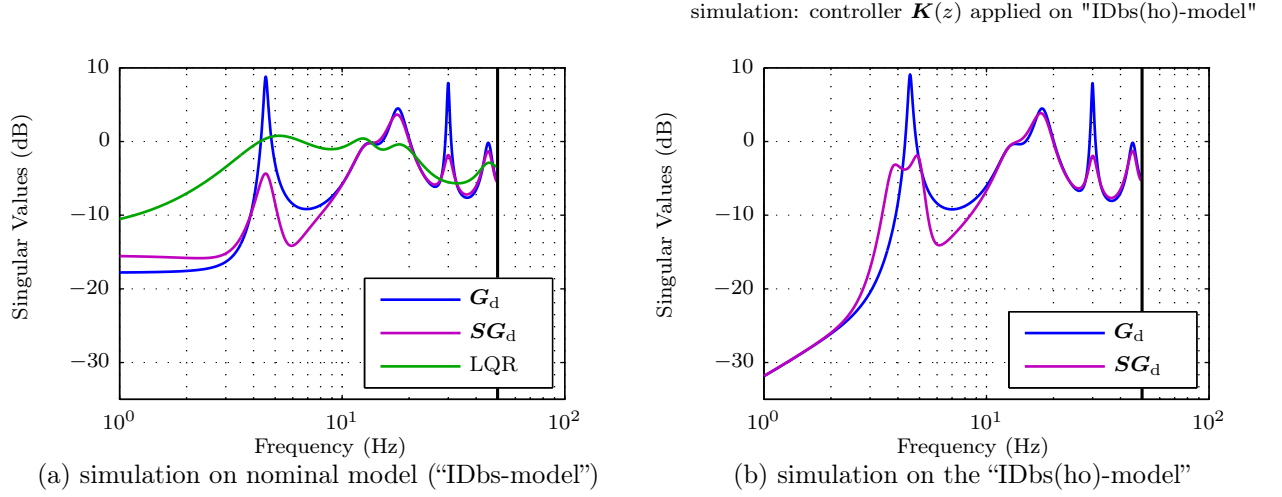


Figure 9.11: Singular values of simulated open-loop and closed-loop behavior (from d to \mathbf{y})

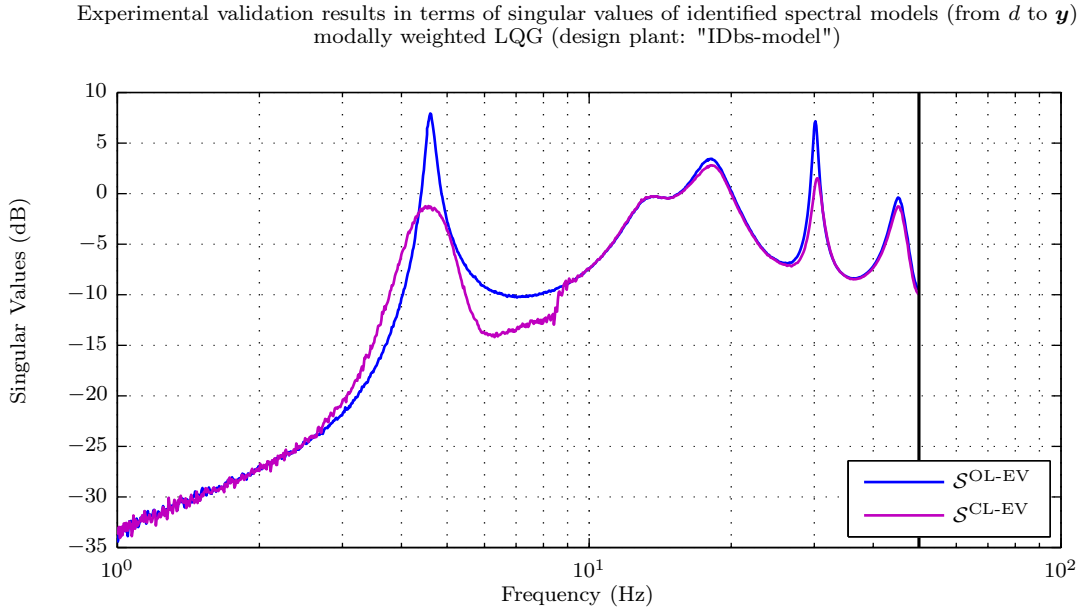


Figure 9.12: Experimental validation results in terms of singular values (from d to \mathbf{y}) of open-loop ($\mathcal{S}^{\text{OL-EV}}$) and closed-loop ($\mathcal{S}^{\text{CL-EV}}$) identified spectral models (modally weighted LQG design based on the "IDbs-model")

9.2.3 \mathcal{H}_∞ loop-shaping design for coprime factor uncertainty

In section 8.8.4 on page 116 two fundamentally different suggestions (when disturbance rejection is an issue) were made on how to derive a reasonable dynamic weighting matrix (compensator) \mathbf{W}_1 to shape the singular values of the open-loop plant \mathbf{G} before robustly stabilizing ("robustifying") the shaped plant (initial loop shape) $\mathbf{G}_s = \mathbf{W}_2 \mathbf{G} \mathbf{W}_1$ with respect to coprime factor uncertainty. One recommendation (see (8.132)) is to choose a dynamic weighting matrix $\mathbf{W}_1(z)$ with

$$\underline{\sigma}(\mathbf{W}_1(e^{j\omega T_s})) \approx \bar{\sigma}(\mathbf{G}^{-1}(e^{j\omega T_s})) \cdot \bar{\sigma}(\mathbf{G}_d(e^{j\omega T_s})) \quad (9.19)$$

or (in some sense more conservative) with

$$\underline{\sigma}(\mathbf{W}_1(e^{j\omega T_s})) \approx \bar{\sigma}(\mathbf{G}^{-1}\mathbf{G}_d(e^{j\omega T_s})). \quad (9.20)$$

The other proposal (in the case of disturbance rejection also applicable if the disturbance transfer function \mathbf{G}_d is unknown) was to utilize the loop shape $\mathbf{L}_{\text{success}}$ of an already successfully validated controller design method, e.g. by choosing a dynamic weighting matrix $\mathbf{W}_1(z) = W_1(z) \cdot \mathbf{I}$ with

$$|W_1(e^{j\omega T_s})| \approx \bar{\sigma}(\widetilde{\mathbf{W}}_1(e^{j\omega T_s})) \quad (9.21)$$

where

$$\widetilde{\mathbf{W}}_1(e^{j\omega T_s}) = \mathbf{G}^{-1}\mathbf{L}_{\text{success}}(e^{j\omega T_s}). \quad (9.22)$$

For the problem at hand, these proposals (equations (9.19) to (9.22)) are visualized in Figure 9.13, where for the loop shape $\mathbf{L}_{\text{success}}$ in (9.22) the loop shape of the modally weighted LQG design (Section 9.2.2) and that of the mixed-sensitivity \mathcal{H}_∞ design (Section 9.2.1) is used, together with the chosen $\mathbf{W}_1(z) = W_1(z) \cdot \mathbf{I}$ used for the \mathcal{H}_∞ loop-shaping design presented in the following. Figure 9.13, shows the loop shapes discussed. The multiplicative matrix norm inequality

$$\bar{\sigma}(\mathbf{G}^{-1}(e^{j\omega T_s})) \cdot \bar{\sigma}(\mathbf{G}_d(e^{j\omega T_s})) \geq \bar{\sigma}(\mathbf{G}^{-1}\mathbf{G}_d(e^{j\omega T_s})) \quad \forall \omega \in \mathbb{R} \quad (9.23)$$

holds. It is evident that $\bar{\sigma}(\mathbf{G}^{-1}\mathbf{L}_{\text{mixedS}}(e^{j\omega T_s}))$ has derivative behavior at low frequencies due to the chosen input and performance weights \mathbf{W}_u respectively \mathbf{W}_p (used in the mixed-sensitivity \mathcal{H}_∞ design). On the other hand, $\bar{\sigma}(\mathbf{G}^{-1}\mathbf{L}_{\text{LQG}}(e^{j\omega T_s}))$ has globally proportional behavior.¹⁴

It should be mentioned that $W_1(z)$ was shaped with respect to (9.20) (conservative version of the variant) which utilizes the disturbance model \mathbf{G}_d . At the time at which $W_1(z)$ was shaped \mathbf{L}_{LQG} and $\mathbf{L}_{\text{mixedS}}$ were not yet available and the approach (9.21)-(9.22) was not yet considered. However, it is evident from Figure 9.13 that these two different approaches can lead to a similar choice of $\mathbf{W}_1(z)$.

By approximating those dynamics of $\bar{\sigma}(\mathbf{G}^{-1}\mathbf{G}_d(e^{j\omega T_s}))$ considered important utilizing a “peak” and rethinking the shape outside the frequency range of interest spanned by the natural frequencies of the first five (structural) modes of the beam with mounted shaker (i.e. using a bandpass), a scalar compensator weight $W_1(s)$ was obtained. Then the compensator $W_1(z)$ (Figure 9.13) was obtained by discretizing $W_1(s)$ using the zero-pole matching method ($T_s = 0.01$ s).

At that point it should be mentioned that the depicted $W_1(z) = k \cdot W(z)$ with dynamics $W(z)$ and static gain k is the one with the largest value of k for which the obtained \mathcal{H}_∞ (loop-shaping) controller achieved stability in the hardware experiment and that numerous controllers were designed by varying k in small steps within a reasonable range. Also a variety of different dynamic shapes $W(z)$ with slightly differently shaped bandpass filters and different peak(s) were tested.

The design presented in the following with $\mathbf{W}_1(z)$ as depicted in Figure 9.13 was considered best with respect to the physical experiment.

¹⁴Actually also $\bar{\sigma}(\mathbf{G}^{-1}\mathbf{L}_{\text{mixedS}}(e^{j\omega T_s}))$ has globally proportional behavior but levels off at a much lower frequency with a value of about -38 dB.

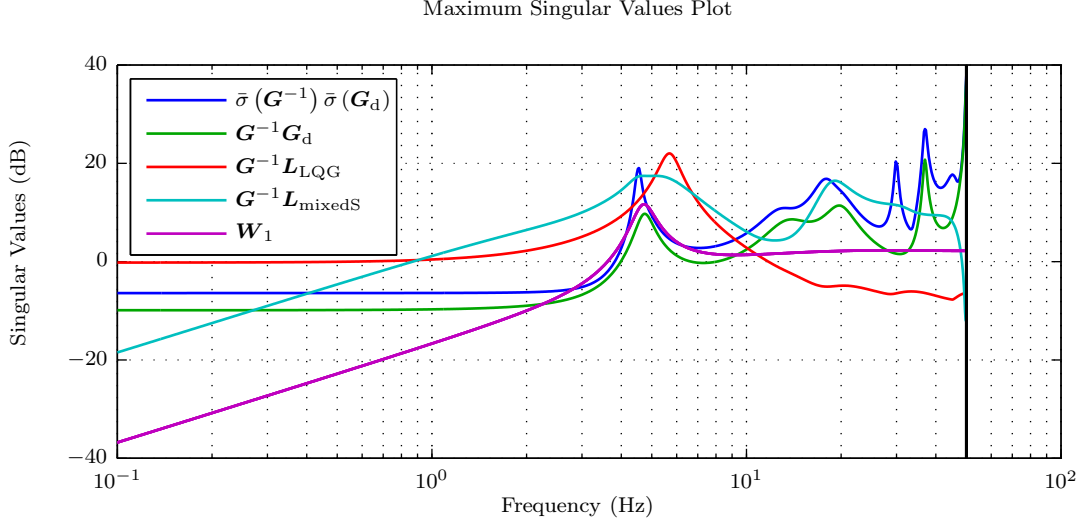


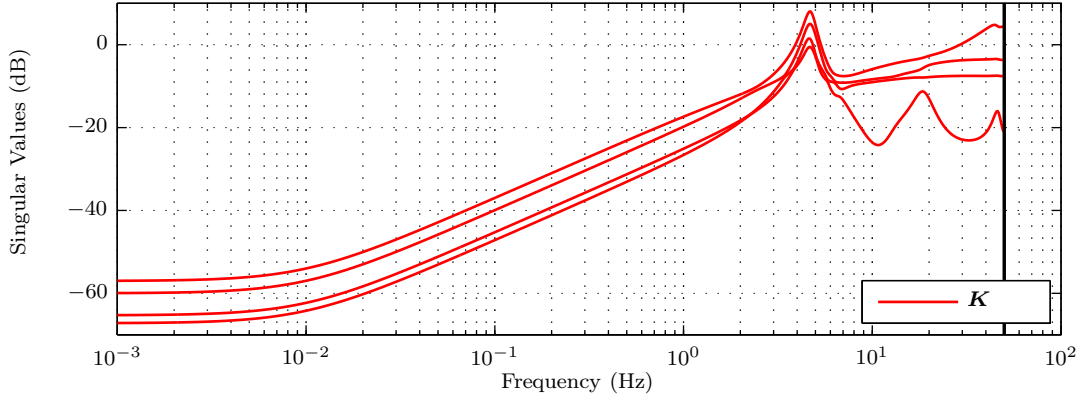
Figure 9.13: Maximum singular values of the weighting matrix (compensator) $\mathbf{W}_1(e^{j\omega T_s}) = \mathbf{W}_1(e^{j\omega T_s}) \cdot \mathbf{I}$ and suggested guidelines

By using the MATLAB[®] command `ncfsyn` a stabilizing, optimal, positive feedback controller $\mathbf{K} = \mathbf{W}_1 \mathbf{K}_s \mathbf{W}_2$ with 41 states ($\mathbf{G}_s(z)$ has 26 states, $\mathbf{K}_s(z)$ has 25 states, and $\mathbf{W}_1(z)$ has 16 states) was obtained, which itself is stable in this case. In general, \mathbf{K}_s has the same number of poles (states) as \mathbf{G}_s [6]. The observation that $\mathbf{K}_s(z)$ has less states than $\mathbf{G}_s(z)$ directly after design has not been investigated further.

Remark: Except for special systems, ones with all-pass factors, there are no pole-zero cancellations between the plant and controller. Pole-zero cancellations are common in some other \mathcal{H}_∞ control problems, like the mixed-sensitivity problem with stacked \mathbf{S}/\mathbf{T} , and are a problem when the plant has lightly damped modes.[6]

As desired, all singular values of \mathbf{K} (Figure 9.14) are high around the natural frequency of the first structural mode. Note that at low frequencies and in particular around the first structural mode the singular values of \mathbf{K} are close, whereas above the natural frequency of the first structural mode this behavior is not observed. This may be connected to the similar shape of the singular values of \mathbf{G}_s (respectively \mathbf{G} , see \mathbf{G}^{IDbs} in Figure 6.5), but seems to be characteristic for this design method.¹⁵ For other controller design methods this behavior of “tight” singular values of \mathbf{K} at frequencies where the design requires high performance was not seen (compare Figure 9.2 (mixed-sensitivity \mathcal{H}_∞ control), Figure 9.19 (DK synthesized μ –“optimal” controller)).

¹⁵If a controller with $\gamma(\mathbf{K}) = \bar{\sigma}(\mathbf{K})/\underline{\sigma}(\mathbf{K})$ close to 1 is utilized, then the sensitivity function is not sensitive to (both diagonal and full-block) input uncertainty. [6] Thus, although input uncertainty is not explicitly modelled for the problem at hand, the design can be expected to have good robustness properties with respect to input uncertainty (at the natural frequency of the first structural mode).

Figure 9.14: Singular values of the feedback controller K

The design achieves a considerably small $\gamma = 1.4$ (i.e. the usually postulated criterion of $\gamma < 4$ is fulfilled) and thus allows for $\epsilon = 71.4\%$ ($\epsilon = 1/\gamma$) coprime factor uncertainty.

In Figure 9.15 the singular values of the desired loop shape (shaped plant) \mathbf{G}_s and those of the actual loop transfer function \mathbf{L} are shown.

Because $\underline{\sigma}(\mathbf{L}(e^{j\omega T_s}))$ is not significantly larger than 1 (actually $\underline{\sigma}(\mathbf{L}(e^{j\omega T_s})) < 1$) the underlying approximation

$$\bar{\sigma}(\mathbf{S}(e^{j\omega T_s})) \approx \frac{1}{\underline{\sigma}(\mathbf{L}(e^{j\omega T_s}))} \quad (9.24)$$

(see (8.108) and (8.109)) which in the case of disturbance rejection is used to postulate a closed-loop equivalent open-loop requirement, where for reasonable disturbance rejection $\underline{\sigma}(\mathbf{L}(e^{j\omega T_s}))$ should have been large (see Table 8.1), is not valid at all.

It would have been desirable by the choice of $\mathbf{W}_1(z)$ ($\mathbf{W}_1(z) = k \cdot W(z) \cdot \mathbf{I}$) to achieve $\underline{\sigma}(\mathbf{G}_s(e^{j\omega T_s}))$ sufficiently large at frequencies where disturbance rejection is an issue (i.e. around the natural frequencies of the structural modes), but this (at least with a scalar $W_1(z)$) could not be accomplished although many different dynamics $W(z)$ (e.g. using sharp peaks) were tried in $\mathbf{W}_1(z)$. For large(r) values of k the design turned out to be unstable in the experiment. Thus, despite the fact that γ is sufficiently small, the undesirably small $\underline{\sigma}(\mathbf{G}_s(e^{j\omega T_s}))$ (around the natural frequencies of the structural modes) leads to an undesirably small $\underline{\sigma}(\mathbf{K}_s(e^{j\omega T_s}))$, which in the following deteriorates the loop shape $\mathbf{L} = \mathbf{G}_s \mathbf{K}_s$ in terms of $\underline{\sigma}(\mathbf{L}(e^{j\omega T_s}))$. Comparing $\underline{\sigma}(\mathbf{G}_s(e^{j\omega T_s}))$ with $\underline{\sigma}(\mathbf{L}(e^{j\omega T_s}))$ in Figure 9.15 around the natural frequencies of the first and fourth structural modes reveals that the degradation in the loop shape caused by the \mathcal{H}_∞ controller \mathbf{K}_s (in terms of $\underline{\sigma}(\mathbf{L}(e^{j\omega T_s}))$) is considerably larger around the natural frequency of the fourth structural mode.

Note that if the scaling matrix \mathbf{D}_e in (6.6) and (6.7) is reduced by multiplying each $\hat{e}_{i\max}$ in \mathbf{D}_e by $1/c$ ($c > 1$), this leads, by applying equations (9.19) to (9.22) to the same suggestion for \mathbf{W}_1 , while \mathbf{G} and thus \mathbf{G}_s will be lifted by c . Hence for input-, output-scaled plants which minimum singular values lie already relatively far above the 0 dB line, the deterioration in terms of $\underline{\sigma}(\mathbf{L}(e^{j\omega T_s}))$ will be less. However, the aspect of input-, output-scaling as outlined in Section 6.2 should be used to compare the relative importance of different transfer paths and not for controller tuning.

On the one hand, the set of perturbed plants described by coprime factor uncertainty, which allows for zeros as well as poles to cross into the RHP [6] (i.e. in the discrete-time case leave the unit circle) is unnecessarily large for the problem at hand (flexible structure),

because a passive flexible structure is stable and thus has no unstable poles. Hence an obtained positive feedback controller \mathbf{K} might be too conservative, achieving only modest performance. On the other hand, the fact that with a larger value of k in $\mathbf{W}_1(z) = k \cdot W(z) \cdot \mathbf{I}$ the obtained positive feedback controller \mathbf{K} was not capable to attain stability in the experiment, despite the circumstance that the design achieved a sufficiently small γ (i.e. large stability margin ϵ with respect to normalized coprime factor uncertainty), indicates that although the set of perturbed plants for which the design was ensured to be robustly stable was considerably large, the real uncertainty of the plant was not taken into account by the design.

Consequently in the case of a flexible structure using an \mathcal{H}_∞ loop-shaping design (i.e., describing the set of perturbed plants utilizing normalized coprime factor uncertainty) might not achieve satisfying results.

Experimental results are presented in the following.

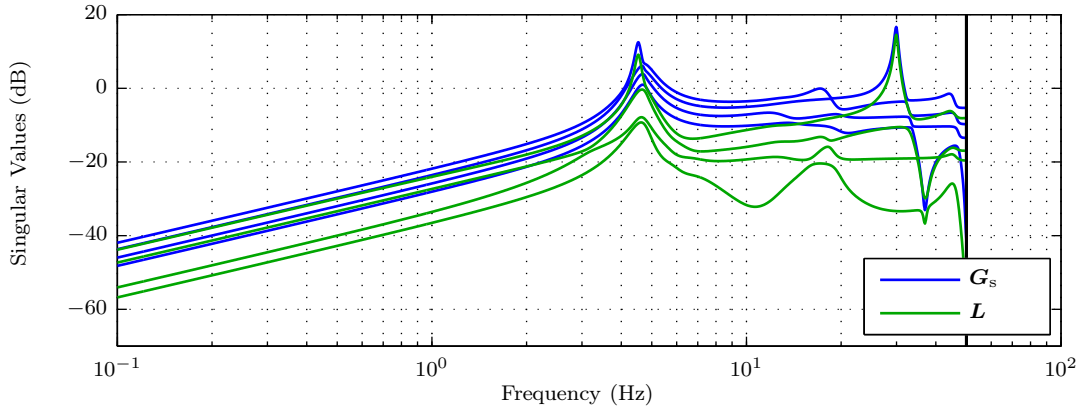


Figure 9.15: Singular values of desired loop shape or shaped plant \mathbf{G}_s ($\mathbf{G}_s(z) = \mathbf{G}(z)\mathbf{W}_1(z)$) and actual loop transfer function \mathbf{L}

The singular value plot (Figure 9.16a) of the simulated (nominal) closed-loop behavior ($\mathbf{y} = \mathbf{S}\mathbf{G}_d d$) looks promising when comparing it to the simulated (nominal) open-loop behavior ($\mathbf{y} = \mathbf{G}_d d$). The first and especially the fourth mode are highly damped by the positive feedback controller \mathbf{K} , while the damping of all other structural modes are not significantly changed. By applying the controller \mathbf{K} on the “IDbs(ho)-model”, the positive feedback system is also stable and the improvement of mode damping (Figure 9.16b) is similar.

Figure 9.17 plots the singular values of the open-loop experimental validation model ($\mathcal{S}^{\text{OL-EV}}$) and those of the closed-loop experimental validation model ($\mathcal{S}^{\text{CL-EV}}$). Although $\underline{\sigma}(\mathbf{L}(e^{j\omega T_s}))$ has its highest value around the natural frequency of the first structural mode (see Figure 9.15), the improvement in mode damping of the first mode is comparatively small (reduction of 5.1 dB). With some surprise the fourth mode is reduced by more than 8.6 dB, which is considered good. The minor improvement of damping of the second and third structural modes are about 0.4 dB and 0.26 dB, while the fifth remains unchanged in damping.

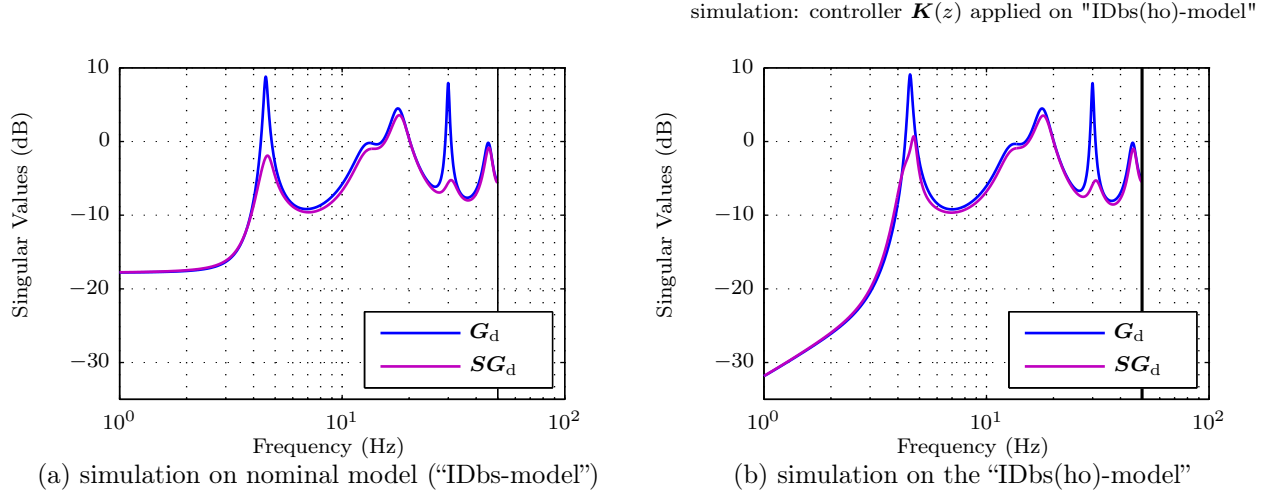


Figure 9.16: Singular values of simulated open-loop and closed-loop behavior (from d to y)

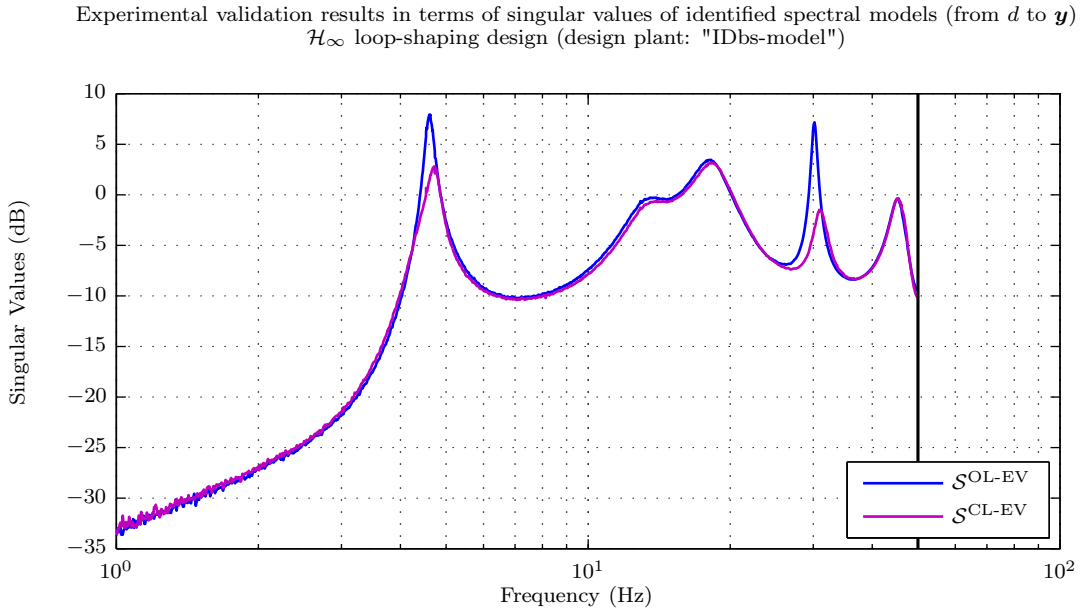


Figure 9.17: Experimental validation results in terms of singular values (from d to y) of open-loop ($\mathcal{S}^{\text{OL-EV}}$) and closed-loop ($\mathcal{S}^{\text{CL-EV}}$) identified spectral models (\mathcal{H}_∞ loop-shaping design based on the "IDbs-model")

9.2.4 DK synthesized μ -"optimal" controller

The DK synthesized μ -"optimal" design is similar to the mixed-sensitivity \mathcal{H}_∞ design of section 9.2.1 except for the modelled uncertainty and the positive sign in front of \mathbf{W}_u (which is irrelevant in the following). Thus the performance weight $\mathbf{W}_P(z)$ and input weight $\mathbf{W}_u(z)$ were chosen in a similar fashion (Figure 9.18).

A scalar performance weight $W_P(s)$ was chosen as a bandpass with four additional peaks. These four peaks were utilized to put strong weights on the low-damped first and fourth modes as well as on the moderately damped third and fifth modes. Thus, by design of

$W_P(s)$, performance is not an issue at low and high frequencies, where actuation is neither required nor desired. Again, the scalar input weight $W_u(s)$ was selected as a bandstop. Thus input usage is highly penalized outside the frequency range of interest spanned by the natural frequencies of the first five (structural) modes of the beam with mounted shaker.

The uncertainty weights $W_{1I}(s)$ and $W_{1O}(s)$ for complex diagonal multiplicative input respectively output uncertainty were chosen as scalar bandstop filters, thus the uncertainty is the same for all inputs/outputs. The attenuation in the stopband is about 26 dB, hence at intermediate frequencies the design allows for 5 % multiplicative (input respectively output) uncertainty. At those low and high frequencies where the uncertainty weights $W_{1I}(s)$ and $W_{1O}(s)$ exceed 0 dB and thus the design allows for more than 100 % multiplicative (input respectively output) uncertainty, the phase of each SISO transfer function representing a physical system on the plant's input side (e.g. high voltage amplifier, piezo patch actuator) respectively output side (e.g. piezo patch sensor) is considered unknown (see (8.52) and (8.53)).

For the additive uncertainty weight $W_{1A}(z)$ the following approach was taken.

A set of plants Π may be represented by additive uncertainty using

$$\mathbf{G}_p = \mathbf{G} + \underbrace{W_{1A}\Delta_A}_{\mathbf{E}_A} \quad (9.25)$$

where Δ_A is considered as a full complex norm-bounded perturbation ($\|\Delta_A\|_\infty \leq 1$) and the scalar weight $W_{1A}(z)$ is chosen such that at each frequency ω

$$|W_{1A}(e^{j\omega T_s})| \geq l_A(\omega) \quad \forall \omega \in \mathbb{R} \quad (9.26)$$

holds. At each frequency ω the smallest scalar $l_A(\omega)$ is given by

$$l_A(\omega) = \max_{\mathbf{G}_p \in \Pi} \bar{\sigma}(\underbrace{\mathbf{G}_p(e^{j\omega T_s}) - \mathbf{G}(e^{j\omega T_s})}_{\mathbf{E}_A(e^{j\omega T_s})}). \quad (9.27)$$

In the following, $\mathbf{G}^{\text{IDbs(ho)}}(z)$ was considered as one perturbed plant in (9.27), thus

$$l_A(\omega) = l_A^{\text{IDbs(ho)}}(\omega) = \bar{\sigma} \left(\underbrace{\mathbf{G}^{\text{IDbs(ho)}}(e^{j\omega T_s}) - \mathbf{G}^{\text{IDbs}}(e^{j\omega T_s})}_{\mathbf{E}_A^{\text{IDbs(ho)}}(e^{j\omega T_s})} \right). \quad (9.28)$$

Then a simplified scalar rational weight $W_{1A}(z)$ was shaped so that at each frequency ω the magnitude of $W_{1A}(e^{j\omega T_s})$ was larger than $l_A^{\text{IDbs(ho)}}(\omega)$. By this means, the chosen shape of $W_{1A}(z)$ accounts for the neglected dynamics of $\mathbf{G}^{\text{IDbs(ho)}}(z)$.

The singular values of the discretized¹⁶ performance ($\mathbf{W}_P(z)$), input ($\mathbf{W}_u(z)$) and uncertainty weights ($\mathbf{W}_{1I}(z)$, $\mathbf{W}_{1O}(z)$, $\mathbf{W}_{1A}(z)$) are depicted in Figure 9.18 together with $l_A^{\text{IDbs(ho)}}(\omega) = \bar{\sigma}(\mathbf{E}_A^{\text{IDbs(ho)}}(e^{j\omega T_s}))$. For simplicity, the weights \mathbf{W}_{2I} , \mathbf{W}_{2O} , and \mathbf{W}_{2A} were chosen as identity matrices and are not depicted.

¹⁶zero-pole matching method; $T_s = 0.01$ s

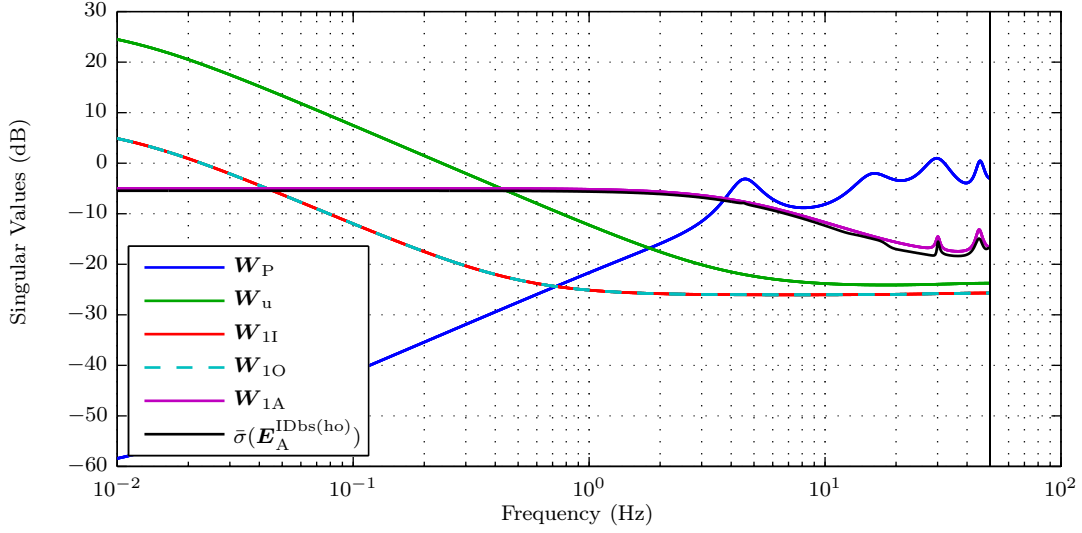


Figure 9.18: Singular values of performance weight \mathbf{W}_P ; input weight \mathbf{W}_u ; \mathbf{W}_{II} , \mathbf{W}_{1O} for multiplicative input respectively output uncertainty, and \mathbf{W}_{1A} for additive uncertainty weighting

By utilizing the MATLAB[®] command `sysic`, the generalized plant $\mathbf{P}(z)$ (24×17) (9.29) of Figure 8.16 on page 110 (where the scalar $w_1 = d$ was chosen as the only exogenous input) was obtained with $n_P = 100$ states.

$$\begin{bmatrix} y_{\Delta_I} \\ y_{\Delta_A} \\ y_{\Delta_O} \\ z_1 \\ z_2 \\ v \end{bmatrix} = \underbrace{\begin{bmatrix} 0 & 0 & 0 & 0 & \mathbf{W}_{II} \\ \mathbf{W}_{1A}\mathbf{W}_{2I} & 0 & 0 & 0 & \mathbf{W}_{1A} \\ \mathbf{W}_{1O}\mathbf{G}\mathbf{W}_{2I} & \mathbf{W}_{1O}\mathbf{W}_{2A} & 0 & 0 & \mathbf{W}_{1O}\mathbf{G} \\ \mathbf{W}_P\mathbf{G}\mathbf{W}_{2I} & \mathbf{W}_P\mathbf{W}_{2A} & \mathbf{W}_P\mathbf{W}_{2O} & \mathbf{W}_P\mathbf{G}_d & \mathbf{W}_P\mathbf{G} \\ 0 & 0 & 0 & 0 & \mathbf{W}_U \\ -\mathbf{G}\mathbf{W}_{2I} & -\mathbf{W}_{2A} & -\mathbf{W}_{2O} & -\mathbf{G}_d & -\mathbf{G} \end{bmatrix}}_{\mathbf{P}} \begin{bmatrix} u_{\Delta_I} \\ u_{\Delta_A} \\ u_{\Delta_O} \\ w_1 \\ u \end{bmatrix} \quad (9.29)$$

In MATLAB[®] the command `ultidyn` can be used to create an uncertain linear time-invariant (LTI) object Δ_i (see (8.56)) of specified input/output size which (if the property 'Type' is set to 'GainBounded') only specified attribute is an upper bound (property 'Bound') on its maximum singular value at all frequencies. To ensure that $\|\Delta_i\|_\infty \leq 1$ (see (8.57)) the property 'Bound' was set to 1.

By this means the complex diagonal Δ_I -block (4×4) and Δ_O -block (4×4) representing the normalized perturbations for multiplicative input respectively output uncertainty were each created by diagonally combining always four different SISO Δ_i -blocks (1×1) utilizing the MATLAB[®] command `blkdiag`, whereas the full complex Δ_A -block (4×4) representing the normalized perturbation for additive uncertainty was directly obtained by specifying the size of an uncertain linear time-invariant object Δ_i with (4×4). Finally, the overall block-diagonal perturbation matrix Δ (8.100) was created by block-diagonally combining the Δ_I -, Δ_A - and Δ_O -block.

Then the command `lft(Delta,P)` was used to obtain a perturbed generalized plant $\mathbf{P}_p = \mathcal{F}_u(\mathbf{P}, \Delta)$ (12×5) which was required for the subsequent command `dksyn`, which

performs an automated DK-iteration. A demonstrative, executable, simple MATLAB[®] example performing DK-iteration is found in [6].

With dynamic scalings $\check{\mathbf{D}}_r(z)$ (24×24) and $\check{\mathbf{D}}_l(z)$ (17×17) ($n_{\check{\mathbf{D}}_r} = n_{\check{\mathbf{D}}_l} = 66$ states) (see (8.95)) the automated DK-iteration synthesized a stable controller $\mathbf{K}^{\text{syn}}(z)$ (4×4) with $n_{\mathbf{K}^{\text{syn}}} = 232$ states¹⁷ ($n_{\mathbf{K}^{\text{syn}}} = n_{\mathbf{P}} + n_{\check{\mathbf{D}}_r} + n_{\check{\mathbf{D}}_l}$). Because, in the case at hand, the generalized plant $\mathbf{P}(z)$ is stable and because the dynamic scaling transfer function matrices $\mathbf{D}_r(z)$ and $\mathbf{D}_l(z)$ (see Figure 8.15) are always chosen stable and minimum-phase, the dynamically scaled plant $\check{\mathbf{P}}(z)$ with (discrete-time) state-space realization

$$\check{\mathbf{P}}(z) \stackrel{\text{ss}}{=} \left[\begin{array}{c|cc} \mathbf{A} & \mathbf{B}_1 & \mathbf{B}_2 \\ \hline \mathbf{C}_1 & \mathbf{D}_{11} & \mathbf{D}_{12} \\ \mathbf{C}_2 & \mathbf{D}_{21} & \mathbf{D}_{22} \end{array} \right] \quad (9.30)$$

is stable, i.e. for all eigenvalues of the state matrix \mathbf{A}

$$|\lambda_i(\mathbf{A})| \leq 1 \text{ for } i = 1, \dots, n_{\check{\mathbf{P}}} \quad (9.31)$$

holds. Thus, independent of \mathbf{B}_2 and \mathbf{C}_2 assumption A.1 in Definition 8.1 is ensured, so that in the K-step (of the DK-iteration algorithm) an internally stabilizing sub-optimal \mathcal{H}_∞ controller $\mathbf{K}^{\text{syn}}(z)$ is synthesized. In other words, in the case at hand, $\mathbf{N}^{\text{syn}}(z) = \mathcal{F}_l(\mathbf{P}(z), \mathbf{K}^{\text{syn}}(z))$ (20×13) is guaranteed to be nominally stable with $\mathbf{K}^{\text{syn}}(z)$ because the generalized plant $\mathbf{P}(z)$ is stable.

With the synthesized controller $\mathbf{K}^{\text{syn}}(z)$ the design just achieved robust performance (i.e. $\max_{\omega} \mu_{\hat{\Delta}}(\mathbf{N}^{\text{syn}}(e^{j\omega T_s})) = 0.9719 < 1$). Where the μ -curve for robust performance (RP) with the synthesized μ -“optimal” controller $\mathbf{K}^{\text{syn}}(z)$ (not shown, but similar to Figure 9.20 for the reduced controller $\mathbf{K}(z)$) showed sharp peaks and its maximum value occurred at $\omega = 29.164 \text{ rad/s}$ (which is close to the natural angular frequency of the first structural mode). Because the controller $\mathbf{K}^{\text{syn}}(z)$ is not the true μ -optimal controller the peaks of the plant and the weights can easily be spotted in the μ -curve for robust performance.

The true μ -optimal controller would have a flat μ -curve (as a function of frequency), except at infinite frequency where μ generally has to approach a fixed value independent of the controller (because $\mathbf{L}(j\infty) = \mathbf{0}$ for real systems). However, with a finite-order controller we will generally not be able (and it may not be desirable) to extend the flatness to infinite frequencies. [6]

With the chosen sampling time the execution on the real-time development system could not be carried out for feedback controllers with more than 70 states. Thus, a subsequent balanced system reduction (based on Hankel singular values) with a multiplicative error method (which tends to produce a better fit for systems with low-damped poles or zeros [14]) that minimizes the relative error between the original and the reduced system was used to perform an order reduction of the synthesized controller $\mathbf{K}^{\text{syn}}(z)$. The intention of the reduction was merely to obtain a reduced controller $\mathbf{K}(z)$ which was executable on the real-time development system.

The reduced controller $\mathbf{K}(z)$, which is also stable, has $n_{\mathbf{K}} = 60$ states and (despite the considerably smaller system order) its singular values are barely distinguishable from those of the synthesized controller $\mathbf{K}^{\text{syn}}(z)$ (Figure 9.19).

¹⁷ $\mathbf{K}^{\text{syn}}(z)$ is of the same system order as the dynamically scaled generalized plant (see Section 8.6.12).

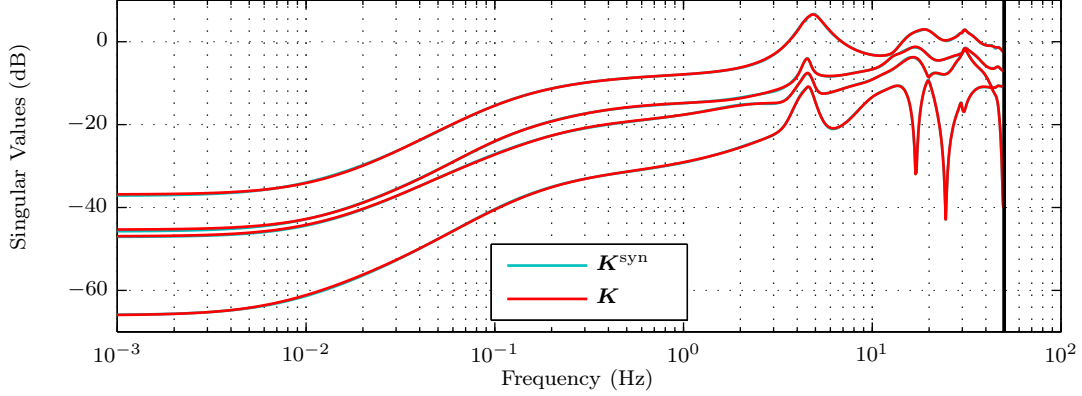


Figure 9.19: Singular values of the feedback controllers \mathbf{K}^{syn} and the reduced controller \mathbf{K}

The nominal closed loop system $\mathbf{N}(z) = \mathcal{F}_l(\mathbf{P}(z), \mathbf{K}(z))$ (20×13) (MATLAB[®] command $\mathbf{N} = \text{lft}(\mathbf{P}, \mathbf{K})$) with the reduced controller $\mathbf{K}(z)$ is internally stable. Hence, also the design with $\mathbf{K}(z)$ achieves nominal stability (NS) (see Definition 8.2 on page 99).

Also the design with the reduced controller $\mathbf{K}(z)$ just achieves robust performance. Thus the performance specification $\|\mathbf{F}\|_\infty < 1$ with \mathbf{F} as in (9.32) ($\mathbf{S}_p = (\mathbf{I} + \mathbf{G}_p \mathbf{K})^{-1}$ is the perturbed sensitivity function) is satisfied for all possible perturbed plants $\mathbf{G}_p(z)$ described by (8.96).

$$\begin{bmatrix} z_1 \\ z_2 \end{bmatrix} = \underbrace{\begin{bmatrix} \mathbf{W}_p \mathbf{S}_p \mathbf{G}_d \\ -\mathbf{W}_u \mathbf{K} \mathbf{S}_p \mathbf{G}_d \end{bmatrix}}_{\mathbf{F}} w_1 \quad (9.32)$$

For the final design (with the reduced controller $\mathbf{K}(z)$) the results of a μ -analysis for nominal performance ($\bar{\sigma}(\mathbf{N}_{22}(e^{j\omega T_s})) = \mu_{\Delta_p}(\mathbf{N}_{22}(e^{j\omega T_s}))$), robust stability ($\mu_{\Delta}(\mathbf{N}_{11}(e^{j\omega T_s}))$) and robust performance ($\mu_{\hat{\Delta}}(\mathbf{N}(e^{j\omega T_s}))$) are depicted in Figure 9.20. In order to account for sharp peaks of the μ -curves the frequency grid was tightened around the frequencies of these peaks.

The objective of nominal performance (NP) is most critical at 45.64 Hz, which is close to the natural frequency of the fifth structural mode, with $\|\mathbf{N}_{22}(e^{j2\pi f T_s})\|_\infty = 0.8711$. For the modelled uncertainty the objective of robust stability (RS) is most critical at 4.0421 Hz with $\max_f \mu_{\Delta}(\mathbf{N}_{11}(e^{j2\pi f T_s})) = 0.6708$, but nevertheless RS is easily satisfied. Especially in the high frequency range $\mu_{\Delta}(\mathbf{N}_{11}(e^{j\omega T_s}))$ is quite low. At any fixed frequency the design can tolerate up to $1/\mu_{\Delta}(\mathbf{N}_{11}(e^{j2\pi f T_s}))$ times the modelled uncertainty before RS is lost.

The design with the reduced controller $\mathbf{K}(z)$ is also most critical at 4.6416 Hz (which is close to the natural frequency of the first structural mode), where the μ -curve for robust performance (RP) $\mu_{\hat{\Delta}}(\mathbf{N}(e^{j2\pi f T_s}))$ reaches its maximum (i.e. $\max_f \mu_{\hat{\Delta}}(\mathbf{N}(e^{j2\pi f T_s})) = 0.9717 < 1$). High values of $\mu_{\hat{\Delta}}(\mathbf{N}(e^{j2\pi f T_s}))$ also occur at the natural frequencies of the third, fifth, and fourth structural modes indicating that with the modelled uncertainty robust performance is just achieved at these frequencies. Nevertheless it is guaranteed that at a certain frequency the design can tolerate up to $1/\mu_{\hat{\Delta}}(\mathbf{N}(e^{j2\pi f T_s}))$ -times the modelled uncertainty and satisfy the performance objective with a margin of $1/\mu_{\hat{\Delta}}(\mathbf{N}(e^{j2\pi f T_s}))$.

The fact that the design achieves RP, with uncertain closed-loop transfer function \mathbf{F} as in (9.32) ensures, because of (8.28), that for any allowed perturbation Δ also $\|\mathbf{W}_p \mathbf{S}_p \mathbf{G}_d\|_\infty < 1$ and $\|\mathbf{W}_u \mathbf{K} \mathbf{S}_p \mathbf{G}_d\|_\infty < 1$ holds.

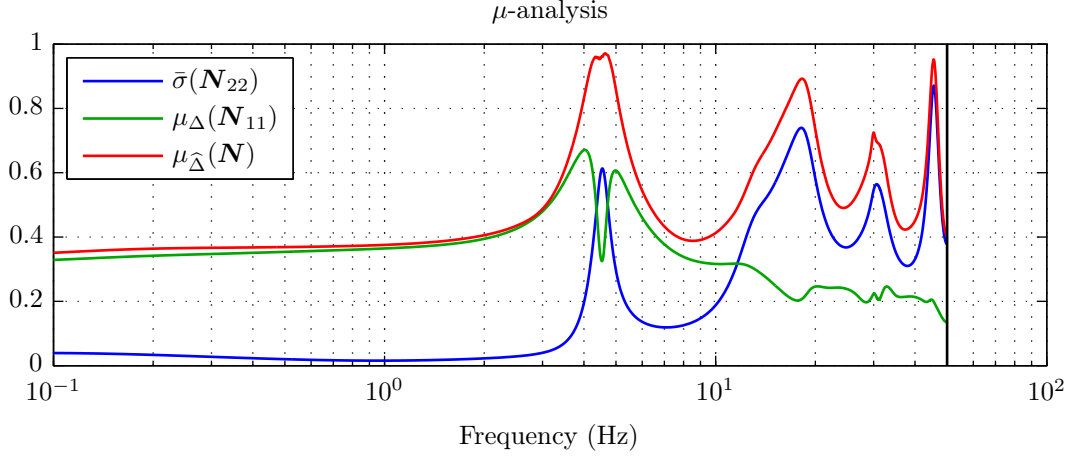


Figure 9.20: μ -analysis (upper bounds) of nominal performance ($\bar{\sigma}(\mathbf{N}_{22}(e^{j2\pi f T_s})) = \mu_{\Delta_P}(\mathbf{N}_{22}(e^{j2\pi f T_s}))$), robust stability ($\mu_{\Delta}(\mathbf{N}_{11}(e^{j2\pi f T_s}))$) and robust performance ($\mu_{\hat{\Delta}}(\mathbf{N}(e^{j2\pi f T_s}))$)

Because the design accounts for the neglected dynamics of $\mathbf{G}^{\text{IDbs(ho)}}(z)$ through additive uncertainty (see shape of $W_{1A}(z)$ in Figure 9.18), $\mathbf{G}^{\text{IDbs(ho)}}(z)$ is included in the set of possibly perturbed plants $\mathbf{G}_p(z)$ described by (8.96). Thus, the performance objective $\|\mathbf{F}\|_{\infty} < 1$ ($\mathbf{F} = \mathcal{F}_u(\mathbf{N}, \Delta)$) is (also) satisfied for this particular perturbed plant (Figure 9.21), where $\|\mathcal{F}_u(\mathbf{N}, \Delta^{\text{IDbs(ho)}})\|_{\infty} = 0.8693$ (which is even lower than $\|\mathbf{N}_{22}(e^{j2\pi f T_s})\|_{\infty} = 0.8711$) is reached at 45.46 Hz. Where, $\Delta^{\text{IDbs(ho)}}(z)$ with $\|\Delta^{\text{IDbs(ho)}}\|_{\infty} = 0.9814 < 1^{18}$ is the particular, known perturbation, which, by utilizing it together with the chosen uncertainty weights (Figure 9.18) in (8.96) results in $\mathbf{G}^{\text{IDbs(ho)}}(z)$. Around the natural frequency of the first structural mode the perturbation $\Delta^{\text{IDbs(ho)}}(z)$ deteriorates the performance objective the most.

For the modelled uncertainty the worst-case performance at a given frequency, i.e. skewed- μ ($\mu^s(\mathbf{N}(e^{j\omega T_s}))$) is also depicted in Figure 9.21. At 45.46 Hz skewed- μ reaches its maximum value of 0.9468. However, in relation to nominal performance ($\bar{\sigma}(\mathbf{N}_{22}(e^{j2\pi f T_s}))$), the perturbation Δ can cause the worst deterioration in performance for the first structural mode. The modelled uncertainty can cause severe performance deterioration at around 4.6 Hz. Note, that $\bar{\sigma}(\mathbf{W}_{1A}(e^{j\omega T_s}))$ allows for large additive uncertainty at these frequencies.

Note that, because the design achieves RP (i.e. $\max_f \mu_{\hat{\Delta}}(\mathbf{N}(e^{j2\pi f T_s})) < 1$) at a given frequency $\mu^s(\mathbf{N}(e^{j2\pi f T_s})) \leq \mu_{\hat{\Delta}}(\mathbf{N}(e^{j2\pi f T_s}))$ holds (see Figure 9.21). This is, because μ^s is always further from 1 than μ (see Definition 8.10).

¹⁸The blocks in $\Delta^{\text{IDbs(ho)}}(z)$ associated with the multiplicative input and output uncertainties can be considered zero (i.e. $\Delta_I^{\text{IDbs(ho)}} = \mathbf{0}$ and $\Delta_O^{\text{IDbs(ho)}} = \mathbf{0}$). Consequently $\bar{\sigma}(\Delta^{\text{IDbs(ho)}}(e^{j\omega T_s})) = \bar{\sigma}(\Delta_A^{\text{IDbs(ho)}}(e^{j\omega T_s}))$ holds. Furthermore, the maximum of $\bar{\sigma}(\Delta_A^{\text{IDbs(ho)}}(e^{j\omega T_s}))$ is reached at 50 Hz where $\bar{\sigma}(\mathbf{E}_A^{\text{IDbs(ho)}}(e^{j\omega T_s}))$ is closest to $\bar{\sigma}(\mathbf{W}_{1A}(e^{j\omega T_s}))$. Note that $\mathbf{E}_A^{\text{IDbs(ho)}} = \mathbf{W}_{1A} \Delta_A^{\text{IDbs(ho)}}$ with $\mathbf{W}_{1A}(z) = W_{1A}(z) \cdot \mathbf{I}$ and thus $\bar{\sigma}(\Delta_A^{\text{IDbs(ho)}}(e^{j\omega T_s})) = \bar{\sigma}(\mathbf{E}_A^{\text{IDbs(ho)}}(e^{j\omega T_s})) / |W_{1A}(e^{j\omega T_s})|$.

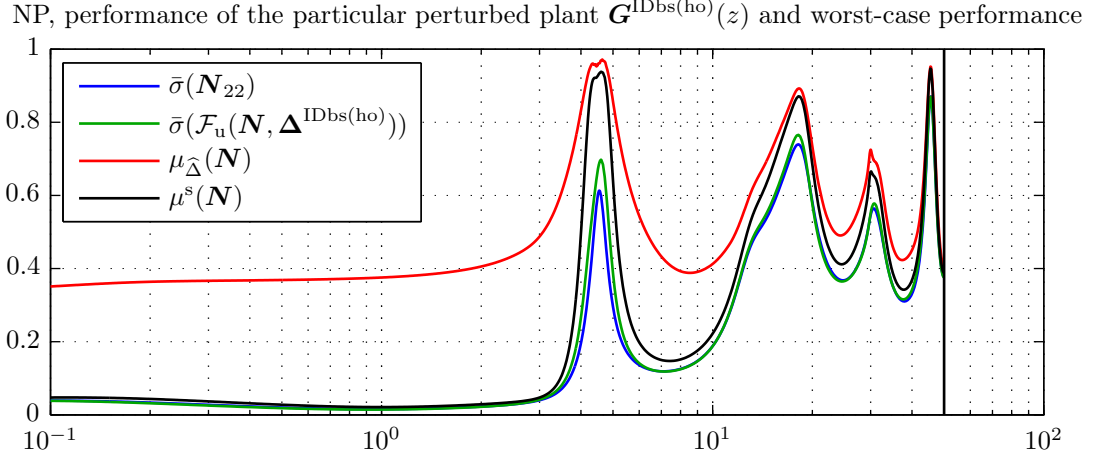


Figure 9.21: Nominal performance ($\bar{\sigma}(\mathbf{N}_{22})$), performance of the particular perturbed plant $\mathbf{G}^{\text{IDbs(ho)}}(z)$ ($\bar{\sigma}(\mathcal{F}_u(\mathbf{N}, \mathbf{\Delta}^{\text{IDbs(ho)}}))$), worst-case performance ($\mu^s(\mathbf{N}(e^{j\omega T_s}))$ - upper bound) and robust performance ($\mu_{\hat{\Delta}}(\mathbf{N})$ - upper bound)

The simulated nominal open-loop ($\mathbf{y} = \mathbf{G}_d d$) and closed-loop behavior ($\mathbf{y} = \mathbf{S}\mathbf{G}_d d$) is compared in Figure 9.22a. The improvements in structural mode damping are not as good as for the (similar) mixed-sensitivity \mathcal{H}_∞ optimal design (see Figure 9.4a on page 124), but nevertheless are considered satisfactory. For the modelled uncertainty the worst-case gain of the closed-loop disturbance path ($\mu^s(\mathbf{S}_p \mathbf{G}_d(e^{j2\pi f T_s}))$) is also depicted in Figure 9.22a. It reveals that (compared to the nominal closed-loop disturbance path, for the modelled uncertainty) the worst possible deterioration in structural mode damping can occur for the first structural mode. At 4.3234 Hz the sensitivity of the worst-case closed-loop disturbance path gain with respect to an individual perturbation block $\mathbf{\Delta}_i$ is by far largest for the full complex additive perturbation block $\mathbf{\Delta}_A$. If the additive uncertainty were enlarged by 1 %, the worst-case gain should increase by about 1.36 % (output argument `info.Sensitivity` of MATLAB[®] command `wcgain`).

As claimed by the shape of the additive uncertainty weight $\mathbf{W}_{1A}(z)$ and ensured by the fact that the design achieves RS, applying the controller $\mathbf{K}(z)$ on the particular perturbed plant $\mathbf{G}^{\text{IDbs(ho)}}(z)$ results in a closed-loop stable system. Furthermore the fact, that the design accounts for the neglected dynamics of $\mathbf{G}^{\text{IDbs(ho)}}(z)$ through additive uncertainty ensures that at a given frequency $\bar{\sigma}(\mathbf{S}^{\text{IDbs(ho)}} \mathbf{G}_d(e^{j\omega T_s})) < \mu^s(\mathbf{S}_p \mathbf{G}_d(e^{j\omega T_s}))$ holds, where $\mathbf{S}^{\text{IDbs(ho)}} = (\mathbf{I} + \mathbf{G}^{\text{IDbs(ho)}} \mathbf{K})^{-1}$. This fact can be verified graphically in Figure 9.22a. Compared to the singular values of the nominal closed-loop disturbance rejection performance ($\mathbf{S}\mathbf{G}_d$), the closed-loop disturbance rejection performance for the plant $\mathbf{G}^{\text{IDbs(ho)}}(z)$ ($\mathbf{S}^{\text{IDbs(ho)}} \mathbf{G}_d$) is worst around the natural frequency of the first structural mode. Note that $\bar{\sigma}(\mathbf{E}_A^{\text{IDbs(ho)}}(e^{j\omega T_s}))$ is large at these frequencies. For the fifth structural mode the disturbance rejection for the plant $\mathbf{G}^{\text{IDbs(ho)}}(z)$ is even slightly better.

In Figure 9.22b the improvement of mode attenuation is shown when the controller $\mathbf{K}(z)$ is applied on the “IDbs(ho)-model”. The simulation not only uses $\mathbf{G}^{\text{IDbs(ho)}}(z)$ (as in Figure 9.22a) but also $\mathbf{G}_d^{\text{IDbs(ho)}}(z)$ to simulate the control behavior.

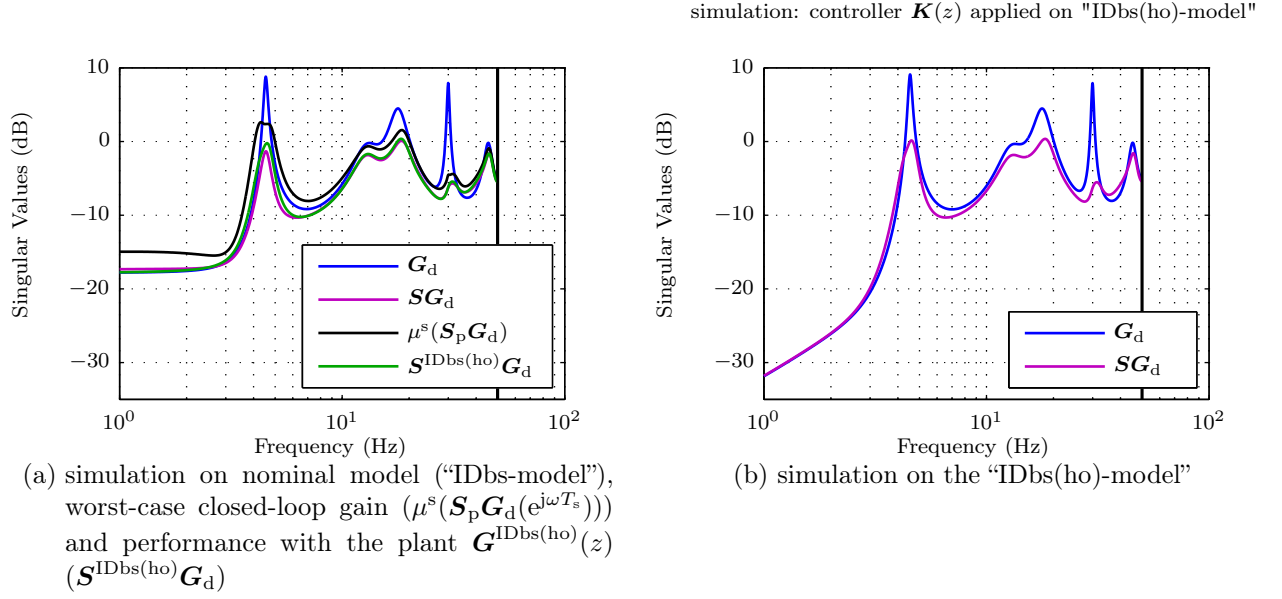


Figure 9.22: Singular values of simulated open-loop and closed-loop behavior (from d to y)

Figure 9.23 plots the singular values of the open-loop experimental validation model ($\mathcal{S}^{\text{OL-EV}}$) and those of the closed-loop experimental validation model ($\mathcal{S}^{\text{CL-EV}}$). In closed loop the first mode peak is reduced by about 5.5 dB and the fourth is reduced by more than 8.55 dB. Also the damping of the second, third, and fifth structural modes is improved (reduction of 1 dB, 2.18 dB, and 0.5 dB respectively). In general the experimentally validated closed-loop behavior ($\mathcal{S}^{\text{CL-EV}}$) is in good accordance to the simulation on the "IDbs(ho)-model".

In the following the symbol " \times " is used to denote that a matrix product of complex-valued matrices is computed separately for each frequency and that the resulting array of complex-valued matrices over frequency yields a non-parametric model (MATLAB[®] class `frd` respectively `ufrd`). For the modelled uncertainty the worst-case gain, i.e. skewed- μ of the closed-loop disturbance path is also depicted in Figure 9.23, where instead of the parametric disturbance model $G_d(z)$, the spectral, non-parametric open-loop experimental validation model $\mathcal{S}^{\text{OL-EV}}(e^{j\omega T_s})$ is utilized for the computation ($\mu^s(\mathcal{S}_p(e^{j\omega T_s}) \times \mathcal{S}^{\text{OL-EV}}(e^{j\omega T_s}))$). For the following conclusion, linearity of the plant "Beam" is assumed. At frequencies where the singular value of the closed-loop experimental validation model ($\mathcal{S}^{\text{CL-EV}}$) exceeds the value of skewed- μ (i.e. $\bar{\sigma}(\mathcal{S}^{\text{CL-EV}}(e^{j\omega T_s})) > \mu^s(\mathcal{S}_p(e^{j\omega T_s}) \times \mathcal{S}^{\text{OL-EV}}(e^{j\omega T_s}))$) the modelled uncertainty was chosen inadequately, whereas the opposite conclusion is not valid. Especially for the fourth structural mode $\bar{\sigma}(\mathcal{S}^{\text{CL-EV}}(e^{j\omega T_s}))$ exceeds its "optimistic" bound. Reconsidering the modelled uncertainty for this mode might be appropriate in order to achieve better results.

For comparison purposes also the singular value plot of the nominal closed-loop disturbance path, where $G_d(z)$ is replaced by $\mathcal{S}^{\text{OL-EV}}(e^{j\omega T_s})$ is depicted in Figure 9.23 ($\mathcal{S} \times \mathcal{S}^{\text{OL-EV}}$).

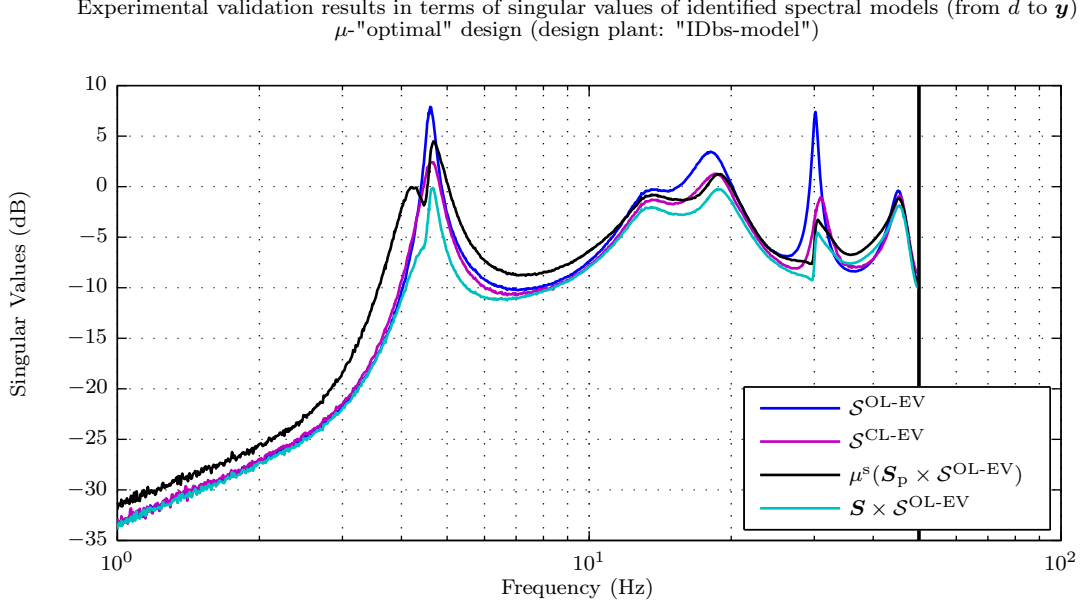


Figure 9.23: Experimental validation results in terms of singular values (from d to y) of open-loop ($\mathcal{S}^{\text{OL-EV}}$) and closed-loop ($\mathcal{S}^{\text{CL-EV}}$) identified spectral models (DK synthesized μ -”optimal” design based on the “IDbs-model”)

9.2.5 Summing-up experiences and experimental results for the control designs based on the identified model

9.2.5.1 Mixed-sensitivity \mathcal{H}_∞ design

The mixed-sensitivity \mathcal{H}_∞ design proved to be well-suited for structural mode damping. A combination of performance and input weight, $W_1(z)$ ($W_1(z) = k_1 \cdot \check{W}_1(z)$) respectively $W_2(z)$ ($W_2(z) = k_2 \cdot \check{W}_2(z)$) was found which yielded a controller $\mathbf{K}(z)$ that achieved good results in the simulation on the “IDbs(ho)-model”. It is convenient to derive a variety of designs by changing only the constant gain k_2 of $W_2(z)$, validate their stability in the experiment, and record a data set for that design with the smallest value of k_2 , which achieved stability in the experiment. Also, a variety of different dynamic shapes $\check{W}_1(z)$ and $\check{W}_2(z)$ with differently shaped bandpass/stoppass filters and different peak(s) were tested.

9.2.5.2 Modally weighted LQG design

The LQG design with modal state weighting matrix \mathbf{Q} was well suitable. It allows simple trading of the importance of mode damping among the structural modes by the diagonal matrix of modal damping factors \mathbf{M} . Because the diagonal weights \mathbf{W} and \mathbf{V} for designing the Kalman filter were based on the covariance information of the `idss` MATLAB® object, the input weight \mathbf{R} was considered as (only) free design parameter. Because for the (strictly) stable nominal plant at hand the LQG-controlled system was guaranteed to be internally stable independent of the chosen LQG design parameters, the simulation on the “IDbs(ho)-model” turned out to be a good indicator for stability as well as performance of a design in the experiment. Thus it was relatively easy to find an adequate initial input weight \mathbf{R} , design a variety of controllers $\mathbf{K}(z)$ by changing \mathbf{R} in small steps, validate their stability in the experiment and record data sets for a couple of designs with small \mathbf{R} , which achieved stability in the experiment.

9.2.5.3 \mathcal{H}_∞ loop-shaping design with coprime factor uncertainty

Not a single design fulfilled the requirement $\underline{\sigma}(\mathbf{L}(e^{j\omega T_s})) > 1$ (at frequencies where performance is/was an issue) which in case of disturbance rejection is used to postulate a closed-loop equivalent open-loop requirement (see Table 8.1 on page 113). Also, the set of perturbed plants described by coprime factor uncertainty, which allows for zeros as well as poles to cross into the RHP [6] (i.e. in the discrete-time case leave the unit circle) is unnecessarily large for the problem at hand (flexible structure), because a flexible structure is stable and thus has no unstable poles. Consequently, in the case of a flexible structure using an \mathcal{H}_∞ loop-shaping design (i.e. describing the set of perturbed plants utilizing normalized coprime factor uncertainty) might yield a conservative controller not capable of achieving satisfying results. Although a sufficiently small γ was achieved, the fact that $\underline{\sigma}(\mathbf{G}_s(e^{j\omega T_s}))$ was undesirably small lead to an undesirably small $\underline{\sigma}(\mathbf{K}_s(e^{j\omega T_s}))$, which decreased the loop shape $\mathbf{L} = \mathbf{G}_s \mathbf{K}_s$. Nevertheless the experimental results achieved by the \mathcal{H}_∞ loop-shaping design were acceptable. It was further shown that to some extent the two different approaches to obtain a reasonable dynamic weighting matrix lead to a similar $\mathbf{W}_1(z)$ (see Figure 9.13 on page 136).

9.2.5.4 DK synthesized μ -“optimal” controller

It was difficult to find a compromise between five frequency-dependent weights. Once decisions on adequate input, output, and additive uncertainty weights had been made (where, by the chosen shape of $\mathbf{W}_{1A}(z)$ the design accounted for the neglected dynamics of $\mathbf{G}^{\text{IDbs(ho)}}(z)$) and a less limiting input weight had been specified, peaks in the performance weight were utilized to increase performance requirements until the peak μ -value for RP was close to 1. Increasing the maximum allowed state order of the fitting D-scalings (property `AutoScalingOrder` of the options object obtained by `dkitopt`) proved to be helpful in order to achieve RP. However, this resulted in a large system order of the controller $\mathbf{K}^{\text{syn}}(z)$. In order to execute the controller on the real-time development system a subsequent balanced system reduction had to be applied on the controller $\mathbf{K}^{\text{syn}}(z)$. Thereby, the primary difficulty was to attain nominal stability (NS) with the reduced controller $\mathbf{K}(z)$. The μ -curve for robust performance (RP) (and also $\max_\omega \mu_{\hat{\Delta}}(\mathbf{N}(e^{j\omega T_s}))$) was not changed significantly if $\mathbf{K}(z)$ had a sufficient number of states. At some frequencies the singular value of the closed-loop experimental validation model ($\mathcal{S}^{\text{CL-EV}}$) exceeds the value of skewed- μ (i.e. $\bar{\sigma}(\mathcal{S}^{\text{CL-EV}}(e^{j\omega T_s})) > \mu^s(\mathbf{S}_p(e^{j\omega T_s}) \times \mathcal{S}^{\text{OL-EV}}(e^{j\omega T_s}))$), so the modelled uncertainty does not represent the real plant uncertainty to the full extent. Furthermore, because, on the other hand the mixed-sensitivity \mathcal{H}_∞ design achieved better results (for all except the third structural mode) in the experiment, the chosen uncertainty (and/or performance weight), was partly chosen conservatively. Nevertheless the improvements in structural mode damping are considered good.

9.3 Controller designs based on the FE model

In this section all continuous-time controller designs are based on the continuous-time “FEbs-model” as design plant. Then the obtained continuous-time controller $\mathbf{K}(s)$ will be discretized using the zero-order hold method ($T_s = 0.01$ s). For simplicity, the notation \mathbf{G} instead of \mathbf{G}^{FEbs} and \mathbf{G}_d instead of $\mathbf{G}_d^{\text{FEbs}}$ is used to denote the nominal plant respectively disturbance model in the following.

9.3.1 Mixed-sensitivity \mathcal{H}_∞ control

Unlike the designs based on the identified model, here the best results were achieved by choosing the performance weight $W_1(s)$ (scalar) as a simple bandpass without peaks. Because in all designs based on the FE model the frequencies f_i^{FEbs} (for $i = 1, \dots, 5$) were utilized to create additional peaks in a weight $\mathbf{W}(s)$, the peaks turned out to be contra-productive when it comes to a simulation on the “IDbs(ho)-model”. Model mismatch is clearly an issue that has to be dealt with. Again, the input weight $W_2(s)$ (scalar) was selected as a bandstop to penalize input usage outside the frequency range of interest. At low frequencies, the low magnitude of $W_1(s)$ (respectively the high magnitude of $W_2(s)$) match the fact that the piezo patch sensors cannot measure static strains (globally derivative behavior). At high frequencies the shape of $W_1(s)$ and $W_2(s)$ account for the fact that the “modally truncated” FE model is imperfect and that the continuous-time controller $\mathbf{K}(s)$ will be discretized (zero-order hold method; $T_s = 0.01$ s) in the end.

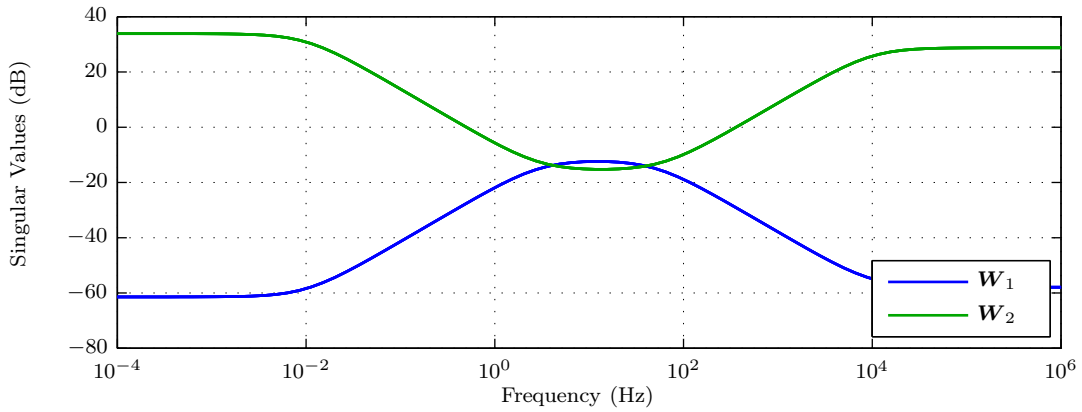


Figure 9.24: Singular values of performance weight $\mathbf{W}_1(s) = W_1(s) \cdot \mathbf{I}$ and input weight $\mathbf{W}_2(s) = W_2(s) \cdot \mathbf{I}$

With the chosen weights the nominal performance condition (8.24) is easily satisfied ($\gamma = 0.2111$), where the synthesized stable continuous-time controller $\mathbf{K}(s)$ has 26 states.

Although a simple bandpass without peaks was used (shape of $W_1(s)$), the singular value plot of the (nominal) continuous-time closed-loop transfer function $\mathbf{S}\mathbf{G}_d$ (Figure 9.25a), exhibits significant damping of the lowest-damped first and fourth modes. Also the damping of the third mode is improved, whereas the dampings of the second and fifth modes are barely improved. This reveals a characteristic property of γ -iteration, where in each iteration step the algorithm focuses on the peak value of the maximum singular value of \mathbf{N} .

The discrete-time simulation (Figure 9.25b) with the discretized controller $\mathbf{K}(z)$ obtained from $\mathbf{K}(s)$ by the zero-order hold method ($T_s = 0.01$ s) and the discrete-time model (“IDbs(ho)-model”) shows an additional peak at a frequency of about 3.44 Hz. To some extent this (emerging) bump can also be spotted in Figure 9.26, where the singular values of the open-loop ($\mathcal{S}^{\text{OL-EV}}$) and closed-loop experimental validation model ($\mathcal{S}^{\text{CL-EV}}$) (from \mathbf{d} to \mathbf{y}) are depicted. As revealed by a comparison between the natural frequencies of the “FEbs-model” and “IDbs-model” (see Table 6.4 on page 77) the FE model shows large deviation of the natural frequency of the fourth mode. In the closed-loop simulation with the “IDbs(ho)-model” the fourth mode was already much less damped as predicted by the simulation of the nominal closed-loop behavior. In the actual experiment ($\mathcal{S}^{\text{CL-EV}}$) this behavior

is even worse. The fourth mode is shifted to a slightly higher frequency (which might be preferable), but damping is hardly changed.

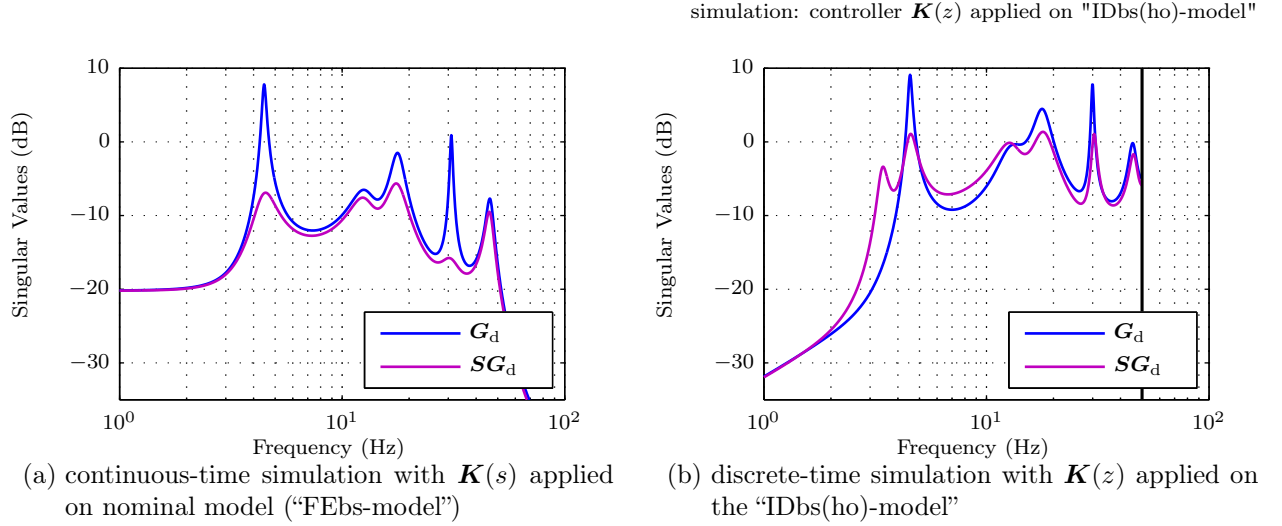


Figure 9.25: Singular values of simulated open-loop and closed-loop behavior (from d to y)

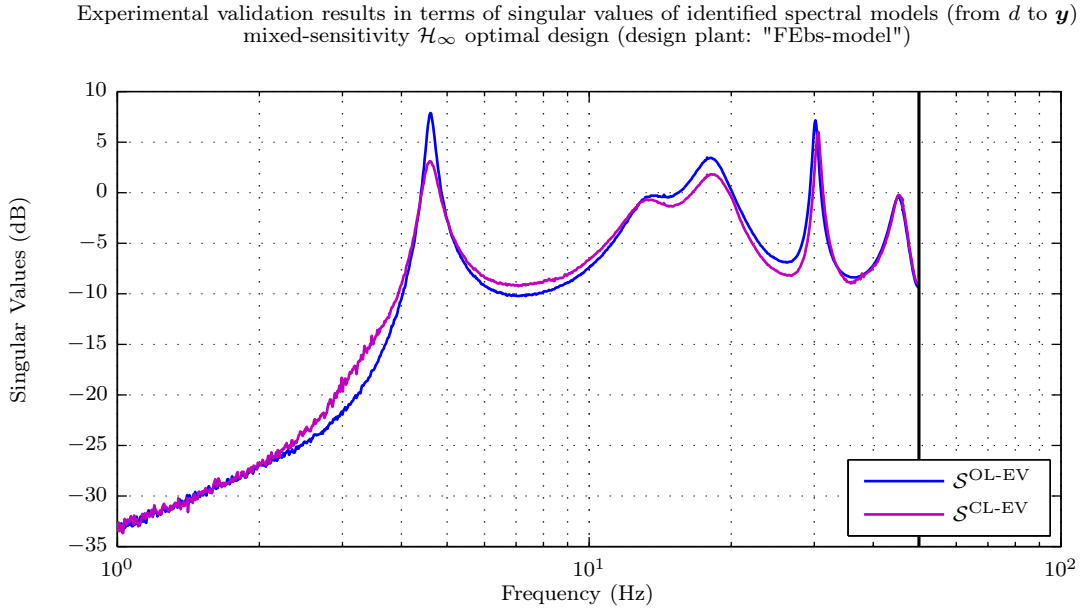


Figure 9.26: Experimental validation results in terms of singular values (from d to y) of open-loop ($\mathcal{S}^{\text{OL-EV}}$) and closed-loop ($\mathcal{S}^{\text{CL-EV}}$) identified spectral models (mixed-sensitivity \mathcal{H}_∞ optimal design based on the "FEbs-model")

Although uncertainty is not explicitly modelled by this mixed-sensitivity \mathcal{H}_∞ design, it is robustly stable for all perturbed plants \mathbf{G}_p with

$$\bar{\sigma}(\mathbf{G}_p(j\omega) - \mathbf{G}(j\omega)) \leq |W_{1A}(j\omega)| \quad \forall \omega \in \mathbb{R} \quad (9.33)$$

where the singular values of $\mathbf{W}_{1A}(j\omega) = W_{1A}(j\omega) \cdot \mathbf{I}$ are depicted in Figure 9.27.

Due to the unstructured nature of additive uncertainty the robust stability property with respect to additive plant uncertainty, which allows for any coupling from the inputs to the outputs with phase relations unknown, may also have advantageous robustness characteristics with respect to discretization errors of the controller $\mathbf{K}(z)$.

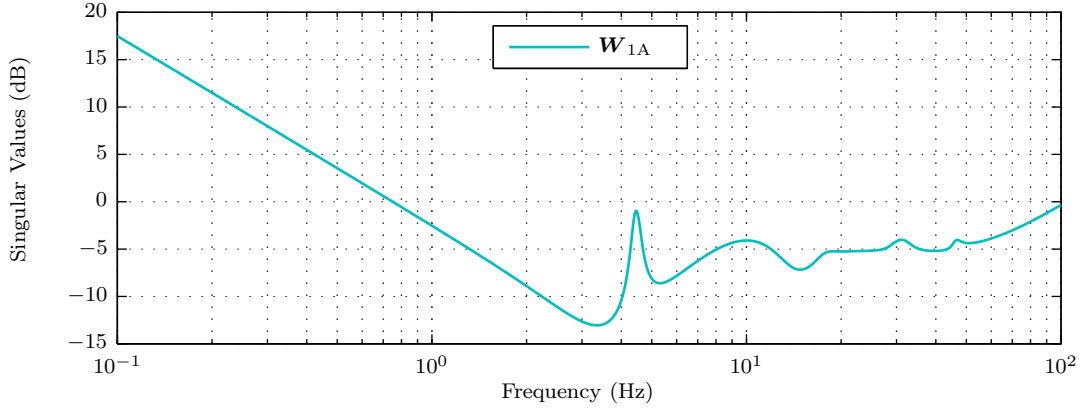


Figure 9.27: Singular values of $\mathbf{W}_{1A}(j\omega) = W_{1A}(j\omega) \cdot \mathbf{I}$ ($|W_{1A}(j\omega)| = \frac{(1-\epsilon)}{\bar{\sigma}(\mathbf{KS}(j\omega))}$ with an infinitesimally small $\epsilon \in \mathbb{R}^+$)

9.3.2 Modally weighted LQG design

The nominal plant is strictly stable, so the LQG-controlled system is guaranteed to be internally stable independent of the chosen LQG design parameters (see explanation in Section 9.2.2). In this section the computational procedure in MATLAB[®] is skipped (for information see Section 9.2.2).

The matrix \mathbf{M} of weighting factors is given in (9.34). The fourth structural mode is weighted strongest, followed by the third and second.

$$\mathbf{M} = \begin{bmatrix} 47 \cdot \mathbf{I}_{[2 \times 2]} & \mathbf{0} & \mathbf{0} & \mathbf{0} & \mathbf{0} \\ \mathbf{0} & 143 \cdot \mathbf{I}_{[2 \times 2]} & \mathbf{0} & \mathbf{0} & \mathbf{0} \\ \mathbf{0} & \mathbf{0} & 281 \cdot \mathbf{I}_{[2 \times 2]} & \mathbf{0} & \mathbf{0} \\ \mathbf{0} & \mathbf{0} & \mathbf{0} & 1548 \cdot \mathbf{I}_{[2 \times 2]} & \mathbf{0} \\ \mathbf{0} & \mathbf{0} & \mathbf{0} & \mathbf{0} & 26 \cdot \mathbf{I}_{[2 \times 2]} \end{bmatrix} \quad (9.34)$$

Again the input weighting matrix \mathbf{R} was chosen as a matrix of diagonally repeated values.

$$\mathbf{R} = 4 \cdot 10^3 \cdot \mathbf{I}_{[4 \times 4]} \quad (9.35)$$

With the state feedback controller \mathbf{K}_{LQR} and preamplifier matrix \mathbf{K}_r (only meaningful for reference tracking) the (continuous-time) closed-loop state-equation (9.36) and output-equation (9.37) for the state feedback control configuration (with control law $\mathbf{u} = \mathbf{K}_r \mathbf{r} - \mathbf{K}_{\text{LQR}} \mathbf{x}$) is given by:

$$\dot{\mathbf{x}} = (\mathbf{A} - \mathbf{BK}_{\text{LQR}})\mathbf{x} + \mathbf{BK}_r \mathbf{r} + \mathbf{B}_d \mathbf{d} \quad (9.36)$$

$$\mathbf{y} = (\mathbf{C} - \mathbf{DK}_{\text{LQR}})\mathbf{x} + \mathbf{DK}_r \mathbf{r} + \mathbf{D}_d \mathbf{d} \quad (9.37)$$

pole	open-loop		closed-loop (LQR)		pole	observer	
	f_i^{FEbs} (in Hz)	ζ_i^{FEbs} (in %)	f_i^{cl} (in Hz)	ζ_i^{cl} (in %)		f_i^{ob} (in Hz)	ζ_i^{ob} (in %)
1,2	4.4601	2.1346	4.5624	21.2276	1,2	4.6745	28.4255
3,4	12.6525	14.0135	12.6790	15.3097	3,4	15.4753	55.5340
5,6	17.7772	7.1113	17.8555	11.7122	5,6	31.7087	80.2925
7,8	30.9467	1.2924	31.4193	17.4606	7	31.9920	100
9,10	46.2427	3.8049	46.2428	3.8093	8	45.7480	100
					9	84.6833	100
					10	288.3345	100

(a) open-loop plant and closed-loop system with state feedback regulator

(b) Kalman observer

Table 9.1: Natural frequencies and damping parameters (poles)

The natural frequencies and damping parameters of the complex conjugate closed-loop poles (of the LQR controlled system) are depicted in Table 9.1a together with those of the (nominal) plant \mathbf{G} . Especially the damping of the lowest-damped fourth and first structural modes are improved.

Although in (9.34) the entries corresponding to the third and second structural mode are rather large, the improvement of damping of these modes is relatively poor (in direct comparison to the achieved damping of the first and fourth structural modes). Here, the chosen, large values of the input weight \mathbf{R} dominate the design.

In Figure 9.28a the singular values of the disturbance path (from d to \mathbf{y}) of the closed-loop system with (LQR) state feedback regulator (equations (9.36)-(9.37)) are depicted. As expected by the closed-loop poles (Table 9.1a), the first and fourth structural modes are highly damped.

For the design based on the “FEbs-model” as design plant choosing the entries of \mathbf{W} and \mathbf{V} as diagonally repeated mean values of the diagonal matrices \mathbf{W} and \mathbf{V} as they were used in Section 9.2.2 (i.e. $\mathbf{W} = 1.3 \cdot 10^{-5} \cdot \mathbf{I}$ and $\mathbf{V} = 10^{-4} \cdot \mathbf{I} \Rightarrow$ ratio about factor ten) turned out to be inappropriate. The singular values of the simulated nominal closed-loop disturbance performance ($\mathbf{S}\mathbf{G}_d$) were barely distinguishable from the open-loop ones (\mathbf{G}_d).

In general, a high weighting of the state estimation error $\tilde{\mathbf{x}} = \mathbf{x} - \hat{\mathbf{x}}$ by using large entries in \mathbf{W} results in a high bandwidth of the Kalman observer and, consequently, large amplification of the measured output by the Luenberger gain matrix \mathbf{H} . Conversely, increasing the entries of \mathbf{V} causes a reduced bandwidth of the Kalman observer with a Luenberger gain matrix \mathbf{H} with smaller values. This is favorable when the measurements \mathbf{y} are noisy. [13]

Although the physical plant “beam” seems to be quite noisy in the given setup, a large \mathbf{W} was indispensable in order to achieve satisfying mode damping, at least in the simulation on the nominal plant and in the discrete-time simulation with the “IDbs(ho)-model”. A physical interpretation of such large \mathbf{W} seems difficult.

$$\mathbf{W} = 10^4 \cdot \mathbf{I}_{[10 \times 10]} \quad \mathbf{V} = \mathbf{I}_{[4 \times 4]} \quad (9.38)$$

Due to the large values of \mathbf{W} the poles of the Kalman observer (Table 9.1b) are considerably faster than those of the closed-loop system with state feedback regulator (LQR).

The singular value plot of the (nominal) continuous-time closed-loop transfer function $\mathbf{S}\mathbf{G}_d$ (Figure 9.28a) exhibits that the disturbance rejection performance of the state feedback

regulated plant (LQR) is not changed much by using the estimated state vector $\hat{\mathbf{x}}$ instead of \mathbf{x} as input to the optimal controller \mathbf{K}_{LQR} .

The singular value plot (Figure 9.28b) of the discrete-time simulation on the “IDbs(ho)-model” (discretized controller $\mathbf{K}(z)$ obtained from $\mathbf{K}(s)$ by the zero-order hold method ($T_s = 0.01$ s)) suggests high performance in particular for the fourth structural mode. There the LQG controller achieves an even better result than the mixed-sensitivity \mathcal{H}_∞ design (compare Figure 9.25b on page 150).

In contrast to the favorable simulation results, the LQG cannot achieve such performance in the experimental validation. The fourth structural mode in the closed-loop experimental validation model ($\mathcal{S}^{\text{CL-EV}}$) (Figure 9.29) exhibits nearly no improvement in damping (0.16 dB). As predicted correctly by the discrete-time simulation (Figure 9.28b), the fourth structural mode is shifted to a higher frequency. The improvement of damping of the first, second, and third structural modes by 4.85 dB, 0.75 dB and 1.3 dB is considered good.

Note that the slight bump in the discrete-time simulation at about 2.8 Hz is also visible in Figure 9.28b.

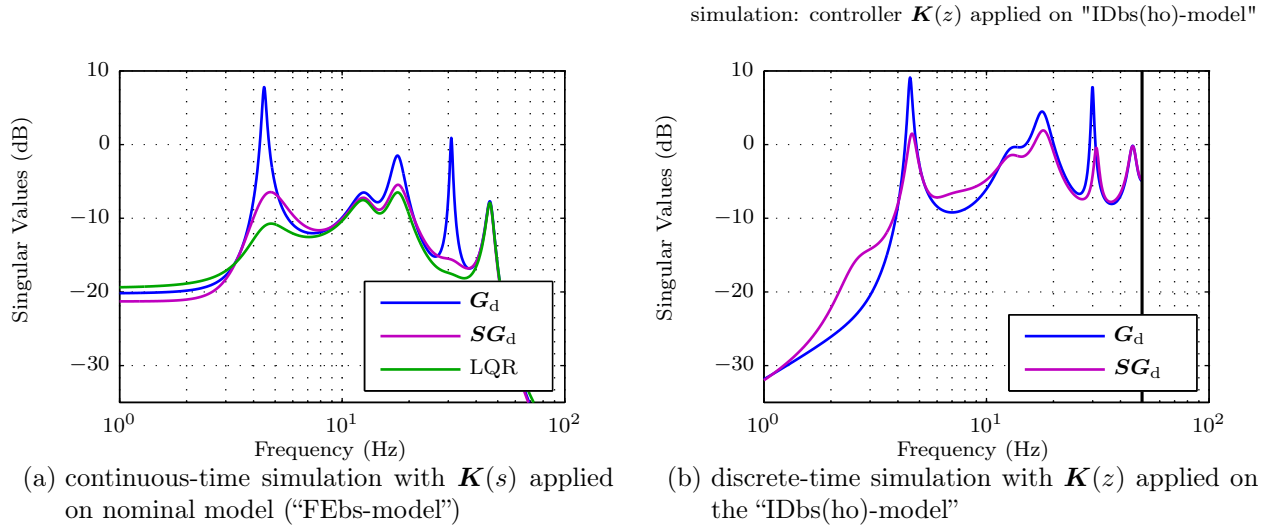


Figure 9.28: Singular values of simulated open-loop and closed-loop behavior (from d to y)

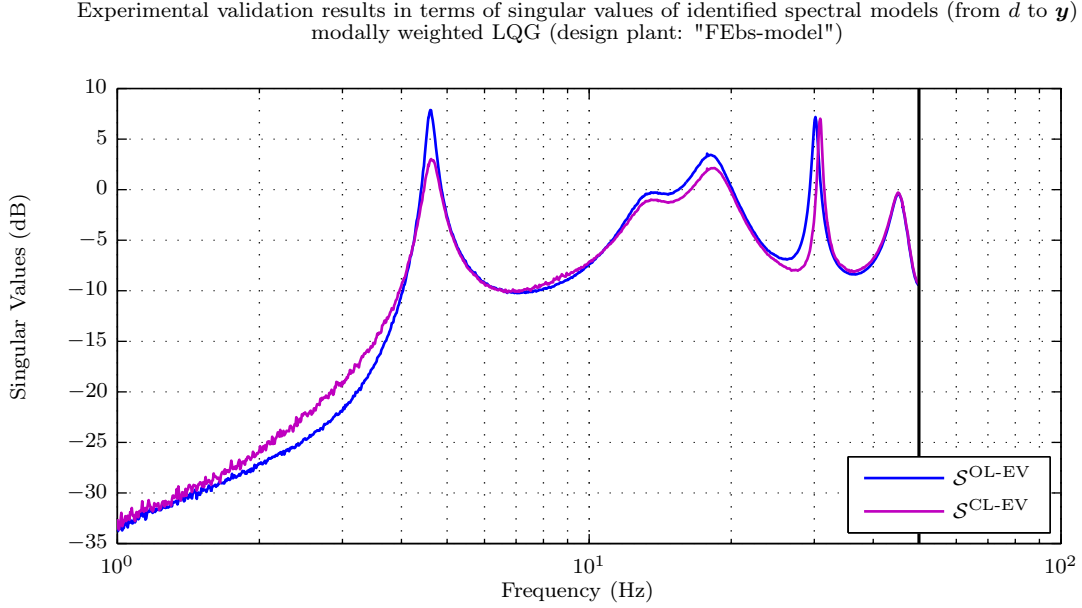


Figure 9.29: Experimental validation results in terms of singular values (from d to y) of open-loop ($\mathcal{S}^{\text{OL-EV}}$) and closed-loop ($\mathcal{S}^{\text{CL-EV}}$) identified spectral models (modally weighted LQG design based on the “FEbs-model”)

9.3.3 \mathcal{H}_∞ loop-shaping design for coprime factor uncertainty

One suggestion (see Section 8.8.4 on page 116) when disturbance rejection is an issue for deriving a reasonable dynamic weighting matrix (compensator) $\mathbf{W}_1(s)$ is to choose

$$\underline{\sigma}(\mathbf{W}_1(j\omega)) \approx \bar{\sigma}(\mathbf{G}^{-1}(j\omega)) \cdot \bar{\sigma}(\mathbf{G}_d(j\omega)) \quad (9.39)$$

or (in some sense more conservative)

$$\underline{\sigma}(\mathbf{W}_1(j\omega)) \approx \bar{\sigma}(\mathbf{G}^{-1}\mathbf{G}_d(j\omega)). \quad (9.40)$$

Another approach is to choose $\mathbf{W}_1(s) = W_1(s) \cdot \mathbf{I}$ with

$$|W_1(j\omega)| \approx \bar{\sigma}(\widetilde{\mathbf{W}}_1(j\omega)) \quad (9.41)$$

where

$$\widetilde{\mathbf{W}}_1(j\omega) = \mathbf{G}^{-1}\mathbf{L}_{\text{success}}(j\omega) \quad (9.42)$$

with $\mathbf{L}_{\text{success}}$ being the loop shape of a successfully validated earlier controller design.

For the problem at hand, these proposals (equations (9.39) to (9.42)) are visualized in Figure 9.30, where for the loop shape $\mathbf{L}_{\text{success}}$ in (9.42) the loop shape of the modally weighted LQG design (Section 9.3.2) and those of the mixed-sensitivity \mathcal{H}_∞ design (Section 9.3.1) is used, together with the chosen $\mathbf{W}_1(s) = W_1(s) \cdot \mathbf{I}$ used for the \mathcal{H}_∞ loop-shaping design presented in the following.

Note that for a real- or complex-valued matrix \mathbf{A} the following holds:

$$\underline{\sigma}(\mathbf{A}) = \frac{1}{\bar{\sigma}(\mathbf{A}^\dagger)}, \quad (9.43)$$

where \mathbf{A}^\dagger is the pseudo-inverse of \mathbf{A} (if \mathbf{A} is square and non-singular, $\mathbf{A}^\dagger = \mathbf{A}^{-1}$ holds). Consequently, for all $\omega \in \mathbb{R}$ $\bar{\sigma}(\mathbf{G}^{-1}(j\omega)) = 1/\underline{\sigma}(\mathbf{G}(j\omega))$ holds, and thus in (9.39) the minimum

singular values of $\mathbf{G}(j\omega)$ co-determine the suggested shape of $\underline{\sigma}(\mathbf{W}_1(j\omega))$. Hence, the fact that the minimum singular values of \mathbf{G}^{FEbs} and \mathbf{G}^{IDbs} differ strongly (see Figure 6.5) leads to quite different recommended $\underline{\sigma}(\mathbf{W}_1(j\omega))$ (respectively $\underline{\sigma}(\mathbf{W}_1(e^{j\omega T_s}))$) for the two individual design plants (compare $\bar{\sigma}(\mathbf{G}^{-1}) \cdot \bar{\sigma}(\mathbf{G}_d)$ in Figure 9.30 and 9.13).

Note in Figure 9.30, that because of the chosen input and performance weights \mathbf{W}_u respectively \mathbf{W}_p (used in the mixed-sensitivity \mathcal{H}_∞ design), $\bar{\sigma}(\mathbf{G}^{-1}\mathbf{L}_{\text{mixedS}}(j\omega))$ has derivative behavior, while $\bar{\sigma}(\mathbf{G}^{-1}\mathbf{L}_{\text{LQG}}(j\omega))$ has (clearly) globally proportional behavior.¹⁹

For simplicity the weighting matrices $\mathbf{W}_1(s) = W_1(s) \cdot \mathbf{I}$ (scalar) and $\mathbf{W}_2 = \mathbf{I}$ were used for shaping the singular values of the open-loop plant \mathbf{G} , however, this might not be a good choice because the plant $\mathbf{G}(s)$ and consequently $\mathbf{G}_s(s) = \mathbf{G}(s)W_1(s)$, are ill-conditioned (i.e. $\mathbf{G}_s(s)$ has a large condition number $\gamma(\mathbf{G}_s) = \bar{\sigma}(\mathbf{G}_s)/\underline{\sigma}(\mathbf{G}_s)$) at frequencies where performance improvements are required. Potentially the design can be optimized by choosing the weightings $\mathbf{W}_1(s)$ and $\mathbf{W}_2(s)$ such that the scaled plant condition number $\gamma(\mathbf{G}_s)$ is improved. If the condition number $\gamma(\mathbf{G})$ of a plant \mathbf{G} is small, then the multivariable effects of uncertainty are not likely to be serious, but the reverse does not hold in general. [6] Particularly for a plant with a small condition number, $\gamma(\mathbf{G}) \approx 1$, the system is insensitive to (both diagonal and full-block) input uncertainty, irrespective of the controller. [6]

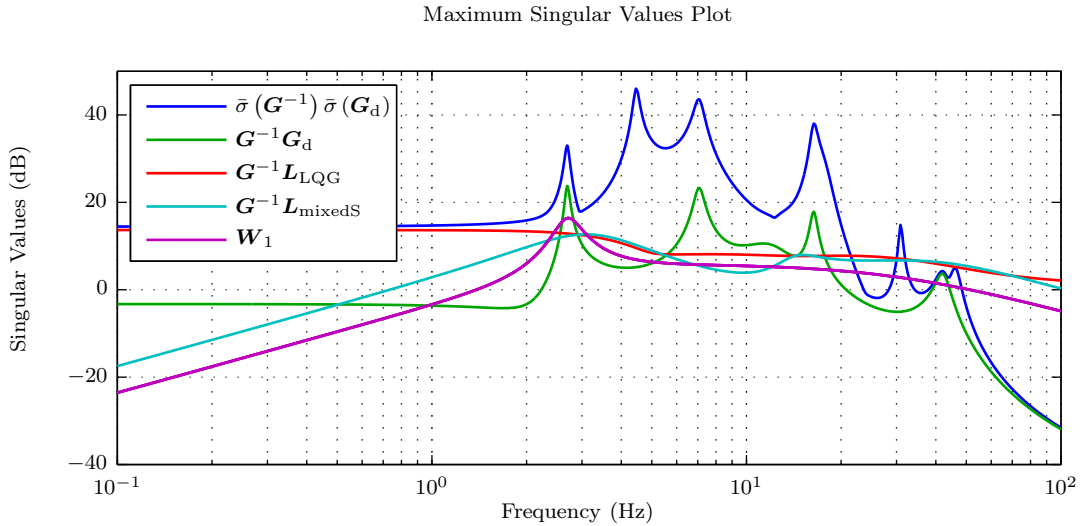


Figure 9.30: Maximum singular values of the weighting matrix (compensator) $\mathbf{W}_1(j\omega) = W_1(j\omega) \cdot \mathbf{I}$ and suggested guidelines

By using the MATLAB[®] command `ncfsyn` a stabilizing, stable, optimal positive feedback controller $\mathbf{K} = \mathbf{W}_1\mathbf{K}_s\mathbf{W}_2$ with 41 states ($\mathbf{G}_s(s)$ has 26 states, $\mathbf{K}_s(s)$ has 25 states, and $\mathbf{W}_1(s)$ has 16 states) was obtained. The singular values of the discretized controller $\mathbf{K}(z)$ obtained from $\mathbf{K}(s)$ by the zero-order hold method ($T_s = 0.01$ s) and those of the continuous-time controller $\mathbf{K}(s)$ are depicted in Figure 9.31.

¹⁹Actually also $\bar{\sigma}(\mathbf{G}^{-1}\mathbf{L}_{\text{mixedS}}(e^{j\omega T_s}))$ has globally proportional behavior but levels off at a much lower frequency with a value of about -37.5 dB.

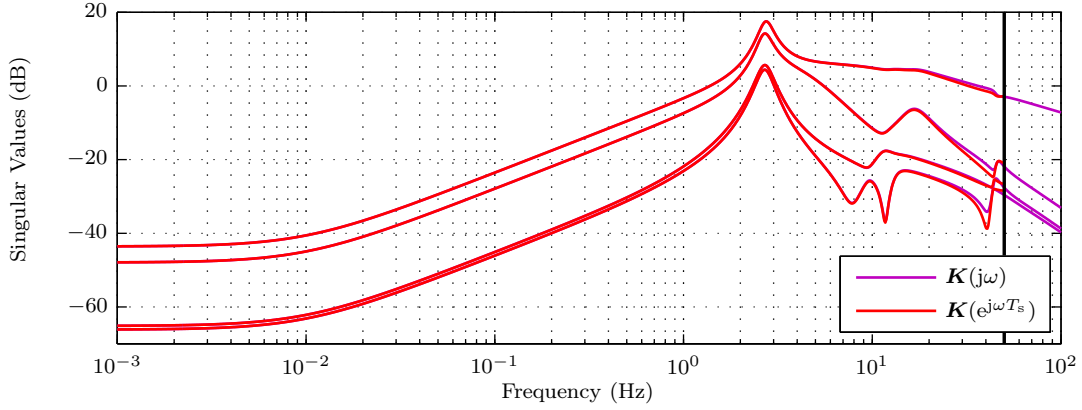


Figure 9.31: Singular values of the positive feedback controller \mathbf{K}

The design achieves a reasonably small $\gamma = 1.4161$ (i.e. the usually postulated criterion of $\gamma < 4$ is fulfilled) and thus allows for $\epsilon = 70.61\%$ ($\epsilon = 1/\gamma$) coprime factor uncertainty. In Figure 9.32 the singular values of the desired loop shape (shaped plant) \mathbf{G}_s and those of the actual loop transfer function \mathbf{L} are shown. For a detailed discussion see Section 9.2.3.

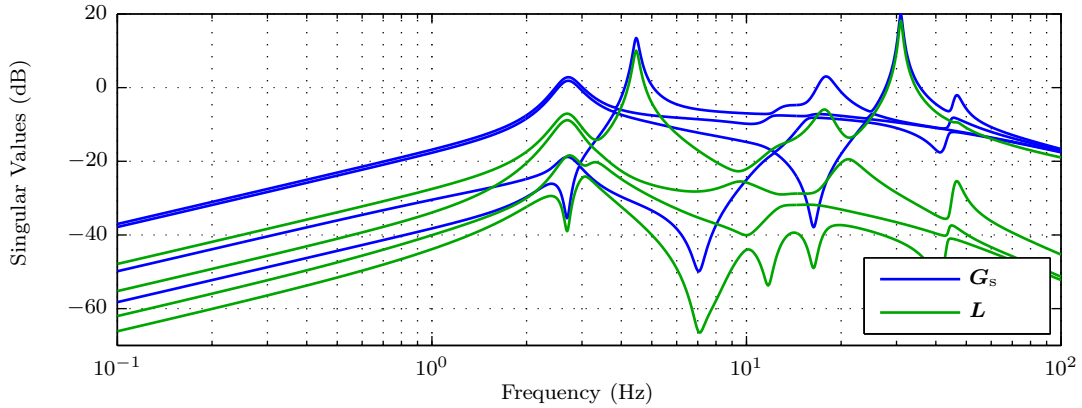


Figure 9.32: Singular values of desired loop shape or shaped plant \mathbf{G}_s ($\mathbf{G}_s(s) = \mathbf{G}(s)\mathbf{W}_1(s)$) and actual loop transfer function \mathbf{L}

The singular value plot of the (nominal) continuous-time closed-loop transfer function $\mathbf{S}\mathbf{G}_d$ (Figure 9.33a) exhibits that the damping of the first, the third, and especially of the fourth structural modes are improved, while the other structural modes remain unchanged. By applying the discrete-time controller $\mathbf{K}(z)$ on the “IDbs(ho)-model”, the positive feedback system is also stable and the simulation (Figure 9.33b) shows an additional peak at a frequency of 3.08 Hz. To some extent this peak can also be spotted in Figure 9.34, where the singular values of the open-loop ($\mathcal{S}^{\text{OL-EV}}$) and closed-loop experimental validation model ($\mathcal{S}^{\text{CL-EV}}$) (from \mathbf{d} to \mathbf{y}) are depicted. Also the shift of the fourth structural mode to a higher frequency, which was seen in the discrete-time simulation on the “IDbs(ho)-model” is confirmed by the closed-loop experimental validation model ($\mathcal{S}^{\text{CL-EV}}$). The improvement in mode damping of the first, third, and fourth structural modes are 3.7 dB, 1.12 dB and 2 dB, whereas the second and fifth structural modes remain unchanged in damping.

For all designs based on the “FEbs-model” (apart from the DGK synthesized μ -“optimal” controller, see Section 9.3.5) the \mathcal{H}_∞ loop-shaping design was the one which achieved the best results when it comes to the difficult²⁰ damping of the fourth structural mode. This is somewhat surprising, because for a flexible structure, which is guaranteed to be stable, the assumption of coprime factor uncertainty (which allows for zeros as well as poles to cross into the RHP) creates an unnecessarily large set of possibly perturbed plants and thus the design is expected to result in a conservative controller. However, note that all controllers based on the “FEbs-model” had to be discretized in the end. Maybe the answer to the surprisingly good performance of the \mathcal{H}_∞ loop-shaping design based on the “FEbs-model” lies within this discretization step, where the otherwise excessively large set of plants described by coprime factor uncertainty might be beneficial to cover the discretization error.

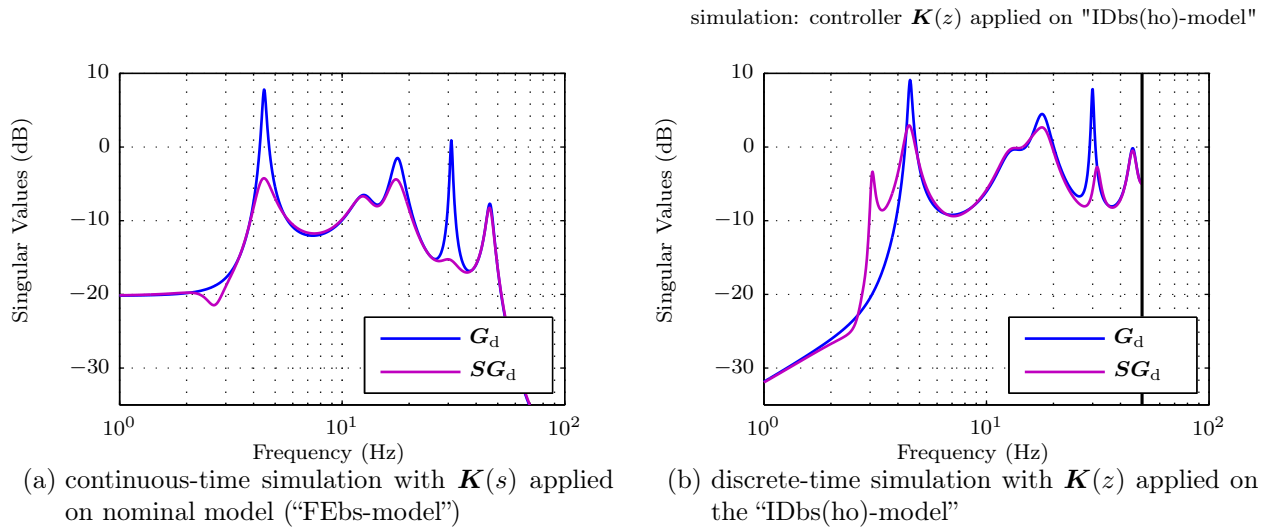


Figure 9.33: Singular values of simulated open-loop and closed-loop behavior (from d to y)

²⁰This is attributed to the critical model mismatch at the fourth structural mode.

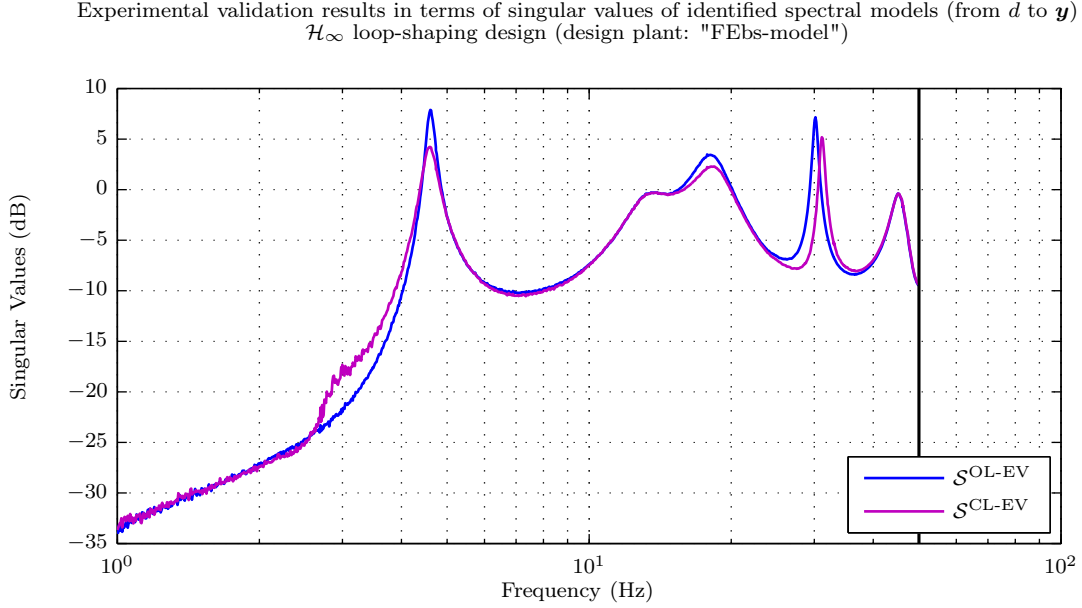


Figure 9.34: Experimental validation results in terms of singular values (from d to y) of open-loop ($\mathcal{S}^{\text{OL-EV}}$) and closed-loop ($\mathcal{S}^{\text{CL-EV}}$) identified spectral models (\mathcal{H}_∞ loop-shaping design based on the “FEbs-model”)

9.3.4 DK synthesized μ -“optimal” controller

The performance weight $W_P(s)$ was chosen as a scalar bandpass with three additional peaks, where these extra peaks were utilized to put strong weight on the first, second, and third structural modes (Figure 9.35). Again, the scalar input weight $W_u(s)$ was selected as a bandstop. By this means input usage is highly penalized outside the frequency range of interest spanned by the natural frequencies of the first five (structural) modes of the beam with mounted shaker.

The uncertainty weights $W_{11}(s)$ and $W_{10}(s)$ for complex diagonal multiplicative input respectively output uncertainty were chosen as scalar bandstop filters - uncertainty is considered equal for all inputs/outputs. In the stopband the attenuation is about 20 dB, hence at intermediate frequencies the design allows for 10 % multiplicative (input respectively output) uncertainty.

In the following the “IDbs(ho)-model” (as well as the “IDbs-model”) stemming from an identification with mounted shaker is considered unknown, i.e. $\bar{\sigma}(\mathbf{E}_A^{\text{IDbs(ho)}}(j\omega))$ is assumed unavailable.²¹ The natural frequencies f_i^{IDbs} (for $i = 1, \dots, 5$) are considered known. However, $\bar{\sigma}(\mathbf{E}_A^{\text{IDbs(ho)}}(j\omega))$ is depicted in Figure 9.35.²²

Because the deviation $\Delta f_i^{\text{bs}} = f_i^{\text{FEbs}} - f_i^{\text{IDbs}}$ in the natural frequency is large for the fourth ($i = 4$) structural mode (see Table 6.4 on page 77), the scalar additive uncertainty weight $W_{1A}(s)$, which has the shape of a bandstop, has an additional peak at the natural frequency f_4^{FEbs} . At low frequencies the high values of $|W_{1A}(j\omega)|$ account for the fact, that because of the “modal truncation” the static error of the “FEbs-model” is large. At high frequencies

²¹In order to obtain $\bar{\sigma}(\mathbf{E}_A^{\text{IDbs(ho)}}(j\omega))$, the identified model $\mathbf{G}^{\text{IDbs(ho)}}(z)$ has to be converted from discrete- to continuous-time prior, where above $1/(2 \cdot T_s) = 50$ Hz statements are not permissible.

²²Designs in which $|W_{1A}(j\omega)|$ was shaped just above $\bar{\sigma}(\mathbf{E}_A^{\text{IDbs(ho)}}(j\omega))$ either did not fulfill NP (and consequently RP) or (with reduced performance requirements) in the simulation on the nominal plant the improvement of structural mode damping was infinitesimal.

the shape of $|W_{1A}(j\omega)|$ accounts for the fact that the “modally truncated” FE model is also imperfect and that the continuous-time controller $\mathbf{K}(s)$ will be discretized (zero-order hold method; $T_s = 0.01$ s) in the end.

The singular values of the weights are depicted in Figure 9.35. For simplicity the weights \mathbf{W}_{2I} , \mathbf{W}_{2O} , and \mathbf{W}_{2A} were chosen as identity matrices and are not depicted.

The normalized perturbations for multiplicative input-respectively output-uncertainty Δ_I (4×4) respectively Δ_O (4×4) are considered as complex diagonal blocks, whereas the normalized perturbation Δ_A (4×4) representing the additive uncertainty is considered as a full complex block.

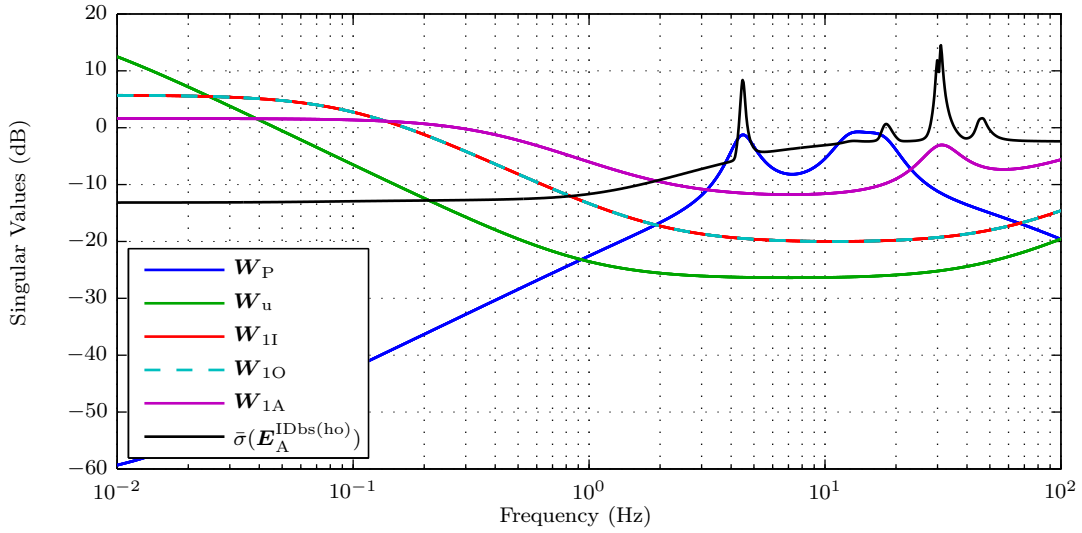


Figure 9.35: Singular values of performance weight \mathbf{W}_P ; input weight \mathbf{W}_u ; \mathbf{W}_{1I} , \mathbf{W}_{1O} for multiplicative input respectively output uncertainty, and \mathbf{W}_{1A} for additive uncertainty weighting

The MATLAB[®] commands utilized to obtain the design are skipped in the following because they were already described in Section 9.2.4.

The generalized plant $\mathbf{P}(s)$ (24×17) (9.44) of Figure 8.16 on page 110 (where the scalar $w_1 = d$ was chosen as the only exogenous input) was obtained with $n_P = 92$ states.

$$\begin{bmatrix} \mathbf{y}_{\Delta_I} \\ \mathbf{y}_{\Delta_A} \\ \mathbf{y}_{\Delta_O} \\ z_1 \\ z_2 \\ v \end{bmatrix} = \underbrace{\begin{bmatrix} \mathbf{0} & \mathbf{0} & \mathbf{0} & \mathbf{0} & \mathbf{W}_{1I} \\ \mathbf{W}_{1A}\mathbf{W}_{2I} & \mathbf{0} & \mathbf{0} & \mathbf{0} & \mathbf{W}_{1A} \\ \mathbf{W}_{1O}\mathbf{G}\mathbf{W}_{2I} & \mathbf{W}_{1O}\mathbf{W}_{2A} & \mathbf{0} & \mathbf{0} & \mathbf{W}_{1O}\mathbf{G} \\ \mathbf{W}_P\mathbf{G}\mathbf{W}_{2I} & \mathbf{W}_P\mathbf{W}_{2A} & \mathbf{W}_P\mathbf{W}_{2O} & \mathbf{W}_P\mathbf{G}_d & \mathbf{W}_P\mathbf{G} \\ \mathbf{0} & \mathbf{0} & \mathbf{0} & \mathbf{0} & \mathbf{W}_U \\ -\mathbf{G}\mathbf{W}_{2I} & -\mathbf{W}_{2A} & -\mathbf{W}_{2O} & -\mathbf{G}_d & -\mathbf{G} \end{bmatrix}}_{\mathbf{P}} \begin{bmatrix} \mathbf{u}_{\Delta_I} \\ \mathbf{u}_{\Delta_A} \\ \mathbf{u}_{\Delta_O} \\ w_1 \\ u \end{bmatrix} \quad (9.44)$$

With scalings $\check{\mathbf{D}}_r = \mathbf{I}$ (24×24) and $\check{\mathbf{D}}_l = \mathbf{I}$ (17×17) (see (8.95)) the automated DK-iteration synthesized a stable controller $\mathbf{K}^{\text{syn}}(s)$ (4×4) with $n_{K^{\text{syn}}} = 92$ states.²³

²³MATLAB[®] used the first attempt with initial scalings.

Because the generalized plant $\mathbf{P}(s)$ is stable it is ensured, that independent of \mathbf{B}_2 and \mathbf{C}_2 assumption A.1 in Definition 8.1 is fulfilled, and thus a stabilizing sub-optimal \mathcal{H}_∞ controller $\mathbf{K}^{\text{syn}}(s)$ is synthesized in the K-step of the DK-iteration algorithm. In other words, because, for the problem at hand $\mathbf{P}(s)$ is stable it is ensured that $\mathbf{N}^{\text{syn}}(s) = \mathcal{F}_1(\mathbf{P}(s), \mathbf{K}^{\text{syn}}(s))$ (20×13) is nominally stable.

The design with the synthesized controller $\mathbf{K}^{\text{syn}}(s)$ just not achieved robust performance (i.e. $\max_\omega \mu_{\hat{\Delta}}(\mathbf{N}^{\text{syn}}(j\omega)) = 1.038 > 1$), but robust stability was well satisfied (i.e. $\max_\omega \mu_{\Delta}(\mathbf{N}_{11}^{\text{syn}}(j\omega)) = 0.73 < 1$).

By using a subsequent balanced system reduction (based on Hankel singular values) with a multiplicative error method, a reduced controller $\mathbf{K}(s)$ was derived. The reduced controller $\mathbf{K}(s)$, which is also stable, has $n_K = 50$ states. Its singular values are slightly different from those of the synthesized controller $\mathbf{K}^{\text{syn}}(s)$ (Figure 9.36). The singular values of the discretized controller $\mathbf{K}(z)$ obtained from $\mathbf{K}(s)$ by the zero-order hold method ($T_s = 0.01$ s) are also depicted in Figure 9.36. Especially in the high frequency range the singular values of $\mathbf{K}(j\omega)$ and $\mathbf{K}(e^{j\omega T_s})$ differ strongly.

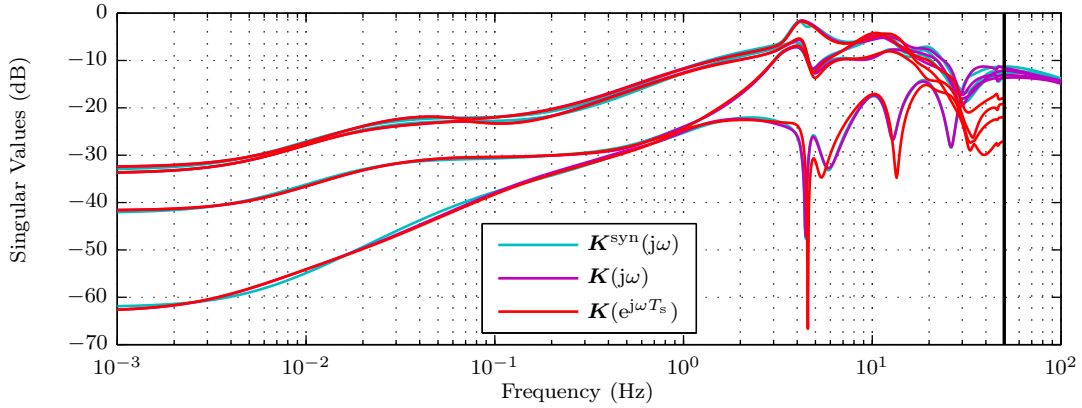


Figure 9.36: Singular values of the feedback controller \mathbf{K}

The nominal closed-loop system $\mathbf{N}(s) = \mathcal{F}_1(\mathbf{P}(s), \mathbf{K}(s))$ (20×13) with the reduced controller $\mathbf{K}(s)$ is internally stable. Thus, also the design with $\mathbf{K}(s)$ achieves nominal stability (NS) (see Definition 8.2 on page 99).

A μ -analysis for nominal performance ($\bar{\sigma}(\mathbf{N}_{22}(j\omega)) = \mu_{\Delta_P}(\mathbf{N}_{22}(j\omega))$), robust stability ($\mu_{\Delta}(\mathbf{N}_{11}(j\omega))$), and robust performance ($\mu_{\hat{\Delta}}(\mathbf{N}(j\omega))$) is depicted in Figure 9.37. In order to account for sharp peaks of the μ -curves the frequency grid was tightened around the frequencies of these peaks.

The objective of nominal performance (NP) is most critical at 4.45 Hz, which is close to the natural frequency of the first structural mode, with $\|\mathbf{N}_{22}(j\omega)\|_\infty = 0.79$. For the modelled uncertainty the objective of robust stability (RS) is most critical at 0.0377 Hz with $\max_\omega \mu_{\Delta}(\mathbf{N}_{11}(j\omega)) = 0.83$. Fortunately the design with the reduced controller $\mathbf{K}(s)$ just achieves robust performance. The μ -curve for robust performance (RP) $\mu_{\hat{\Delta}}(\mathbf{N}(j\omega))$ reaches its maximum, i.e. $\max_\omega \mu_{\hat{\Delta}}(\mathbf{N}(j\omega)) = 0.991 < 1$ at 4.42 Hz (which is again close to the natural frequency of the first structural mode).

For the modelled uncertainty the worst-case performance at a given frequency, i.e. skewed- μ ($\mu^s(\mathbf{N}(j\omega))$) is also depicted in Figure 9.37. At 4.4 Hz, skewed- μ reaches its maximum value of 0.987. Also in relation to nominal performance ($\bar{\sigma}(\mathbf{N}_{22}(j\omega))$), the perturbation Δ can cause the worst deterioration in performance for the first structural mode.

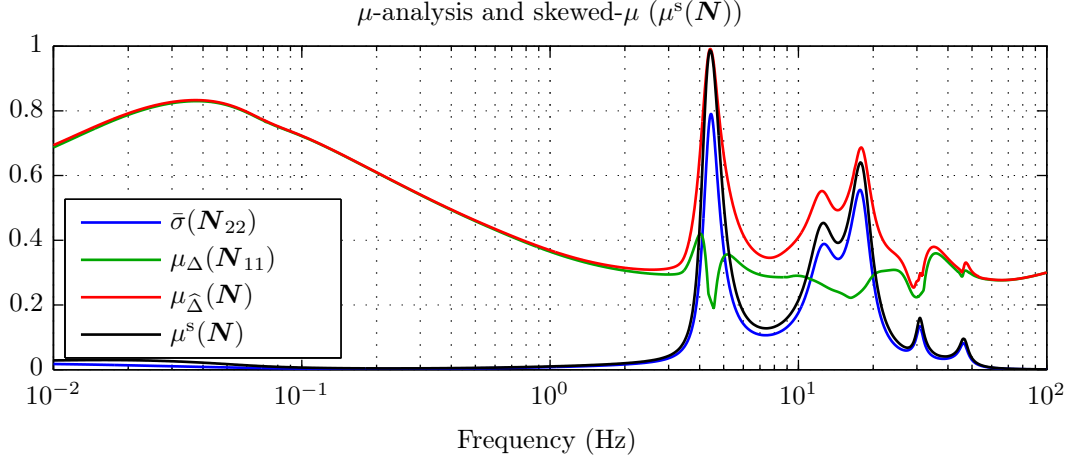


Figure 9.37: μ -analysis (upper bounds) of nominal performance ($\bar{\sigma}(\mathbf{N}_{22}(j\omega)) = \mu_{\Delta_P}(\mathbf{N}_{22}(j\omega))$), robust stability ($\mu_{\Delta}(\mathbf{N}_{11}(j\omega))$) and robust performance ($\mu_{\hat{\Delta}}(\mathbf{N}(j\omega))$) and worst-case performance ($\mu^s(\mathbf{N}(j\omega))$ - upper bound)

The simulated nominal open-loop ($\mathbf{y} = \mathbf{G}_d d$) and closed-loop behavior ($\mathbf{y} = \mathbf{S}\mathbf{G}_d d$) is compared in Figure 9.38a where the improvements in structural mode damping are moderate. Note that the fifth structural mode is even slightly amplified. Considering an additional peak for this mode in the performance weight might be adequate. As revealed by the μ -curve for RP, which is quite low for the fourth and fifth structural modes, achieving RP might not be hard for such modified design. For the modelled uncertainty the worst-case gain of the closed-loop disturbance path ($\mu^s(\mathbf{S}_p \mathbf{G}_d(j\omega))$) is also depicted in Figure 9.38a. At 4.36 Hz, the sensitivity of the worst-case closed-loop disturbance path gain with respect to an individual perturbation block Δ_i is largest for the full complex additive perturbation block Δ_A . If the additive uncertainty is enlarged by 1 %, the worst-case gain increases by 0.14 %.

When applying the discrete-time controller $\mathbf{K}(z)$ on the “IDbs(ho)-model”, the negative feedback system is also stable and the simulation (Figure 9.38b) shows that the fifth and especially the second structural mode are amplified, while for the others damping is moderately improved.

The singular values of the open-loop experimental validation model ($\mathcal{S}^{\text{OL-EV}}$) and those of the closed-loop experimental validation model ($\mathcal{S}^{\text{CL-EV}}$) are depicted in Figure 9.39. The improvements in structural mode damping are not satisfactory, with 1.78 dB, 0.56 dB, and 1.42 dB for the first, third, and fourth structural modes, whereas the second is amplified by 0.4 dB and the fifth remains unchanged.

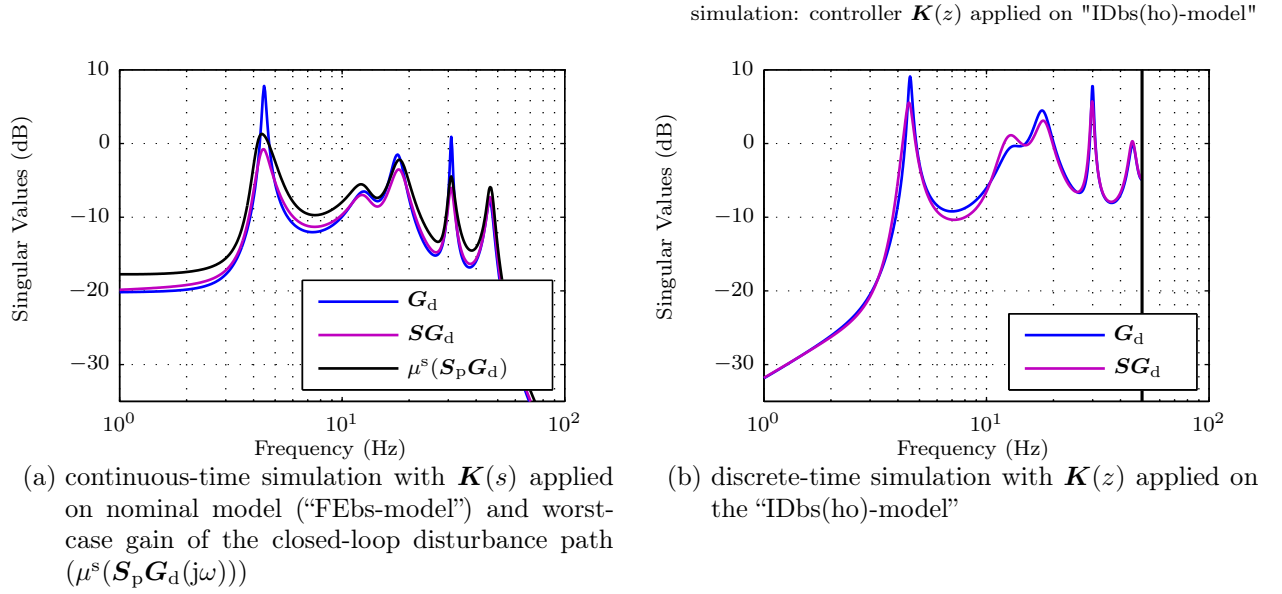


Figure 9.38: Singular values of simulated open-loop and closed-loop behavior (from d to y)

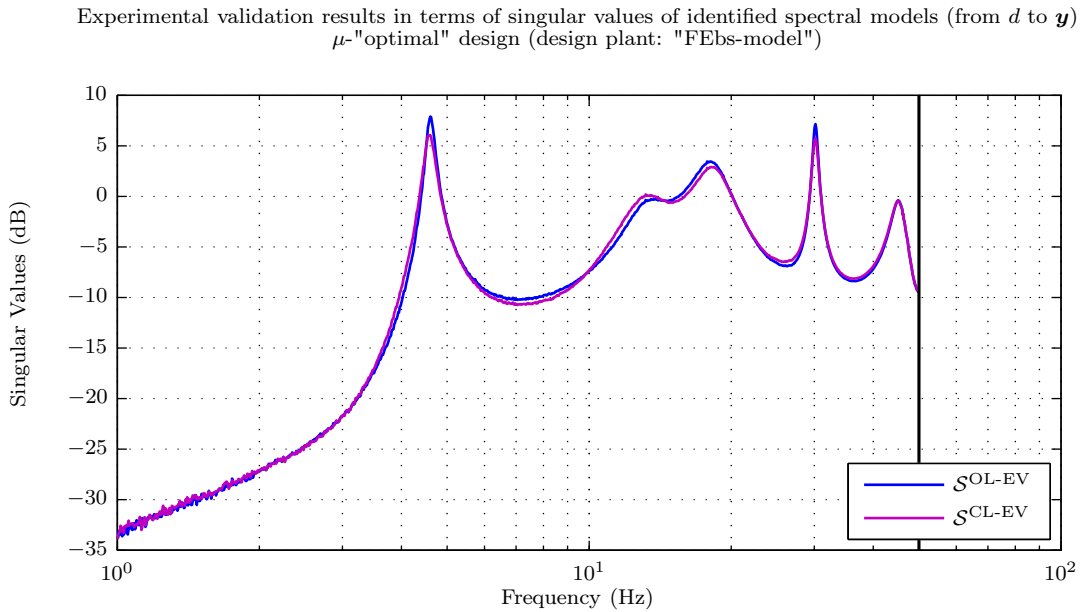


Figure 9.39: Experimental validation results in terms of singular values (from d to y) of open-loop ($\mathcal{S}^{\text{OL-EV}}$) and closed-loop ($\mathcal{S}^{\text{CL-EV}}$) identified spectral models (DK synthesized μ -"optimal" design based on the "FEbs-model")

9.3.5 DGK synthesized μ -"optimal" controller (considering parametric uncertainty in ω_i)

The following design shall be understood as an exemplary design for using parametric uncertainty instead of additive uncertainty.

Additive uncertainty with a full complex uncertainty block Δ_A ($\|\Delta_A\|_\infty \leq 1$), allows for any coupling from its inputs to its outputs with phase relations unknown. Parametric

(real-valued) uncertainty in the state matrix \mathbf{A} is utilized to describe complex relationships between uncertain real-valued parameters and the resulting system dynamics. In the case of the mechanical beam (without its physical systems on the input-side respectively output-side) these parameters are e.g. mode frequencies or dampings. Also designs which utilized both kinds of uncertainty descriptions (additive and parametric uncertainty) simultaneously have been validated successfully in the experiment.

Figure 9.40 shows the singular values of the scalar frequency-dependent weights. The performance weight $W_P(s)$ is shaped as bandpass with extra peaks at the natural frequencies of the first and fourth structural modes. Again, the scalar input weight $W_u(s)$ is formulated as bandstop. The uncertainty weights $W_{1I}(s)$ and $W_{1O}(s)$ for complex diagonal multiplicative input respectively output uncertainty were chosen as scalar bandstop filters. In the stopband the attenuation is 26 dB, hence at these frequencies the design allows for 5 % multiplicative (input respectively output) uncertainty.

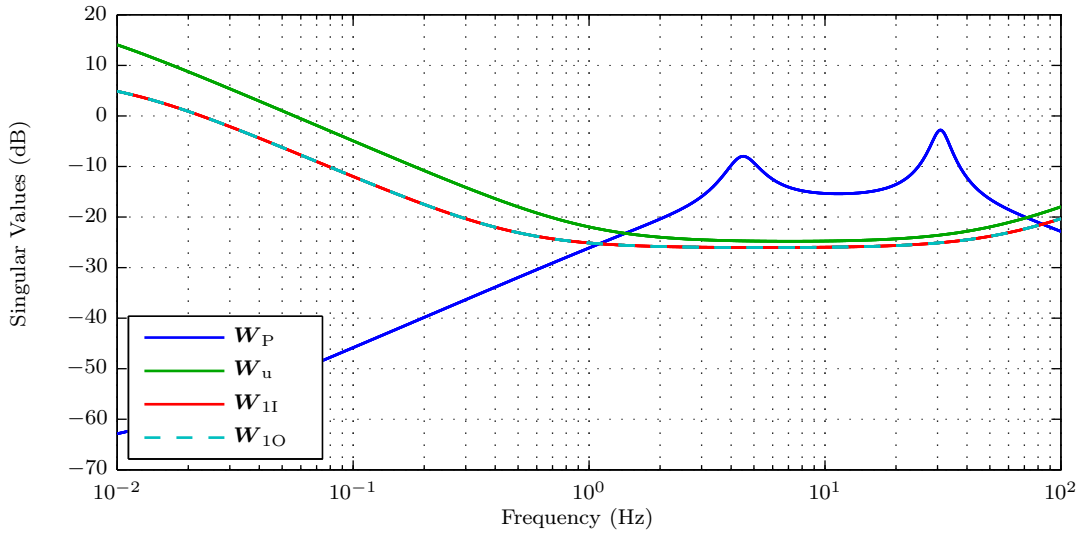


Figure 9.40: Singular values of performance weight \mathbf{W}_P ; input weight \mathbf{W}_u ; \mathbf{W}_{1I} , \mathbf{W}_{1O} for multiplicative input respectively output uncertainty weighting

Section 8.6.2.1 showed the onset to consider parametric (real-valued) uncertainty in the state matrix \mathbf{A} of a plant with a single structural mode with natural angular frequency ω_i and modal damping coefficient ζ_i . It is observed that the stability of a feedback controlled design with a perturbed plant \mathbf{G}_p for flexible structure control is less sensitive with respect to a perturbation of a structural mode's modal damping coefficient ζ_i (as long as it is positive), than with respect to a perturbed natural angular frequency ω_i . To optimally exploit the problem structure and maximize performance, and because a mixed μ -problem (DGK-iteration) produces high complexity, parametric uncertainty is only considered in the natural angular frequency ω_i and only within the state matrix \mathbf{A} .

Remark: Because for the problem at hand, the nominal plant \mathbf{G} was obtained by an analytical model (FE model), it is in principle possible to consider uncertainty directly in the diagonal elements $\omega_i^{\text{FEb(ho)}}$ respectively $\zeta_i^{\text{FEb(ho)}}$ of the matrices of natural angular frequency $\mathbf{\Omega}$ and modal damping \mathbf{Z} (see Section 5.2.2). Depending on the state-space representation

(see Section 5.3.2) this can affect all state-space matrices. By mounting a shaker as outlined in Section 5.6, MATLAB[®] transformed the perturbed state-space system so that only the state matrix \mathbf{A} and output matrix \mathbf{C} contained uncertain parameters and the uncertainty of a mode of the beam without shaker ($\omega_{ip}^{\text{FEb(ho)}}$ and/or $\zeta_{ip}^{\text{FEb(ho)}}$) spread its influence over all other modes of the beam with mounted shaker. It was tested by a singular values plot of the perturbed system of the beam with mounted shaker that a mode $j \neq i$ becomes only slightly perturbed in comparison to the mode i (tested for $i = 1, \dots, 5$). In the whole **uss** object (uncertain state-space model) as well as in the perturbed state matrix \mathbf{A}_p and perturbed output matrix \mathbf{C}_p each uncertain parameter $\zeta_{ip}^{\text{FEb(ho)}}$ occurred once and each uncertain parameter $\omega_{ip}^{\text{FEb(ho)}}$ occurred three times. MATLAB[®] reduction commands like **modsep** and **modred** are not applicable on **uss** objects. Thus it was not possible in the scope of this work to perform a “modal truncation” of the uncertain model. For these reasons this approach to include parametric uncertainty was discarded. Instead, the effects of uncertain parameters ω_i and/or ζ_i on the matrices (\mathbf{A} , \mathbf{B} , \mathbf{C} , \mathbf{D}) of a state-space representation are considered directly by using a LFT (see [7, 12]).

In the following it is shown how to obtain a perturbed (block-diagonal) state matrix \mathbf{A}_p (as shown in (8.37) for a single structural mode i) starting from the state-space representation of a nominal continuous-time LTI system (with only structural modes) in the modal form used by MATLAB[®] (command **sys_M** = **canon(sys, 'modal')**), where each structural mode i (for $i = 1, \dots, n/2$) is represented in the block diagonal state matrix \mathbf{A}_M by the (2×2) block

$$\mathbf{A}_{Mi} = \begin{bmatrix} -\zeta_i \omega_i & \omega_i \sqrt{1 - \zeta_i^2} \\ -\omega_i \sqrt{1 - \zeta_i^2} & -\zeta_i \omega_i \end{bmatrix}. \quad (9.45)$$

The necessary steps to derive a perturbed state matrix \mathbf{A}_p are the following:

- obtain (nominal) natural angular frequencies ω_i and modal damping coefficients ζ_i (for $i = 1, \dots, n/2$) (e.g. using MATLAB[®] command **[Wn,Zeta] = damp(sys)**)
- perform a state transformation (see (A.12) - (A.13)) with the non-singular (block-diagonal) transformation $(n \times n)$ matrix

$$\mathbf{T} = \begin{bmatrix} \mathbf{T}_1 & \mathbf{0} & \mathbf{0} & \mathbf{0} & \mathbf{0} \\ \mathbf{0} & \ddots & \mathbf{0} & \mathbf{0} & \mathbf{0} \\ \mathbf{0} & \mathbf{0} & \mathbf{T}_i & \mathbf{0} & \mathbf{0} \\ \mathbf{0} & \mathbf{0} & \mathbf{0} & \ddots & \mathbf{0} \\ \mathbf{0} & \mathbf{0} & \mathbf{0} & \mathbf{0} & \mathbf{T}_{\frac{n}{2}} \end{bmatrix}, \quad \text{where } \mathbf{T}_i = \begin{bmatrix} \frac{-\zeta_i}{\sqrt{1 - \zeta_i^2}} & \frac{-\sqrt{1 - \zeta_i^2}}{\omega_i - \omega_i \zeta_i^2} \\ 1 & 0 \end{bmatrix} \quad (9.46)$$

to obtain the system in the third modal form where each structural mode i (for $i = 1, \dots, n/2$) is represented in the block diagonal state matrix \mathbf{A} by the (2×2) block

$$\mathbf{A}_i = \begin{bmatrix} 0 & 1 \\ -\omega_i^2 & -2\zeta_i \omega_i \end{bmatrix}. \quad (9.47)$$

- choose for each uncertain structural mode i a relative magnitude of the real-valued uncertainty weight $w_{i\omega}$ and/or $w_{i\zeta}$
- in MATLAB[®], create for each uncertain structural mode i an uncertain real parameter $\delta_{i\omega}$ ($-1 \leq \delta_{i\omega} \leq 1$) and/or $\delta_{i\zeta}$ ($-1 \leq \delta_{i\zeta} \leq 1$) with nominal value zero utilizing

`ureal` and use it accordingly to (8.35) respectively (8.36) to generate a perturbed natural angular frequency ω_{ip} respectively perturbed modal damping coefficient ζ_{ip} . (e.g. `Wn_i_p = Wn_i*(1+w_Wn_i*ureal('delta_Wn_i',0,'Range',[-1,1]));`)

- for each uncertain structural mode i utilize ω_{ip} and/or ζ_{ip} instead of ω_i respectively ζ_i in (9.47) to create the perturbed block \mathbf{A}_{pi} (`umat` object)
- obtain the perturbed (block-diagonal) state matrix \mathbf{A}_p by block-diagonally rebuilding the (block-diagonal) state matrix \mathbf{A} , thereby use for each uncertain structural mode i the perturbed block \mathbf{A}_{pi} instead of \mathbf{A}_i
- use \mathbf{A}_p instead of \mathbf{A} in the state-space representation (third modal form)

In the following all natural angular frequencies ω_i (for $i = 1, \dots, 5$) were considered uncertain. For each (uncertain) structural mode i the chosen relative magnitude of the real-valued uncertainty weight $w_{i\omega}$ is listed in Table 9.2 together with its nominal natural angular frequency ω_i and resulting maximum absolute (symmetric) deviation $\Delta\omega_i$ (respectively $\Delta f_i = \Delta\omega_i/2\pi$). Where $w_{i\omega}$ was chosen so that $\Delta\omega_i > 2\pi \cdot |f_i^{\text{FEbs}} - f_i^{\text{IDbs}}|$ (for $f_i^{\text{FEbs}} - f_i^{\text{IDbs}}$ see Table 6.4 on page 77). Note that for the fifth and especially fourth structural modes, where large deviations in the natural angular frequency are assumed the absolute magnitude of the parametric uncertainty ($|\omega_i w_{i\omega} \delta_{i\omega}|$ with $-1 \leq \delta_{i\omega} \leq 1$) is allowed to be largest.

In the following the perturbed plant with parametric uncertainty only is called $\mathbf{G}_{\text{ppar}}(s)$.

structural mode i	relative magnitude of the uncertainty $w_{i\omega}$ (in %)	nominal natural angular frequency ω_i (in rad/s)	max. absolute (symmetric) deviation $\Delta\omega_i = \omega_i w_{i\omega}$ (in rad/s)	max. absolute (symmetric) deviation $\Delta f_i = \frac{\Delta\omega_i}{2\pi}$ (in Hz)
1	6.55	28.02	1.84	0.293
2	7.58	79.49	6.03	0.960
3	1.51	111.69	1.69	0.269
4	12.86	194.44	25.01	3.981
5	6.76	290.55	19.66	3.129

Table 9.2: relative magnitude $w_{i\omega}$ of the (symmetric) uncertainty of the natural angular frequency ω_i ($\omega_{ip} = \omega_i(1 + w_{i\omega}\delta_{i\omega})$ with $-1 \leq \delta_{i\omega} \leq 1$)

In MATLAB[®], instead of the state-space model (`ss` object) of $\mathbf{G}(s)$, the uncertain state-space model (`uss` object) of $\mathbf{G}_{\text{ppar}}(s)$ (with perturbed state matrix \mathbf{A}_p (`umat` object)) was passed to the command `sysic`, which was utilized as before to construct the generalized plant as given in (9.44). This time, however, this was done without the interconnection structure associated to the input, and output vector, $\mathbf{u}_{\Delta\mathbf{A}}$ respectively $\mathbf{y}_{\Delta\mathbf{A}}$. The resulting perturbed generalized plant with parametric uncertainty is called $\mathbf{P}_{\text{ppar}}(s)$ in the following.

Example 9.2 shows for the case of a mixed μ -problem how a perturbed generalized plant $\mathbf{P}_p = \mathcal{F}_u(\mathbf{P}, \Delta)$ necessary for DGK-iteration (command `dksyn`) is obtained in MATLAB[®], starting with a given $\mathbf{P}_{\text{ppar}}(s)$.

Example 9.2: Obtaining a perturbed generalized plant $\mathbf{P}_p = \mathcal{F}_u(\mathbf{P}, \Delta)$ for DGK-iteration (mixed μ -problem) in MATLAB[®]

```

1 % given:
2 % P_ppar ... uncertain state-space model with parametric uncertainty
3 % Delta_I ... normalized complex diag. perturbation block for input unc.
4 % Delta_O ... normalized complex diag. perturbation block for output unc.
5
6 % obtaining generalized plant "P" and real valued perturbation block for
7 % parametric uncertainty "Delta_par":
8 [P,Delta_par] = lftdata(P_ppar);
9 % obtaining overall, block-diagonal perturbation "Delta":
10 Delta = blkdiag(Delta_par,Delta_I,Delta_O);
11 % obtaining perturbed generalized plant for DGK-iteration "P_p":
12 P_p = lft(Delta,P);

```

Utilizing the commands in Example 9.2 MATLAB[®] took care of the additional interconnection structure in $\mathbf{P}(s)$ necessary for the parametric state-space uncertainty.

In MATLAB[®] the implemented algorithms for handling parametric uncertainty obtained the diagonal real-valued uncertainty block $\Delta_{\text{par}i}$, utilized to perturb the natural angular frequency ω_i in the (2×2) block \mathbf{A}_i (related with the structural mode i), as follows:

$$\Delta_{\text{par}i} = \begin{bmatrix} \delta_{i\omega} & 0 \\ 0 & \delta_{i\omega} \end{bmatrix} \quad (9.48)$$

Note that in (9.48) the parameter $\delta_{i\omega}$, associated with the natural angular frequency ω_i , occurs only two times instead of three times (as in (8.40)). In the case at hand, the normalized ($\|\Delta(j\omega)\|_\infty \leq 1$), overall, block-diagonal perturbation $\Delta(s)$ (18×18) has the following structure:

$$\Delta(s) = \begin{bmatrix} \Delta_{\text{par}} & \mathbf{0} & \mathbf{0} \\ \mathbf{0} & \Delta_{\text{I}}(s) & \mathbf{0} \\ \mathbf{0} & \mathbf{0} & \Delta_{\text{O}}(s) \end{bmatrix} \quad (9.49)$$

with

$$\Delta_{\text{par}} = \begin{bmatrix} \Delta_{\text{par}1} & \mathbf{0} & \mathbf{0} \\ \mathbf{0} & \ddots & \mathbf{0} \\ \mathbf{0} & \mathbf{0} & \Delta_{\text{par}5} \end{bmatrix}, \quad (9.50)$$

$$\Delta_{\text{I}}(s) = \text{diag}\{\Delta_{\text{I}1}(s), \dots, \Delta_{\text{I}4}(s)\}, \quad \text{and} \quad \Delta_{\text{O}}(s) = \text{diag}\{\Delta_{\text{O}1}(s), \dots, \Delta_{\text{O}4}(s)\}. \quad (9.51)$$

The generalized (30×23) plant $\mathbf{P}(s)$ was as outlined in Example 9.2) obtained with $n_{\text{p}} = 68$ states.

With identity scalings $\check{\mathbf{D}}_{\text{r}} = \mathbf{I}$ (30×30) and $\check{\mathbf{D}}_{\text{l}} = \mathbf{I}$ (23×23) ($n_{\check{\mathbf{D}}_{\text{r}}} = n_{\check{\mathbf{D}}_{\text{l}}} = 0$ states) (see (8.95)) the automated DGK-iteration synthesized a stabilizing, stable controller $\mathbf{K}^{\text{syn}}(s)$ (4×4) with $n_{\text{K}^{\text{syn}}} = 68$ states, which just achieved robust performance (i.e. $\max_{\omega} \mu_{\hat{\Delta}}(\mathbf{N}^{\text{syn}}(j\omega)) = 0.9767 < 1$).

Again, by using a subsequent balanced system reduction (based on Hankel singular values) with a multiplicative error method, a reduced controller $\mathbf{K}(s)$ was obtained. The reduced controller $\mathbf{K}(s)$, which is also stable, has $n_{\text{K}} = 50$ states. In Figure 9.41 the singular values of $\mathbf{K}(j\omega)$ are indistinguishable from those of the synthesized controller $\mathbf{K}^{\text{syn}}(j\omega)$.

Note that at a frequency of 30.9 Hz (which is close to the natural frequency of the fourth structural mode of $\mathbf{G}(s)$) the singular values (and especially the maximum singular values) of $\mathbf{K}(j\omega)$ have a sharp peak. The singular values of the discretized controller $\mathbf{K}(z)$ obtained from $\mathbf{K}(s)$ by the zero-order hold method ($T_s = 0.01$ s) are also depicted in Figure 9.41. Especially in the high frequency range the singular values of $\mathbf{K}(j\omega)$ and $\mathbf{K}(e^{j\omega T_s})$ differ strongly.

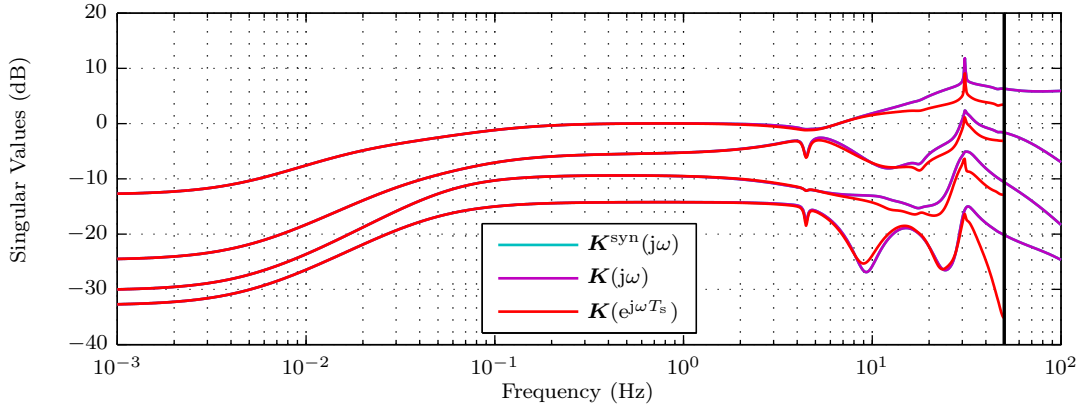


Figure 9.41: Singular values of the feedback controller \mathbf{K}

The nominal closed loop system $\mathbf{N}(s) = \mathcal{F}_1(\mathbf{P}(s), \mathbf{K}(s))$ (26×19) with the reduced controller $\mathbf{K}(s)$ is internally stable. Consequently the design achieves nominal stability (NS).

A μ -analysis for nominal performance ($\bar{\sigma}(\mathbf{N}_{22}(j\omega)) = \mu_{\Delta_P}(\mathbf{N}_{22}(j\omega))$), robust stability ($\mu_{\Delta}(\mathbf{N}_{11}(j\omega))$), and robust performance ($\mu_{\hat{\Delta}}(\mathbf{N}(j\omega))$) is depicted in Figure 9.42. Again, to account for sharp peaks of the μ -curves the frequency grid was tightened around the frequencies of these peaks.

Close to the natural frequency of the first structural mode the objective of nominal performance (NP) is most critical, with $\|\mathbf{N}_{22}(j\omega)\|_{\infty} = 0.6825$. In the frequency range of interest the objective of robust stability (RS) is easily satisfied for the modelled uncertainty (RS is most critical at $5.35 \cdot 10^{-3}$ Hz with $\max_{\omega} \mu_{\Delta}(\mathbf{N}_{11}(j\omega)) = 0.5934$). Also the design with the reduced controller $\mathbf{K}(s)$ just achieves robust performance, where the μ -curve for robust performance (RP) $\mu_{\hat{\Delta}}(\mathbf{N}(j\omega))$ reaches its maximum, i.e. $\max_{\omega} \mu_{\hat{\Delta}}(\mathbf{N}(j\omega)) = 0.9768 < 1$ close to the natural frequency of the first structural mode at 4.4601 Hz.

For the modelled uncertainty the worst-case performance at a given frequency, i.e. skewed- μ ($\mu^s(\mathbf{N}(j\omega))$) is also depicted in Figure 9.42. At 4.4602 Hz skewed- μ reaches its maximum value of 0.9631. However, in relation to nominal performance ($\bar{\sigma}(\mathbf{N}_{22}(j\omega))$), the perturbation Δ can cause the worst deterioration in performance for the fourth structural mode. This means that the modelled uncertainty causes severe performance deterioration at 30.85 Hz. Note that for the fourth structural mode ($i = 4$) $|\omega_i w_{i\omega} \delta_{i\omega}|$ allows for a large maximum absolute (symmetric) deviation (with $-1 \leq \delta_{i\omega} \leq 1$).

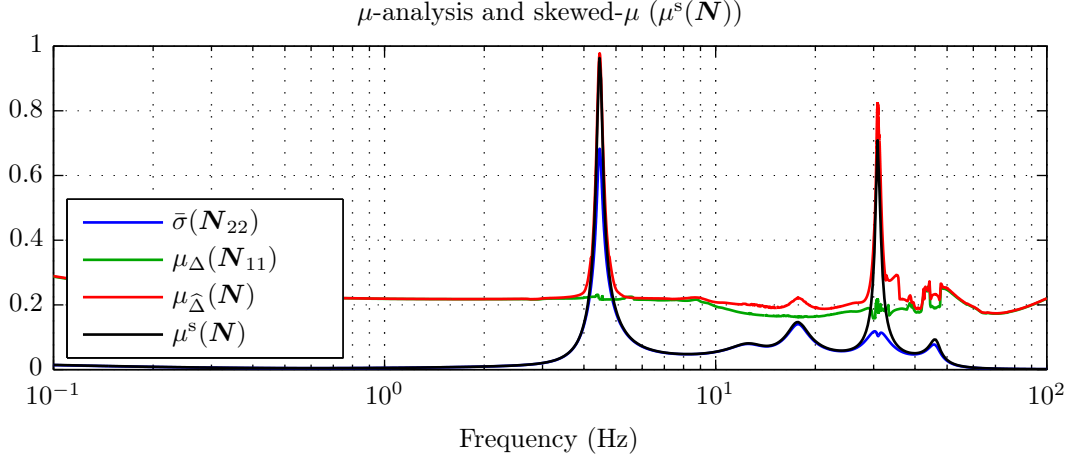


Figure 9.42: μ -analysis (upper bounds) of nominal performance ($\bar{\sigma}(\mathbf{N}_{22}(j\omega)) = \mu_{\Delta_P}(\mathbf{N}_{22}(j\omega))$), robust stability ($\mu_{\Delta}(\mathbf{N}_{11}(j\omega))$) and robust performance ($\mu_{\hat{\Delta}}(\mathbf{N}(j\omega))$) and worst-case performance ($\mu^s(\mathbf{N}(j\omega))$ - upper bound)

The simulation on the nominal plant (Figure 9.43a) reveals, that the fourth structural mode is excellently damped by the continuous-time controller $\mathbf{K}(s)$, whereas the improvements in damping for all other structural modes are only moderate. Despite the fact that the modelled parametric uncertainty for the natural frequency f_4 (in the perturbed state matrix \mathbf{A}_p) allows for a large maximum absolute symmetric deviation Δf_4 of nearly 4 Hz, even the worst-case gain of the closed-loop disturbance path ($\mu^s(\mathbf{S}_p \mathbf{G}_d(j\omega))$) exhibits a minor improvement in damping for this mode (of 1.3 dB, Figure 9.43a). On the other hand, although the maximum allowed absolute symmetric deviation $\Delta f_1 \approx 0.3$ Hz is more than ten times smaller than Δf_4 (the relative magnitude $w_{1\omega}$ of the allowed uncertainty is about half of $w_{4\omega}$), the worst-case gain (as well as the nominal gain) of the closed-loop disturbance path exhibits no significant improvement in damping for the first structural mode. This indicates that small deviations in the natural frequency of the low damped first structural mode may even easier provoke performance problems. Fortunately, however, the magnitude of the deviation $\Delta f_i^{\text{bs}} = f_i^{\text{FEbs}} - f_i^{\text{IDbs}}$ is small for the first structural mode (see Table 6.4 on page 77). This might be the reason that for control designs based on the FE model, improving the damping of the first structural mode in the experiment was not as hard as for the fourth structural mode. Consequently, if the first structural mode of the FE model would have a large deviation it would be impossible to use the FE model as a design plant if the task would be to improve the damping of the first structural mode.

By applying the discrete-time controller $\mathbf{K}(z)$ on the “IDbs(ho)-model”, the negative feedback system is also stable. In Figure 9.43b the singular values of the discrete-time simulation on the “IDbs(ho)-model” are depicted. In terms of the difficult damping of the fourth structural mode this design with parametric uncertainty achieves much better results in the discrete-time simulation than the design in Section 9.3.4 with additive uncertainty (compare with Figure 9.38b). Also the damping of the fifth structural mode, for which the magnitude of the deviation $\Delta f_i^{\text{bs}} = f_i^{\text{FEbs}} - f_i^{\text{IDbs}}$ (see Table 6.4 on page 77) is also large, is improved in the discrete-time simulation. Note that the discrete-time controller $\mathbf{K}(z)$ “splits” the fourth peak into two and that the part which occurs at the higher frequency is much higher.

Unfortunately, in the experiment (Figure 9.44) this behavior is even worse. The part of the split peak which occurs at the higher frequency is so highly developed, that there

are no improvements in damping at all for the fourth structural mode. The first and third structural modes are only slightly better damped, and regrettably the fifth structural mode is actually amplified. All in all, the design cannot convince in the experimental validation. The good results in the discrete-time simulation for the fourth and fifth structural mode are non-existent in the experiment.

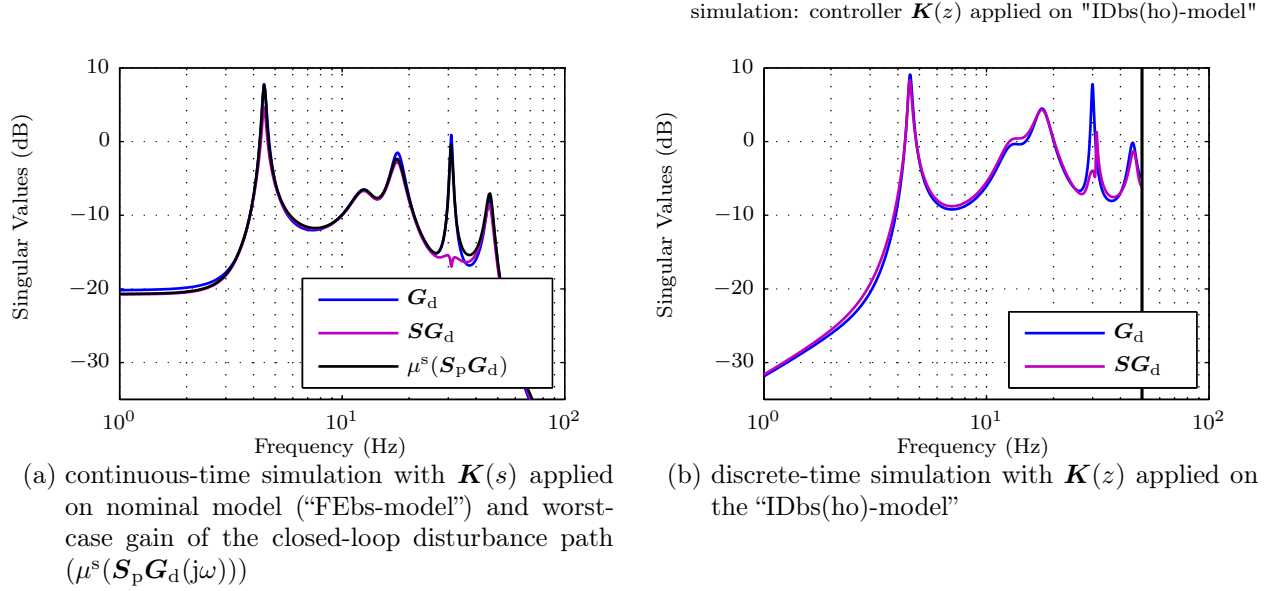


Figure 9.43: Singular values of simulated open-loop and closed-loop behavior (from d to y)

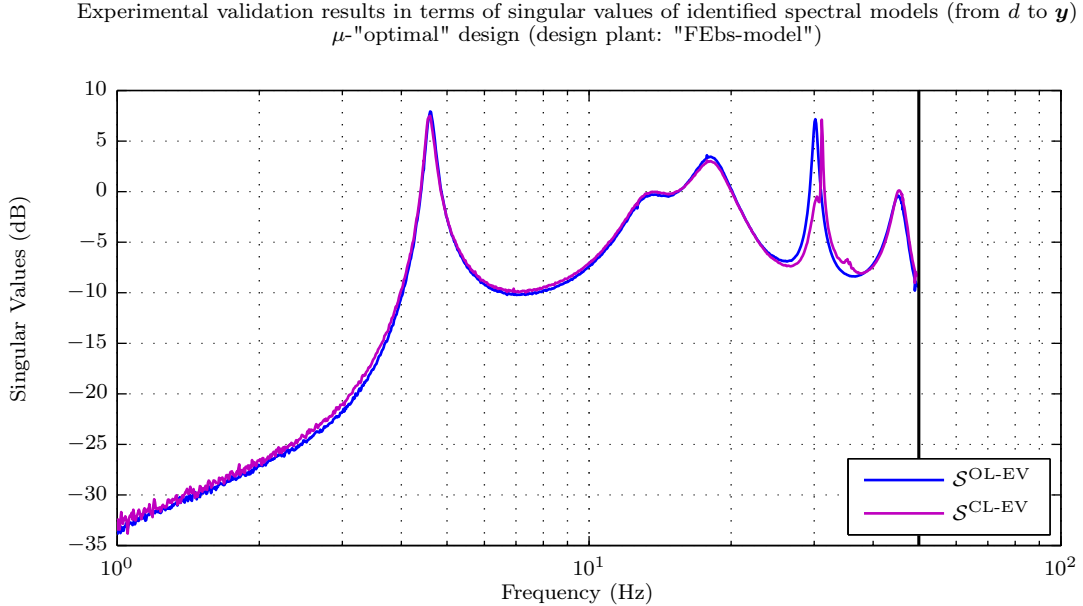


Figure 9.44: Experimental validation results in terms of singular values (from d to y) of open-loop ($\mathcal{S}^{\text{OL-EV}}$) and closed-loop ($\mathcal{S}^{\text{CL-EV}}$) identified spectral models (DGK synthesized μ -"optimal" design based on the "FEbs-model")

Possible reasons for the lack of improved damping in the fourth structural mode in the experiment (assuming linearity of the experimental plant) are:

1. The maximum absolute (symmetric) deviation of the mode's frequency of nearly 4 Hz may not be large enough.
2. The approach of considering parametric ω_i uncertainty in the state matrix \mathbf{A} only may not be sufficient.
3. Since the singular values (and especially the maximum singular values) of the continuous-time controller $\mathbf{K}(s)$ have a quite sharp peak at the natural frequency of the fourth structural mode, the discretization errors of the discretized controller $\mathbf{K}(z)$ obtained from $\mathbf{K}(s)$ by the zero-order hold method may deteriorate the robustness properties of the design.

Remarks:

- ad 1. Also designs with enlarged maximum absolute symmetric deviation were computed. However, these designs either did not fulfill RP or the worst-case gain of the closed-loop disturbance path ($\mu^s(\mathbf{S}_p \mathbf{G}_d(j\omega))$) exceeded $\bar{\sigma}(\mathbf{G}_d(j\omega))$ at the natural frequency of the fourth structural mode.
- ad 2. Considering parametric ω_i uncertainty in the state matrix \mathbf{A} is straightforward because in the third modal form the state matrix \mathbf{A} explicitly contains the parameter ω_i . The input and output matrices, \mathbf{B} respectively \mathbf{C} , however, do not explicitly contain the natural angular frequency ω_i (see (5.78)). Note that the modal matrix Φ was obtained by the generalized eigenvalue/eigenvector problem (see (5.36)) and thus does depend on the natural angular frequencies ω_i . It was used as transformation matrix (see (5.43)), so \mathbf{B} and \mathbf{C} actually do depend on ω_i . Finding an adequate parametric uncertainty description for \mathbf{B} and \mathbf{C} would require further studies.
- ad 3. Additionally considering additive uncertainty (especially for the fourth structural mode) might help to “robustify” the design with respect to discretisation errors of the discretized controller $\mathbf{K}(z)$ obtained from $\mathbf{K}(s)$ by the zero-order hold method.

It is observed that the best experimental result with respect to improved damping of the fourth structural mode was achieved with a design which included an additive and a parametric (as well as a complex diagonal input respectively output) uncertainty model (Figure 9.45). A reduction in mode peak magnitude of 2.53 dB was accomplished, which is actually the best achieved result over all design methods applied on the FE model, but with the disadvantage of amplifying the third structural mode peak by 1.18 dB (requiring further tuning). However, this design has not led to performance guarantees on the whole set of uncertain plants and has not been considered further.

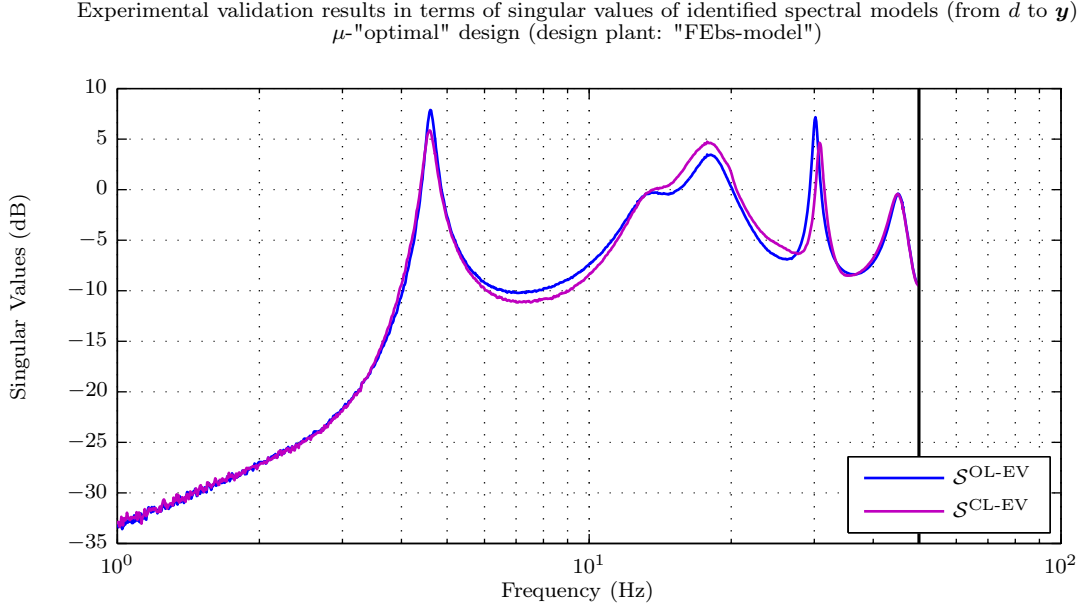


Figure 9.45: Experimental validation results in terms of singular values (from d to y) of open-loop ($\mathcal{S}^{\text{OL-EV}}$) and closed-loop ($\mathcal{S}^{\text{CL-EV}}$) identified spectral models (alternative DGK synthesized μ -“optimal” design based on the “FEbs-model”)

9.3.6 Summing-up experiences and experimental results for the control designs based on the analytical model (FE model)

9.3.6.1 Mixed-sensitivity \mathcal{H}_∞ design

The mixed-sensitivity \mathcal{H}_∞ design is found well-suitable to address structural mode damping. However, utilizing peaks in the frequency-dependent weights turned out to be counterproductive if model mismatch is significant. Again, it was relatively convenient by changing only the constant gain k_2 of $W_2(z)$ in small steps to derive a variety of designs, simulate their performance on the “IDbs(ho)-model” (discrete-time simulation), validate their stability in the experiment, and record a data set for that design with the smallest value of k_2 which achieved stability in the experiment. The robust stability property of the design with respect to additive plant uncertainty seems beneficial to cope with discretization errors of the discretized controller $\mathbf{K}(z)$ obtained from $\mathbf{K}(s)$ by the zero-order hold method. However, for the fourth structural mode improvements were not convincing and for the fifth structural mode no improvements were achieved.

9.3.6.2 Modally weighted LQG design

The LQG design with modal state weighting matrix \mathbf{Q} worked only well for the first three structural modes. The presumably large deviation in the natural frequencies of the fourth and fifth structural mode made it impossible to attain damping improvements for these modes. If the weighting of the fifth structural mode was enlarged, stability problems occurred in the experiment. The ratio of the mean values of the diagonal matrices \mathbf{W} and \mathbf{V} as used for the design based on the identified plant turned out to be inappropriate here. The singular values of the simulated nominal closed-loop disturbance performance ($\mathbf{S}\mathbf{G}_d$) were barely distinguishable from the open-loop ones (\mathbf{G}_d). Thus, \mathbf{W} and \mathbf{V} could not be

considered as given and they had to be considered additional design parameters. Consequently, for each chosen ratio of $\mathbf{W} = W \cdot \mathbf{I}$ and $\mathbf{V} = V \cdot \mathbf{I}$ a variety of controllers $\mathbf{K}(s)$ was computed for a range of \mathbf{R} values. The ratio of \mathbf{W} and \mathbf{V} was chosen so that in the simulation on the nominal plant the LQR and LQG controller achieved similar performance improvements (Kalman observer tuning). Simulating the behavior of the discrete-time controller $\mathbf{K}(z)$ on the “IDbs(ho)-model” turned out to be helpful, especially to address stability issues (performance predictions were only partially correct).

9.3.6.3 \mathcal{H}_∞ loop-shaping design with coprime factor uncertainty

The requirement $\underline{\sigma}(\mathbf{L}(j\omega)) > 1$ (at frequencies where performance is an issue) used to postulate a closed-loop equivalent open-loop requirement for disturbance rejection could not be fulfilled. The plant $\mathbf{G}(s)$ is ill-conditioned (i.e. $\mathbf{G}_s(s)$ has a large condition number $\gamma(\mathbf{G}_s) = \bar{\sigma}(\mathbf{G}_s)/\underline{\sigma}(\mathbf{G}_s)$) at frequencies where performance improvements are required, so choosing the compensator weight $W_1(s)$ scalar was probably not a good choice. Although a sufficiently small γ was achieved by the different designs, the loop shape was severely deteriorated because $\underline{\sigma}(\mathbf{G}_s(j\omega))$ was undesirably small. Surprisingly, the damping improvement for the fourth structural mode was significant. One answer to the surprisingly good achievement of the \mathcal{H}_∞ loop-shaping design based on the “FEbs-model” could lie in the discretisation step of the controller where the otherwise excessively large set of plants described by coprime factor uncertainty might have been beneficial to address the discretisation error.

9.3.6.4 DK synthesized μ -“optimal” controller

The primary difficulty/goal was to attain an improvement in damping for the fourth structural mode while avoiding an amplification of the third and fifth structural mode. Utilizing peaks in the performance weight at the natural frequencies of the first and fourth structural modes yielded a design which amplified the third structural mode strongly. Utilizing a peak in the additive uncertainty weight to avoid an amplification of the third structural mode did not work as expected. However utilizing a peak in the performance weight attained an improvement in damping for that mode. In general the trade-off among the weights to attain RP was quite difficult. The presumably large deviation in the natural frequency of the fourth structural mode could not be taken into account by shaping $|W_{1A}(j\omega)|$ just above $\bar{\sigma}(\mathbf{E}_A^{\text{IDbs(ho)}}(j\omega))$, because then even in the simulation on the nominal plant an improvement in structural mode damping was not possible. Thus, in the end, a smaller peak was used for the additive uncertainty weight at f_4^{FEbs} . In general the achieved improvements in structural mode damping did not justify the necessary design effort for this method.

9.3.6.5 DGK synthesized μ -“optimal” controller

The mixed μ -problems (DGK-iteration) became highly complex and time consuming, even with only a few uncertain parameters involved. Sometimes numerical problems prevented a successful design at all. Moreover, many designs could not be implemented on the hardware because it was not possible to attain a reduced controller $\mathbf{K}(s)$ which achieved nominal stability. Using parametric uncertainty instead of additive uncertainty did not work as well. Although the design allowed for a maximum absolute symmetric deviation Δf_4 of nearly 4 Hz (in the state matrix) for the fourth structural mode (where $\Delta f_4 > |f_4^{\text{FEbs}} - f_4^{\text{IDbs}}|$) and the fact that the worst-case gain of the closed-loop disturbance path ($\mu^s(\mathbf{S}_p \mathbf{G}_d(j\omega))$) predicted an improvement (at least a small one), it was not possible in the hardware experiment to

attain an improvement in damping for that mode (with presumably large deviation in its natural frequency). The singular values of the continuous-time controller $\mathbf{K}(s)$ have a sharp peak at the natural frequency of the fourth structural mode. Hence, the deterioration of the robustness properties of the design due to the conversion of the controller $\mathbf{K}(s)$ from continuous- to discrete-time (discretisation error) is considered as the most likely reason for the missing improvements in the hardware experiment. By considering an additional additive uncertainty weight, which might have helped to “robustify” the design with respect to discretisation errors of the discrete-time controller $\mathbf{K}(z)$, in terms of improving the damping of the fourth structural mode, a better design was obtained.

In general, in order to retain the robustness properties of a design (especially with respect to parametric uncertainty) it might be beneficial to convert the continuous-time design plant to discrete-time a priori, consider an adequate uncertainty description and obtain the controller $\mathbf{K}^{\text{syn}}(z)$ directly in the discrete-time domain. However, considering parametric uncertainty in the natural angular frequency ω_i (and perhaps modal damping coefficient ζ_i) for a discrete-time design plant would require further studies.

Chapter 10

Conclusions

In this work, optimal and robust control design methods were utilized for active vibration damping of a simply supported thin structural beam. The design plants for these sophisticated control design methods were obtained in two fundamentally different ways, by means of a measurement data-driven approach, called system identification, respectively by an analytical (theoretical) approach based on a finite-element (FE) model. Nonlinear effects, especially the hysteresis of the piezo patch actuators and sensors were not regarded, which is justified by the problem setup and the achieved results in structural mode damping.

10.1 Identified Plant Model

The identification procedure outlined in Chapter 4 utilized colored noise signals with a low bandwidth at the input channels but also a high sampling rate of the measurement data and proved to work well. All five structural modes below 50 Hz as predicted by the FE model could be identified from the down-sampled data and the parametric models showed high consistency with the non-parametric models. Because of instantaneous collocation feed-through terms, a non-zero feed-through matrix \mathbf{D} significantly improved the quality of the identified state-space models. Because the system response of the experimental plant “beam” was mainly determined by its complex conjugate poles with low-damping (structural modes), the common approach in active control of structures of extracting the modes of interest by “modal truncation” is well suitable. In the frequency range of interest the frequency response (especially of non-collocated actuator and sensor pairings) was hardly changed by this model reduction (see Figures 4.2 and 4.4). Furthermore, also the truncated model achieved a high fit in cross-validation and turned out to be well-suited as a design plant.

10.2 Controller Designs Based on the Identified Model

Mixed-sensitivity \mathcal{H}_∞ control stands out clearly because of its simplicity in design, implicit robustness with respect to additive uncertainty and especially because of the excellent results in structural mode damping achieved in the experiment. In general, no increased effort in uncertainty modeling is necessary for the identified model. In DK-synthesized control it was not trivial how to choose good uncertainty weights for maximum control performance.

A summary of the individual control designs based on the identified model, respectively the lessons learned during the design, was given in Section 9.2.5.

10.3 Analytical Model (FE Model)

Utilizing Hermitian beam elements for discretizing the beam is found to be a good choice, because for the problem at hand the necessary simplifying assumptions (see Section 5.1) are well fulfilled. Only the bending around a principal axis of inertia was examined. Nonlinear effects, especially those of the actuators and sensors were not modelled.

Despite the neglect of various effects (see Section 5.10) respectively unknown parameters, the analytical models (FE model) and the identified models matched very well in both cases, pure beam as well as beam with mounted shaker which justifies the considered assumptions. Because of the “shaker mounting” via feedback loops it was essential to use high resolution in spatial discretization for the beam with unmounted shaker in the first place.

A common problem in dynamic FE modeling, the determination of the damping matrix, was performed by assuming Rayleigh damping where the parameters α and β were computed by utilizing knowledge about the identified model. Furthermore, by transforming the system from nodal to modal coordinates replacing the first five modal damping coefficients in the diagonal matrix of modal damping by those of the identified model of the pure beam was feasible.

Because of the high resolution in spatial discretization the system order of the obtained state-space models was very large. However, due to the fact that the systems had well-separated oscillatory eigenmodes with low damping, the order could be effectively reduced in the modal representation (modal form) by truncating higher modes (“modal truncation”) without significantly changing the system behavior in the frequency range of interest.

10.4 Controller Designs Based on the Analytical Model (FE Model)

It has been shown that an FE model utilizing a simple one-dimensional finite element for spatial discretization can actually be used as design plant, which at the beginning of this work was in question. However, in order to achieve satisfactory results in structural mode damping for a particular mode, an increased effort in modeling of uncertainty (DGK controller) has to be accepted. Various approaches of uncertainty descriptions were investigated and specific further recommendations were given.

A summary of the individual control designs based on the analytical model, respectively the lessons learned during the design, was given in Section 9.3.6.

10.5 Tabular Overview of the Investigated Controller Design Methods

In Table 10.1 an overview on the achieved improvements, conclusions, and suitability of the investigated controller design methods for structural mode damping for this particular problem setup is given.

design plant	control design method	robustness properties (implicit/modelled)	overall achieved improvements	special improvements for a particular mode	general suitability	effort in designing	cost-benefit ratio	supposed special benefits	encountered problems/disadvantages
identified model (discrete-time design plant)	Mixed-Sensitivity \mathcal{H}_∞ (Fig. 9.5 on page 124)	• implicit RS for additive uncertainty (in this case)	excellent (10)	-	high	moderate	excellent	-	-
	Modally Weighted LQG (Fig. 9.12 on page 134)	• non-existent (see [6])	good (8)	-	high	low	good	-	-
	\mathcal{H}_∞ Loop-Shaping (Fig. 9.17 on page 139)	• implicit RS for coprime factor uncertainty	moderate (6)	-	low	moderate	moderate	• $\gamma(\mathbf{K}) \approx 1 \Rightarrow$ benefits with respect to input uncertainty	• inappropriate uncertainty description
	DK Synthesized (Fig. 9.23 on page 147)	• mult. input & output uncertainty • additive uncertainty	good (8)	-	high	high	moderate	-	• unc. weight selection • high system order • NS with reduced $\mathbf{K}(z)$ (occasionally)
analytical model (continuous-time design plant)	Mixed-Sensitivity \mathcal{H}_∞ (Fig. 9.26 on page 150)	• implicit RS for additive uncertainty (in this case)	moderate (5)	-	high	moderate	good	• additive unc. “robustifies” with respect to discretisation errors ($\mathbf{K}(s) \xrightarrow{\text{zoh}} \mathbf{K}(z)$)	-
	Modally Weighted LQG (Fig. 9.29 on page 154)	• non-existent (see [6])	moderate (4)	-	moderate	low	good	-	-
	\mathcal{H}_∞ Loop-Shaping (Fig. 9.34 on page 158)	• implicit RS for coprime factor uncertainty	moderate (5)	“difficult” 4th structural mode	high	moderate	good	• $\gamma(\mathbf{K}) \approx 1 \Rightarrow$ benefits with respect to input uncertainty • coprime factor unc. “robustifies” with respect to discretisation errors ($\mathbf{K}(s) \xrightarrow{\text{zoh}} \mathbf{K}(z)$)	• (inappropriate uncertainty description)
	DK Synthesized (Fig. 9.39 on page 162)	• mult. input & output uncertainty • additive uncertainty	low (3)	-	low	high	moderate	-	• unc. weight selection • high system order • NS with reduced $\mathbf{K}(s)$ (occasionally)
	DGK Synthesized (without additive unc.) (Fig. 9.44 on page 169)	• ω_i in state matrix, • mult. input & output uncertainty	low (1)	-	low	very high	low	-	• unc. weight selection • high system order • NS with reduced $\mathbf{K}(s)$ (often) • numerical problems crashed algorithms
	DGK Synthesized (with additive unc.) (Fig. 9.45 on page 171)	• ω_i in state matrix, • mult. input & output uncertainty • additive uncertainty	low (3)	“difficult” 4th structural mode	high	extremely high	low	• additive unc. “robustifies” with respect to discretisation errors ($\mathbf{K}(s) \xrightarrow{\text{zoh}} \mathbf{K}(z)$)	• unc. weight selection • high system order • NS with reduced $\mathbf{K}(s)$ (often) • numerical problems crashed algorithms

Table 10.1: Overview controller design methods (including the author’s opinion)

Appendix A

Selected Fundamentals

A.1 Transfer Functions for MIMO Systems

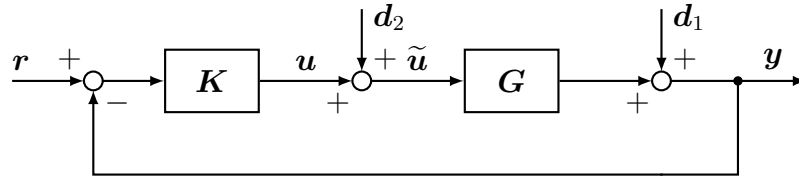


Figure A.1: One degree-of-freedom negative feedback control systems

For the negative feedback system in Figure A.1, the loop transfer function \mathbf{L} is defined as the transfer function as seen when the loop is broken at the output of the plant \mathbf{G} .

$$\mathbf{L} = \mathbf{G}\mathbf{K} \quad (\text{A.1})$$

In the case of this negative feedback arrangement, the (output) sensitivity function \mathbf{S} ($\mathbf{y} = \mathbf{S}\mathbf{d}_1$) and (output) complementary sensitivity function \mathbf{T} ($\mathbf{y} = \mathbf{T}\mathbf{r}$) are defined as

$$\mathbf{S} = (\mathbf{I} + \mathbf{G}\mathbf{K})^{-1} \quad (\text{A.2})$$

$$\mathbf{T} = \mathbf{I} - \mathbf{S} = \mathbf{G}\mathbf{K}\mathbf{S} \quad (\text{A.3})$$

The loop transfer function \mathbf{L}_I is defined as the transfer function as seen when the loop is broken at the input to the plant \mathbf{G} .

$$\mathbf{L}_I = \mathbf{K}\mathbf{G} \quad (\text{A.4})$$

In the case of this negative feedback arrangement, the input sensitivity function \mathbf{S}_I ($\tilde{\mathbf{u}} = \mathbf{S}_I\mathbf{d}_2$) and input complementary sensitivity function \mathbf{T}_I ($\mathbf{u} = -\mathbf{T}_I\mathbf{d}_2$) are defined as

$$\mathbf{S}_I = (\mathbf{I} + \mathbf{K}\mathbf{G})^{-1} \quad (\text{A.5})$$

$$\mathbf{T}_I = \mathbf{I} - \mathbf{S}_I = \mathbf{K}\mathbf{G}\mathbf{S}_I \quad (\text{A.6})$$

Remark: When positive feedback is used in Figure A.1, $\mathbf{S} = (\mathbf{I} - \mathbf{G}\mathbf{K})^{-1}$ and $\mathbf{S}_I = (\mathbf{I} - \mathbf{K}\mathbf{G})^{-1}$.

In Figure A.2 a one degree-of-freedom negative feedback configuration is depicted. The plant \mathbf{G} and controller \mathbf{K} interconnection is driven by output disturbances \mathbf{d} , reference commands \mathbf{r} , and measurement noise \mathbf{n} . Via the control signals \mathbf{u} the outputs \mathbf{y} shall be controlled.

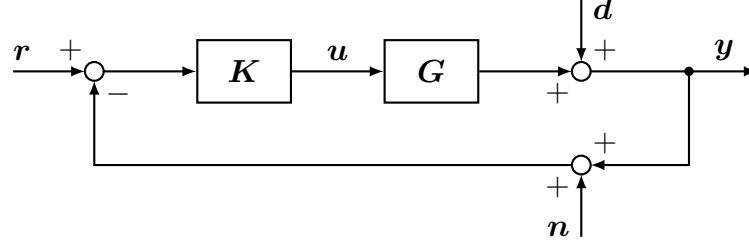


Figure A.2: One degree-of-freedom (negative) feedback configuration

In terms of the sensitivity function $\mathbf{S} = (\mathbf{I} + \mathbf{G}\mathbf{K})^{-1}$ and the complementary sensitivity function $\mathbf{T} = \mathbf{I} - \mathbf{S} = \mathbf{G}\mathbf{K}\mathbf{S}$, the following relations hold:

$$\mathbf{y}(s) = \mathbf{T}(s)\mathbf{r}(s) + \mathbf{S}(s)\mathbf{d}(s) - \mathbf{T}(s)\mathbf{n}(s) \quad (\text{A.7})$$

$$\mathbf{u}(s) = \mathbf{K}(s)\mathbf{S}(s)(\mathbf{r}(s) - \mathbf{d}(s) - \mathbf{n}(s)) \quad (\text{A.8})$$

By an investigation of (A.7) and (A.8) the following conclusions in terms of closed-loop requirements, in addition to the requirement that \mathbf{K} stabilizes \mathbf{G} can be made (see Table A.1): [6]

control objective	typical frequency range	closed-loop requirement
disturbance rejection	ω low	$\bar{\sigma}(\mathbf{S}(j\omega))$ small
reference tracking	ω low	$\bar{\sigma}(\mathbf{T}(j\omega)) \approx \underline{\sigma}(\mathbf{T}(j\omega)) \approx 1$
noise attenuation	ω high	$\bar{\sigma}(\mathbf{T}(j\omega))$ small
input usage (control energy) reduction	ω high	$\bar{\sigma}(\mathbf{K}\mathbf{S}(j\omega))$ small

Table A.1: Closed-loop requirements (in addition to the requirement that \mathbf{K} stabilizes \mathbf{G}) (adopted from [6])

In case of a SISO system, a magnitude plot of a typical loop transfer function L , sensitivity function S , and complementary sensitivity function T is shown in Figure A.3.

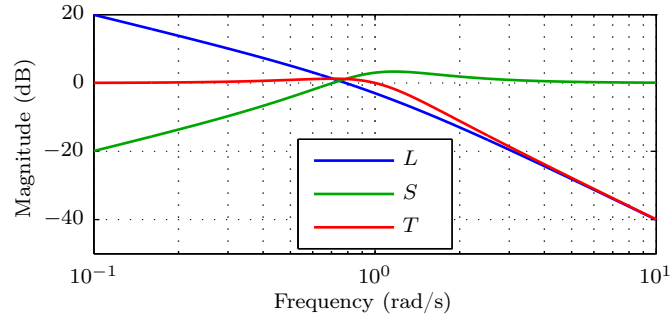


Figure A.3: Magnitude plot of typical loop transfer function L , sensitivity function S and complementary sensitivity function T (SISO case, $L(s) = \frac{1}{s(s+1)}$)

A.2 A Plant in State-Space and Transfer Function Representation

A.2.1 State-space representation

In Figure A.4 the state-equation (A.9) and output equation (A.10) of an LTI system in state-space representation are depicted graphically.

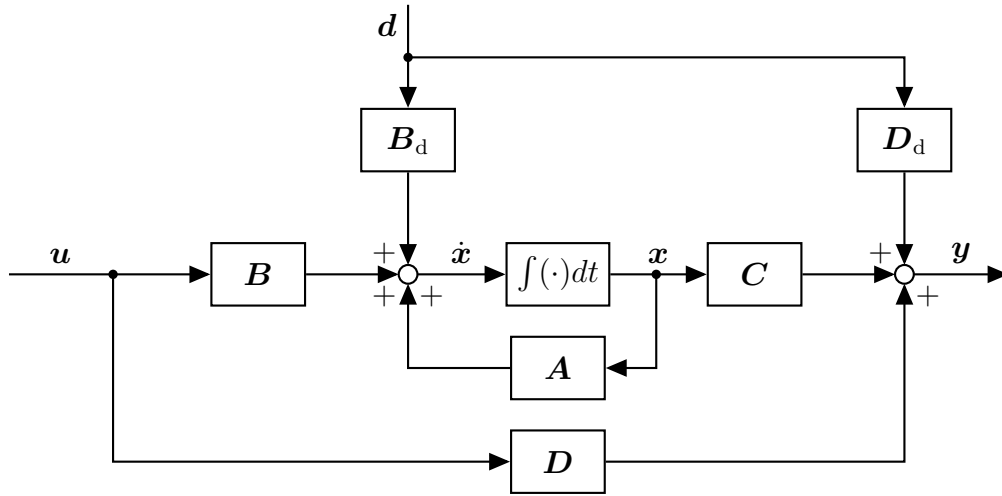


Figure A.4: State-Space Representation

$$\dot{x} = Ax + Bu + B_d d \quad x(t=0) = x_0 \quad (\text{A.9})$$

$$y = Cx + Du + D_d d \quad (\text{A.10})$$

\mathbf{A} :	$(n \times n)$	-	state matrix	\mathbf{x} :	$(n \times 1)$	-	state vector
\mathbf{B} :	$(n \times r)$	-	input matrix	\mathbf{u} :	$(r \times 1)$	-	input vector
\mathbf{B}_d :	$(n \times q)$	-	disturbance input matrix	\mathbf{d} :	$(q \times 1)$	-	disturbance vector
\mathbf{C} :	$(m \times n)$	-	output matrix	\mathbf{y} :	$(m \times 1)$	-	output vector
\mathbf{D} :	$(m \times r)$	-	feed-through matrix				
\mathbf{D}_d :	$(m \times q)$	-	disturbance feed-through matrix				

By applying a similarity transformation (where \mathbf{T} is a non-singular $(n \times n)$ transformation matrix)

$$\mathbf{x} = \mathbf{T}\mathbf{x}^{\text{new}}, \quad (\text{A.11})$$

the state-space representation with state vector \mathbf{x} can be transformed into a new representation with state vector \mathbf{x}^{new} .

$$\dot{\mathbf{x}}^{\text{new}} = \underbrace{\mathbf{T}^{-1}\mathbf{A}\mathbf{T}}_{\mathbf{A}^{\text{new}}} \mathbf{x}^{\text{new}} + \underbrace{\mathbf{T}^{-1}\mathbf{B}}_{\mathbf{B}^{\text{new}}} \mathbf{u} + \underbrace{\mathbf{T}^{-1}\mathbf{B}_d}_{\mathbf{B}_d^{\text{new}}} \mathbf{d} \quad (\text{A.12})$$

$$\mathbf{y} = \underbrace{\mathbf{C}\mathbf{T}}_{\mathbf{C}^{\text{new}}} \mathbf{x}^{\text{new}} + \mathbf{D}\mathbf{u} + \mathbf{D}_d\mathbf{d} \quad (\text{A.13})$$

Because the set of non-singular transformation matrices is an infinite set, one and the same system can be posed in an infinite set of state-space representations.

A.2.2 Transfer function representation

Laplace transformation of the state-equation (A.9) with vanishing initial condition ($\mathbf{x}_0 = \mathbf{0}$) and the output-equation (A.10) leads to (A.14) and (A.15):

$$s\mathbf{x}(s) = \mathbf{A}\mathbf{x}(s) + \mathbf{B}\mathbf{u}(s) + \mathbf{B}_d\mathbf{d}(s) \quad (\text{A.14})$$

$$\mathbf{y}(s) = \mathbf{C}\mathbf{x}(s) + \mathbf{D}\mathbf{u}(s) + \mathbf{D}_d\mathbf{d}(s) \quad (\text{A.15})$$

Inserting $\mathbf{x}(s) = (s\mathbf{I} - \mathbf{A})^{-1}(\mathbf{B}\mathbf{u}(s) + \mathbf{B}_d\mathbf{d}(s))$ into the Laplace-transformed output equation (A.15) yields equation (A.16).

$$\mathbf{y}(s) = \underbrace{[\mathbf{C}(s\mathbf{I} - \mathbf{A})^{-1}\mathbf{B} + \mathbf{D}]}_{\mathbf{G}(s)} \mathbf{u}(s) + \underbrace{[\mathbf{C}(s\mathbf{I} - \mathbf{A})^{-1}\mathbf{B}_d + \mathbf{D}_d]}_{\mathbf{G}_d(s)} \mathbf{d}(s) \quad (\text{A.16})$$

Let a minimal state-space representation of $\mathbf{G}(s)$ respectively $\mathbf{G}_d(s)$ be given by

$$\mathbf{G}(s) \stackrel{\text{ss}}{=} \left[\begin{array}{c|c} \mathbf{A} & \mathbf{B} \\ \hline \mathbf{C} & \mathbf{D} \end{array} \right], \quad \mathbf{G}_d(s) \stackrel{\text{ss}}{=} \left[\begin{array}{c|c} \mathbf{A} & \mathbf{B}_d \\ \hline \mathbf{C} & \mathbf{D}_d \end{array} \right]. \quad (\text{A.17})$$

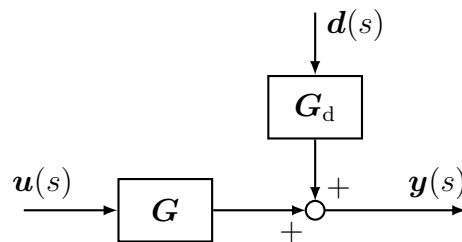


Figure A.5: Transfer function representation

A.3 Proper Systems

Definition A.1: Proper and bi-proper systems, SISO case [7]

- A system $G(s)$ is *strictly proper* if $G(j\omega) \rightarrow 0$ as $\omega \rightarrow \infty$. It can be represented as state-space system and has no feed-through term ($d = 0$).
- A system $G(s)$ is *bi-proper* or *semi-proper* if $G(j\omega) \rightarrow d$, $d \in \mathbb{R} \setminus \{-\infty, 0, \infty\}$ as $\omega \rightarrow \infty$. It can be represented as state-space system with finite, nonzero feed-through term d .
- A system $G(s)$ which is strictly proper or bi-proper is *proper*.
- A system $G(s)$ is *improper* if $|G(j\omega)| \rightarrow \infty$ as $\omega \rightarrow \infty$. Improper systems cannot be represented as state-space systems with state-space matrices (A, B, C, D) .^a

^aAn improper systems can be represented as descriptor state-space model, which have the following modified state equation: $E\dot{x} = Ax + Bu$.

Definition A.1 directly extends to multi-input multi-output (MIMO) systems. State space systems are always proper. If $\mathbf{D} \neq \mathbf{0}$, they are bi-proper, otherwise they are strictly proper.

A.4 Singular Value Decomposition (SVD)

Definition A.2: Singular Value Decomposition (SVD) [7, 6]

Any real- or complex-valued $(m \times n)$ matrix \mathbf{A} may be factorized using the SVD

$$\mathbf{A} = \mathbf{U}\mathbf{\Sigma}\mathbf{V}^H \quad (\text{A.18})$$

$$\mathbf{\Sigma} = \begin{cases} \begin{bmatrix} \mathbf{\Sigma}_1 \\ \mathbf{0} \end{bmatrix} & \text{if } m > n \\ \mathbf{\Sigma}_1 & \text{if } m = n \\ \begin{bmatrix} \mathbf{\Sigma}_1 & \mathbf{0} \end{bmatrix} & \text{if } m < n \end{cases}, \quad \mathbf{\Sigma}_1 = \begin{bmatrix} \sigma_1 & 0 & \dots & 0 \\ 0 & \sigma_2 & \ddots & \vdots \\ \vdots & \ddots & \ddots & 0 \\ 0 & \dots & 0 & \sigma_k \end{bmatrix}, \quad k = \min(m, n) \quad (\text{A.19})$$

Thereby, the $(m \times m)$ matrix \mathbf{U} and the $(n \times n)$ matrix \mathbf{V} are unitary matrices ($\mathbf{U}^H = \mathbf{U}^{-1}$, $\mathbf{V}^H = \mathbf{V}^{-1}$), and the $(m \times n)$ matrix $\mathbf{\Sigma}$ contains a diagonal matrix $\mathbf{\Sigma}_1$ ($k \times k$), whose real, non-negative, diagonal entries $\bar{\sigma} \equiv \sigma_1 \geq \sigma_2 \geq \dots \geq \sigma_k \equiv \underline{\sigma} \geq 0$ are called the singular values of \mathbf{A} .

The singular values are computed as the positive square roots of the $k = \min(m, n)$ largest eigenvalues of both $\mathbf{A}\mathbf{A}^H$ and $\mathbf{A}^H\mathbf{A}$.

$$\sigma_i(\mathbf{A}) = \sqrt{\lambda_i(\mathbf{A}\mathbf{A}^H)} = \sqrt{\lambda_i(\mathbf{A}^H\mathbf{A})} \quad (\text{A.20})$$

The not unique matrices \mathbf{U} and \mathbf{V} are matrices of eigenvectors of $\mathbf{A}\mathbf{A}^H$ respectively $\mathbf{A}^H\mathbf{A}$. The corresponding column vectors \mathbf{u}_i of \mathbf{U} and row vectors \mathbf{v}_i^H of \mathbf{V}^H are called (left respectively right) singular vectors.

A.5 Pseudo-Inverse (Generalized Inverse)

This section is based on [6].

Definition A.3: Pseudo-Inverse [6]

Consider the set of linear equations

$$\mathbf{y} = \mathbf{A}\mathbf{x} \quad (\text{A.21})$$

with a given $(m \times 1)$ vector \mathbf{y} and a given $(m \times n)$ matrix \mathbf{A} . A *least squares* solution to (A.21) is a $(n \times 1)$ vector \mathbf{x} such that $\|\mathbf{x}\|_2 = \sqrt{x_1^2 + x_2^2 + \dots + x_n^2}$ is minimized among all vectors for which $\|\mathbf{y} - \mathbf{A}\mathbf{x}\|_2$ is minimized. The solution is given in terms of the pseudo-inverse (Moore-Penrose generalized inverse) of \mathbf{A} : [6]

$$\mathbf{x} = \mathbf{A}^\dagger \mathbf{y} \quad (\text{A.22})$$

The pseudo-inverse may be obtained from an SVD of $\mathbf{A} = \mathbf{U}\mathbf{\Sigma}\mathbf{V}^H$ (see Definition A.2) by

$$\mathbf{A}^\dagger = \mathbf{V}_r \mathbf{\Sigma}_r^{-1} \mathbf{U}_r^H = \sum_{i=1}^r \frac{1}{\sigma_i(\mathbf{A})} \mathbf{v}_i \mathbf{u}_i^H \quad (\text{A.23})$$

where r is the number of non-zero singular values of \mathbf{A} (i.e. $r = \text{rank}(\mathbf{A})$). In (A.23) the matrices \mathbf{U}_r ($m \times r$) and \mathbf{V}_r ($n \times r$) contain only the first r columns of \mathbf{U} respectively \mathbf{V} as introduced in (A.18) and the $(r \times r)$ diagonal matrix $\mathbf{\Sigma}_r$ contains only the first r (non-zero) singular values of \mathbf{A} .

The following holds:

$$\underline{\sigma}(\mathbf{A}) = \frac{1}{\bar{\sigma}(\mathbf{A}^\dagger)} \quad (\text{A.24})$$

Note that the $(n \times m)$ matrix \mathbf{A}^\dagger exists for any matrix \mathbf{A} , even for a singular square matrix and a non-square matrix. The pseudo-inverse also satisfies

$$\mathbf{A}\mathbf{A}^\dagger\mathbf{A} = \mathbf{A} \quad \text{and} \quad \mathbf{A}^\dagger\mathbf{A}\mathbf{A}^\dagger = \mathbf{A}^\dagger \quad (\text{A.25})$$

Note the following cases (where r is the rank of \mathbf{A}): [6]

1. $r = m = n$, i.e. \mathbf{A} is non-singular. In this case $\mathbf{A}^\dagger = \mathbf{A}^{-1}$ is the inverse of \mathbf{A} .
2. $r = n \leq m$, i.e. \mathbf{A} has full column rank. This is the “conventional least squares problem” where $\|\mathbf{y} - \mathbf{A}\mathbf{x}\|_2$ is to be minimized, and the solution is

$$\mathbf{A}^\dagger = (\mathbf{A}^H \mathbf{A})^{-1} \mathbf{A}^H \quad (\text{A.26})$$

In this case $\mathbf{A}^\dagger \mathbf{A} = \mathbf{I}$, so \mathbf{A}^\dagger is a *left inverse* of \mathbf{A} .

3. $r = m \leq n$, i.e. \mathbf{A} has full row rank. In this case an infinite number of solutions to (A.21) exist and it is sought for the one that minimizes $\|\mathbf{x}\|_2$. This is

$$\mathbf{A}^\dagger = \mathbf{A}^H (\mathbf{A}\mathbf{A}^H)^{-1} \quad (\text{A.27})$$

In this case $\mathbf{A}\mathbf{A}^\dagger = \mathbf{I}$, so \mathbf{A}^\dagger is a *right inverse* of \mathbf{A} .

4. $r < k = \min(m, n)$ (general case). In this case both matrices $\mathbf{A}^H \mathbf{A}$ and $\mathbf{A}\mathbf{A}^H$ are rank deficient. In the general case (A.23) has to be used to obtain the pseudo-inverse and \mathbf{A} has neither a left nor a right inverse.

A.6 Norms

This Section was adopted from [7]. The definitions make use of a vector space \mathbf{V} and a field \mathbb{F} . A precise definition of \mathbf{V} and \mathbb{F} is found in [7]

Norms are utilized in order to measure the size of an algebraic object. These objects can be scalars, vectors, matrices, signals in the time- or frequency domains, or linear operators such as transfer functions.[7]

Definition A.4: Norm [7]

A norm of \mathbf{x} (where \mathbf{x} is an element of a vector space \mathbf{V} over a field \mathbb{F}) is a real number, denoted $\|\mathbf{x}\|$, that satisfies the following properties:

- | | |
|--|---|
| N1.: $\ \mathbf{x}\ > 0$ | non-negativity |
| N2.: $\ \mathbf{x}\ = 0 \Leftrightarrow \mathbf{x} = \mathbf{0}$ | positivity (For <i>semi-norms</i> , only $\mathbf{x} = \mathbf{0} \Rightarrow \ \mathbf{x}\ = 0$ is true.) |
| N3.: $\ \alpha \cdot \mathbf{x}\ = \alpha \cdot \ \mathbf{x}\ $ for all scalars $\alpha \in \mathbb{F}$ | homogeneity |
| N4.: $\ \mathbf{x}_1 + \mathbf{x}_2\ \leq \ \mathbf{x}_1\ + \ \mathbf{x}_2\ $ | triangle inequality |

A.6.1 Vector- and matrix norms

Definition A.5: Vector p -norm [7]

For a vector $\mathbf{x} = [x_1, \dots, x_m]^T \in \mathbb{F}^m$ with m elements, the vector p -norm is defined as:

$$\|\mathbf{x}\|_p = \left(\sum_{i=1}^m |x_i|^p \right)^{\frac{1}{p}}, \quad p \geq 1. \quad (\text{A.28})$$

A shortlist of common vector norms is given in the following:[7]

- | | | |
|--|--------------|--|
| Vector 1-norm (sum norm): | $p = 1$ | $\ \mathbf{x}\ _1 = \sum_{i=1}^m x_i $ |
| Vector 2-norm (Euclidean norm): | $p = 2$ | $\ \mathbf{x}\ _2 = \sqrt{\sum_{i=1}^m x_i ^2} = \sqrt{\mathbf{x}^H \mathbf{x}}$
\mathbf{x}^H is the Hermitian transpose (conjugate transpose) of \mathbf{x} |
| Vector ∞-norm (max norm): | $p = \infty$ | $\ \mathbf{x}\ _\infty = \max_{i=1}^m x_i $ |

Definition A.6: Matrix norm [7]

A norm of a constant $(m \times n)$ -matrix $\mathbf{A} \in \mathbb{F}^{m \times n}$ is called a *matrix norm* if it fulfills the four axioms N1–N4 in Definition A.4 and additionally the multiplicative property:

$$\|\mathbf{AB}\| \leq \|\mathbf{A}\| \cdot \|\mathbf{B}\| \quad (\text{A.29})$$

for all \mathbf{A}, \mathbf{B} for which the product \mathbf{AB} exists (i.e., which are of compatible inner dimensions).

If a norm on a matrix only satisfies the four axioms N1–N4 in Definition A.4, the norm is called generalized matrix norm and has weaker properties.[7, 6]

A shortlist of common matrix norms is given in the following for a matrix $\mathbf{A} = [a_{ij}] \in \mathbb{C}^{m \times n}$:

Sum matrix norm:	$\ \mathbf{A}\ _{\text{sum}} = \sum_{i,j} a_{ij} $
Frobenius matrix norm (Euclidean norm):	$\ \mathbf{A}\ _{\text{F}} = \sqrt{\sum_{i,j} a_{ij} ^2} = \sqrt{\text{trace}(\mathbf{A}^{\text{H}} \mathbf{A})}$
	\mathbf{A}^{H} is the Hermitian transpose (conjugate transpose) of \mathbf{A}

Induced norms of linear operators, particularly of matrices, are of special interest:

Definition A.7: Induced norm [7]

Given a constant matrix \mathbf{A} and the linear mapping $\mathbf{z} = \mathbf{A}\mathbf{w}$ for compatible vectors \mathbf{z}, \mathbf{w} , the induced p -norm $\|\cdot\|_p$ is defined as:

$$\|\mathbf{A}\|_p = \max_{\mathbf{w} \neq \mathbf{0}} \frac{\|\mathbf{z}\|_p}{\|\mathbf{w}\|_p} = \max_{\mathbf{w} \neq \mathbf{0}} \frac{\|\mathbf{A}\mathbf{w}\|_p}{\|\mathbf{w}\|_p} \quad (\text{A.30})$$

The induced norm is a matrix norm and thus satisfies the multiplicative property (A.29).

For the case $p = 2$ (induced 2-norm), the **singular value norm** or **spectral norm** is obtained:

$$\|\mathbf{A}\|_{i2} = \bar{\sigma}(\mathbf{A}) = \sqrt{\rho(\mathbf{A}^{\text{H}} \mathbf{A})} = \sqrt{\rho(\mathbf{A} \mathbf{A}^{\text{H}})} \quad (\text{A.31})$$

where $\bar{\sigma}(\cdot)$ is the maximum singular value (see Definition A.2) and $\rho(\cdot)$ is the spectral radius:

Definition A.8: Spectral radius [7]

The spectral radius $\rho(\mathbf{A})$ of a matrix \mathbf{A} is the maximum of the eigenvalue magnitudes:

$$\rho(\mathbf{A}) = \max_i |\lambda_i(\mathbf{A})| \quad (\text{A.32})$$

The spectral radius is not a norm, but represents an important lower bound on any matrix norm [6]:

$$\rho(\mathbf{A}) \leq \|\mathbf{A}\| \quad (\text{A.33})$$

A.6.2 Signal norms

Signal norms, also called temporal norms, are formulated for time-varying (or frequency-varying) signals $\mathbf{z}(t)$. [7] This section was adopted from [7]. More information about signal norms can be found there.

Definition A.9: Temporal p -norm, l_p -norm [7]

Given a time-varying vector signal $\mathbf{z}(t) = [z_1(t), \dots, z_n(t)]$, its temporal p -norm or l_p -norm $\|\mathbf{z}(t)\|_p$ is defined by

$$\|\mathbf{z}(t)\|_p = \left(\int_{-\infty}^{\infty} \sum_{i=1}^n |z_i(\tau)|^p d\tau \right)^{\frac{1}{p}} \quad (\text{A.34})$$

A shortlist of common temporal norms of signals is given in the following:

1-norm in time (integral absolute error, IAE): $p = 1 \quad \|\mathbf{z}(t)\|_1 = \int_{-\infty}^{\infty} \sum_{i=1}^n |z_i(\tau)| d\tau$

2-norm in time (quadratic norm, integral square error, ISE, energy of the signal): $p = 2 \quad \|\mathbf{z}(t)\|_2 = \sqrt{\int_{-\infty}^{\infty} \sum_{i=1}^n |z_i(\tau)|^2 d\tau}$

∞ -norm in time (peak value in time): $p = \infty \quad \|\mathbf{z}(t)\|_{\infty} = \max_{\tau} (\max_{i=1}^n |z_i(\tau)|)$

Note that the commonly used signal RMS (root mean square) norm, also called power norm, is only a semi-norm (compare Definition A.4, N2 is not fulfilled – a nonzero signal may very well have an RMS value of zero): [7]

$$\|\mathbf{z}(t)\|_{\text{pow}} = \|\mathbf{z}(t)\|_{\text{RMS}} = \lim_{T \rightarrow \infty} \sqrt{\frac{1}{2T} \int_{-T}^T \sum_{i=1}^n |z_i(\tau)|^2 d\tau} \quad (\text{A.35})$$

A.6.3 System norms

This section was adopted from [7]. More information about system norms can be found there.

The concept of system norms is distinct from that of temporal norms. Given a linear dynamic system \mathbf{G} , system norms are typically defined as the worst-case temporal p -norm of the output signal of \mathbf{G} which is excited by an input signal of a specific class $\mathbf{u} \in \mathbf{U}$. [7]

A.6.3.1 \mathcal{H}_∞ system norm

Definition A.10: \mathcal{H}_∞ system norm [7]

Given a proper, stable linear system $\mathbf{G}(s)$ ($\mathbf{z}(s) = \mathbf{G}(s)\mathbf{w}(s)$), its \mathcal{H}_∞ system norm is defined as

$$\|\mathbf{G}(s)\|_\infty = \max_{\mathbf{w}(t) \neq \mathbf{0}} \frac{\|\mathbf{z}(t)\|_2}{\|\mathbf{w}(t)\|_2} = \max_{\|\mathbf{w}(t)\|_2=1} \|\mathbf{z}(t)\|_2 \quad (\text{A.36})$$

The \mathcal{H}_∞ system norm is an induced norm, and thus a matrix norm for which in further consequence the multiplicative property (A.29) holds.

For a stable, proper $\mathbf{G}(s)$, another definition of $\|\mathbf{G}\|_\infty$ based on the singular values of $\mathbf{G}(s)$ (see Section A.4) is:

$$\|\mathbf{G}(s)\|_\infty = \sup_{\omega \in \mathbb{R}} \bar{\sigma}(\mathbf{G}(j\omega)) \quad (\text{A.37})$$

Thus the \mathcal{H}_∞ norm is the peak of the maximum singular value magnitude over all frequencies.

For the numeric computation of the \mathcal{H}_∞ norm of a given system, an iterative bisection procedure is typically used to approximate the \mathcal{H}_∞ norm up to a demanded precision. The following norm definition involves a Hamiltonian matrix \mathbf{H} formed from the system state-space matrices ($\mathbf{G}(s) \stackrel{\text{ss}}{=} \left[\begin{array}{c|c} \mathbf{A} & \mathbf{B} \\ \hline \mathbf{C} & \mathbf{D} \end{array} \right]$). Assuming $\mathbf{G}(s)$ stable, then

$$\|\mathbf{G}(s)\|_\infty = \inf_{\gamma > 0} \gamma : \mathbf{H}(\gamma) \text{ has no imaginary eigenvalues} \quad (\text{A.38})$$

holds, where

$$\mathbf{H}(\gamma) = \begin{bmatrix} \mathbf{A}_H(\gamma) & \mathbf{B}\mathbf{R}^{-1}(\gamma)\mathbf{B}^T \\ -\mathbf{C}^T(\mathbf{I} + \mathbf{D}\mathbf{R}^{-1}(\gamma)\mathbf{D}^T)\mathbf{C} & -\mathbf{A}_H^T(\gamma) \end{bmatrix} \quad (\text{A.39})$$

with $\mathbf{A}_H(\gamma) = \mathbf{A} + \mathbf{B}\mathbf{R}^{-1}(\gamma)\mathbf{D}^T\mathbf{C}$, and $\mathbf{R}(\gamma) = \gamma^2\mathbf{I} - \mathbf{D}^T\mathbf{D}$.

If \mathbf{G} is not stable, its \mathcal{H}_∞ norm is infinite.

List of Figures

2.1	Experimental set-up	4
2.2	Characteristic curve of a piezo patch actuator (assuming linearity) (adopted from [8])	5
2.3	Schematic illustration of the experimental set-up (framework surrounding the beam is not drawn)	7
2.4	Simulink [®] subsystem: “MIMO beam”	9
3.1	Infinitesimally small beam element (adopted from [9])	10
3.2	Beam simply supported at both ends	12
4.1	Schematic illustration of an input signal of an actuator; quasi-continuous-time signal (stair-case signal)	16
4.2	Bode magnitude plot for parametric and non-parametric (\mathcal{S}) identified models of the beam with unmounted shaker	19
4.3	Singular values plot for parametric and non-parametric (\mathcal{S}) identified models of the beam without shaker	20
4.4	Bode magnitude plot for parametric and non-parametric (\mathcal{S}) identified models of the beam with mounted shaker	22
4.5	Singular values plot for parametric and non-parametric (\mathcal{S}) identified models of the beam with mounted shaker	24
5.1	Hermitian Beam Element for bending around the (local) y -axis (adopted from [3])	26
5.2	Example beam with three Hermitian Beam elements for bending around the y -axis.	28
5.3	Assembling the global stiffness matrix \mathbf{K} for a beam with three elements. . .	29
5.4	Modal damping coefficient $\zeta(\omega)$ in case of Rayleigh Damping and modal damp- ing coefficients ζ_i (for $i = 1, \dots, 5$) of the identified model $\mathbf{H}_{10+6}^{r\{10+0\}}$ of the beam without shaker	31
5.5	Generalized element node loads (positive direction) for a Hermitian beam element	32
5.6	Consistent node loads for a Hermitian beam element	33
5.7	Three element beam with four piezo actuators and the shaker force as inputs. .	34
5.8	Three element beam with four sensors. x_i is the local sensor position within an element.	36
5.9	Simplified model concept piezo patch actuator (utilizing moment input of FE model and state-space feed-through matrix \mathbf{D})	43
5.10	Three element beam with one acceleration sensor at the shaker position. x_s is the local length to the acceleration sensor within the third element.	45

5.11	Eigenvectors of the first 5 translational (left) / rotatory (right) degrees of freedom (pure beam)	49
5.12	Statical deformation of the pure beam, when a single force $F_d = 10$ N is applied at $l_s = 1.378$ m.	51
5.13	Statical deformation of the pure beam, when two opposite single moments (same value: $M = 10$ Nm) are applied via piezo actuator number three.	53
5.14	Convergence of the FE solution for different resolutions of the spatial discretization (hinged-hinged supported pure beam) $M_1 = 80$ Nm, $M_2 = 50$ Nm, $M_3 = -100$ Nm, $M_4 = 20$ Nm, $F_s = -90$ N (Loads as depicted in Figure 5.7 on page 34)	55
5.15	Comparison between $\varepsilon_{\text{bending}}$ and $\varepsilon_{\text{overall}}$ (hinged-hinged supported pure beam with 100 elements and 200 modes) $M_1 = 80$ Nm, $M_2 = 50$ Nm, $M_3 = -100$ Nm, $M_4 = 20$ Nm, $F_s = -90$ N (Loads as depicted in Figure 5.7 on page 34)	56
5.16	Model concept used for the shaker mounting. (m_1 is the mass of both mounting prisms. For simplification only one prism is drawn.)	57
5.17	Shaker modeling via feedback loops around the FE model of the pure beam	58
5.18	Statical deformation of the beam with mounted shaker, when a single force $F_d = 10$ N is applied at the shaker position $l_s = 1.378$ m. A cross is used to mark the position of the shaker coupling point.	60
5.19	Statical deformation of the beam with mounted shaker, when two opposite single moments (same value: $M = 10$ Nm) are applied via piezo actuator number three. A cross is used to mark the position of the shaker coupling point.	62
5.20	First five displacement- (w), slope- ($\frac{dw}{dx}$), and curvature- ($\frac{d^2w}{dx^2}$) proportional mode shapes of the FE beam with mounted shaker	64
5.21	Non-linear function of the force exerted by a piezo patch actuator to a structure (due to an applied voltage input signal) of the own elongation	65
6.1	Comparing FE and ID (“high order”) models of the beam with unmounted shaker in a Bode magnitude plot	72
6.2	Comparing FE and ID (“high order”) models of the beam with mounted shaker in a Bode magnitude plot	74
6.3	Comparing FE and ID (“high order”) disturbance models of the beam with mounted shaker in a Bode magnitude plot	76
6.4	Comparing FE and ID (“high order”) disturbance models of the beam with mounted shaker in a phase plot for output y_6 (associated with the force sensor)	77
6.5	Comparing FE and ID models of the beam with mounted shaker in a singular values plot (inputs u_1 to u_4 ; outputs y_1 to y_4)	78
7.1	LQG architecture	80
7.2	LQG controller and noisy plant	81
8.1	General control configuration (for controller synthesis)	83
8.2	Case where $\bar{\sigma}(\mathbf{S}(j\omega))$ exceeds its upper bound $ W^{-1}(j\omega) $, resulting in $\ W\mathbf{S}\ _\infty > 1$ (adopted from [6])	86
8.3	Exemplary weighting function $W(s)$ for damping of low-damped structural modes	88
8.4	$\mathbf{S}\mathbf{G}_d/\mathbf{K}\mathbf{S}\mathbf{G}_d$ mixed-sensitivity optimization (regulation)	89
8.5	Uncertain plant, $\mathbf{y} = \mathbf{G}_p\mathbf{u}$, represented by LFT (\mathbf{H} - Δ_{par} -structure)	93

8.6	Additive uncertainty	94
8.7	Multiplicative uncertainty	95
8.8	Exemplary Nyquist plot of $h_i(j\omega)$ and disc-shaped uncertainty region (at a given frequency ω) generated by complex additive uncertainty $h_{pi}(s) = h_i(s) + w_{Ai}(s)\Delta_{Ai}(s)$ with $ \Delta_{Ai}(j\omega) \leq 1$ (SISO case!). The set of possible plants $h_{pi}(s)$ includes the origin at frequencies ω where $ w_{Ai}(j\omega) \geq h_i(j\omega) $, or equivalently $ w_{Ii}(j\omega) \geq 1$ (adopted from [6])	96
8.9	General control configuration with uncertainty (for controller synthesis) . . .	96
8.10	Rearranging an uncertain system into the \mathbf{N} - $\mathbf{\Delta}$ -structure (adopted from [6])	98
8.11	\mathbf{N} - $\mathbf{\Delta}$ -structure for robust performance analysis	99
8.12	Uncertain closed-loop transfer function \mathbf{F}	99
8.13	\mathbf{M} - $\mathbf{\Delta}$ -structure for robust stability analysis	100
8.14	RP as a special case of RS with a block-diagonal $\hat{\mathbf{\Delta}} = \begin{bmatrix} \mathbf{\Delta} & \mathbf{0} \\ \mathbf{0} & \mathbf{\Delta}_P \end{bmatrix}$. As always NS has to be verified separately! (adopted from [6])	106
8.15	Use of block-diagonal scalings, $\hat{\mathbf{\Delta}} = \mathbf{D}_l \hat{\mathbf{\Delta}} \mathbf{D}_r^{-1}$ (adopted from [6])	108
8.16	Augmented plant interconnection with with multiplicative input uncertainty, additive uncertainty, and multiplicative output uncertainty	110
8.17	Design trade-offs for the multivariable loop transfer function $\mathbf{L} = \mathbf{G}\mathbf{K}$ (adopted from [6])	113
8.18	\mathcal{H}_∞ robust stabilization problem for coprime factor uncertainty	114
8.19	The shaped plant and controller	115
9.1	Singular values of performance weight $\mathbf{W}_1(z) = W_1(z) \cdot \mathbf{I}$ and input weight $\mathbf{W}_2(z) = W_2(z) \cdot \mathbf{I}$	122
9.2	Singular values of the feedback controller \mathbf{K}	122
9.3	Singular values plot of the closed-loop performance transfer function (vector) \mathbf{N} ($\mathbf{z} = \mathbf{N}w$, where $w = d$) and its individual stacked components	123
9.4	Singular values of simulated open-loop and closed-loop behavior (from d to \mathbf{y})	124
9.5	Experimental validation results in terms of singular values (from d to \mathbf{y}) of open-loop ($\mathcal{S}^{\text{OL-EV}}$) and closed-loop ($\mathcal{S}^{\text{CL-EV}}$) identified spectral models (mixed-sensitivity \mathcal{H}_∞ optimal design based on the “IDbs-model”)	124
9.6	Experimental validation results in terms of (disturbance path) Bode plots of open-loop ($\mathcal{S}^{\text{OL-EV}}$) and closed-loop ($\mathcal{S}^{\text{CL-EV}}$) identified spectral models (mixed-sensitivity \mathcal{H}_∞ optimal design based on the “IDbs-model”)	125
9.7	Measured open-loop and closed-loop output signal $\mathbf{y}(t)$ and control signal $\mathbf{u}(t)$ (disturbance excitation $d(t) = 1/4 \cdot \sin(2\pi f_1^{\text{IDbs}} t)$)	127
9.8	Measured open-loop and closed-loop output signal $\mathbf{y}(t)$ and control signal $\mathbf{u}(t)$ (disturbance excitation $d(t) = 1/4 \cdot \sin(2\pi f_4^{\text{IDbs}} t)$)	128
9.9	Measured open-loop and closed-loop output signal $\mathbf{y}(t)$ and control signal $\mathbf{u}(t)$ (disturbance excitation $d(t) = \sigma(t) - \sigma(t - \Delta t_1)$)	129
9.10	Singular values of $\mathbf{W}_{1A}(e^{j\omega T_s}) = W_{1A}(e^{j\omega T_s}) \cdot \mathbf{I}$ ($ W_{1A}(e^{j\omega T_s}) = \frac{(1-\epsilon)}{\sigma(\mathbf{K}\mathbf{S}(e^{j\omega T_s}))}$ with an infinitesimally small $\epsilon \in \mathbb{R}^+$)	130
9.11	Singular values of simulated open-loop and closed-loop behavior (from d to \mathbf{y})	134
9.12	Experimental validation results in terms of singular values (from d to \mathbf{y}) of open-loop ($\mathcal{S}^{\text{OL-EV}}$) and closed-loop ($\mathcal{S}^{\text{CL-EV}}$) identified spectral models (modally weighted LQG design based on the “IDbs-model”)	134

9.13	Maximum singular values of the weighting matrix (compensator) $\mathbf{W}_1(e^{j\omega T_s}) = W_1(e^{j\omega T_s}) \cdot \mathbf{I}$ and suggested guidelines	136
9.14	Singular values of the feedback controller \mathbf{K}	137
9.15	Singular values of desired loop shape or shaped plant \mathbf{G}_s ($\mathbf{G}_s(z) = \mathbf{G}(z)\mathbf{W}_1(z)$) and actual loop transfer function \mathbf{L}	138
9.16	Singular values of simulated open-loop and closed-loop behavior (from d to \mathbf{y})	139
9.17	Experimental validation results in terms of singular values (from d to \mathbf{y}) of open-loop ($\mathcal{S}^{\text{OL-EV}}$) and closed-loop ($\mathcal{S}^{\text{CL-EV}}$) identified spectral models (\mathcal{H}_∞ loop-shaping design based on the “IDbs-model”)	139
9.18	Singular values of performance weight \mathbf{W}_P ; input weight \mathbf{W}_u ; \mathbf{W}_{11} , \mathbf{W}_{10} for multiplicative input respectively output uncertainty, and \mathbf{W}_{1A} for additive uncertainty weighting	141
9.19	Singular values of the feedback controllers \mathbf{K}^{syn} and the reduced controller \mathbf{K}	143
9.20	μ -analysis (upper bounds) of nominal performance ($\bar{\sigma}(\mathbf{N}_{22}(e^{j2\pi f T_s})) = \mu_{\Delta_P}(\mathbf{N}_{22}(e^{j2\pi f T_s})))$, robust stability ($\mu_{\Delta}(\mathbf{N}_{11}(e^{j2\pi f T_s}))$) and robust performance ($\mu_{\Delta}(\mathbf{N}(e^{j2\pi f T_s}))$)	144
9.21	Nominal performance ($\bar{\sigma}(\mathbf{N}_{22})$), performance of the particular perturbed plant $\mathbf{G}^{\text{IDbs(ho)}}(z)$ ($\bar{\sigma}(\mathcal{F}_u(\mathbf{N}, \Delta^{\text{IDbs(ho)}}))$), worst-case performance ($\mu^s(\mathbf{N}(e^{j\omega T_s}))$ - upper bound) and robust performance ($\mu_{\Delta}(\mathbf{N})$ - upper bound)	145
9.22	Singular values of simulated open-loop and closed-loop behavior (from d to \mathbf{y})	146
9.23	Experimental validation results in terms of singular values (from d to \mathbf{y}) of open-loop ($\mathcal{S}^{\text{OL-EV}}$) and closed-loop ($\mathcal{S}^{\text{CL-EV}}$) identified spectral models (DK synthesized μ -”optimal” design based on the “IDbs-model”)	147
9.24	Singular values of performance weight $\mathbf{W}_1(s) = W_1(s) \cdot \mathbf{I}$ and input weight $\mathbf{W}_2(s) = W_2(s) \cdot \mathbf{I}$	149
9.25	Singular values of simulated open-loop and closed-loop behavior (from d to \mathbf{y})	150
9.26	Experimental validation results in terms of singular values (from d to \mathbf{y}) of open-loop ($\mathcal{S}^{\text{OL-EV}}$) and closed-loop ($\mathcal{S}^{\text{CL-EV}}$) identified spectral models (mixed-sensitivity \mathcal{H}_∞ optimal design based on the “FEbs-model”)	150
9.27	Singular values of $\mathbf{W}_{1A}(j\omega) = W_{1A}(j\omega) \cdot \mathbf{I}$ ($ W_{1A}(j\omega) = \frac{(1-\epsilon)}{\bar{\sigma}(\mathbf{K}\mathbf{S}(j\omega))}$ with an infinitesimally small $\epsilon \in \mathbb{R}^+$)	151
9.28	Singular values of simulated open-loop and closed-loop behavior (from d to \mathbf{y})	153
9.29	Experimental validation results in terms of singular values (from d to \mathbf{y}) of open-loop ($\mathcal{S}^{\text{OL-EV}}$) and closed-loop ($\mathcal{S}^{\text{CL-EV}}$) identified spectral models (modally weighted LQG design based on the “FEbs-model”)	154
9.30	Maximum singular values of the weighting matrix (compensator) $\mathbf{W}_1(j\omega) = W_1(j\omega) \cdot \mathbf{I}$ and suggested guidelines	155
9.31	Singular values of the positive feedback controller \mathbf{K}	156
9.32	Singular values of desired loop shape or shaped plant \mathbf{G}_s ($\mathbf{G}_s(s) = \mathbf{G}(s)\mathbf{W}_1(s)$) and actual loop transfer function \mathbf{L}	156
9.33	Singular values of simulated open-loop and closed-loop behavior (from d to \mathbf{y})	157
9.34	Experimental validation results in terms of singular values (from d to \mathbf{y}) of open-loop ($\mathcal{S}^{\text{OL-EV}}$) and closed-loop ($\mathcal{S}^{\text{CL-EV}}$) identified spectral models (\mathcal{H}_∞ loop-shaping design based on the “FEbs-model”)	158
9.35	Singular values of performance weight \mathbf{W}_P ; input weight \mathbf{W}_u ; \mathbf{W}_{11} , \mathbf{W}_{10} for multiplicative input respectively output uncertainty, and \mathbf{W}_{1A} for additive uncertainty weighting	159
9.36	Singular values of the feedback controller \mathbf{K}	160

9.37	μ -analysis (upper bounds) of nominal performance ($\bar{\sigma}(\mathbf{N}_{22}(j\omega)) = \mu_{\Delta_P}(\mathbf{N}_{22}(j\omega))$), robust stability ($\mu_{\Delta}(\mathbf{N}_{11}(j\omega))$) and robust performance ($\mu_{\hat{\Delta}}(\mathbf{N}(j\omega))$) and worst-case performance ($\mu^s(\mathbf{N}(j\omega))$ - upper bound)	161
9.38	Singular values of simulated open-loop and closed-loop behavior (from d to \mathbf{y})	162
9.39	Experimental validation results in terms of singular values (from d to \mathbf{y}) of open-loop ($\mathcal{S}^{\text{OL-EV}}$) and closed-loop ($\mathcal{S}^{\text{CL-EV}}$) identified spectral models (DK synthesized μ -“optimal” design based on the “FEbs-model”)	162
9.40	Singular values of performance weight \mathbf{W}_P ; input weight \mathbf{W}_u ; \mathbf{W}_{11} , \mathbf{W}_{10} for multiplicative input respectively output uncertainty weighting	163
9.41	Singular values of the feedback controller \mathbf{K}	167
9.42	μ -analysis (upper bounds) of nominal performance ($\bar{\sigma}(\mathbf{N}_{22}(j\omega)) = \mu_{\Delta_P}(\mathbf{N}_{22}(j\omega))$), robust stability ($\mu_{\Delta}(\mathbf{N}_{11}(j\omega))$) and robust performance ($\mu_{\hat{\Delta}}(\mathbf{N}(j\omega))$) and worst-case performance ($\mu^s(\mathbf{N}(j\omega))$ - upper bound)	168
9.43	Singular values of simulated open-loop and closed-loop behavior (from d to \mathbf{y})	169
9.44	Experimental validation results in terms of singular values (from d to \mathbf{y}) of open-loop ($\mathcal{S}^{\text{OL-EV}}$) and closed-loop ($\mathcal{S}^{\text{CL-EV}}$) identified spectral models (DGK synthesized μ -“optimal” design based on the “FEbs-model”)	169
9.45	Experimental validation results in terms of singular values (from d to \mathbf{y}) of open-loop ($\mathcal{S}^{\text{OL-EV}}$) and closed-loop ($\mathcal{S}^{\text{CL-EV}}$) identified spectral models (alternative DGK synthesized μ -“optimal” design based on the “FEbs-model”) .	171
A.1	One degree-of-freedom negative feedback control systems	177
A.2	One degree-of-freedom (negative) feedback configuration	178
A.3	Magnitude plot of typical loop transfer function L , sensitivity function S and complementary sensitivity function T (SISO case, $L(s) = \frac{1}{s(s+1)}$)	179
A.4	State-Space Representation	179
A.5	Transfer function representation	180

List of Tables

2.1	Mechanical dimensions of the experimental set-up	7
2.2	Components of the control system setup	8
3.1	Frequency equations and their roots for important boundary conditions. The natural frequencies can be computed by $\omega_i = \lambda_i^2 \sqrt{\frac{EJ_y}{\rho A}}$. (adopted from [9]) . .	14
4.1	Cross-validation results for the models of the beam without shaker	18
4.2	Natural frequencies of the model $\mathbf{H}_{10+6}^{r\{10+0\}}$ of the beam without shaker . . .	20
4.3	Cross-validation results for the models of the beam with mounted shaker . .	21
4.4	Natural frequencies of the model $\mathbf{H}_{10+8}^{r\{10+0\}}$ of the beam with mounted shaker	24
5.1	Coincidence table for a beam with three elements.	28
5.2	Required physical parameters of the beam for computing its natural frequencies via analytical equations (see [9]).	47
5.3	Comparing analytical and FE solution for the natural frequencies of the pure beam (beam with unmounted shaker) for different boundary conditions. . . .	48
5.4	Statical solution for F_{est} and w_{sp} (see Figure 5.16) when a single force $F_d = 10 \text{ N}$ is applied to the beam with mounted shaker	59
5.5	Statical solution for F_{est} and w_{sp} (see Figure 5.16) when two opposite single moments (same value: $M = 10 \text{ Nm}$) are applied to the beam with mounted shaker via piezo actuator number three.	61
5.6	Computed ratio between max. applied force and blocking force for a hinged-hinged beam	66
6.1	Model origin of input-output scaled final models of the hinged-hinged beam with unmounted shaker	70
6.2	Model origin of input-output scaled final models of the hinged-hinged beam with mounted shaker	70
6.3	Comparing natural frequencies and modal damping coefficients between FE and identified models of the beam with unmounted shakers (“FEb-model”, “IDb-model”)	73
6.4	Comparing natural frequencies and modal damping coefficients between FE and identified models of the beam with mounted shakers (“FEbs-model”, “IDbs-model”)	77
8.1	Closed-loop equivalent open-loop requirements (in addition to the requirement that \mathbf{K} stabilizes \mathbf{G}) [6], ω_B is the bandwidth frequency ($\bar{\sigma}(\mathbf{S}(j\omega_B)) = \frac{1}{\sqrt{2}}$) .	113
9.1	Natural frequencies and damping parameters (poles)	152

9.2	relative magnitude $w_{i\omega}$ of the (symmetric) uncertainty of the natural angular frequency ω_i ($\omega_{ip} = \omega_i(1 + w_{i\omega}\delta_{i\omega})$ with $-1 \leq \delta_{i\omega} \leq 1$)	165
10.1	Overview controller design methods (including the author's opinion)	176
A.1	Closed-loop requirements (in addition to the requirement that \mathbf{K} stabilizes \mathbf{G}) (adopted from [6])	178

Bibliography

- [1] Rolf Isermann. *Identifikation dynamischer Systeme 1*. Springer, 1992.
- [2] Rolf Isermann. *Identifikation dynamischer Systeme 2*. Springer, 1992.
- [3] Franz Rammerstorfer. Grundlagen der Finite Elemente Methoden. Technical report, Vienna University of Technology, lecture notes, SS 2010.
- [4] Markus Merkel. *Eindimensionale Finite Elemente*. Springer, 2010.
- [5] Wodek K. Gawronski. *Advanced Structural Dynamics an Active Control of Structures*. Springer, 2004.
- [6] Sigurd Skogestad and Ian Postlethwaite. *Multivariable Feedback Control*. Wiley, 2005.
- [7] Alexander Schirrer. *Efficient robust control design and optimization methods for flight control*. PhD thesis, 2011.
- [8] Piezo Patch Transducer for Energy Harvesting; DuraAct PI: Ultra Precision Motion Control:, 10 2012. <http://www.duraact.net/>.
- [9] Heinz Parkus. *Mechanik der festen Körper*. Springer, 2005.
- [10] Christian Bucher. Mechanik 2. Technical report, Vienna University of Technology, lecture notes, WS 2012/13.
- [11] Hans Troger. Mechanik 3. Technical report, Vienna University of Technology, lecture notes, 2005.
- [12] Christian Benatzky. *Theoretical and experimental investigation of an active vibration damping concept for metro vehicles*. PhD thesis, TU Vienna, 2006.
- [13] Stefan Jakubek. Zustandsregelung von Mehrgrößensystemen. Technical report, Vienna University of Technology, lecture notes, SS 2010.
- [14] Inc. The MathWorks. Control System Toolbox - Getting Started Guide. Technical report, R2011b.
- [15] Declan G Bates and Ian Postlethwaite. *Robust Multivariable Control of Aerospace Systems*. DUP Science, 2002.
- [16] Duncan McFarlane Keith Glover. A Loop Shaping Design Procedure Using \mathcal{H}_∞ Synthesis. *IEEE Transactions on Automatic Control*, 37:759–769, 1992.
- [17] Martin Kozek and Stefan Jakubek. Identifikation - Experimentelle Modellbildung. Technical report, Vienna University of Technology, lecture notes, v2.0, 2010.